TRANSVERSE AND LONGITUDINAL BENDING OF SEGMENTAL CONCRETE BOX GIRDER BRIDGES

Marcus Maguire

Dissertation submitted to the faculty of the

Virginia Polytechnic Institute and State University

in partial fulfillment of the requirements for the degree of

Doctor of Philosophy

in

Civil Engineering

Carin L. Roberts-Wollmann, Chair

Thomas E. Cousins

Cristopher D. Moen

Roberto T. Leon

6/26/2013

Blacksburg, VA

Keywords: Field Testing, Transverse Bending, Segmental Concrete Box Girders

Abstract

Post-tensioned segmental concrete box girders have been in use in the United States since the early 1970s. This unique bridge system uses post-tensioning to connect many smaller concrete bridge segments into very efficient long span bridges. However, because of the slender components, localized transverse bending becomes more critical when compared to more conventional bridge types. Bridge owners are finding that ratings for standard loads and permit trucks are often controlled by the transverse behavior of the girders near concentrated wheel loads. The popular analysis methods used today range from two dimensional frame models to three dimensional finite element models of the entire bridge. Currently, engineers must make sound engineering judgments on limited available information, while balancing safety and economy.

To quantify and understand longitudinal and transverse behavior, the results from three live load tests of single cell segmental concrete box girder bridges are presented. Each bridge was instrumented with longitudinal and transverse strain sensors on at least two cross sections as well as rotation and deflection sensors, when possible. Two dimensional transverse frame models and three dimensional shell models were compared to the test results for each subject bridge. The two dimensional frame analyses using the common bottom web pin and roller boundary conditions provide mean absolute percent error in excess of 250%. Conversely, the newly introduced boundary conditions using pin supports at the top and bottom of each web was shown to reduce mean absolute percent error to 82%, which is on the same order of magnitude as longitudinal beamline analysis.

The three dimensional shell models were insensitive to several changes including mesh fineness, number of spans modeled, and support conditions. Using uniform surface loading, the transverse modeling procedure was shown to provide significantly more accurate results than the common two dimensional frame models. A faster and more convenient analysis method using a program generated, structure specific, influence surface was also outlined. This method produced similar results when compared to the uniform surface loading method, while allowing additional automation for easier load application.

Table of Contents

Table of Figures

Table of Tables

1 Introduction

Post-tensioned segmental concrete box girders have been in use in the United States since the early 1970s. This unique bridge system uses post-tensioning to connect many smaller concrete bridge segments into very efficient long span bridges. Segmental box girder bridges are marked by their large, but slender cross sections. The most common cross sections for segmental concrete bridges are winged, single celled, box girders. These girders can be of constant cross-section throughout the bridge length, using span-by-span construction or variable depth using balanced cantilever construction. Because these girders are large with slender components, local effects become more critical when compared to more conventional bridge types.

During bending, the longitudinal stress distribution in the flanges becomes more concentrated near the flange-to-web intersection, especially near the piers. This phenomenon, called shear lag, is most often quantified in design by the effective width method. Shear lag, identified in the late 1800's, is a relatively well-understood mechanical phenomenon; however, there are few full-scale field-tests of segmental concrete bridges that investigate this effect. Damage or distress caused by shear lag has not posed a problem in segmental concrete box girders, likely due to thickening of components near flange-to-web intersections and the design code effective width procedures.

Bridge owners are finding that ratings for standard loads and permit trucks are controlled by the transverse behavior of the girders near concentrated wheel loads. Transverse analysis, in its most common form, is two-dimensional and neglects important mechanical behavior. The design of slender segmental concrete box girder components (wings, webs, top and bottom slabs) requires that local transverse bending is checked. The design loads determine flange and web sizing as well as the required prestressed and mild reinforcement. For typical load rating, web and cantilever wing stresses limit live load capacity. The methods used to determine these effects range in complexity. The popular analysis methods used today range from two dimensional frame models to three dimensional finite element models of the entire bridge. However, there is little guidance or research on how well each method performs. Currently, engineers must make sound engineering judgments on limited available information, while balancing safety and economy.

These two dimensional frame and three dimensional finite element models often neglect the effect of barrier rails and other appurtenances on structural stiffness and strength .This is done for two reasons: 1) The barrier rail may be purposefully removed during future bridge alterations or damaged through vehicular collision, and 2) the difficulty of including barrier affects in structural models. Previous research programs have noted the effects of barrier rails in various bridge types (e.g., Hawkins and Clark 1983, Kuhn 2008 Akinci et al. 2008, Mabsout et al. 1997). There is evidence of barrier rail interaction with shear lag (Hawkins and Clark 1983) and transverse analysis (Kuhn 2008). Quantification of this interaction will be directly beneficial to both designers and load raters looking for designs that are more efficient or additional live load reserve. In situations where barrier rails increase stiffness and/or strength, more efficiency in design can be achieved and future posting of deteriorated or damaged segmental concrete box girder bridges can be improved.

1.1 Objectives

The objectives for this research are as follows: 1) to quantify the effects of local transverse bending and to propose a more accurate technique for analyzing for this behavior, 2) investigate analysis techniques for modeling barrier rails for use in transverse bending analyses, and 3) to evaluate the level of shear lag in segmental post tensioned concrete bridges subject to live loading. The literature review found a significant lack of experimental information regarding transverse bending and shear lag in real structures. To add to the available information on these two objectives, the results from three live load tests of single cell segmental concrete box girder bridges are presented. The first bridge, tested in April, 2011 was the Seabreeze Bridge in Daytona, Florida. The second bridge was the Smart Road Bridge, located in Blacksburg, Virginia and was tested in May, 2012. The final bridge tested was the Varina-Enon Bridge approach structure, in Richmond, Virginia and was tested in the August, 2012.

The investigation into each structure focused on measuring longitudinal strains, deflections and rotations to quantify longitudinal behavior and measuring transverse strains to quantify localized transverse bending. The results from the field tests are used to evaluate predictions from popular analysis techniques for longitudinal and transverse analysis. The experimental results are used to

outline modifications to the traditional two dimensional frame analysis method and to propose an easy-to-implement, three dimensional, analysis technique that improves the accuracy of transverse bending predictions.

2 Literature Review

There are few known issues reported regarding shear lag in practice (Roberts 1993), but the phenomenon remains a common topic among researchers. Additionally, damage or distress associated with transverse bending is not a problem. This may be due to the ways designers have approached these problems in the past, by using conservative and simplified analysis techniques.

Transverse bending limit states do affect the load and permit rating for segmental box girders. Improved methods based on comparison between true box girder response and typical design assumptions will result in designs that are more efficient and higher ratings for existing bridges. Furthermore, the body of literature focusing on transverse bending is not large, making it difficult for designers to know the accuracy of their analysis assumptions. The literature review below summarizes previous work performed with respect to segmental box girder design. The following is a background on shear lag, transverse analysis and a review of box girder live load testing.

2.1 Shear Lag

Elementary bending theory assumes, among other things, plane sections before bending remain plane after bending. This creates a linear strain profile through the depth of any given cross section. This assumption is very good when beam cross-section components are non-slender, the shear stiffness of the member is high and the effects of bending dominate the cross-section. Figure 1 demonstrates how shear flow between intersecting parts of a member, such as the web and flange, causes longitudinal displacement of the material such that it is larger near component intersections. Longitudinal deformations, largest near the intersection, cause non-linear transverse and longitudinal stress distributions in the various components with peaks near the intersections (Reissner 1938). Figure 2 demonstrates the difference between simple bending theory strain distribution and the shear lag phenomenon.

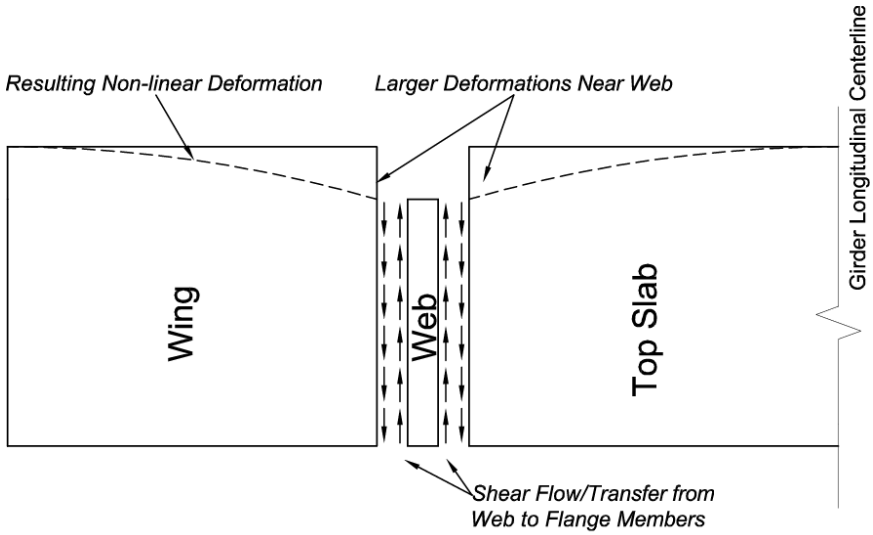

Figure 1 – Non-linear Longitudinal Deformations Caused by Shear Lag

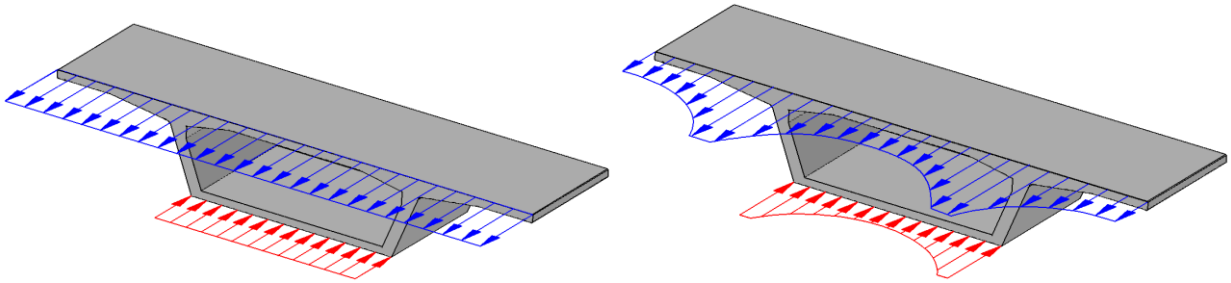

(a) (b)

Figure 2 – Strain Distribution across Box Girder Flanges (a) Without Shear Lag (b) With Shear Lag

The shear lag phenomenon is essentially the effect of a stress concentration, much like at a crack or a hole, caused by the stress raiser of the web-flange interface. These stress concentrations can be very significant, especially for slender members. Additionally, the difference between the stress near the flange and reduced stress farther away from the concentration reduces cross-section efficiency. Often, concrete box girder designers will increase the thickness of components near concentrations to increase their efficiency.

2.1.1 Historical Solutions to the Shear Lag Problem

The shear lag effect was first identified with respect to ship construction where wide thin membranes (hulls) were stiffened with relatively small ribs as early as 1894, as reported by Miller (1920). For this reason, the early academic discussion on shear lag centered around ship and monocoque structures for maritime and aircraft design. Many analytical methods exist, which attempt to define the non-linear longitudinal stresses.

The equivalent sheet and stringer analogies were primarily developed for monocoque structures as early as the 1930s (Younger 1930; Kuhn 1937; Hadji-Argyris and Cox 1944; Williams 1960). The equivalent sheet method distributes the longitudinal stringers into an axial force-carrying sheet and assumes the original plate transferred only shear force. The finite stringer approach assumes all axial capacity lumped together at the longitudinal stiffeners, connected by a shear transferring plate. These methods more recently analyzed for use in civil engineering structures by Evans and Taherian (1977, 1980), result in large sets of differential equations and often require significant assumptions.

Many research programs have focused on a bi-harmonic analysis of the shear lag problem. This analysis technique breaks up the web and flanges into individual plates connected at the original joints in the problem. Each plate is assumed to be in a state of plane stress such that a following fourth-order partial differential equation (a bi-harmonic equation) describes compatibility for a differential element:

$$\frac{\partial^4 \varphi}{\partial x^4} + \frac{\partial^4 \varphi}{\partial x^2 \partial y^2} + \frac{\partial^4 \varphi}{\partial y^4} = 0 \qquad \textit{Equation 1}$$

Where:

- $\varphi = \varphi(x, y)$ is the Airy stress function (Chou and Pagano, 1967)

Many researchers have attempted to work through this solution, typically described through Fourier series, with various modifications (Winter 1940; Kristek et al., 1990; Song 1990a; Tahan et al. 1997). All bi-harmonic solutions are computationally intense, prohibiting hand solution for design. Song (1990a) implemented the above harmonic analysis into a FORTRAN computer program, SHLAG, which provides the harmonic solution for beams of any support conditions.

Interestingly, the bi-harmonic analyses neglect material behavior (Young's Modulus, Shear Modulus) in their solution.

Shear lag solutions have also been treated using an energy approach. Energy based analyses assume the (unknown) strain distribution along the flanges to be a specific form (e.g., polynomial). The internal and external energy/work is then accounted for using the principle of minimum potential energy (Reissner 1946) and/or the method of least work (Reissner 1941). These techniques were first outlined by Reissner, but have been modified by numerous authors (Kuzmanovic and Graham, 1981; Horie et al. 1984; Dezi and Mentrasti 1985).

The above methods have been implicitly deemed too complicated and tedious because they are rarely, if ever, used in design. This is also evident in how design specifications from around the world account for shear lag. The following examines the shear lag and effective width with respect to design codes in more detail.

2.1.2 Effective Flange Width for Box Girders

When using elementary beam theory, the non-linear stress distributions due to shear lag, cause difficulty. Designers are able to simplify design by employing a uniform stress distribution on a reduced flange width, as shown in Figure 3, which allows design with elementary beam theory. Von Karman (1924) introduced the term "Die Mittragende Breite" or "the effective width" for this process, although this design technique was already relatively widespread in design. More rigorously defined, to determine the effective flange, one must equate the area of the effective stress distribution across the flange with the area of the real non-linear distribution. The following equation reflects this relationship:

$$b_e = \frac{1}{\sigma_{max}} \int_{y=0}^{b} \sigma_x(y) dy \qquad \textit{Equation 2}$$

Where:

- b_e is the effective flange width
- σ_{max} is the maximum normal stress in the flange (typically over web-flange junction)
- y is the position along the flange

- b is the maximum width of the flange
- $\sigma_x(y)$ is the normal stress distribution, as a function of y along the width of the flange

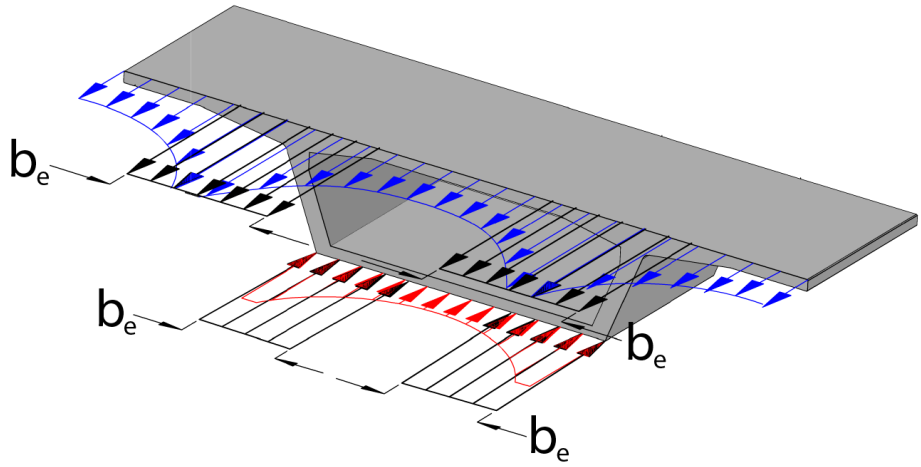

Figure 3 – Effective Flange Width Definition

The effective flange width applies to tension and compression non-linear stress distributions. The use of an effective flange width affects cross-section properties used in design. The flange reduction causes changes in the area, moment of inertia and neutral axis, which affects resulting design calculations.

Many numerical studies (Moffatt and Dowling 1978, Kumar 2010, Tenchev 1996, Sa-nguanmanasak 2006) have indicated a wide range of parameters affect the effective flange width, including load type, support conditions, material stiffness, thickness of the intersecting members and tension flange cracking.

Design specifications around the world govern the effective flange width for their respective regions. The following summarizes major specification's effective flange width recommendations.

2.1.2.1 AASHTO Standard

The American Association of State Highway Transportation Officials (AASHTO) Standard Specifications (AASHTO 1977) recommend the following for box girders:

$$b_e = minimum \begin{cases} \frac{L}{4} \\ 12h_f + b_w \\ \frac{b_f}{2} \end{cases} \qquad \textit{Equation 3}$$

Where:

- b_e is the effective flange width
- L is the span length
- h_f is the average depth of the flange
- b_w is the web thickness
- b_f is the flange width

Equation 3 is similar to the ACI 318 building code (ACI 2008) for concrete T-beams, which is not presented.

2.1.2.2 AASHTO LRFD/AASHTO Bridge Design Specifications

The AASHTO Load and Resistance Factor Design (LRFD) Specifications (2010) present an empirical approach for determining the effective flange width of box girders. Based on finite element studies and sensitivity analysis by Chen et al. (2005), AASHTO presents the effective flange width equal to the physical flange width if:

- $b \leq 0.1 l_i$
- $b \leq 0.3 d_o$

Otherwise, the effective width of outstanding flanges may be taken as specified in Table 1, Figure 4 and Figure 5 where:

- d_o is the depth of the superstructure (in.)
- b is the physical flange width on each side of the web, e.g., b_1, b_2, and b_3 as shown in Figure 5 (in.)
- b_e is the effective flange width corresponding to the particular position of the section of interest in the span as specified in Table 1 (in.)
- b_m is the effective flange width for interior portions of a span as determined from Figure 4; a special case of b_e (in.)

- b_s is the effective flange width at interior support or for cantilever arm as determined from Figure 4; a special case of b_e (in.)
- a is the portion of span subject to a transition in effective flange width taken as the lesser of the physical flange width on each side of the web shown in Figure 5 or one quarter of the span length (in.)
- l_i is a notional span length specified in Table 1 for the purpose of determining effective flange widths using Figure 4

Table 1 – Pattern of Effective Flange Width (Adapted from AASHTO LRFD 2010; Figure 4.6.2.6.2-1)

System		Pattern of b_m/b
Single-Span Girder $l_i = 1.0*l$		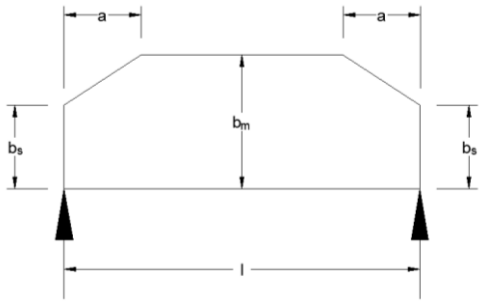
Continuous Girder	End Span $l_i = 0.8*l$	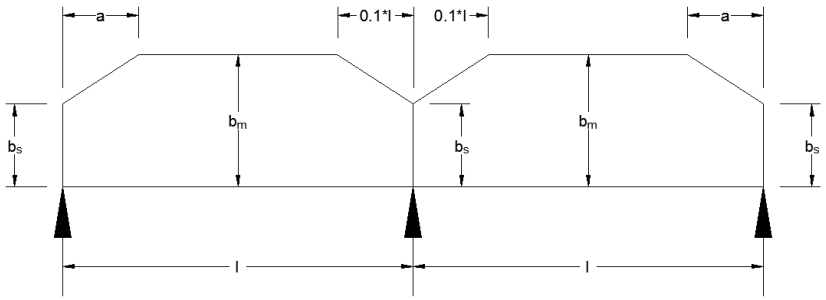
	Interior Span $l_i = 0.6*l$	
Cantilever Arm $l_i = 1.5*l$		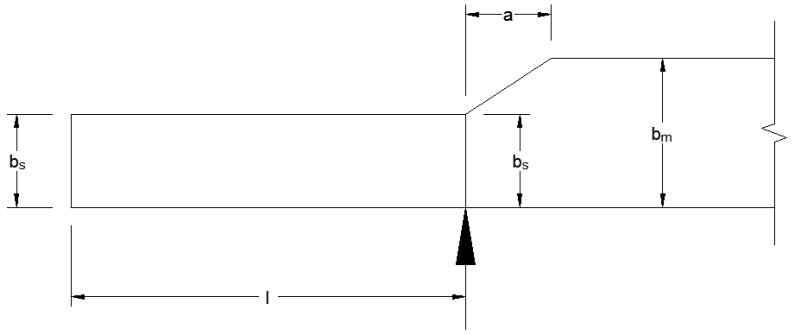

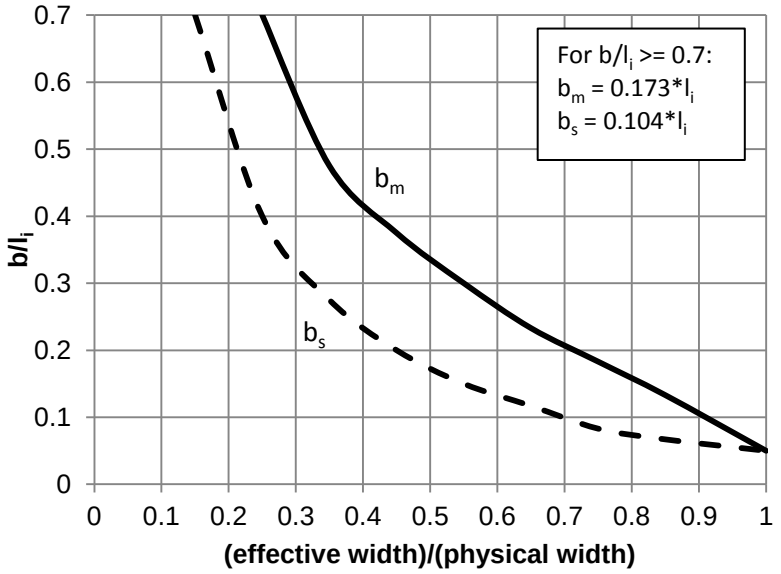

Figure 4 – Effective Flange Width Empirical Curve (adapted from AASHTO LRFD 2010; Figure 4.6.2.6.2-2)

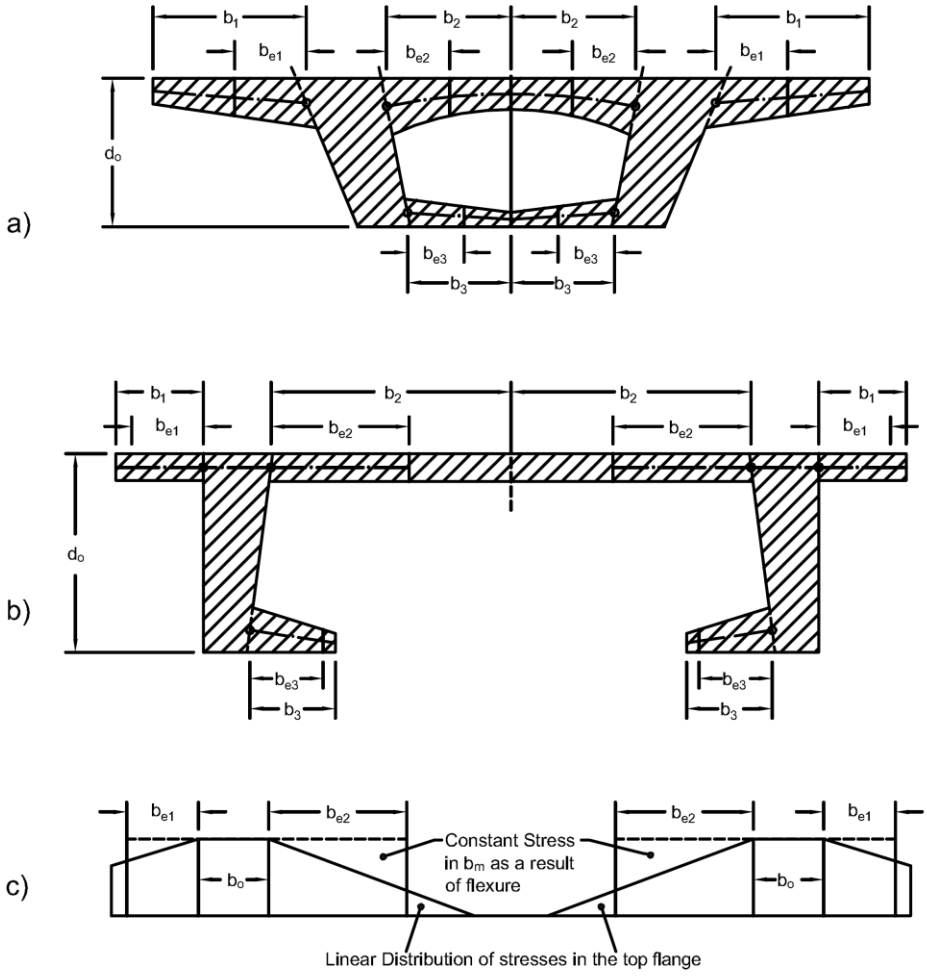

Figure 5 – Examples of Effective Flange Dimensions (Adapted from AASHTO LRFD 2010; Figure 4.6.2.6.2-3)

The AASHTO Interim 2003 Guide Specifications for Design and Construction of Segmental Concrete Bridges (from here on referred to as AASHTO Segmental) employ a similar approach to AASHTO LRFD. The AASHTO Segmental guide replaces the linearly varying effective flange width in Table 2, with a single step reduction, presented in Table 3. Roberts (1993) suggested this modification to reduce tedious and unnecessary re-calculation of section properties inside the linearly varying region.

Table 2 – Pattern of Effective Flange Width (Adapted from AASHTO Segmental 2003; Figure 4.6.2.6.2-1)

System	Pattern of Effective Flange Widths	Effective Span Length
Single-Span Girder	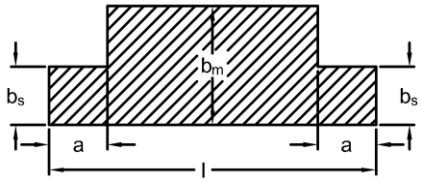	$l_i = l$
End Span of Continuous Girder	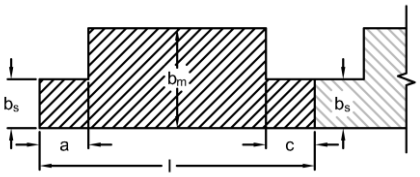	$l_i = 0.8*l$
Inner Span of Continuous Girder	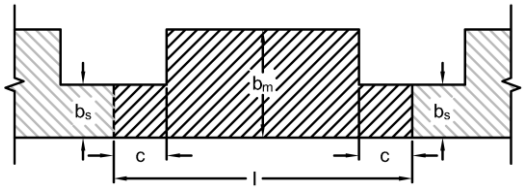	$l_i = 0.6*l$
Cantilever Arm	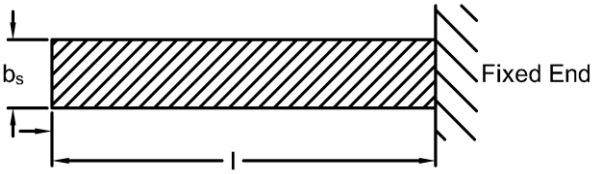	$l_i=1.5*l$

*a = largest b, but not exceeding 0.25*l*

*c = 0.1*l*

2.1.2.3 Canadian Design Code

Clause 5.8.2.1 of the Canadian Highway Bridge Design Code (CSA, 2000) covers the effective flange width for composite and non-composite concrete slab-on-girder bridges. These effective flange widths apply to both concrete and steel box girder bridges. The following equations define the effective flange width:

$$\frac{B_e}{B} = 1 - \left\{1 - \frac{L}{15B}\right\} \quad for\ \frac{L}{B} < 15 \qquad \textit{Equation 4}$$

$$\frac{B_e}{B} = 1 \quad for \ \frac{L}{B} > 15 \qquad \textit{Equation 5}$$

Where:

- B_e is the dimension shown in Figure 6 defining the reduced overhang width of the effective width
- B is the dimension shown in Figure 6 defining original overhang width or half the clear span
- L is the length between inflection points as defined in Figure 7

Equation 4 and Equation 5 are based on a curve fit to numerical parametric study results, performed using a finite strip analysis procedure (Cheung and Chan, 1978). Like the AASHTO LRFD specifications, the Canadian Highway Bridge Design Code does not account for many factors that, as presented above, affect the effective width.

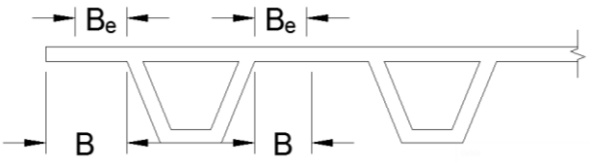

Note: *For the purpose of determining effective flange width only, in a bridge that is free of moment restraint at its ends, in lieu of the above, the positive moment region of an end span may be taken as the outermost 80% of it, and the positive moment region of an interior span may be taken as the central 60% of it.*

Figure 6 – Visualization of B_e and B (Adapted from CAN/CSA-S6-00 2000 Figure 5.8.2.1)

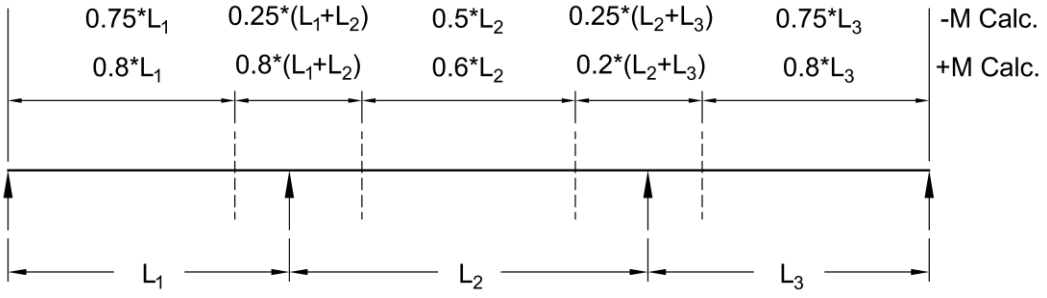

Figure 7 – Assumed Points of Bending Moment Inflection for Equation 4 and Equation 5 (Adapted from CSA 2000 Figure A5.1(a))

2.1.2.4 Eurocode 2

Concrete, steel and composite structures each have separate effective width provisions in the European design standards (Eurocode 2, 1992). Presented here are only the concrete structures provisions for effective width. See EN 1993-1-5 and EN 1994-1-1 for effective width for steel structures and composite structures, respectively.

Clause 2.5.2.2.1 *Effective width of flanges* (all limit states), from EN 1992-1-1:1992 Design of Concrete Structures is quoted as follows:

(1) In T beams the effective flange width depends on the web and flange dimensions, the type of loading, the span, the support conditions and the transverse reinforcement.

(2) For analysis, when a great accuracy is not required (e.g., continuous beams in buildings), a constant width may be assumed over the whole span.

(3) The effective width for a symmetrical T beam may be taken as:

$$b_{eff} = b_w + \frac{1}{5} l_o < b \qquad \textit{Equation 6}$$

and, for an edge beam (i.e., with flange on one side only):

$$b_{effi} = b_w + \frac{1}{10} l_o \leq b_i + b_w \; (i = 1 \; or \; 2) \qquad \textit{Equation 7}$$

(for the notations see Figure 8 and Figure 9 below).

(4) The distance l_o between points of zero moment may be obtained from Figure 9 for typical cases.

The following conditions should be satisfied:

i) The length of the cantilever should be less than half the adjacent span.

ii) The ratio of adjacent spans should lie between 1 and 1.5.

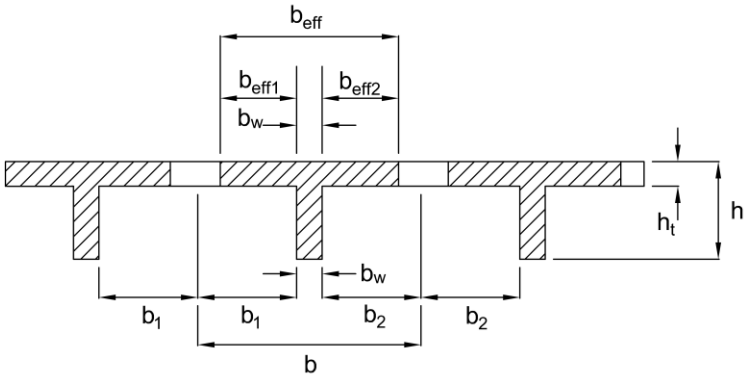

Figure 8 – Eurocode 2 Effective Flange Width Definitions (Adapted from Eurocode 2 1992: Figure 2.2)

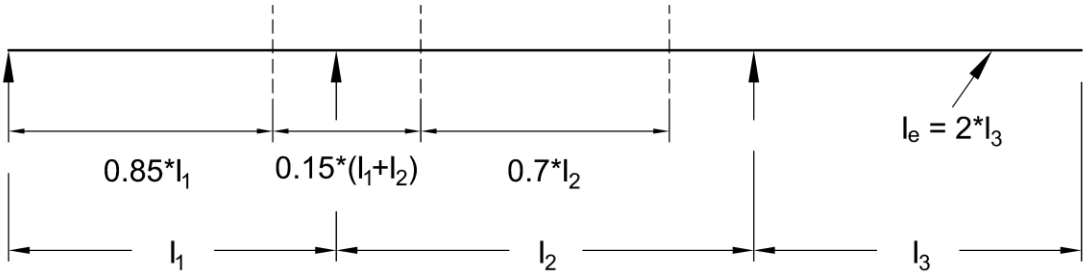

Figure 9 – Eurocode 2 Effective Length Definitions (Adapted from Eurocode 2 1992: Figure 2.3)

Equation 7 is a modified form of Equation 6 for asymmetric flanges often present for external beams.

2.1.2.5 JRA Design Specification

The 1996 Japanese Design Specification for Highway Bridges (as reported by Ahn et al. 2004) distinguished between the effective flange width for distributed loads and for concentrated loads. For members with distributed loads:

$$\lambda = b \quad for \ \frac{b}{L} > 0.05 \qquad \textit{Equation 8}$$

$$\lambda = \left[1.1 - 2\left(\frac{b}{L}\right)\right] b \quad for \ 0.05 < \frac{b}{L} \leq 0.30 \qquad \textit{Equation 9}$$

$$\lambda = 0.15L = 1 \quad for \ 0.30 \leq \frac{b}{L} \qquad \textit{Equation 10}$$

For members under the effects of a concentrated load:

$$\lambda = b \quad for\ \frac{b}{L} > 0.02 \qquad \textit{Equation 11}$$

$$\lambda = \left[1.06 - 3.2\left(\frac{b}{L}\right) + 4.5\left(\frac{b}{L}\right)^2\right] b \quad for\ 0.02 < \frac{b}{L} \leq 0.30 \qquad \textit{Equation 12}$$

$$\lambda = 0.15L \quad for\ 0.30 \leq \frac{b}{L} \qquad \textit{Equation 13}$$

Where:

- λ is the one side effective flange width (cm)
- b is one half clear distance between girders/box webs or overhang width (cm)
- L is the equivalent span length (cm) as presented by CAN/CSA-S6-00 in Figure 7 for +M

2.1.3 Effective Flange Width Summary

Presented in Figure 10 is a comparison of the above design codes. Assumptions used for this figure include, simple span beams (effective length equals total length) and a web thickness to flange width ratio of 0.1. Interestingly, the width-to-length ratio is the only parameter for the above provisions, while it is clear from the discussion on shear lag, additional parameters are important. Only the Japanese specifications include a provision for the loading type. Geometry and the effects of horizontal bridge curvature are not accounted for by any provision.

There is a large discrepancy as to when the full flange width is effective. The JRA point load cutoff is at 0.02 and the Eurocode interior beam cutoff is at approximately 0.23 with the other cases somewhere in between. Overall, the JRA specifications seem to be the most conservative, while the European standards are the least conservative. The Canadian code and the AASHTO code are very similar throughout the range of width-to-span ratios.

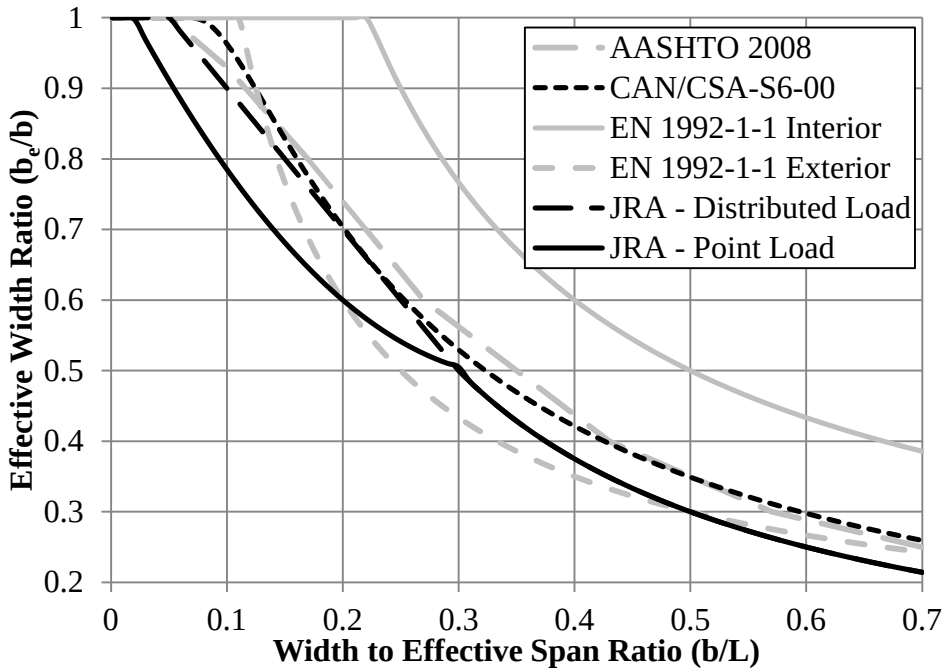

Figure 10 – Comparison of Effective Width Ratio versus Width-to-Span Ratio for Design Codes

These above relationships are empirical and only account for the effects of the width and length of the bridge. There is an obvious disconnect between the rigorous shear lag solution methods and the design code empirical relationships. According to many of the shear lag methods in the previous section and other studies there are more factors affecting the effective width (Moffatt and Dowling 1975, 1978, Kumar 2010; Tenchev, 1996; Sa-nguanmanasak 2006).

2.2 Concrete Segmental Box Girder Transverse Bending

Most engineers never determine the slab design transverse bending moments for a slab-on-girder system because design is often empirical or tabulated. Using the strip method, engineers use tabulated moments for various girder spacing; see Table A4-1 in AASHTO (2010) for an equivalent strip outlined in Section 4.6.2.1.6. For slab-on-girder bridges, the slab design and moments have little effect on the other bridge components.

In a single or multi-cell concrete box girder, transverse deck slab moments are distributed around the cross section to other components such as the webs and bottom slab. Dead loads,

prestressing, lane load and concentrated wheel loads all cause transverse moments in every cross sectional component.

Transverse bending analysis of a concrete box girder can be simple or complex depending on the desired level of accuracy. Many mechanical analogies and models exist, which are accurate to different degrees as well as situations (Barker and Puckett 2007). Schlaich and Sheef (1982) decomposed different loading eccentricities into tabulated response characteristics. These responses could be summed using superposition to determine the local moments. Maisel and Roll (1974) outline many methods for analysis of transverse bending due to local effects. These included folded plate theory, finite strip, finite element and shell theories, each of which could be used for design of all structural effects. Also mentioned was simple influence surface adjusted two dimensional equivalent frame analysis for local trasverse bending effects. The two dimensional equivalent frame analysis is recommended by many designers for simple bridge types (Moreton 1998, Tassin 1998, PTI 1978) and researchers (Libby 1996, Kurian and Menon 2005).

2.2.1 Overview of Two Dimensional Frame Analysis

Equivalent frame analysis only requires a structural analysis program with beam elements or, for the meticulous engineers, their favorite classical indeterminate analysis method. Typically, transverse section properties (area, moment of inertia, etc.) for a unit length cross section, often 1 ft, are calculated and entered into a two dimensional frame analysis program. Non-prismatic beam elements or several prismatic variable thickness beam elements can be used to discretize the variable thickness fillets near the web joints. Rigid link elements are used to model the joints at the top and bottom of the web. By hand this would be very tedious and therefore, not recommended.

Figure 11 shows an example of breaking up a unit length cross section into a series of beam elements to create the frame model. Most often, pin and roller supports are located at the web-to-bottom slab connection. Obviously, it is difficult to adequately represent the true boundary conditions of a three dimensional system in two dimensions so the pin and roller are often considered “good enough”.

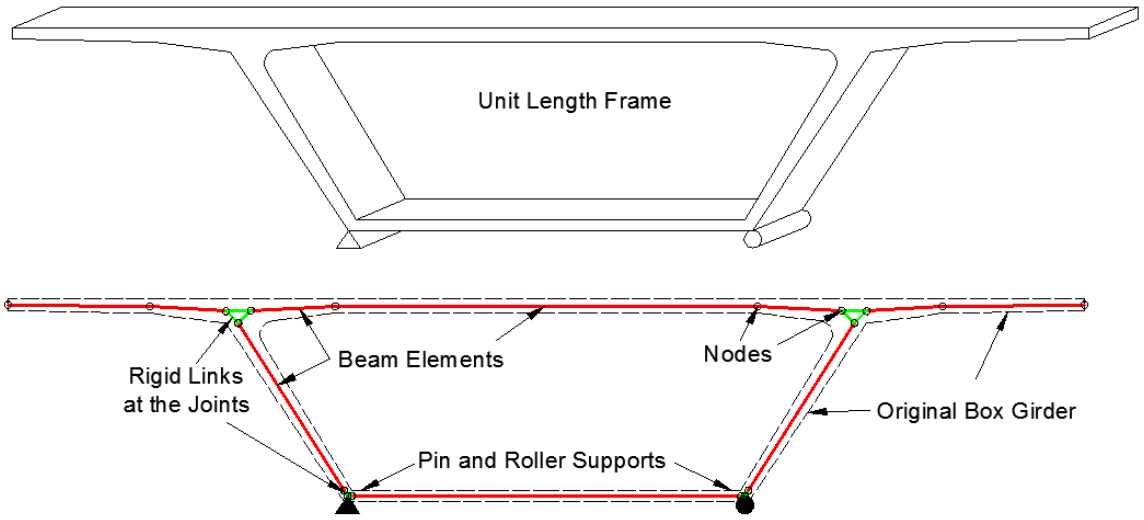

Figure 11 – Box Girder Frame Element Discretization Example

Following creation of the unit length frame model, loads are applied. Dead load/self weight acts on all elements and therefore is distributed over the entire cross section. When using transverse post-tensioning, these forces can be broken into equivalent external loads, scaled appropriately for the unit width and applied to the model. A 640 lb/ft distributed load over a 10 ft width in the 12 ft design lane represents vehicular lane loading.

The most complicated part the two dimensional analysis model is applying the wheel loads. As the wheel loads are applied to the top slab, the resulting slab moments spread out in the transverse and longitudinal directions through plate action. This three dimensional behavior is difficult to relate to a two dimensional model. To accomplish this, designers often use a range of techniques, outlined below.

The easiest transverse analysis technique assumes that the moments spread from an applied point load at a 45^{o} angle to the flange-to-web joint as illustrated in Figure 12. The resulting moments per unit width are calculated using the end-moments of a fixed unit width beam scaled by the resulting longitudinal 45^{o} projection on the joint (see L_1 and L_2 in Figure 12). Equal and opposite

end-moments are applied directly to a two dimensional frame model at the node representing the end of the loaded member end.

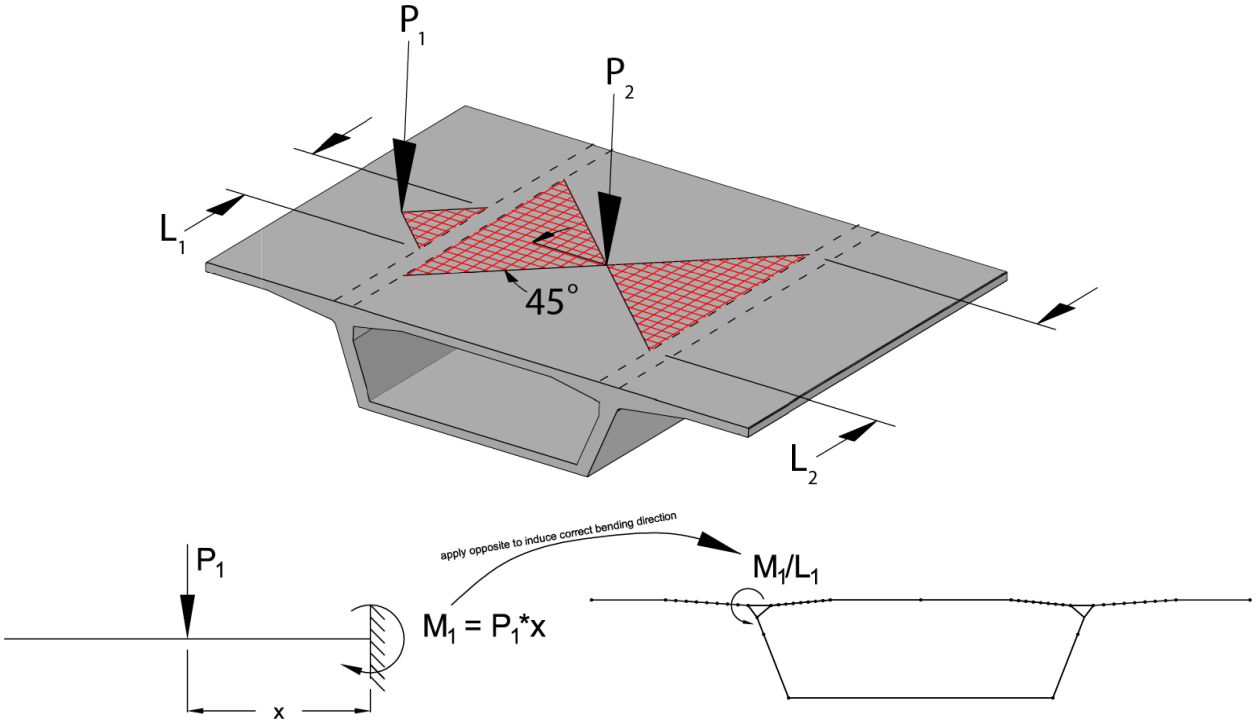

Figure 12 – Visual Demonstration for 45^o Spreading Technique

Because the above only applies point moments to the model, the analysis will not directly determine the moments on the loaded member (slab or wing). To find the moments on the loaded member, one must follow a procedure similar to that of non-nodal loads often presented in matrix analysis text books (Sennett 1994). This method is also discussed in the Post-Tensioned Box Girder Manual (PTI 1978). By applying the calculated end moments and the unknown scaled loads on a simply supported model for the loaded member, simple hand calculations can find the scaled wheel loads and resulting moment diagram. One determines the design moments for the load case by adding the results from the moments from the two models. Figure 13 demonstrates the two moment diagrams that must be added together using the 45^o moments for P_2 from Figure 12.

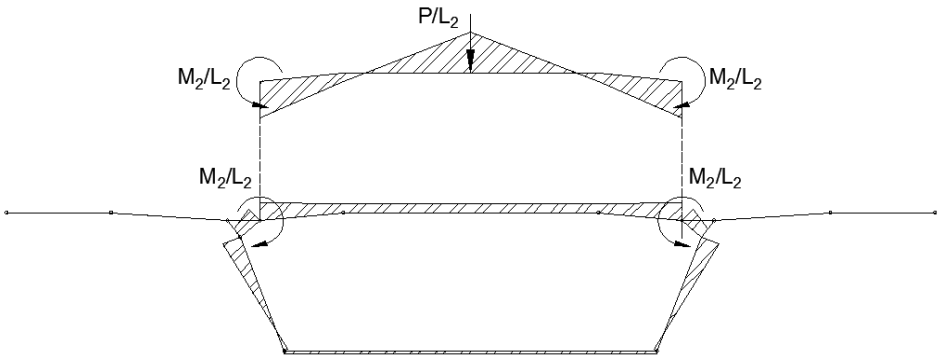

Figure 13 – Loaded Member Design Moment Example

Similar to the 45^{o} assumption one can use an influence surface to estimate point moments. Similar to an influence line, influence surfaces plot the magnitude of moment or shear at a specific reference location, due to a unit load anywhere on a plate, for specified boundary conditions. Various authors have published these surfaces; the most common are Pucher (1977) for constant thickness plates and Homburg (1968) for variable thickness plates. Figure 14 presents an influence surface for a cantilever plate of infinite length used to determine the fixed end moment published by Pucher (1977).

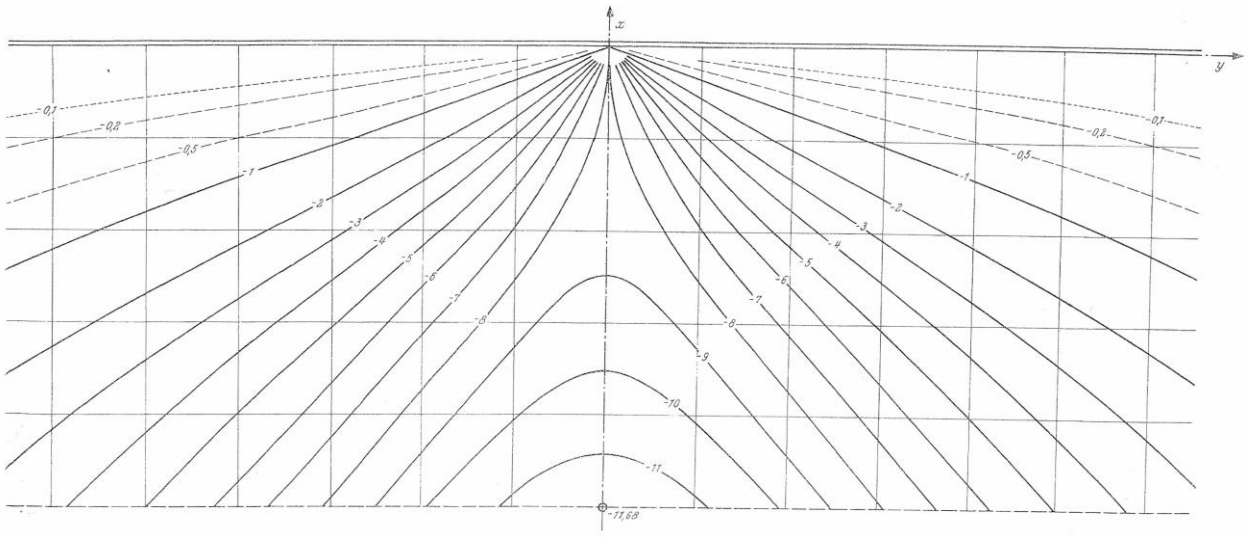

Figure 14 – Example Influence Surface for Support Moment of a Constant Thickness Cantilever Plate Strip (Pucher 1977)

After applying the wheel patch loads or a wheel point load to the scaled influence surface, as seen in Figure 15, the influence surface will give the plate moment at its reference point in moment per unit length. This moment is applied directly to the two dimensional frame model as discussed above. The model is then analyzed to calculate member moments. Additionally, the procedure to determine moments on the loaded member, one follows the same procedure outlined above (Sennett 1994, PTI 1978).

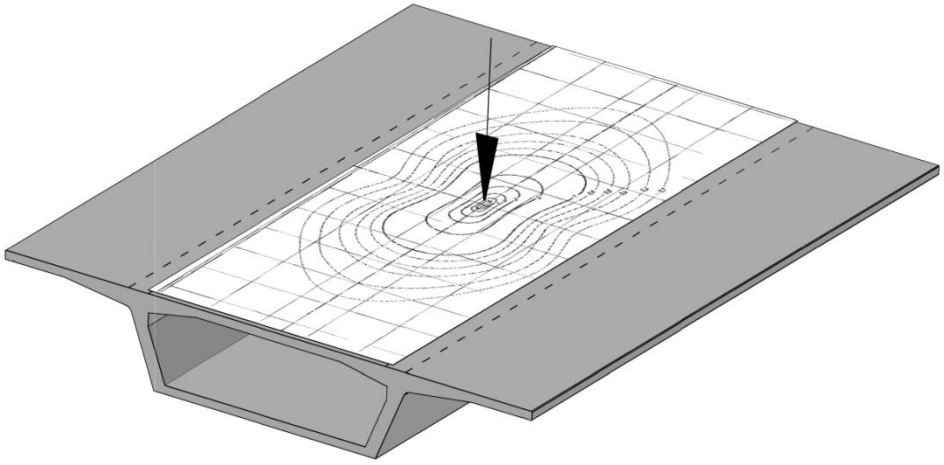

Figure 15 – Demonstration of Influence Surface Use (Influence Surface Adapted from Pucher 1977)

Another technique, allows the calculation of an effective length. This method is briefly outlined in design codes such as AASHTO LRFD, the Indian Design Code and British Standards (Kurian and Menon 2005, 2008). In AASHTO LRFD 2010, this technique is allowed under the subheading "Cross Sectional Frame Action" in Section 4.6.2.1.7 to determine the force effects in cellular cross-sections with integral components such as webs and bottom flanges. To calculate the equivalent strip for many deck types, designers can use the equations in Table 3, where:

- S is the spacing of supporting components (ft)
- h is the depth the deck (in.)
- L is the span length of deck (ft)
- P is the axle load (kip)
- S_b is the spacing of grid bars (in.)
- $+M$ is positive moment

- $-M$ is negative moment
- X is the distance from load to point of support (ft)

Table 3 – Definition of Equivalent Strips (Adaptation from AASHTO 2010 Table 4.6.2.1.3-1)

Type of Deck	Direction of Primary Strip Relative to Traffic	Width of Primary Strip (in.)
Cast-in-place Concrete	Overhang	45.0+10.0X
	Either Parallel or Perpendicular	+M: 26.0+6.6S
		-M: 48.0+3.0S
Cast-in-place concrete with stay in place concrete formwork	Either Parallel or Perpendicular	+M: 26.0+6.6S
		-M: 48.0+3.0S
Precast, post-tensioned concrete	Either Parallel or Perpendicular	+M: 26.0+6.6S
		-M: 48.0+3.0S

A similar approach can be used with influence surfaces or the 45^{o} moment spreading assumption. Fixed end moments for the loaded member (cantilever for the wing, fix-fix for top slab) are calculated and divided by the maximum moment/length caused by the point/patch load(s) on the influence surface. This calculation gives an equivalent strip, which can scale the wheel line loads on the two dimensional frame model in the same manner as above. When using the equivalent strip method, designers use the same two dimensional model shown in Figure 13 and calculation of all non-wheel load effects is identical. Wheel line point loads, divided by the equivalent strip distance, are placed on the model in worst-case locations. Using this method, the above "non-nodal load" procedure is unnecessary. The moments obtained from the two dimensional model are considered the design forces caused by the localized truck loading. The axial loads, especially those in the webs, are often neglected as they are assumed to be accounted for by the shear design.

The main distinctions between the methods presented above are the point moment versus the effective width methods. The point moment methods directly impose the assumed moments at member ends, while the point load methods scale the wheel line loads. Because the equivalent strip method is uncommon in design practice, the point moment method will be considered the standard for the remainder of this report.

The 45^{o} assumption, rarely used for final design, is common for getting quick "ballpark" numbers. More often, a fundamentally sound technique like the influence surface methods above or finite element solution discussed below is used for final analysis.

There are significant limitations to the frame analysis. As discussed above, the two dimensional frame analysis is an analogy, used to describe three dimensional behavior. The simply supported boundary conditions used do not mimic the three dimensional load distributing effects during loading or distortion. Additionally, the boundary conditions used for selecting/scaling the loads assume fixed conditions for the loaded member, likely resulting in over conservative applied loads. Conditions on a real member do not reflect the stiffness imposed by influence surfaces and would not generate the same load magnitudes. Few previous research programs have discussed how well this analogy compares to real behavior. It is important to investigate this method, which is still in use at various stages of design. Engineers are aware this method is not accurate, and current design practice typically uses more sophisticated computer analyses.

2.2.2 Current Practice: Transverse Analysis

In the last 20 years, powerful computer analysis programs have become ubiquitous in the engineering design community. However, as recently as the early 2000s, frame analysis was still used throughout the design process at many consulting firms, according to former design engineers (Cristopher D. Moen, personal communication, July 20, 2011). Today, two dimensional frame analysis is used for rating at the State DOT's as well as for simple and/or preliminary design at firms (David Goodyear, personal communication, November 9, 2011, Chris Hall, personal communication, July 1, 2011).

Currently, some design offices are creating shell models of box girder bridges specifically for transverse design. These models incorporate local box girder geometry and enough of the bridge longitudinally to capture the effect of the load truck. Models that capture the system more accurately are common for complex structural systems (Moreton 1997). Designers tend to stay away from solid elements because they have an increased computational cost. These models are time consuming and are often not worth the additional effort over computationally cheap shell elements.

When using shell models, as with all finite modeling, complications arise with computational time, model detail and mesh refinement. Mesh refinement is difficult to know a priori, which is a concern during analysis. Furthermore, for a designer, this is a tedious process and time consuming. For this reason, designers often overlook this process or aim for a "good enough" analysis. An additional aim of this research is to develop recommendations on the fineness of the shell and/or solid element mesh to save designers time when producing an accurate model.

2.3 Segmental Box Girder Live Load / Structural Testing

Structural load testing of segmental concrete bridges is relatively uncommon. The first segmental concrete bridge was completed in the United States in 1973, followed by many studies throughout the 1970s and 1980s. Interestingly, in the literature there are significantly fewer live load tests than long term monitoring systems. This may be because long-term effects, such as construction loading, temperature, creep and shrinkage are often more important than the actual live loading. The following summarizes 11 research programs in which segmental box girder bridge live load tests were performed. This information was valuable to the current study because it provided an important comparison to the current live load testing program and real life background on local phenomena.

2.3.1 Thoman et al. (1984)

This study was concerned with validating cantilever wing design for segmental box girders. The authors tested the Southway Bridge in Clarkston, WA. The bridge was loaded in two positions with three concrete blocks weighing 58 kip and spaced at 14 ft to represent HS20-44 spacing. Unfortunately, the authors did not elaborate on the test position longitudinal locations. Researchers tested the bridge without the planned asphalt overlay, sidewalk and barrier rails. They determined that these appurtenances would reduce stresses by 23%. A fixed cantilever plate finite element model predicted 734 psi and a Homberg chart predicted 807 psi. Measured cantilever strains indicated 752 psi and 1028 psi in Load Positions 1 and 2, respectively. The authors concluded that the Homberg influence surface predicts cantilever deck behavior "exceptionally well" even though the second load position induced 27% more stress than predicted.

2.3.2 Roberts (1993)

A very thorough study of the precast segmental bridge known as the "San Antonio Y", in San Antonio, TX, by Roberts (1993), resulted in numerous recommendations to AASHTO guidelines, including updates to the shear lag provisions. Roberts found the post-tensioning forces dominated the shear lag effects, but did not consider live load during the shear lag measurements. Three dimensional computer models predicted deflections and compared very well overall to measured deflections. Conclusions indicated that full, un-cracked, transformed, cross-sectional properties, including the external tendons, predicted deflections reasonably.

2.3.3 Davis et al. (1999)

This study, performed on an elevated highway in Austin, TX, focused on many response aspects. The investigation began during the construction phase and culminated in a series of full-scale live load tests. Post tensioning losses, thermal gradients (and their effects), live load response, local zone behavior (near diaphragms and anchorage zones), and the semi-continuous details were all investigated. The very complex structure included many different cross-sections with unique geometry. (Davis et al. 1999)

Strains measured during post-tensioning, dead load and live load testing were oriented longitudinally. The researchers concluded that live load stresses, neutral axis locations and deflections could be adequately predicted using the AASHTO LRFD effective flange width provisions. There was often little reduction in flange width due to the effective width estimation. Using an effective flange width approach, live load stresses were consistently overestimated by as much as 40%. However, the researchers found that these "adequately estimated" stresses did not always accompany measured strain concentrations at the flange-to-web connection. For most instrumented cross-sections, there were not enough strain measurements to capture a complete strain profile. The AASHTO effective flange width, used to modify section properties, also gave sufficiently accurate deflection predictions. The authors measured very small live load deflections, especially when compared to dead load deflections.

The observed strain distributions indicated the flanges had nearly constant stress distributions under live load. The researchers clearly stated that the girders did not experience significant

shear lag at sections of high moment or strain gradient. This indicates that the AASHTO effective flange width procedures are conservative for live load.

2.3.4 McClure and West (1980)

For the Pennsylvania Department of Transportation, a single span 121 ft long curved prestressed concrete box girder was constructed and tested at service levels and to failure. Deflections, rotations, longitudinal and transverse strains were measured and compared to simplified design methods and finite element models.

When compared to finite element results (solid modeling), the deflections were estimated within 15% and beam theory predicted values 14% greater than the finite element model (McClure and West, 1984). Measured rotations proved erratic when compared to finite element results (McClure and West, 1980). The authors maintained that errors in rotation measurement and truck position contributed to these large discrepancies. Keeping the truck in the correct load path proved difficult due to the horizontal bridge curvature.

Experimental longitudinal stresses were 15% below finite element predictions. Finite element and experimental stresses produced linear flange stress distributions due to truck loadings. In all cases, the experimental data confirmed that there was no substantial shear lag.

The researchers went to great lengths to discredit their work with transverse strains and analysis. There were issues with load placement and temperature effects. Additionally, it is this author's opinion that the instruments were often located in places of low transverse bending strain, compounding their issues. The finite element mesh was not fine enough to capture the local bending effects, and the authors worked hard to explain their difficulty in comparing the predicted stresses to the experimental stresses.

The predicted finite element stresses were considerably less than the experimental stresses, reinforcing the need for a finer mesh. The researchers also used a two dimensional frame model to analyze transverse bending. Frame model predictions for top flange transverse stresses near the load were conservative and reasonable, but measured strains were rarely located at points of

maximum strain. In addition, the frame model predicted stresses were up to four times the measured stress in the bottom flange. Moreover, there were times the frame model predicted large positive bending, but the measurements suggested negative bending. This illustrated the inadequacy of the frame models with respect to capturing the real transverse behavior. The finite element model better captured this behavior even though its strain measurements were often unreasonable. Measured web stresses were always near zero due to the poor instrumentation location. The authors concluded that the frame analysis method was a good and conservative method for local transverse bending analysis, but it seems their results were largely inconclusive.

2.3.5 McClure et al. (1980)

To augment data from live load testing of the above Pennsylvania Bridge, the researchers tested four individual box girder segments under simulated field conditions in the lab. The segments were tested to determine the two dimensional frame analysis accuracy. Not presented here is the fatigue and punching shear testing and conclusions for these specimens.

The segments were equipped with end frame pseudo-diaphragms to apply simulated longitudinal post-tensioning forces. In this setup, it is unclear how well the diaphragms simulated three dimensional transverse bending and the longitudinal bending conditions like a real bridge. Therefore, the results should be viewed with respect to this limitation.

Electrical resistance strain gages, placed around the inside and outside of the box segment, allowed researchers to compute the applied moments. Two 20 kip loads, simulating a standard AASHTO wheel load plus impact, were placed in three different transverse positions. The researchers compared experimental stresses to results from the two dimensional frame analysis using an effective strip procedure (AASHTO Standard, 1977) and an influence surface (Homberg 1963).

Similar to the full-scale bridge test by McClure and West, the most accurate estimations occured in the top flange. The web and bottom slab stresses were often highly overestimated. The researchers concluded that conservative prediction using a two dimensional frame analysis was possible. In a real bridge structure, greater moment spreading would be observed due to larger

segments and true boundary conditions. The above comparisons would become even more conservative in a real structure for this reason.

2.3.6 Takebayashi et al. (1994)

In this study, the researchers performed a full-scale destructive test on a precast segmental box girder with dry joints, external tendons and a constant cross-section. This test was an interesting opportunity to investigate the many issues with this bridge type. Most relevant to the current research are the longitudinal strains located around the box cross-section.

Takebayashi et al. (1994) state that the compressive strain above the web is larger than at the cantilever or midsection of the box. During the non-linear phase of loading, the ratio of high-to-low compressive strain in the top slab is approximately 1.33 at an arbitrary loading point. If one fits a parabolic strain profile to the strains, a 0.875 b_e/b ratio, as defined by Equation 2, was calculated. When comparing this data to other research programs, consider that strains are not elastic, which would exacerbate the shear lag effect. Furthermore, the ratio of slab strains changed significantly throughout loading, especially in the inelastic range, indicating shear lag was not constant with respect to load.

2.3.7 Breen and Kashima (1991)

The authors created a one-sixth scale model of a balanced cantilever constructed segmental concrete box girder bridge, built in Corpus Christie, TX. Topics of investigation included behavior during construction and service, ultimate and failure load tests. Longitudinal and transverse strains were measured, as well as deflections, reactions, cracking and slip between segments.

Linear elastic analysis programs, BMCOL (frame analysis) and MUPDI (folded plate analysis) predicted elastic strains well, according to the authors. These programs worked well due to the lack of warping and bi-axial bending in the structure due to relatively minor eccentric loading. However, the BMCOL program could not predict transverse behavior, such as moments and deflections. Deflections and reactions were predicted well when compared to experimental resultsNear the loading, MUPDI was accurate for longitudinal strains, off by 9% on average, and

transverse deflections, off by 3% on average. Away from the loading, the percent differences from measured values were large because the measured magnitudes become small. MUPDI was able to determine a non-linear longitudinal stress distribution; however, it did not capture the shear lag effect accurately. The prediction misses the shear lag distribution by up to 16% in the top and bottom slabs. After fitting a parabola to the measured slab strains, one can calculate an effective flange width of 0.82 b_e/b ratio, using Equation 2.

This study included a limited investigation into transverse analysis. Kashima (1974) noted the difficulties involved in scaling the slab accurately for a proper transverse analysis comparison. The researchers placed strain gauges under the wing and at the center of the top slab to measure maximum transverse moments. When compared to results from the folded plate analysis, the predicted to experimental ratio for transverse strains was between 1.02 and 1.14.

2.3.8 Hawkins and Clark (1983)

The Denny Creek Viaduct, located 50 miles east of Seattle on I-90, is a 20 span segmental structure with 188 ft spans. The cross section consisted of multiple segments, including the U-shaped first segment, top slab and wing segments.

The researchers instrumented three cross-sections, one near the pier, at the quarter point and at midspan, with 14 longitudinally oriented Carlson strain gauges. Hawkins and Clark (1983) did not comment on the observed shear lag, but significant shear lag was present. Predicted live load strains are relatively accurate using a "linear elastic displacement analysis" that was not explained in the final report (the interim report with this explanation could not be obtained).

The maximum longitudinal strain high to low ratio in the bottom slab was [-21.0 μstrain] / [-1.8 μstrain] = 11.6. As in the previous sections, a simple parabolic distribution was fit to the observed strains in this component and using Equation 2, $b_e/b = 0.41$. However, the observed shear lag in the other components is not as severe. For instance, the top and bottom slab, b_e/b ratios are 0.82 and 0.61, respectively, however, they are still highly reduced.

The researchers did not measure transverse bending strains on the Denny Creek Viaduct. However, seven dial gauges measured deflection across the bridge cantilever slab at the expansion joint. Measured deflection at the curb was 0.09 in. for the eccentric load case designed to produce maximum deflection at that location. The calculated deflection at the curb was 0.129 in. using the gross cross-sectional properties of the slab and ignoring the barrier rail's contribution. Details on this calculation method were also not in the final report. Based on these findings, the Hawkins and Clark recommended that barrier curbs should be included in slab analysis and design.

2.3.9 Kuhn (2008)

The Seven Mile, Niles Channel and Channel Five Bridges are all segmental box girder bridges constructed with the span-by-span method and do not have epoxy or reinforcement between segments (dry joints). These three bridges were load tested to determine how much the barrier rail influences the transverse moments.

Transverse strains were measured along longitudinal lines on the structures. The measured strains were then converted to moments assuming elastic sections, using strain compatibility, transformed section properties and an assumed modulus of elasticity. The measured moments were compared to the moments calculated from a Homberg (1963) influence surface and finite element models with and without barriers (with and without joints). When compared to the test results, the Homberg influence surface moments were very conservative. Homberg moments over-predicted moments by up to 131 percent for the cantilever and 48.9 percent for the continuous charts. Interestingly, the Homberg cantilever plate and continuous plate chart moments were 31.6 percent below and 15.2 percent above the finite element moments (without barriers). Following calibration, the finite element models could very accurately predict the transverse moments after the addition of the barrier.

2.3.10 Duemmel et al. (1992)

The James River Bridge is a cable stayed twin box girder bridge. Strain gages placed on two segments' cross-sections, above webs and at component midpoints, measure longitudinal strains during live load testing.

The maximum strain observed over all load cases was -8 με (compression) in the bottom flange at the segment near the pier. The maximum strain observed in the midspan segment was only +3 με. Duemmel et al. (1992) stated that the longitudinal strain distribution was uniform across the twin girder cross-section, regardless of truck position and segment. Additionally, shear lag effects due to live load were non-existent. The finite element model highly overestimated live load strains at both cross-sections; however, Duemmel et al. (1992) only present average strain across the top and bottom flanges. The model predicted -28 μstrain in the bottom flange (compared to -8 με measured maximum) for the pier segment and +15 με in the midspan segment's bottom flange (compared to +3 με measured maximum).

2.3.11 Floyd and Sutton (1985)

This study's main purpose was to determine the local transverse bending effects and compare them to finite element models. In the final report, Floyd and Sutton (1985) determined two dimensional frame models to be too inaccurate for design and did not consider this technique.

At four bridge cross-sections, the center of each top slab, bottom slab (only on two cross-sections) and web, a strain gage pair measured the strain to compute the moment at that section. Strain gages were also located on the reinforcement at these locations as well. The researchers placed live load in 32 static load configurations. An elastic finite element analysis code, developed by Batala (1976) for use during the Turkey Run Bridge design, employed superimposed plate bending elements and plane strain elements. The mesh was very coarse transversely with a single element representing each wing, bottom slab and web and two elements for the top slab. The longitudinal element length varied. (Holman 1977)

Overall, the experimental transverse bending moments were much less than finite element analysis predictions. However, at one cross-section, under one longitudinal load orientation, the observed moments were much higher than predicted. Measured transverse moments at midspan sections with large moments averaged a 0.61 experiment-to-prediction ratio. Similarly, measured transverse moments at sections near the pier averaged a 0.40 experiment-to-prediction ratio.

2.4 Literature Review Summary

Table 4 presents a list of segmental bridge live load tests and a checklist highlighting the measured phenomena for each test. The measurements were broken up into longitudinal strains, transverse strains, displacements and long-term behavior (e.g., time dependent phenomena, behavior during erection).

Table 4 – Live Load Testing Literature Summary

	Structural/Live Load Testing			Long Term Effects
Author	Longitudinal Strain	Transverse Bending	Displacements	
McClure and West (1980)	×	×	×	×
McClure et al. (1980)		×		
Hawkins and Clark (1983)	×	×	×	×
Thoman et. al. (1984)		×		
Floyd and Sutton (1985)		×		
Breen and Kashima (1991)	×	×	×	
Duemmel et al. (1992)	×			×
Roberts (1993)			×	×
Takebayashi (1995)	×		×	
Davis et al. (1999)	×		×	×
Kuhn (2008)		×		

Six research programs (McClure and West 1980, Hawkins and Clark 1983, Breen and Kashima 1991, Duemmel et al. 1992, Takebayashi 1995, Davis et al. 1999) measured longitudinal strains and compared them with various models. The results were unanimously conservative. Simple beam line models agreed well for low or no shear lag situations (Davis et al. 1999). Finite element models, which are able to predict shear lag, often predicted average strains well. It is important to note that shear lag is most severe, and concerning, during the construction phase and tendon stressing. For this reason more studies have focused on this phase than on live load testing (e.g. Davis et al. (1999), Roberts (1993))

However, these models also had difficulty predicting the non-linear shear lag effects (Hawkins and Clark (1983) Breen and Kashima (1991)). The finite element comparisons often used coarse meshing which likely caused issues with accuracy. Interestingly, discussion or conclusions with

respect to live load testing and shear lag rarely included a discussion with previous literature. This may be due to the various programs' parallel activities.

Table 5 presents calculated and observed effective width ratios (be/b) from nine locations on seven different girders. For this investigation, a parabolic fit to the strain measurements for a particular member or a linear fit if only two data points were present. The area under the estimated curve was determined and used to calculate the effective flange width using Equation 2, using strain instead of stress. The effective flange width was then divided by the true member width to determine the effective flange width ratio. It is clear that the majority of tests had no observable flange width reduction, which was in one case very conservative, see Davis et al. (1999) – Mainline Girder in Table 5. On the other hand, in the cases where there was significant observed shear lag (>15% flange width reduction), all predicted methods were unconservative, predicting little or no flange width reduction. From the previous literature, effective width provisions do not take into account many factors identified as important to the shear lag phenomenon. Additionally, shear lag is under-predicted using these provisions, as demonstrated in Table 5. Additional investigation into the shear lag effect should include live load testing on segmental box girder bridges to determine the applicability of these design provisions to current designs.

Table 5 – Calculated and Observed Effective Width Ratios (b_e/b) from Live Load Testing

		Member	Observed	AASHTO Standard	AASHTO Segmental	CAN / CSA - 00	Eurocode	JRA Point Load
Davis et al. (1999) – Mainline Girder	INTERIOR SPAN - MIDSPAN	Wing	1.00	0.97	0.64	0.61	0.55	0.54
Davis et al. (1999) – Ramp Girder	INTERIOR SPAN - PIER	Top Slab	1.00	1.00	1.00	1.00	1.00	0.91
Davis et al. (1999) – Ramp Girder	INTERIOR SPAN - MIDSPAN	Top Slab	1.00	1.00	1.00	1.00	1.00	0.84
Takebayashi et al. (1994)	SIMPLE SPAN - MIDSPAN	Top Slab	0.84	1.00	1.00	1.00	1.00	0.91
Breen and Kashima (1991)	INTERIOR SPAN - MIDSPAN	Top Slab	0.82	1.00	1.00	1.00	1.00	0.91
Hawkins and Clark (1983)	INTERIOR SPAN - MIDSPAN	Bottom Slab	0.62	1.00	0.95	1.00	1.00	0.83
	INTERIOR SPAN - PIER	Bottom Slab	0.41	1.00	0.80	0.98	0.91	0.76
McClure and West (1980)	SIMPLE SPAN - MIDSPAN	Top Slab	1.00	1.00	1.00	1.00	1.00	0.97

Transverse analysis accuracy varies significantly with respect to the analysis method. McClure and West (1980) and McClure et al. (1980) compared results to two dimensional frame analysis, while Thoman et al. (1984) and Kuhn (2008) compared results directly to influence surface values. These researchers unanimously found the influence surface analysis method to be very conservative. Researchers comparing measured transverse bending to finite element or plate models (McClure and West (1980) and Floyd and Sutton (1985)) also found very conservative estimations. Regardless of analysis technique, predictions consistently over predict design values. The literature shows a need for prediction of these effects. This will give bridge raters and designers quick and simple guidelines for accurate estimation of these effects and may result in cost savings for design and increased permit loading for rating.

3 Load Test Experimental Setup

Three bridges were load tested to investigating global behavior, shear lag and transverse bending of segmentally post-tensioned concrete bridges. The three bridges studied were the Seabreeze Bridge in Daytona, Florida, the Smart Road Bridge in Blacksburg, VA and the Varina-Enon Bridge in Richmond, VA. Bridge testing was performed between April 2011 and August 2012.

These three bridges were selected because they represent three significantly different structures. Each bridge was continuous, with interior span lengths of 247ft, 480 ft, and 150 ft for the Seabreeze, Smart Road and Varina-Enon Bridges, respectively. The span-to-depth ratios for each structure, using the midspan depth, are 31, 40 and 13, for the Seabreeze, Smart Road and Varina-Enon Bridges, respectively. The Seabreeze and Smart Road Bridges used internal post-tensioning and were erected using balanced cantilever construction. The Varina-Enon Bridge was erected using span-by-span construction and externally post-tensioned. The Smart Road Bridge was cast-in-place and integral with the piers, whereas the Seabreeze and Varina-Enon Bridges had precast segments and were supported using pot bearings and elastomeric pads, respectively.

Figure 16 presents a comparison between the wing, top slab and bottom slab components for each single cell structure. The aspect ratio calculation used the component transverse length divided by the minimum thickness of each component. The Varina-Enon Bridge has the most slender components of all the tested structures, especially the top slab. The Smart Road Bridge in all cases has the least slender components and the Seabreeze Bridge landed in the middle in all cases.

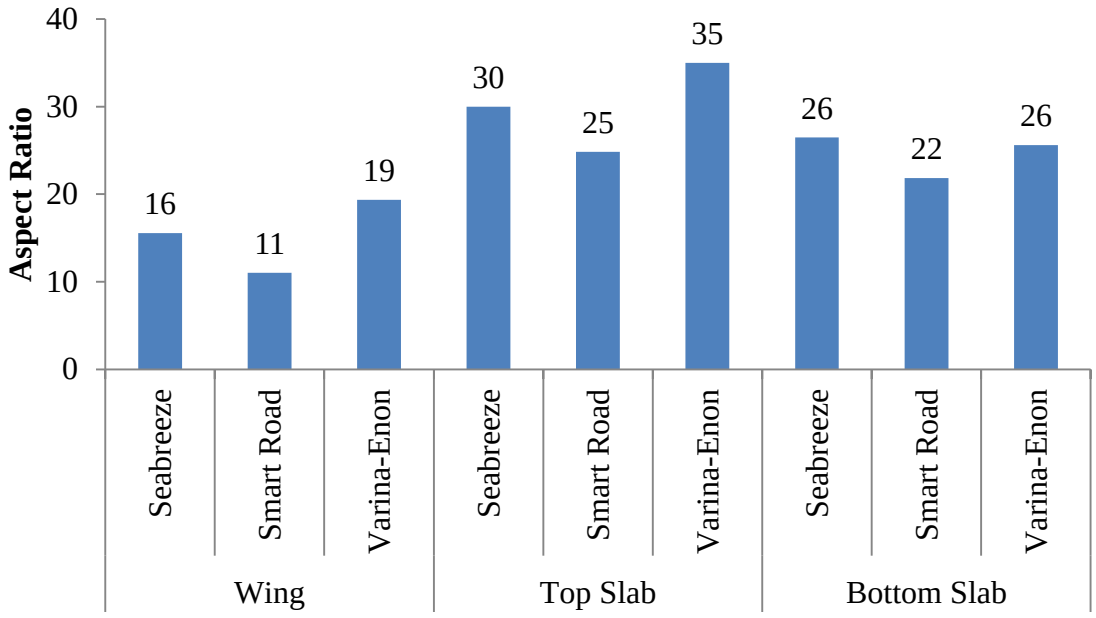

Figure 16 – Aspect Ratio Comparison for Components of Each Tested Bridge

Each bridge was instrumented with several longitudinal and transverse strain gages, on at least two cross sections. Instrumented cross sections were selected based on important design locations (near pier and midspan). The longitudinal strain sensors were intended to identify the distribution of strains in the flanges to investigate if shear lag was present in each structure. The transverse strain sensors were placed at points of maximum transverse bending on a cross section near the pier and a cross section at midspan. The purpose of the two transverse instrumented cross sections was to determine if the transverse strain distribution changed near the pier diaphragm. The main limitation of the transverse strain measurements was that only one sensor could be placed on the plate surfaces at each measurement location rather than one on each side. This makes it impossible to separate bending and axial force at transverse sensor location.

Additionally, deflection and rotation measurements were placed around the structures. The purpose of these global type measurements was to compare to longitudinal analysis assumptions and verify a reasonable value for elastic modulus.

3.1 Data Acquisition, Instrumentation and Testing

The following section outlines the standard testing procedures and instrumentation used for the field tests presented in this document. Two data acquisition systems were used for the field tests

and several sensor types were employed, all of which are outlined in the following sections. Additionally, details regarding data post processing are contained in Appendix E.

3.1.1 Data Acquisition Systems

3.1.1.1 Seabreeze Bridge Data Acquisition

The data acquisition system and software used for the Seabreeze Bridge Test data collection were the Campbell Scientific's CR9000X Datalogger and RTDAQ Software, respectively. All instruments, with wires rolled up on spools, were connected to the datalogger using an efficient, pre-wired, military connector style system, which is shown in Figure 17.

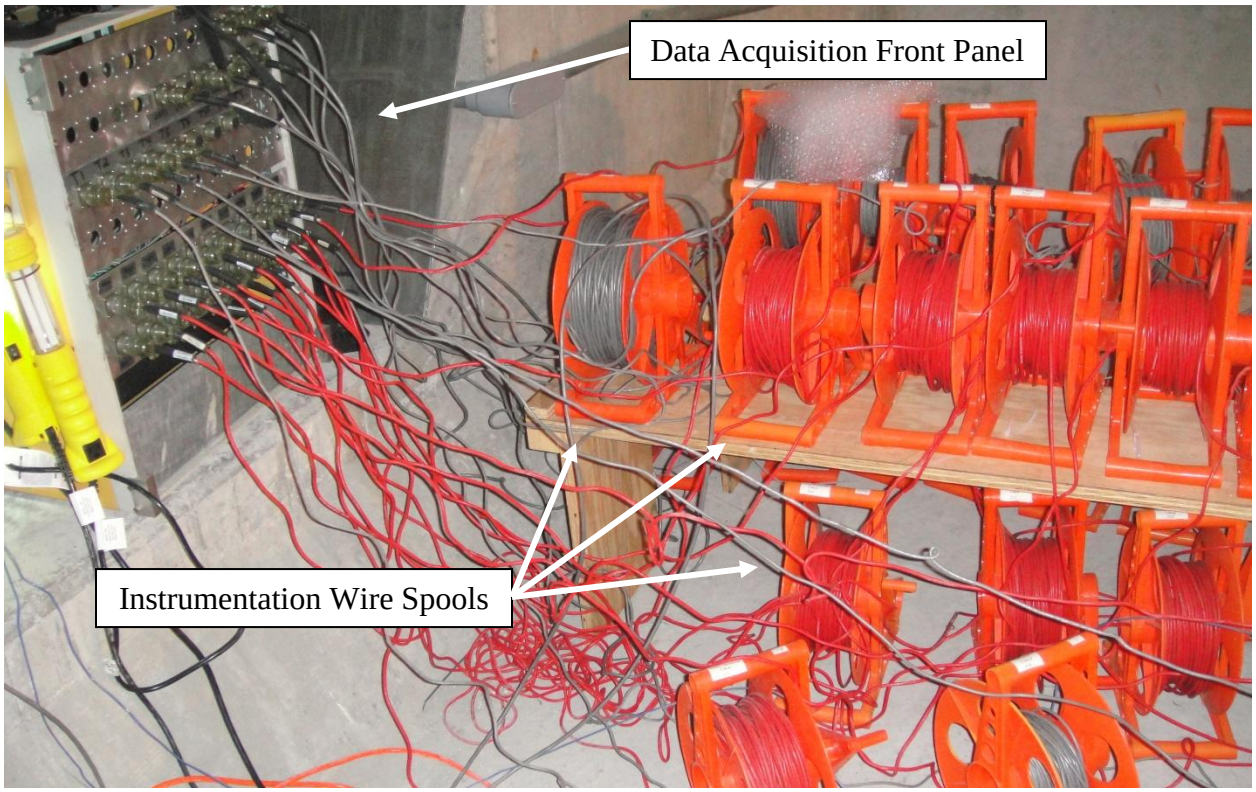

Figure 17 – Data Acquisition System Front Panel and Spools during Seabreeze Test Setup

The data acquisition system used for the Smart Road Bridge and the Varina-Enon Bridge Tests was the Structural Testing System (STS) manufactured by Bridge Diagnostics Inc. This data acquisition system is tailored for bridge testing and offers very convenient wireless testing. Sensors are connected to the STS nodes, shown in Figure 18. The nodes communicate wirelessly

to a wireless router, which wirelessly communicates to a computer loaded with the appropriate software.

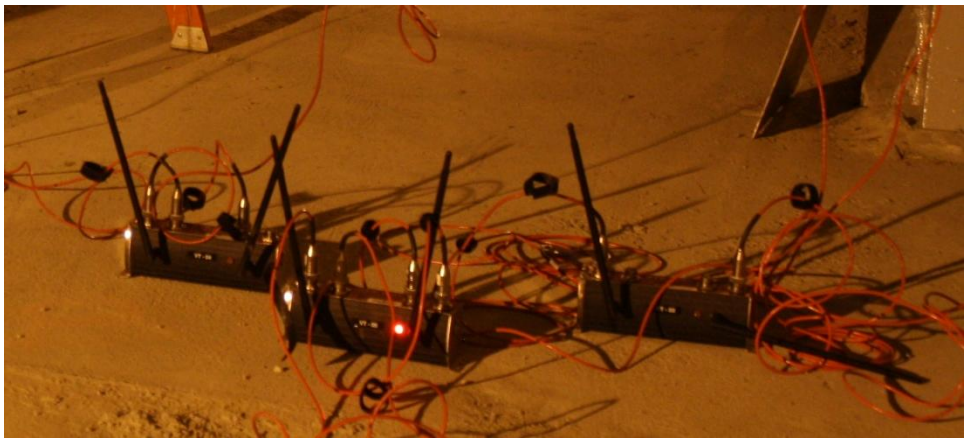

Figure 18 – Structural Testing System Wireless Nodes

The setup used on the Smart Road Bridge required instruments on the interior and top of the bridge deck. The wireless signal degraded significantly when transmitted through the concrete members, so one router on the inside and a router on the outside were connected using an Ethernet cable. This enabled a strong signal for communication to both interior and exterior sensors.

The data acquisition system used and sampling rates for each test are summarized in Table 6. In the case of the Seabreeze and Varina-Enon Bridge tests, the sampling rate was limited by the maximum sampling rate of the CR9000X combined with the number of sensors. For the Varina-Enon bridge similar consideration was made, however, a faster sampling was necessary due to the high speed trucks For the Smart Road bridge, the 20 Hz sampling rate was judged to be fast enough for quasi-static testing.

Table 6 – Data Acquisition and Sampling Rate Summary

Bridge	Data Acquisition System	Sampling Rate (Hz)
Seabreeze	CR9000X	25
Smart Road	STS	20
Varina-Enon	STS	50

3.1.2 Sensor Description

3.1.2.1 Strain Transducers

The strain transducers used in the Seabreeze Bridge live load testing were manufactured by Bridge Diagnostics, Inc. (BDI). An example of an attached transducer can be found in Figure 19, below. These gages were selected because of their reusability, fast installation, and simple removal.

The three inch gage length strain sensors contain a full Wheatstone bridge using four bonded strain gages. This configuration allows the transducer to compensate for thermal output, increases the signal to noise ratio and significantly reduces the effect of long cable lengths, when compared to a typical quarter bridge bonded strain gage. The transducers were calibrated within 1 year of the test dates by the manufacturer and are accurate to within 2% of their measurement. Strain sensor calibration information is on file at Virginia Tech. Resolution of the strain transducers on the data acquisition systems employed is well below 1 με and rarely requires post-processing or filtering.

Figure 19 – Strain Transducer 2008 on outside of Seabreeze Bridge

Transducer installation is quick and requires only light grinding to remove debris or coating from the bonding surface. Scouring the concrete surface in a cross-hatch pattern creates a rougher surface area for bonding. Small metal tabs, bonded to the prepared surface with a fast-set epoxy, are attached with nuts to the transducers. The transducers are attached to these metal tabs by nuts and immediately following installation, are ready to transmit data.

Strain transducers installed on the outside of the bridge are often subject to wind and temperature fluctuations. These environmental effects can create erratic noise in the signal as well as temperature-induced drift. The manufacturer recommends protecting the installed transducer with foam housing to reduce these effects. Foam housings were installed for all instruments attached to the exterior of the bridge, an example of which can be seen in Figure 20. Conditions inside the box were stable enough to prevent any temperature or wind induced fluctuations. Following testing, there was no evidence of significant drift or extra noise in the exterior signal when compared to instruments on the interior.

Figure 20 – Strain Transducer 2008 with Weather Protection

3.1.2.2 Deflectometers

Vertical deflections were measured using deflectometers at the midspan of the girders. The homemade deflectometers, shown in Figure 21, convert a full bridge strain measurement into a deflection measurement. The strain signal from the strain gages bonded at the base of the deflectometer cantilever is easily converted to a deflection measurement. The sensors are calibrated using a two-point calibration on the CR9000X, because it is a built-in function and a best-fit calibration to several points on the STS. Each calibration was performed 72 hours prior to the field test. Each deflectometer was calibrated to an accuracy of 0.001 in using a dial gage at the Virginia Tech Thomas Murray Structures Laboratory. Following calibration, several expected deflections are imposed on the sensor in the lab to verify the accuracy of the final calibration.

Figure 21 – Deflectometers on Bottom Slab of Seabreeze Bridge

Deflectometers are attached to the concrete surface using the same fast-set epoxy used for the strain transducers. The concrete surface is ground to create a flat surface free of debris or any coating. A hatch pattern of shallow grooves is then created and the deflection transducer is attached to the prepared surface. This process was used for the deflectometers installed for the

testing in this document. Current versions of the deflectometers use steel tabs, similar to the strain transducers for easy installation, removal, and cleanup.

Following installation, the deflectometer cantilever arm is pre-deflected beyond the expected deflection and fixed to the ground using a heavy weight or permanent structure (e.g. signpost). As the bridge is loaded, the structure will deflect, reducing the deflection in the cantilever arm. This change in deflection causes a strain change in the arm, which is measured using a full Wheatstone bridge strain gage configuration by the data acquisition system. Additional information regarding calibration and function of the deflectometers can be found in Collins (2010).

3.1.2.3 Inclinometers

Three SBS1U Servo Inclinometers, manufactured by Reiker, were used for the Seabreeze Bridge test. Under ideal condition, these inclinometers are capable of a resolution of to 2.7×10^{-6} degrees and have a range of +/- 2 degrees. Independent tests conducted by the research team have determined that the manufacturer reported settling time of the instrument (approximately 2 seconds) is adequate for pseudo-static testing (defined below). The inclionmeters were calibrated by the manufacturer within 1 year of testing and calibration information is on file at the Virginia Tech Thomas M. Murray Structures Laboratory.

3.1.2.4 Truck Tracking

As the sensor data is collected, each set of readings is accompanied by a timestamp. It is helpful when viewing tabulated test data, ex post facto, to convert this time series data to truck position so the truck location is known, especially when investigating local effects. For the Seabreeze Bridge Test, a manually operated strain transducer was used to send a signal to the data acquisition system. A quarter bridge bonded strain gage attached to a thin, bent, strip of metal was used to send a signal spike to the data acquisition system by pushing the free ends together. The transducer, assembled by Virginia Tech, is shown in Figure 22. The strain based trigger was not calibrated, only raw voltage measurements were used to identify activation.

Figure 22 – Truck Tracking Trigger Mechanism

During the Smart Road Bridge and Varina-Enon Bridge Tests, the signal spike was sent to the data acquisition using a built in function on the STS data acquisition software to put a special timestamp in the data file upon clicking a button in the graphical user interface. This was functionally equivalent to the tracking mechanism for the Seabreeze Bridge.

Prior to the each live load test, lines were drawn on the bridge deck perpendicular to the direction of traffic at each pier, midspan point, and instrumented cross section. As the front axle crossed each of the perpendicular lines on the bridge deck the tracking signal was activated. For instance during the Seabreeze Bridge live load testing, the transducer was activated, as the front truck tire was at Pier 4, at Section A through E, at the end of the bridge and when the final truck tire was completely off the bridge, signaling the end of the test. During data post-processing, it was assumed that the truck maintained a constant speed between each tracking location, as the drivers were informed to do. This information was used to convert the data timestamps to truck front axle position.

3.1.2.5 Loading Procedures

Two loading procedures were used for the field testing in this document: quasi-static and high-speed testing. Quasi-static testing, performed on all bridges in this report, places a truck in the

pre-determined transverse position and the driver is instructed to maintain a constant speed of 2-3 mph. A member of the testing team walks the truck across the spans of interest to help the driver maintain a constant speed and maintain correct transverse position, as marked with paint or chalk on the bridge deck. This method is commonly accepted to be functionally equivalent to static testing (Potisuk and Higgins 2007) and also provides more information and often requires less time when compared to static testing. These tests require bridge closure or lane closure and typically, traffic is not on the bridge during data collection.

High-speed testing placed the truck in a traffic lane and the drivers were instructed to maintain the speed limit as long as they are on the bridge. This type of truck crossing was only performed on the Varina-Enon Bridge in this document. These tests require a rolling bridge closure to ensure there is no other traffic on the structure. For the Varina-Enon Bridge test, law enforcement slowed traffic down behind the trucks to allow a test free of other vehicles. The inaccuracies associated with the truck maintaining its transverse position are a major drawback to this type of truck crossing. Furthermore, if not accompanied by a static test in the same transverse position, the dynamic affect is not easily separated.

Typically, each test was repeated a minimum of two times to verify the sensor response. However, there were instances of only one crossing for each load case. These are documented in the following testing plans for each bridge test.

3.2 Seabreeze Bridge Test Plan

Testing of the westbound structure of the Seabreeze Bridge as a part of the Long Term Performance Project commenced in April 2011. The Seabreeze Bridge, located in Daytona Beach, FL and constructed in 1997, is a variable depth, segmental concrete box girder structure, built using balanced cantilever construction. The bridge contains ten spans, 247 ft interior spans and 174 ft end spans, with a total length of 2290 ft. Figure 23 shows the variable depth dimensions with the pier cross section (left) and the midspan cross section (right), respectively. The girder cross section is a concrete winged box with a total width of 49 ft. The 9 in. thick top slab is 22.3 ft wide (web-to-web) with 11.7 ft cantilever wings. The top slab and wings are haunched near the flange-to-web intersections. Cross section depth varies from 8 ft to 13.3 ft deep, with 14 in. thick webs.

Due to the very large scale of the bridge, the instrumentation was focused on Spans 2 and 3. The test setup consisted of 28 total instruments, two distinct instrument orientations and five unique load cases. The research team decided not to monitor the curved portions of the box due to the relatively large radius of curvature and the simpler nature of the straight sections.

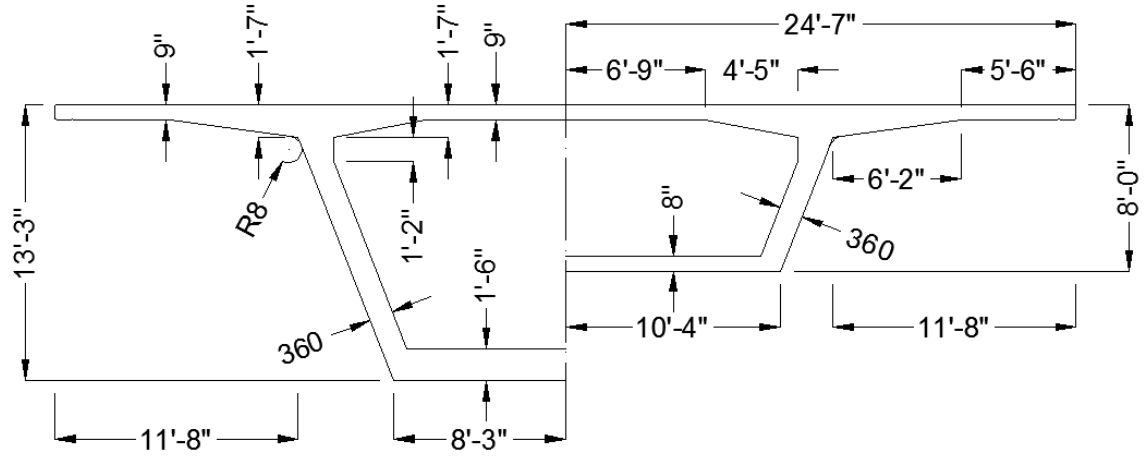

Figure 23 – Seabreeze Bridge Variable Depth Box Girder Pier and Midspan Cross Sections

The general goals of the experimental procedures were to quantify the current response of the bridge in order to identify the nature of any future degradation as per the goals of the LTBP. Specifically, researchers focused on parameters significant to design of segmental concrete box girder bridges and selected instrumentation to quantify this behavior. Instruments were placed in positions to monitor longitudinal and transverse strains, as well as global behavior such as bearing rotation and deflection.

3.2.1 Instrumentation Layout

Instrumentation was broken into two separate orientations to accommodate different load cases and to maximize the effectiveness of the available strain transducers. Instruments were grouped into what will be referred to as the longitudinal orientation and the transverse orientation. Details on the two orientations can be found in the following sections. These orientations had the majority of the strain transducers aligned in either the transverse or the longitudinal direction in order to measure strains in those directions, which are both important to design.

The focus of testing was on the half spans near Pier 2. Instruments were centered on five cross-sections near Pier 2, mostly focusing on Span 2 near the pier. Each of the five cross-sections are shown in Figure 24. Section A was near midspan and was instrumented to measure both strains and deflections. The intent of the strains at Sections B and C were to see how strains changed near the "disturbed" pier region. Section D was instrumented to measure the rotation of the pier and pier segment, and Section E only investigated the vertical deflection of that location. Sections A, B and C changed between the two sensor orientations, but Sections D and E remained the same.

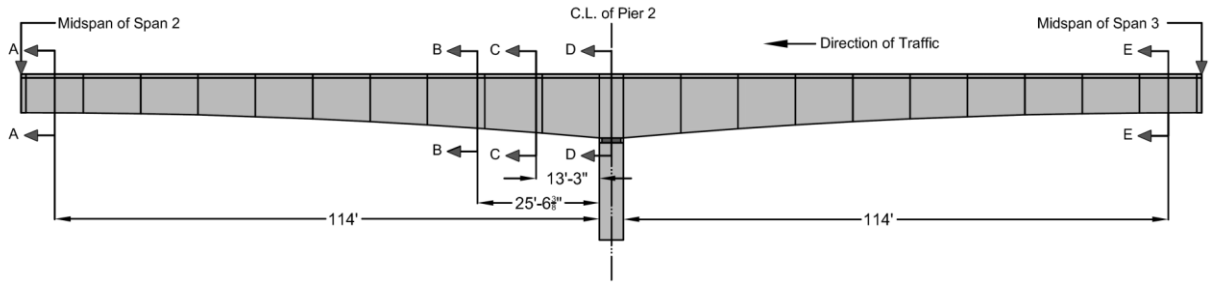

Figure 24 – Instrumentation Section Locations near Pier 2 for the Seabreeze Live Load Test

The transverse and longitudinal rotation on the pier diaphragm and the longitudinal rotation at the top of the pier were monitored at Section D. Inclinometers were placed inside the box girder as seen in Figure 25. Figure 26 shows the orientation of the inclinometer on the top of the pier. Deflectometers were placed at the bottom of the webs at Section A and Section E to measure global deflection.

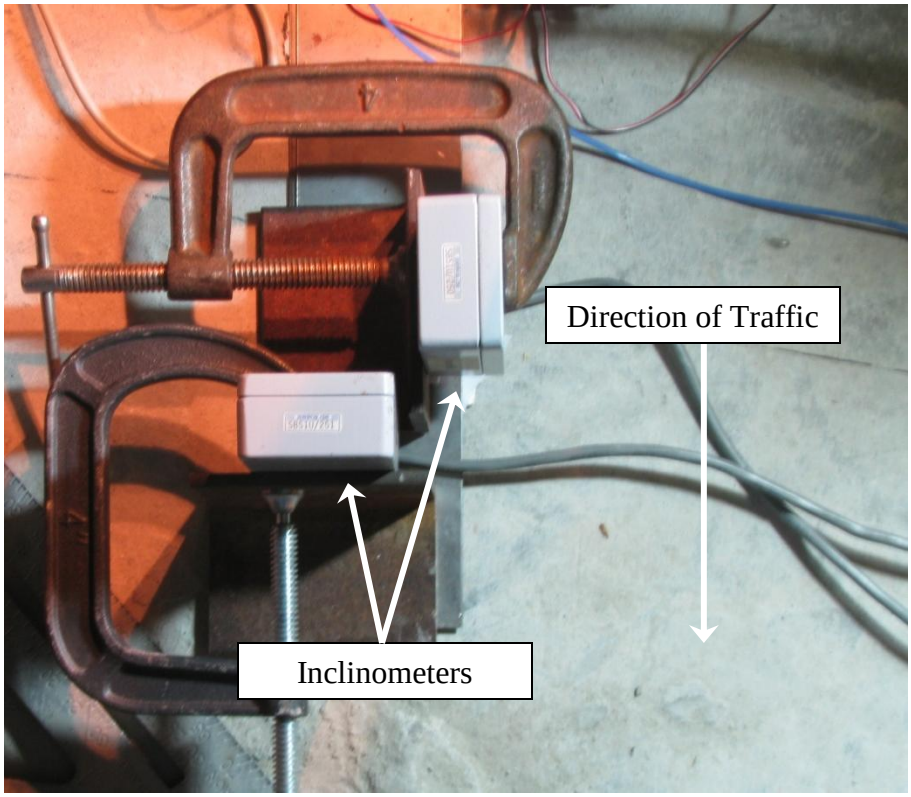

Figure 25 – Orthogonal Inclinometers on Diaphragm inside Seabreeze Bridge

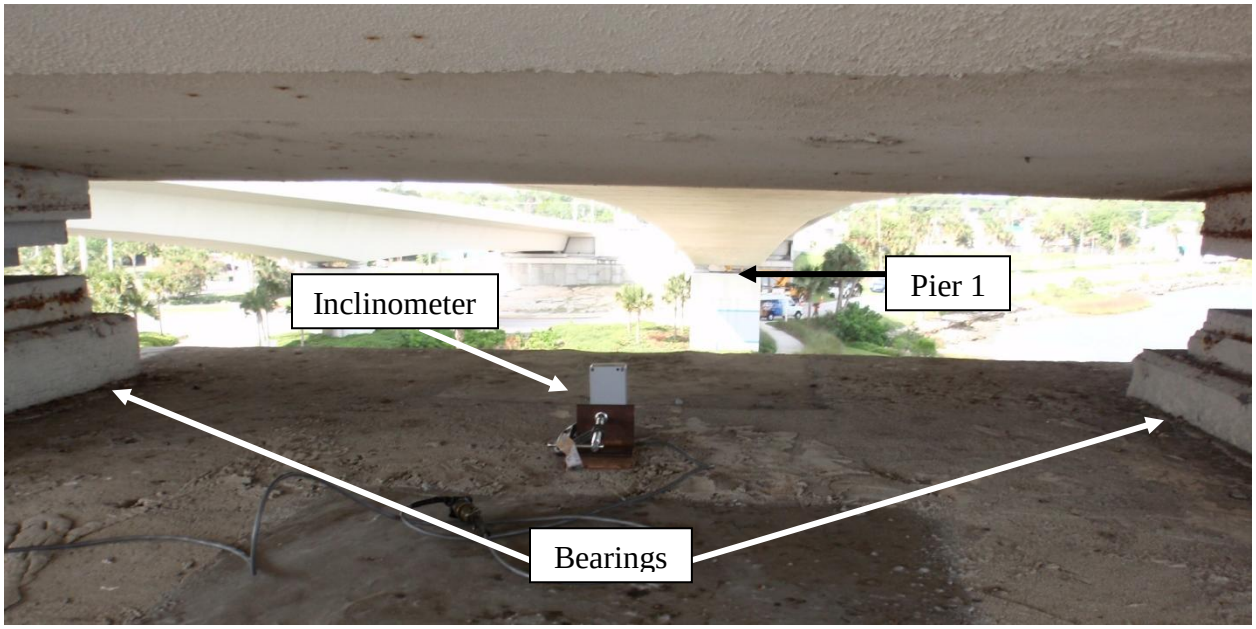

Figure 26 – Inclinometer on Top of Pier 2 of Seabreeze Bridge

3.2.1.1 Longitudinal Transducer Orientation

Instruments on the outside of the box were difficult to place because of the articulating arm truck and the elements. For this reason, the instruments located on the outside of the cross-section were minimized and stationary through all tests. It should also be noted that to characterize the strains in the box, and to make efficient use of the transducers available, transducers were only placed on the side of the box opposite the sidewalk for all tests. The legend for all instrumentation figures, regardless of orientation, can be found in Figure 27. In an effort to keep the longitudinal orientation and transverse orientations separate, an L (for Longitudinal) and a T (for Transverse) is placed in front of the section letter. For the longitudinal transducer orientation, the majority of strain transducers were oriented to measure longitudinal strains, as indicated in Figure 28 for Section A, Figure 29 for Section B and Figure 30 for Section C. The exceptions are the transversely oriented strain transducers on the wing in Sections LA and LC. This instrument was used for comparisons in the transverse orientation.

The remaining strain transducers were placed on the inside of the box with the primary purpose of measuring longitudinal global bending strains and the shear lag phenomenon. The four sensor locations inside the box were approximately one web thickness away from the webs and in the center of the top and bottom slabs. Sections A, B and C have nearly identical locations of strain transducers to make quantitative comparisons between the sections.

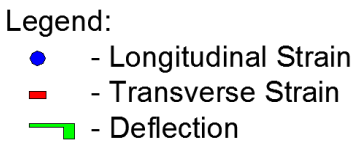

Figure 27 – Legend for all Cross-Section Instrumentation

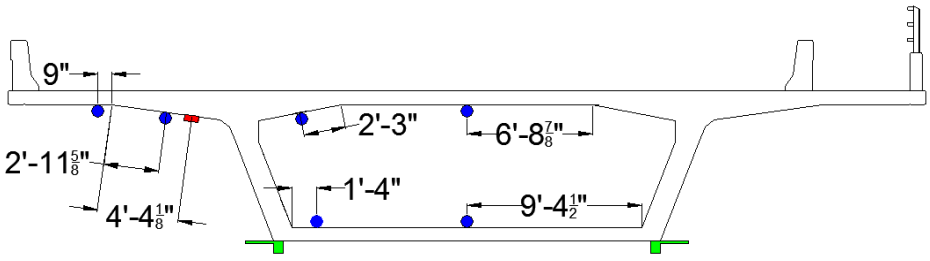

Figure 28 – Section A Instrumentation

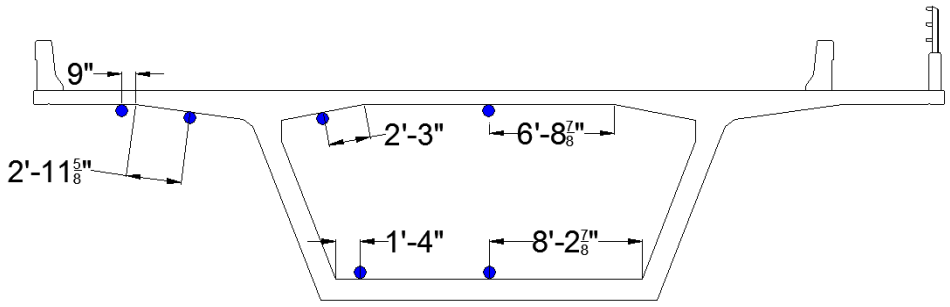

Figure 29 – Section B Instrumentation

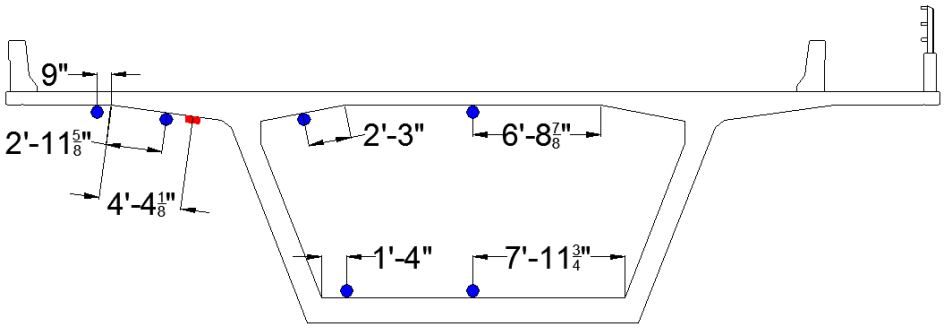

Figure 30 – Section C Instrumentation

3.2.1.2 Transverse Transducer Orientation

The second instrumentation orientation is referred to as the transverse orientation. In this orientation, the majority of the strain transducers on the inside of the box girder were relocated and reoriented to read several transverse bending strains. Instruments on the outside of the box remained stationary for reasons outlined in the preceding section. Transverse strain measurements were placed only on the side of the box girder opposite the sidewalk to maximize use of the limited number of strain transducers.

The transverse instrument orientations for Section A, B and C can be found in Figure 31, Figure 32 and Figure 33, respectively. Take note that Section B does not contain transverse instruments and was used primarily for comparison purposes between transducer orientations.

Transverse transducers inside the box were placed one member depth away from the junction of the slabs and web cross-section components to minimize local effects. Sections A and C have

nearly identical transducer locations to make quantitative comparisons between the two locations. Instrumentation on the exterior of the box girder remained stationary when switching to the transverse orientation.

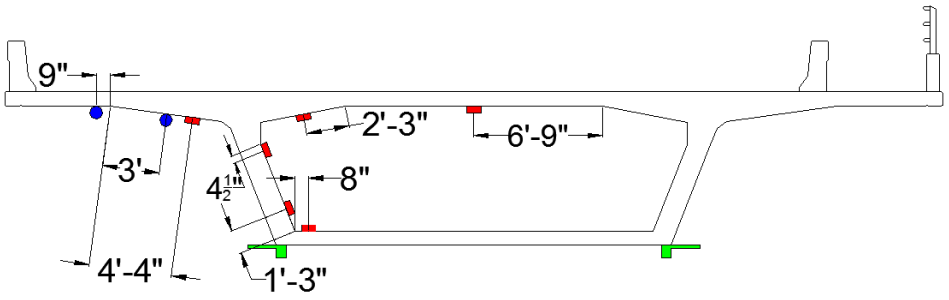

Figure 31 – Section A Instrumentation

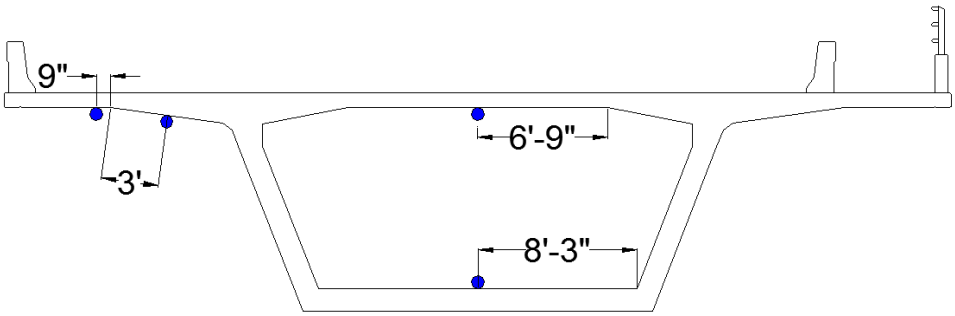

Figure 32 – Section B Instrumentation

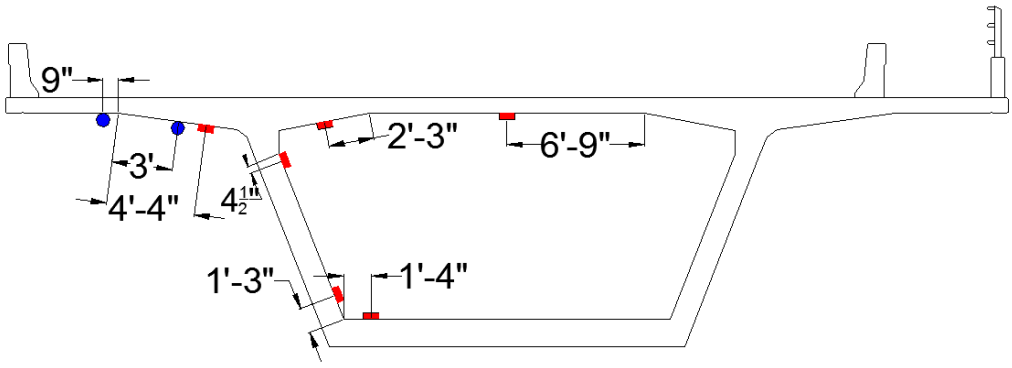

Figure 33 – Section C Instrumentation

3.2.2 Loading Procedure

Loading for the live load test of the Seabreeze Bridge consisted of five unique load cases with the custom Florida Department of Transportation (FDOT) load truck. Testing was considered

quasi-static, with the truck moving at a walking pace throughout the load test. Details of the loading procedure are as follows.

3.2.2.1 FDOT Load Truck

The custom FDOT load truck is used by the FDOT for load testing of bridges throughout the state of Florida. Figure 34 shows the dimensions and axle weights for the Seabreeze Bridge load truck. The truck was loaded with steel blocks prior to testing and can be oriented to modify the loading. This pattern resulted in the largest applied load, while still respecting the current load rating.

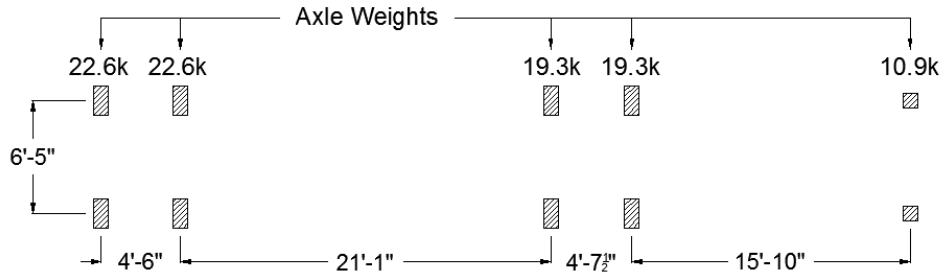

Figure 34 – FDOT Custom Test Truck Dimensions and Axle Weights

3.2.2.2 Load Cases

The five load cases for the live load testing of the Seabreeze Bridge can be found in Figure 35. Each load case lined the front tires up in the transverse location shown, and the truck drove at the slowest maintainable speed (approximately 1 to 5 mph) throughout testing. This is referred to as quasi-static testing and the researchers have found this to be more useful and yield equivalent results to static testing.

Load Case 1 (LC1) maximized loading on the cantilever wing of the box girder by placing the load truck as close as possible to the barrier. Load Cases 2 and 3 (LC2, LC3) placed a truck centered in the left and right traffic lanes, respectively. This was important for a baseline reading of response in these two lanes for planning of a long term monitoring system as well as identification of the response this bridge undergoes regularly. Additionally, the LC3 orientation minimizes the effects of torsion on the cross section. Load Case 4 (LC4) places the passenger

wheel line over the center of the top slab, with the driver's side wheel-line shifted toward the instrumentation cluster. This load case maximizes top slab bending response in the transverse direction. Load Case 5 (LC5) is a near mirror of LC2 and places a truck nearest the right hand barrier. This provides an opportunity for a mirror comparison and possibly insight into how the barrier and sidewalk are affecting the response.

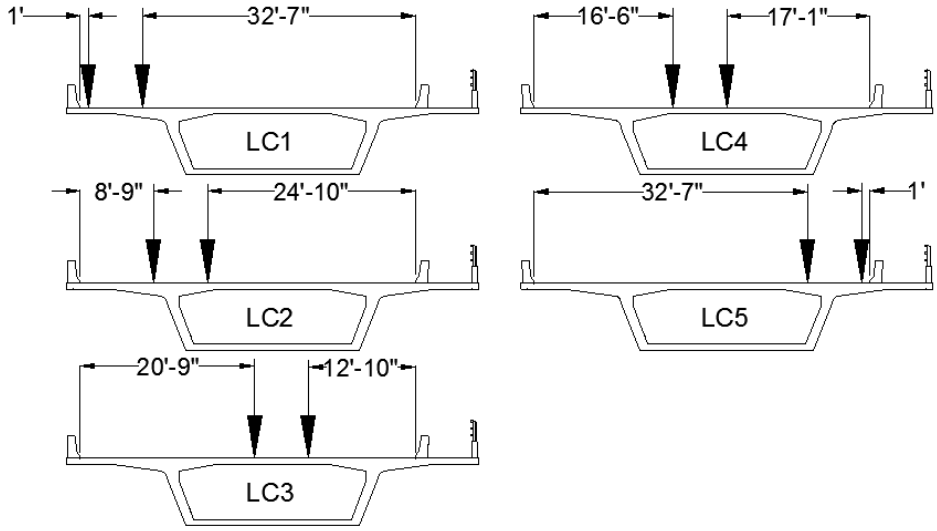

Figure 35 – Seabreeze Bridge Load Cases

For the longitudinal transducer orientation, LC1 through LC5 was performed, but only LC1, LC3, and LC4 were performed in the transverse transducer orientation due to time restrictions. Each load case was repeated twice for each instrument orientation, for 16 total truck passes.

3.3 Smart Road Bridge Test Plan

The Smart Road Bridge, located in Blacksburg, Virginia, is part of the Virginia Tech Transportation Institute facility known as the Smart Road and can be found in Figure 36. Constructed in 1998 using cast-in-place, balanced cantilever construction with integral piers, the Smart Road Bridge is currently the tallest bridge in Virginia. The superstructure cross section, presented in Figure 37, is a winged box girder with two lanes and a depth ranging from 12 ft at midspan to 31 ft at the piers. The top slab is 18.76 ft wide with a 9 in. and 22 in depth slab at the centerline and web locations, respectively. The bridge consists of five, variable depth spans with 472 ft interior and 284 ft exterior spans for a total length of 1,985 ft.

Figure 36 – Smart Road Bridge Spanning Ellet Valley near Blacksburg, VA

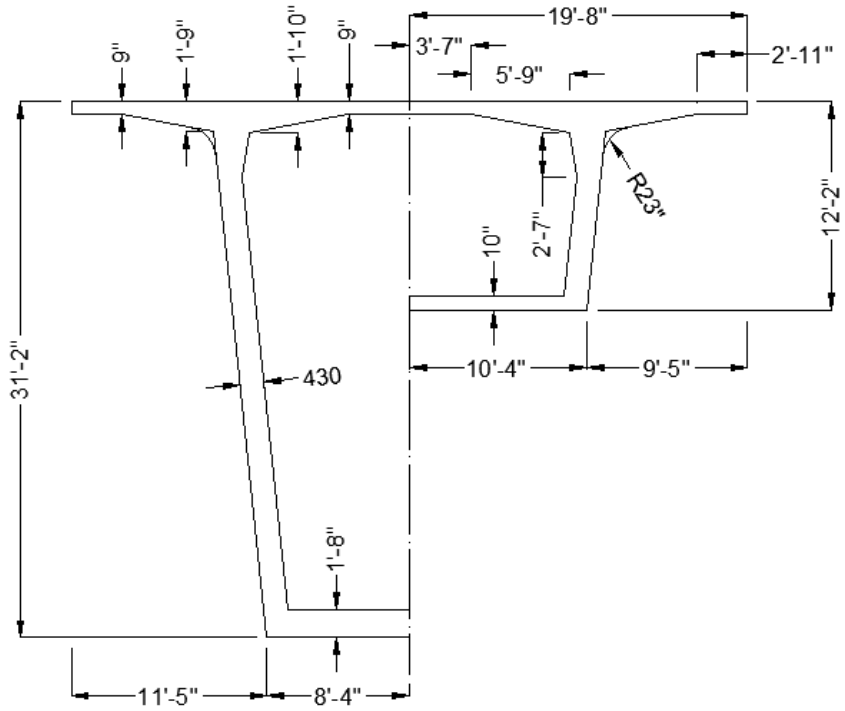

Figure 37 – Smart Road Bridge Maximum (left) and Minimum (right) Cross Sections

3.3.1 Instrumentation Layout

The focus of testing on the Smart Road Bridge was on the northern half of Span 3. Sensors were centered on two cross-sections. Figure 38 presents a partial elevation indicating the two instrumented cross-sections. Section A, located at midspan of Span 3, longitudinal and transverse strain transducer placement is shown in Figure 39 and Figure 40, respectively. Section B, located at quarter span of Span 3, longitudinal and transverse strain transducer placement is shown in Figure 41 and Figure 42, respectively. Access during the test limited all instrumentation to the interior of the structure and on the deck. Transverse strain sensors on the deck were placed out of the truck tire paths, as can be seen in Figure 43. All strain transducers on the exterior of the box girder used weather/sunlight protection as shown in Figure 20.

Transverse transducers inside the box were placed at a minimum one member depth away from the junction of the slabs and web cross-section components to minimize local effects. Longitudinal strains were measured at various points on the slabs to capture any non-linear longitudinal strain (shear lag) distribution.

All strain transducers were placed in similar orientations at both Sections for comparison purposes. All Load Cases, discussed below, were performed with instruments at Section B, then instruments were removed and reattached at Section A and all Load Cases were repeated.

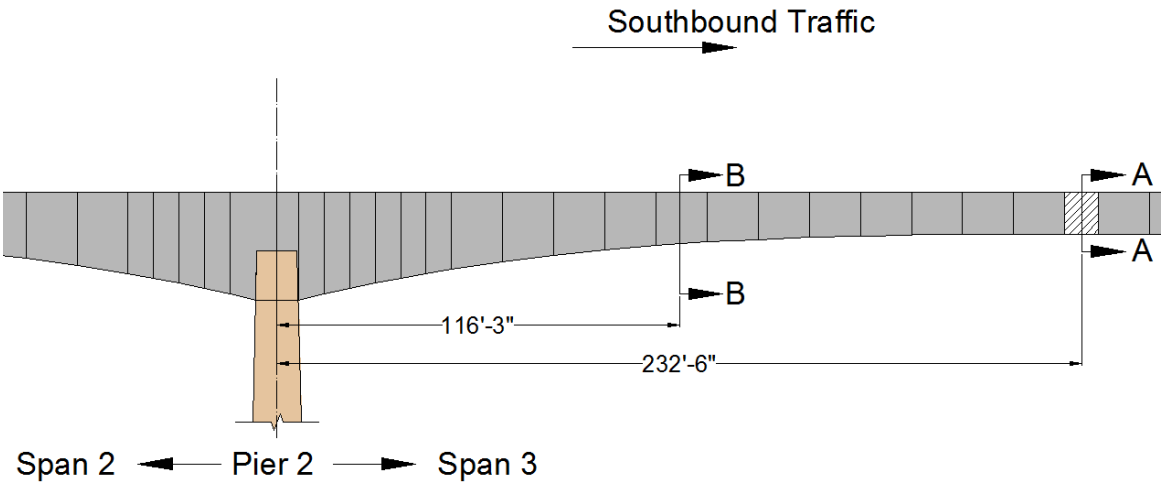

Figure 38 – Smart Road Bridge Elevation View of Span 2 and 3

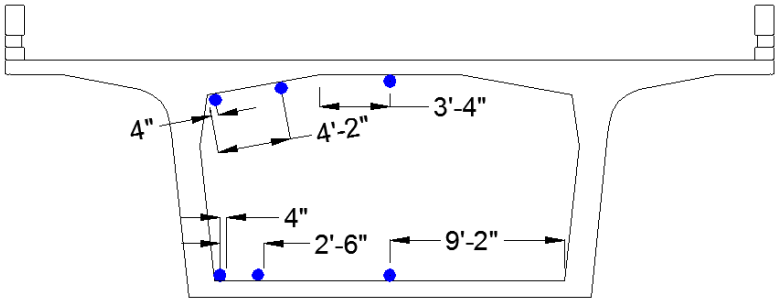

Figure 39 – Smart Road Bridge Section A Longitudinal Strain Instrumentation – Looking in the Direction of Southbound Traffic

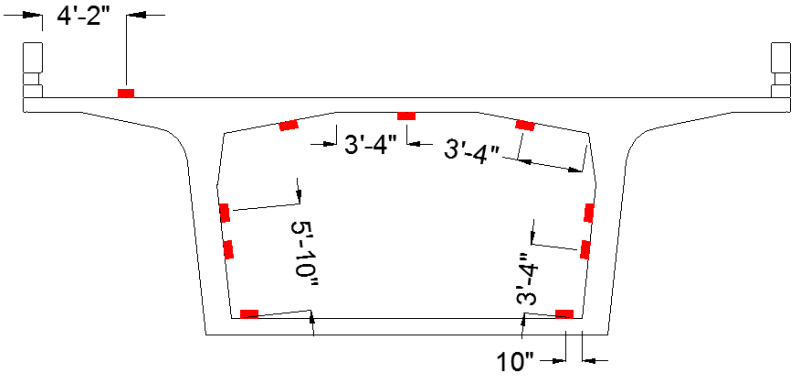

Figure 40 – Smart Road Bridge Section A Transverse Strain Instrumentation – Looking in the Direction of Southbound Traffic

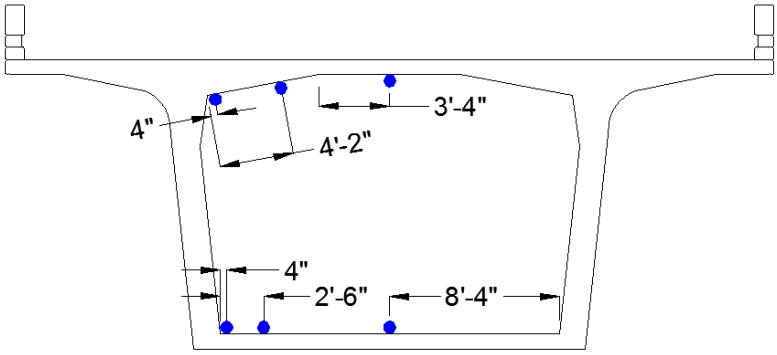

Figure 41 – Smart Road Bridge Section B Longitudinal Strain Instrumentation – Looking in the Direction of Southbound Traffic

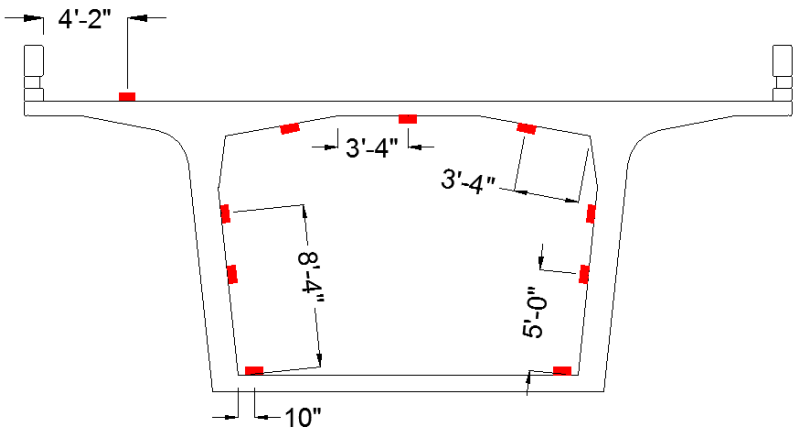

Figure 42 – Smart Road Bridge Section B Transverse Strain Instrumentation – Looking in the Direction of Southbound Traffic

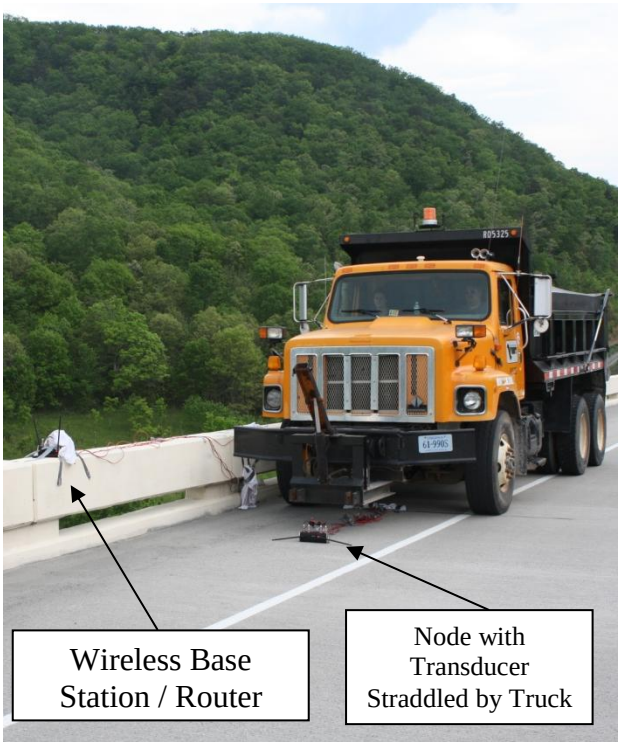

Figure 43 – Strain Sensor on the Bridge Deck Straddled by the Load Truck

3.3.2 Loading Procedure

Loading for the live load test of the Smart Road Bridge consisted of five unique load cases with two Virginia Department of Transportation (VDOT) load trucks. Testing was considered quasi-

static, with the truck moving at a walking pace throughout the load test. Details of the loading procedure are as follows.

3.3.2.1 VDOT Dump Trucks

Standard, three-axle, VDOT dump trucks were used for the Smart Road Bridge testing. Figure 44 and Figure 45 show the measured dimensions and axle weights for the load trucks. Both trucks had all dimensions within 1 in. of the other. The trucks were loaded with gravel from a nearby quarry.

Figure 44 – VDOT Three-Axle Dump Truck Photo

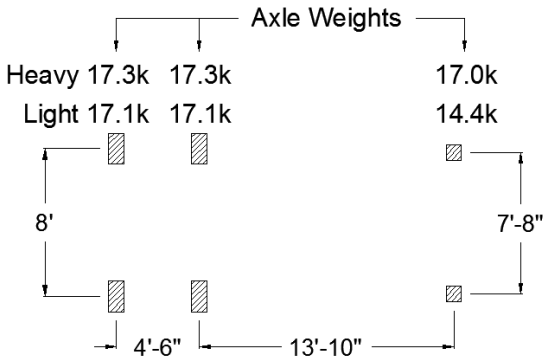

Figure 45 – VDOT Three Axle Dump Truck Average Measured Dimensions

3.3.2.2 Quasi-Static Load Cases

The five load cases for the live load testing of the Smart Road Bridge can be found in Figure 46, note the legend is the same as for Figure 35. There were two iterations for each load case, while

Section B was instrumented. However, due to time constraints, only LC3 and LC5 had multiple iterations when Section A was instrumented. Each load case lined the front tires up in the transverse location shown, and the truck drove at the slowest maintainable speed (approximately 1 to 5 mph) throughout testing.

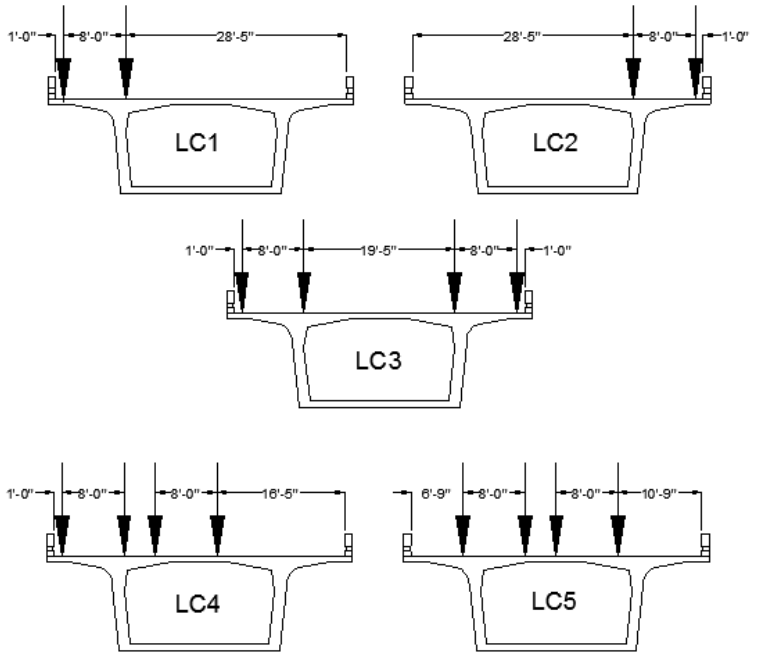

Figure 46 – Load Case Descriptions for Smart Road Bridge Load Test

3.4 Varina-Enon Bridge Test Plan

Built in 1990, the 4,680 ft long Varina-Enon Bridge carries Interstate 295 across the James River near Richmond, VA. The bridge consists of separate north and south bound structures with a series of continuous segmental box girder approach structures and a 630 ft long cable stayed main span. The main span, while not the focus of the current investigation, was the second cable stayed structure in the United States and was the first bridge in the world to use precast concrete delta frames.

The approach and main spans, erected using span-by-span segmental construction, use external tendons with epoxied joints. The Varina-Enon Bridge is the second tallest bridge in Virginia with a navigation clearance of 150 ft.

The superstructure cross section, presented in Figure 47, is a winged box girder with three northbound traffic lanes. The Varina-Enon Bridge was erected using span-by-span construction and has a constant depth cross section of 12 ft and a width of nearly 58 ft. The focus of this investigation is on the first approach span of the northbound structure.

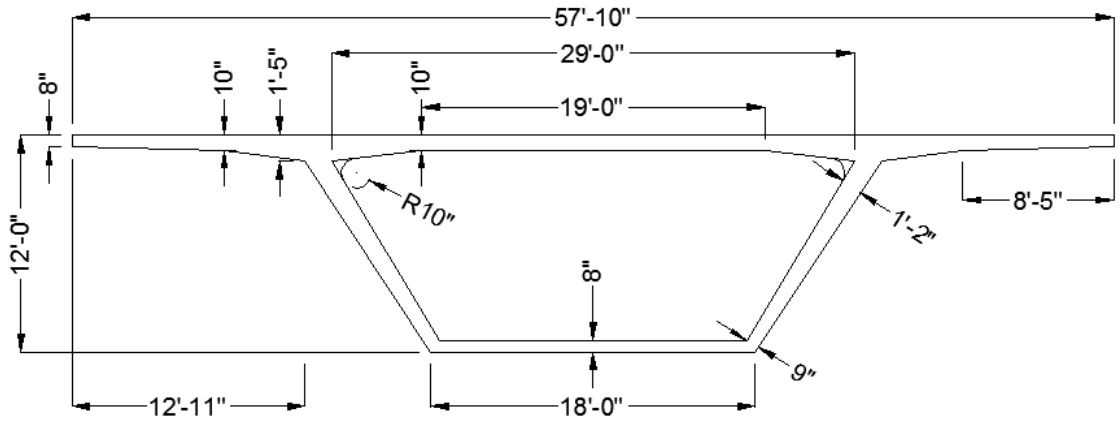

Figure 47 – Varina-Enon Bridge Cross Section Dimensions

3.4.1 Instrumentation Layout

The instrumentation was focused on Spans 5 and 6 on the southernmost northbound, six span, approach structure. All sensor locations indicate the "as-installed" location and are measured from the nearest or most convenient point of reference.

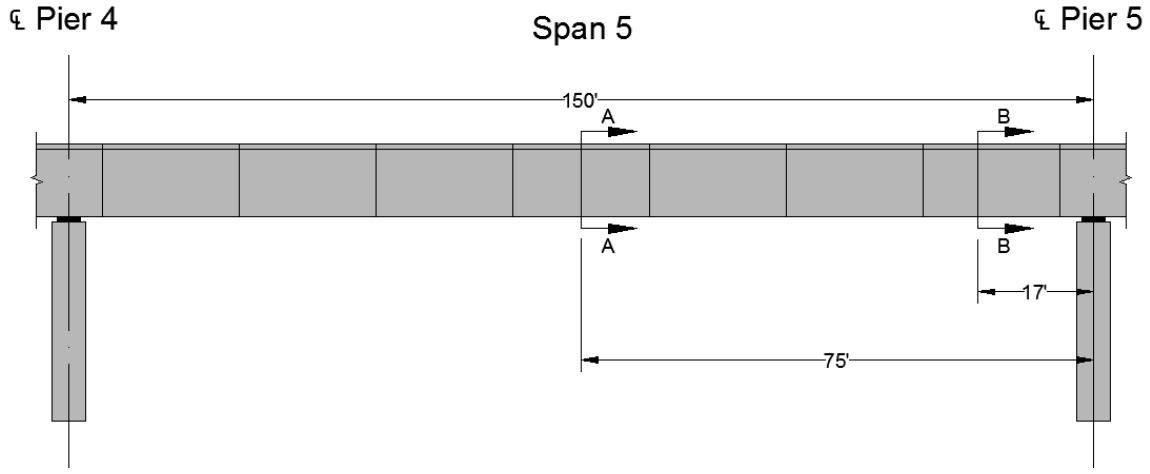

Figure 48 – Varina-Enon Bridge Span 5 Elevation View Span 5 Instrument Locations

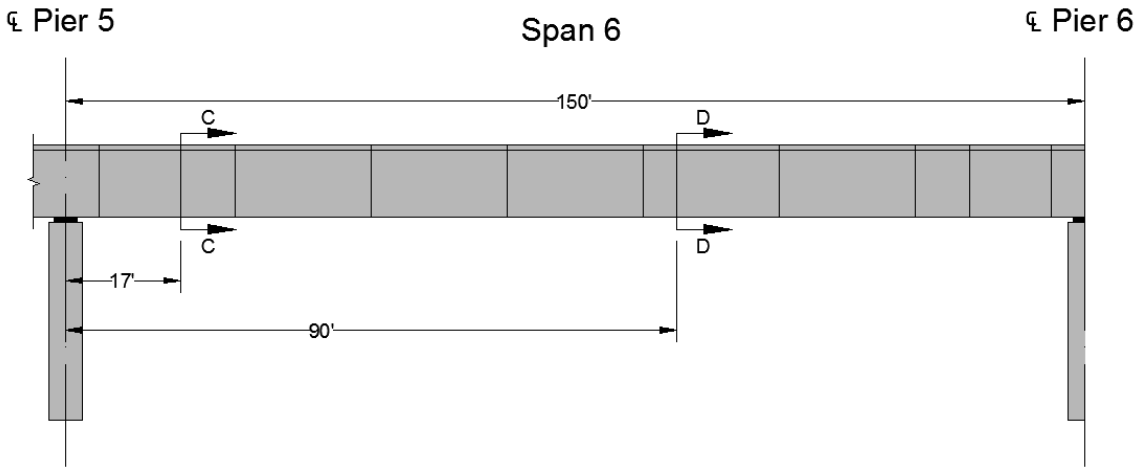

Figure 49 – Varina-Enon Bridge Span 6 Elevation View Span 6 Instrument Locations

Deflection was measured at Section A on Span 5. Longitudinal strain sensors were located on Section B as shown in Figure 50. Transversely oriented strain sensors were located at Section C as shown in Figure 51.

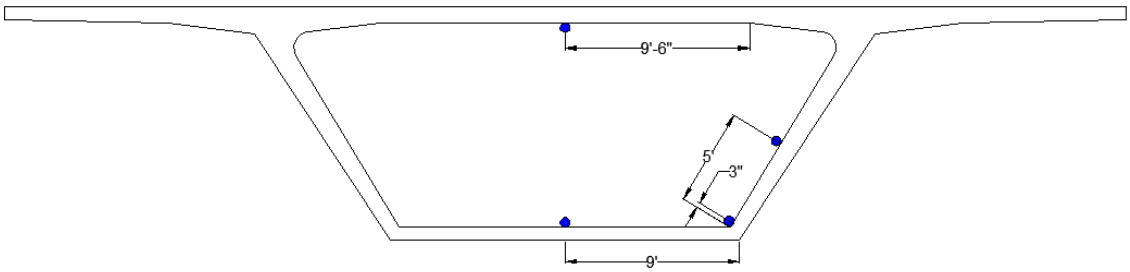

Figure 50 – Section B Longitudinal Strain Sensor Locations, Looking North

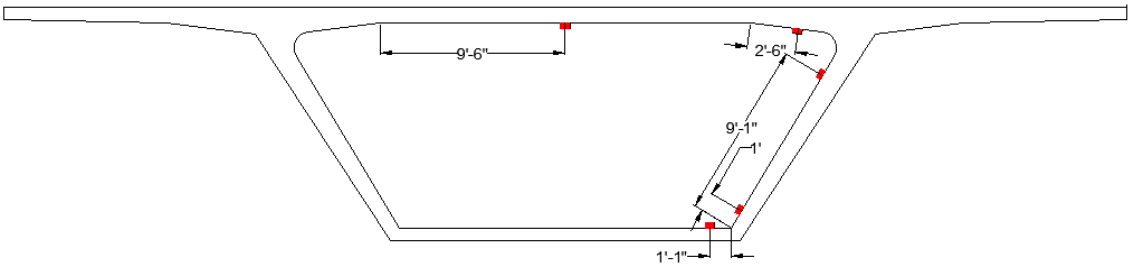

Figure 51 – Section C Transverse Strain Sensor Locations, Looking North

Figure 52 presents the longitudinal strain transducers located on Section F. This longitudinal strain instrumentation was intended to provide information about any non-linear strain distribution (shear lag) at the maximum positive moment location. Figure 53 shows the transverse strain transducer locations on Section F.

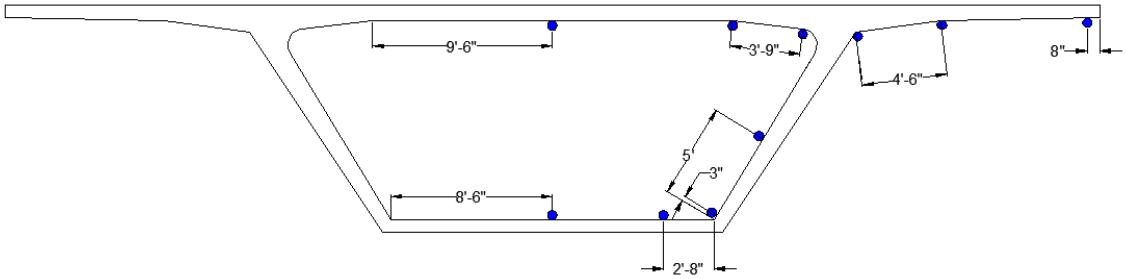

Figure 52 – Section D Longitudinal Strain Sensors, Looking North

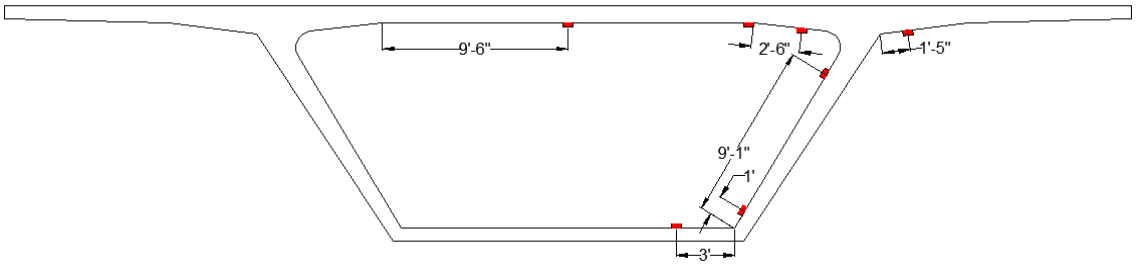

Figure 53 – Section D Transverse Strain Sensors, Looking North

3.4.2 Loading Procedure

Loading for the live load test of the Varina-Enon Bridge consisted of three high-speed load cases and three quasi-static load cases. The high-speed load trucks were two VDOT low profile tractor-trailers with a single VDOT dump trucks carried by each trailer. Quasi-static testing used the VDOT dump trucks only.

3.4.2.1 Load Trucks

The tractor-trailers are shown in Figure 54 carrying the VDOT dump trucks during the Varina-Enon load test. Figure 55 shows the dimensions and load arrangement of the tractor-trailer trucks, note that transverse wheel spacing was not recorded. The tractor-trailers were used only for high-speed testing. During the high speed loading, data was collected while the trucks were

on Spans 4 through 6. Following the high-speed load cases, workers removed the VDOT dump trucks trailers and the individual trucks were then used for quasi-static loading. During quasi-static loading, the trucks were driven from Pier 4 to Pier 6 and data was collected while the trucks were on Span 5 and Span 6. Figure 56 present the VDOT dump truck measured dimensions and axle weights.

Figure 54 – VDOT Tractor-Trailers with Dump Trucks

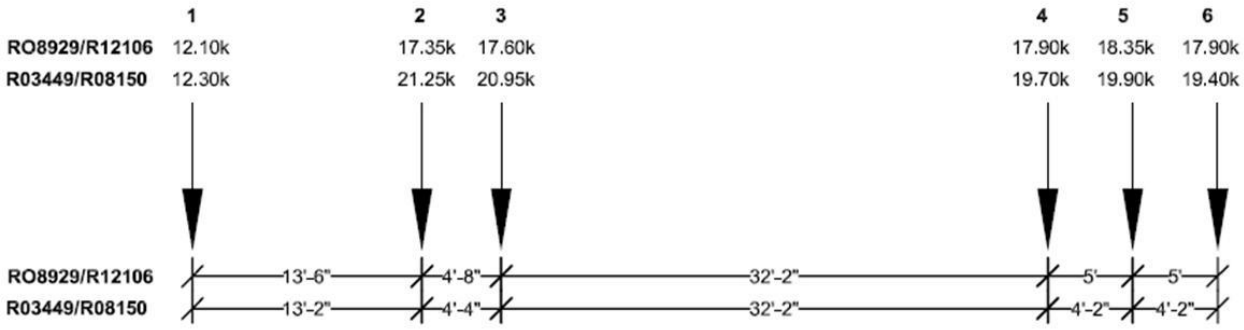

Figure 55 – VDOT Tractor-Trailer Measured Dimensions

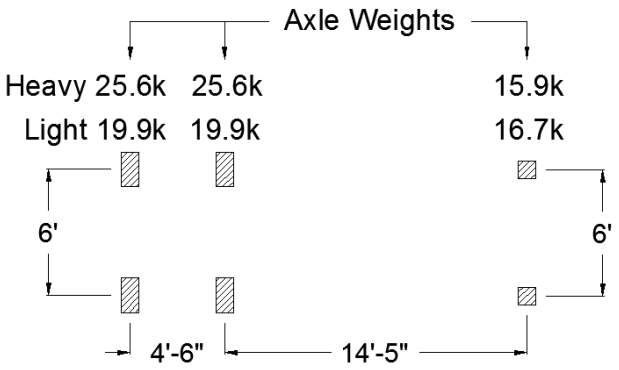

Figure 56 – VDOT Dump Trucks for Varina-Enon Bridge Test

3.4.2.2 High Speed and Quasi-Static Load Cases

The three high-speed load cases for the Varina-Enon Bridge load test are shown in Figure 46 on the left and labeled LC1 though LC3. Load Case 1 centers the tractor-trailer in the center driving lane, LC2 centers the tractor-trailer in the left hand driving lane and LC3 is the summation of LC1 and LC2. The quasi-static load cases, LC4 through LC6 are also presented in Figure 57. Note that the front to back trucks in LC5 had 12 ft spacing between the rear tires of the front truck and the front tires of the rear truck. The purpose of the quasi-static load cases was primarily to monitor transverse strains. Unfortunately, due traffic control limitations only the right hand lane and shoulder could be closed for quasi-static testing. Additionally, traffic could not be stopped. For this reason, significant traffic was present on the bridge at times during LC4 through LC6. There were two repetitions for each load case, with the exception of LC6, which could not be repeated due to time constraints.

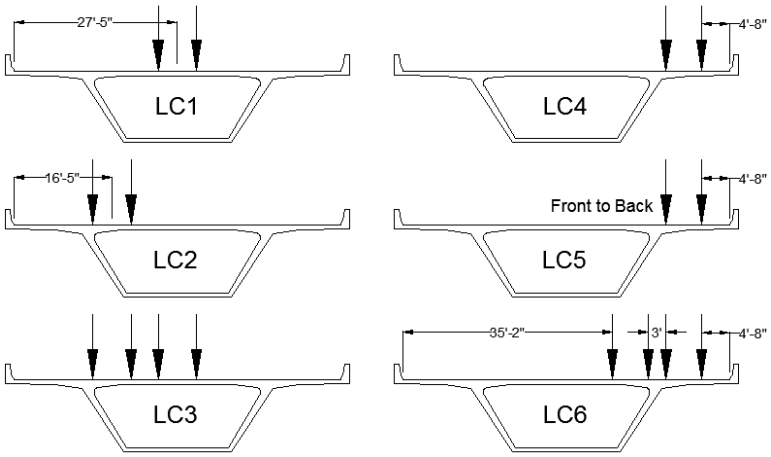

Figure 57 –Load Cases for Varina-Enon Load Test

4 Experimental Results and Discussion

The following sections discuss the results from the Seabreeze, Smart Road, and Varina-Enon Bridge live load tests. Table 7 provides a summary of the instrumentation on each bridge, where an "×" indicates the sensor type used. Each bridge was instrumented with longitudinal and transverse strain sensors at two or more cross sections. The longitudinal strain sensors were intended to identify the distribution of strains in the flanges to investigate if significant shear lag was present. The purpose of the transverse strain sensors was to quantify the transverse bending and understand the transverse strain bending behavior. Additionally, rotations and deflections were measured in order to evaluate longitudinal model accuracy. Appendix E contains information regarding data filtering and presentation.

Table 7 – Summary of Instrumentation

Bridge	Section	Vertical Deflection	Rotation	Longitudinal Strains	Transverse Strains
Seabreeze Bridge	A	×		×	×
	B			×	×
	C			×	
	D		×		
	E	×			
Smart Road Bridge	A			×	×
	B			×	×
Varina-Enon Bridge	A	×		×	
	B			×	
	C				×
	D			×	×

4.1 Seabreeze Bridge

The Seabreeze Bridge, a ten span single cell segmental box girder, was instrumented at five cross sections (see Figure 24). At Section A, deflection and longitudinal and transverse strain were measured (see Figure 28 and Figure 31). At Section B only longitudinal strain was measured (see Figure 29 and Figure 32. At Section C, longitudinal and transverse strains were measured (see Figure 30 and Figure 33). At Section D, longitudinal rotation inside the box and at the top of Pier 2 were measured. At Section E, vertical deflection was measured. The following sections

describe the data from the Seabreeze Bridge load test. Additional data for the Seabreeze Bridge load test is presented in Appendix A.

4.1.1 Longitudinal Strains

Longitudinal strains were measured at six locations on three separate bridge cross sections, Sections A, B and C in Figure 24. Figure 58 through Figure 60 present typical longitudinal strain versus front axle position at Section A, B and C, respectively. The remainder of longitudinal strain influence lines for each Seabreeze Bridge load case can be found in Appendix A. The plots in Figure 58 through Figure 60 include both repetitions of each LC1.

Three sharp top flange strain spikes are present when the truck crosses the instrumented section. This is caused by the close proximity of the wheel loads to the sensors. The more locally flexible locations, middle top slab and exterior wing, display more severe strain spikes than found in the sensors near the haunches. The effect is less severe with greater distance between the tire loads and the sensors, and non-existent in the bottom flange sensors, as shown in the longitudinal strain versus truck position plots.

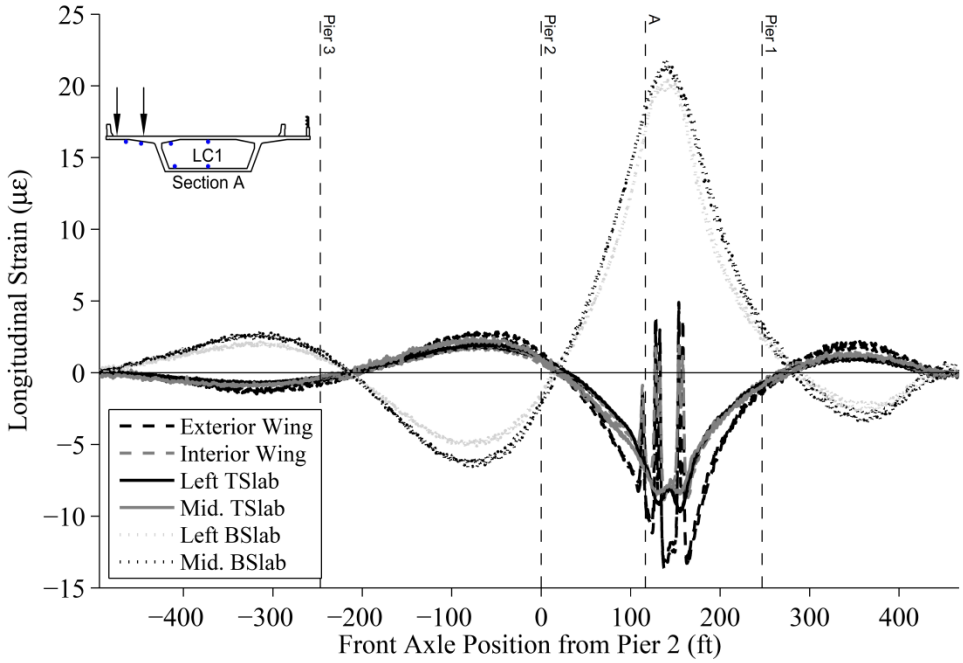

Figure 58 – Seabreeze Bridge Longitudinal Strains from LC1 at Section A – All Iterations

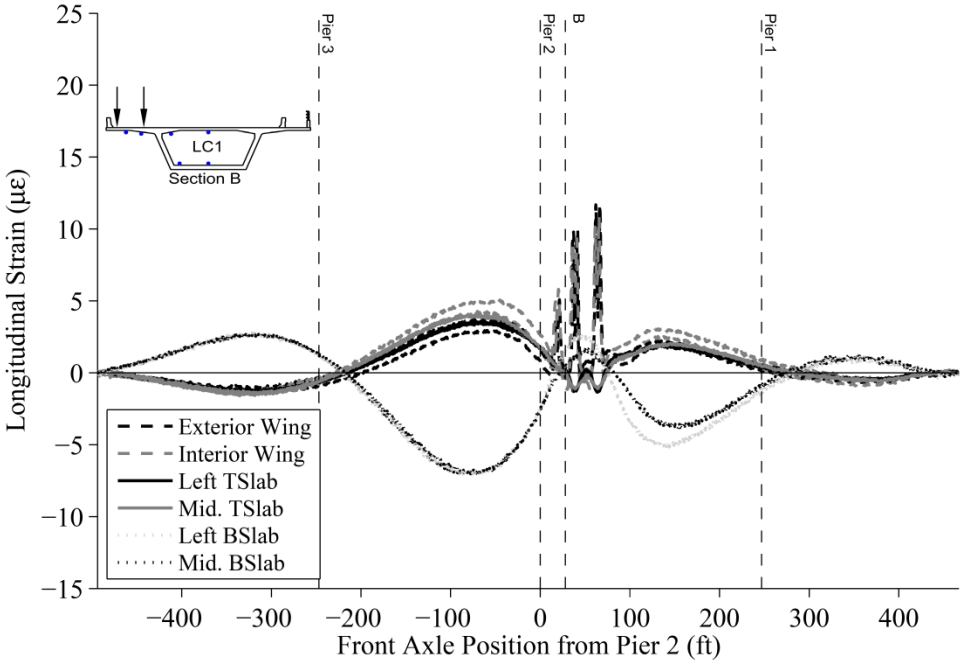

Figure 59 – Seabreeze Bridge Longitudinal Strains from LC1 at Section B – All Iterations

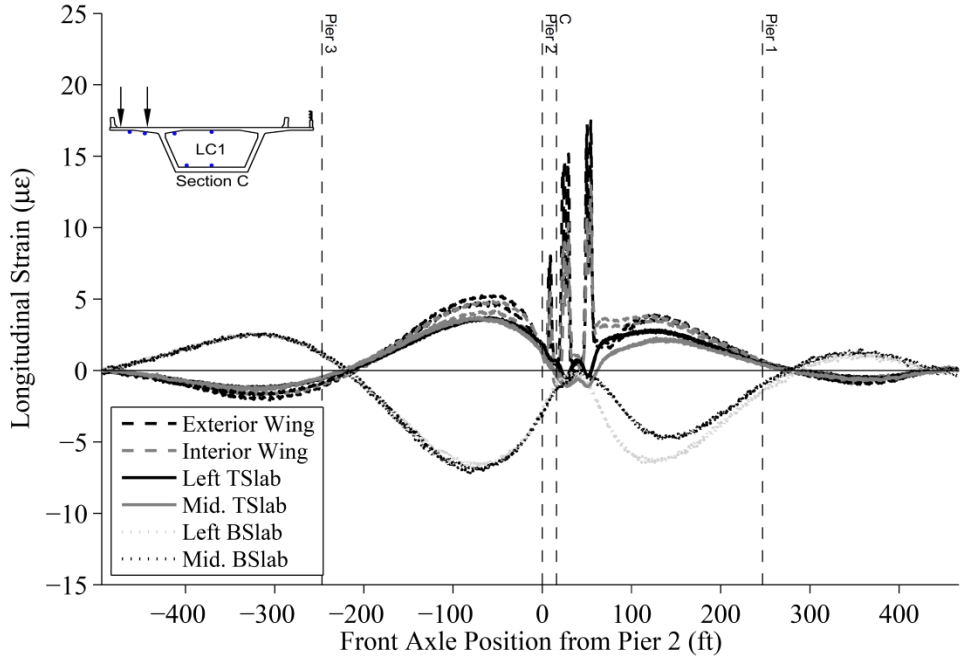

Figure 60 – Seabreeze Bridge Longitudinal Strains from LC1 at Section C, – All iterations

The two iterations for each load case were averaged to obtain the maximum and minimum strains given in Table 8 through Table 10. The absolute maximum response at each gage location is shown in bold. For Section A and B, LC1 caused the maximum response in all strain

transducers except the middle top slab location, which was maximum in LC4. Similarly, on Section C, the wing and web-wing transducer locations were maximum during LC1, but the web-top slab and web-bottom slab locations were maximum during LC4. Each of the Section C maximum occurred due to the local effects of the truck tires very near the instruments. However, each Section C minimum occurred while the truck created negative bending while on Span 3.

Table 8 – Seabreeze Bridge Section A Maximum and Minimum Longitudinal Strains

		Section A				
		LC1	LC2	LC3	LC4	LC5
Ext. Wing	Max (με)	5	3	3	4	3
	Min (με)	**-13**	-11	-10	-10	-10
Web-Wing	Max (με)	2	2	2	2	2
	Min (με)	**-9**	-8	-7	-7	-7
Web-Tslab	Max (με)	2	2	2	3	2
	Min (με)	**-10**	-9	-6	-7	-5
Mid-Tslab	Max (με)	2	3	20	**31**	3
	Min (με)	-8	-9	-24	-22	-8
Web-Bslab	Max (με)	**20**	20	17	19	15
	Min (με)	-5	-5	-5	-5	-5
Mid-Bslab	Max (με)	**21**	21	21	20	21
	Min (με)	-6	-6	-6	-6	-6

Table 9 – Seabreeze Bridge Section B Maximum and Minimum Longitudinal Strains

		Section B				
		LC1	LC2	LC3	LC4	LC5
Ext. Wing	Max (με)	**12**	3	3	3	3
	Min (με)	-1	-1	-1	-1	-1
Web-Wing	Max (με)	**10**	4	4	4	4
	Min (με)	-1	-2	-2	-2	-2
Web-Tslab	Max (με)	**4**	4	3	4	4
	Min (με)	-1	-3	-3	-4	-1
Mid-Tslab	Max (με)	4	4	27	**38**	4
	Min (με)	-2	-3	-18	-16	-1
Web-Bslab	Max (με)	3	3	3	3	3
	Min (με)	**-7**	-7	-7	-7	-7
Mid-Bslab	Max (με)	3	3	3	3	3
	Min (με)	**-7**	-7	-7	-7	-7

Table 10 – Seabreeze Bridge Section C Maximum and Minimum Longitudinal Strains

		Section C				
		LC1	LC2	LC3	LC4	LC5
Ext. Wing	Max (με)	**17**	5	5	5	4
	Min (με)	-2	-2	-2	-2	-2
Web-Wing	Max (με)	**13**	4	4	4	3
	Min (με)	-2	-2	-2	-2	-1
Web-Tslab	Max (με)	1	1	1	1	0
	Min (με)	**-18**	-2	-3	-5	-1
Mid-Tslab	Max (με)	4	5	3	**5**	3
	Min (με)	-1	-1	-1	-2	-1
Web-Bslab	Max (με)	4	4	26	**35**	4
	Min (με)	-1	-1	-8	-7	-1
Mid-Bslab	Max (με)	3	3	3	3	3
	Min (με)	**-7**	-7	-7	-7	-7

Figure 61 through Figure 63 present the longitudinal strains at Sections A through C, during LC5, when the truck is near midspan. This longitudinal truck location causes the maximum

global bending response at all locations and the transverse truck location is the furthest away from the top flange sensors. The LC5 transverse location minimizes local effects in the top flange sensors, allowing a clearer example of the top flange strain distribution.

Section A does not exhibit significant shear lag in the top flange as the strain values are lower at all locations near the web. On the top flange this may indicate the web thickness and lower sensor location (with respect to the neutral axis) results in smaller top flange strains. The Section A sensors show lower strains near the web than the middle web indicating there is some torsional effect, this may also be contributing to the larger strains near the middle of the wing and top slab components. More longitudinal strain measurement locations may help identify any torsional behavior in the future.

Section B and C are far from the truck when it is at midspan and are therefore free from the local truck effect during maximum negative bending. At these locations, the strain profile is very constant and indicates no appreciable shear lag.

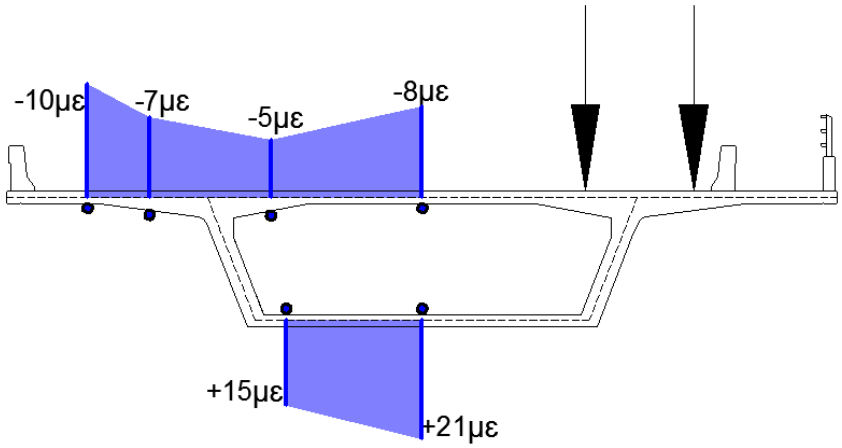

Figure 61 – Seabreeze Bridge Section A Maximum Longitudinal Strain Distribution – LC5 – Iteration 2

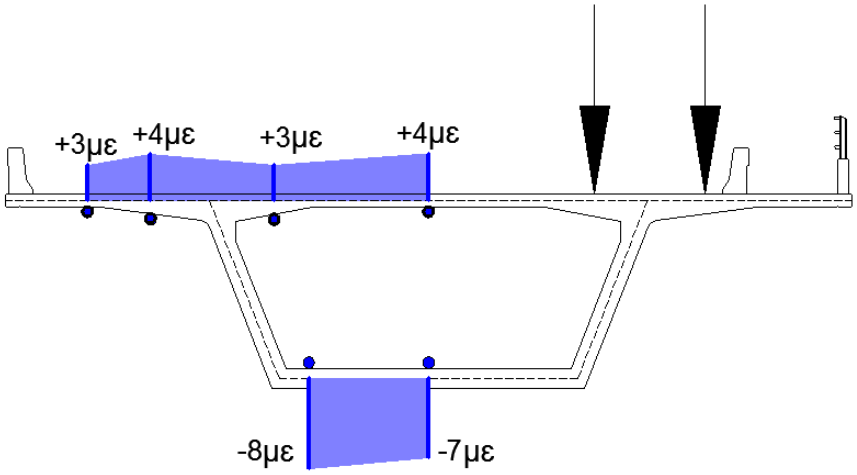

Figure 62 – Seabreeze Bridge Section B Maximum Longitudinal Strain Distribution – LC1 – Iteration 2

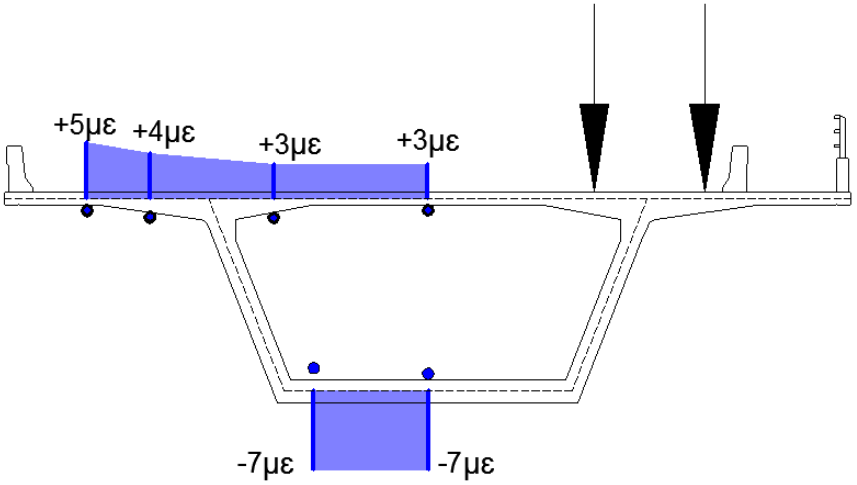

Figure 63 – Seabreeze Bridge Section C Maximum Longitudinal Strain Distribution – LC5 – Iteration 2

For comparison, maximum results from LC1 are plotted on the cross section for Figure 64 thorugh Figure 66 for Section A, B, C respectively. The results from LC1 at Section A exhibit some uncertainty in maximum compression strains due to the local truck loads shown in Figure 58. In Figure 64, this is shown by the larger compressive strain at the exterior wing location than in Figure 61. Additionally, the bottom web strain distribution is constant, where, in contrast to Section A during LC5 shown in Figure 61, the left bottom slab strain is much lower than the middle. Comparison between LC1 and LC5 further indicates the drop in strain at the left bottom slab location during LC5 is caused by torsion rather than any shear lag effect. During LC1,

Section B and C again do not indicate any significant shear lag as the strain distribution remains relatively constant on all components.

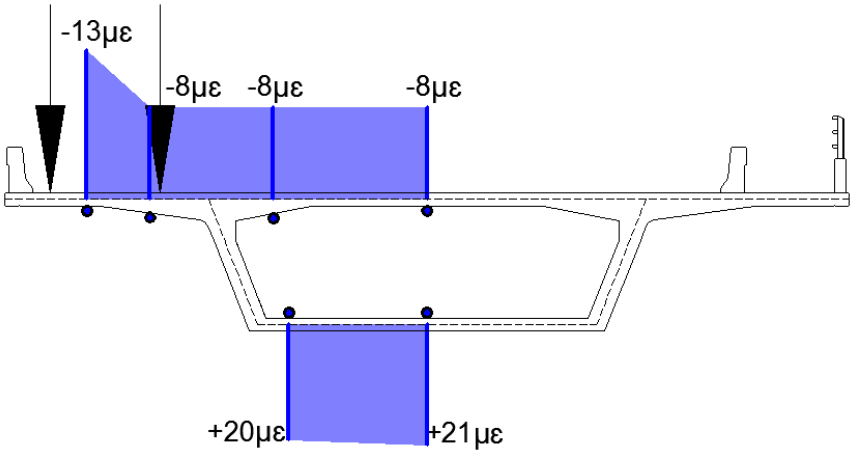

Figure 64 – Seabreeze Bridge Section A Maximum Longitudinal Strain Distribution – LC1 – Iteration 2

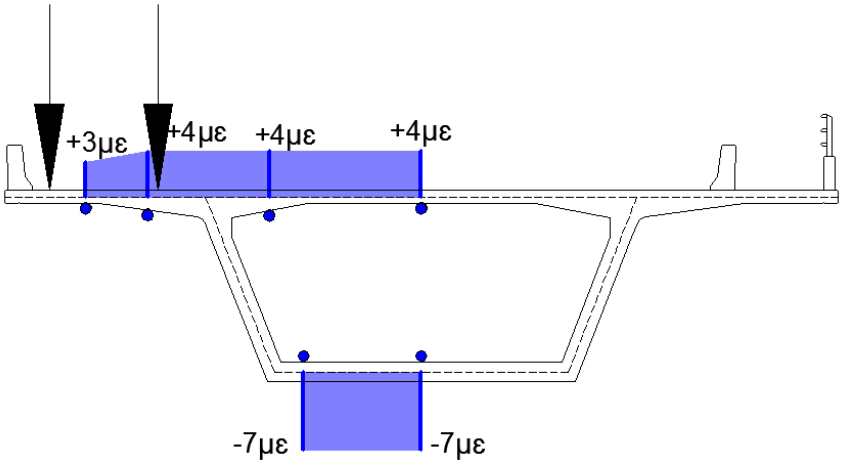

Figure 65– Seabreeze Bridge Section B Maximum Longitudinal Strain Distribution – LC1 – Iteration 1

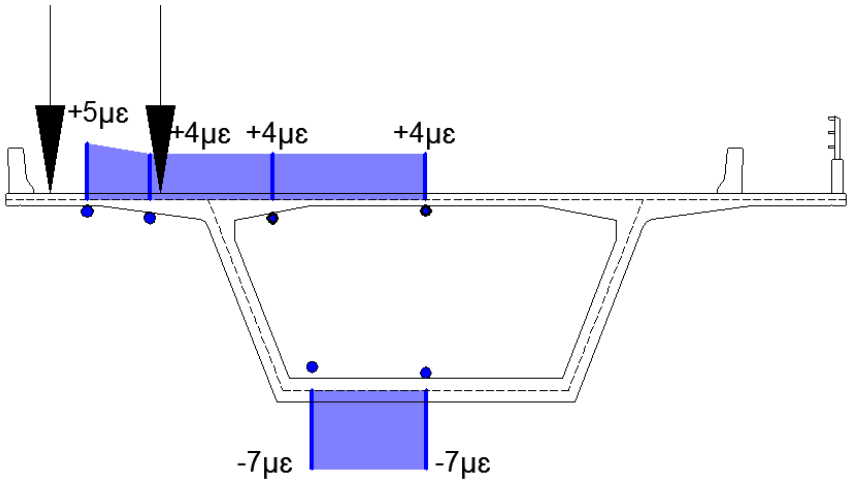

Figure 66– Seabreeze Bridge Section C Maximum Longitudinal Strain Distribution – LC1 – Iteration 1

Table 11 presents the effective flange width ratio (b_e/b) predictions for the Seabreeze Bridge measurement locations for various design provisions. There were only two measurements per component, which limited how accurate shear lag could be identified. However, they were adequate to conclude there was no significant shear lag observed on the Seabreeze Bridge. Section A design code predictions do not indicate significant shear lag, except the AASHTO Standard and the JRA Specifications, which are the most severe of all design codes (see Figure 10). Smaller effective flange widths are predicted for nearly every design code at Section C, however, but there was no evidence of significant shear lag in the measurements.

Table 11 – Seabreeze Bridge b_e/b Predictions

Bridge	Section	Member	AASHTO Standard	AASHTO Segmental	AASHTO LRFD	CSA	Euro-code	JRA
Seabreeze	A	Wing	0.87	0.95	0.95	1.00	1.00	0.83
		Top Slab	0.92	0.97	0.97	1.00	1.00	0.84
		Bottom Slab	1.00	0.98	0.98	1.00	1.00	0.87
	C	Wing	0.87	0.75	0.87	0.92	1.00	0.75
		Top Slab	0.92	0.80	0.91	0.92	1.00	0.75
		Bottom Slab	1.00	0.88	1.00	0.99	1.00	0.84

The local effects cause very large longitudinal stresses when compared to the non-localized bending stresses. These stresses/strains are not considered in design, as it is stated in the AASHTO Guide Specifications for Design and Construction of Segmental Concrete Bridges Commentary (AASHTO Segmental) Section 3.3.3 (AASHTO 1999).These localized stresses can add as much as three times the observed bending strain in the top slab, as shown in Figure 59 and Figure 60. This finding should prompt discussion about the validity of this design simplification.

4.1.2 Transverse Strains

Transverse strains were measured at six locations on Sections A and C. Figure 67 and Figure 68 present typical transverse strain versus truck position from Pier 2 for both iterations of LC1 at Sections A and C, respectively. Similar plots for transverse strain versus truck position for the other load cases can be found in Appendix A.

Two distinct “humps” can be seen as the heavier load truck axle groups crossed the instrumented sections. A smaller, first hump, often imperceptible is caused by the lighter front axle. This was expected as the axle weights increase toward the rear of the vehicle. The truck had difficulty maintaining a constant speed near midspan, which can be seen as a slight offset of the influence lines between iterations for a given location.

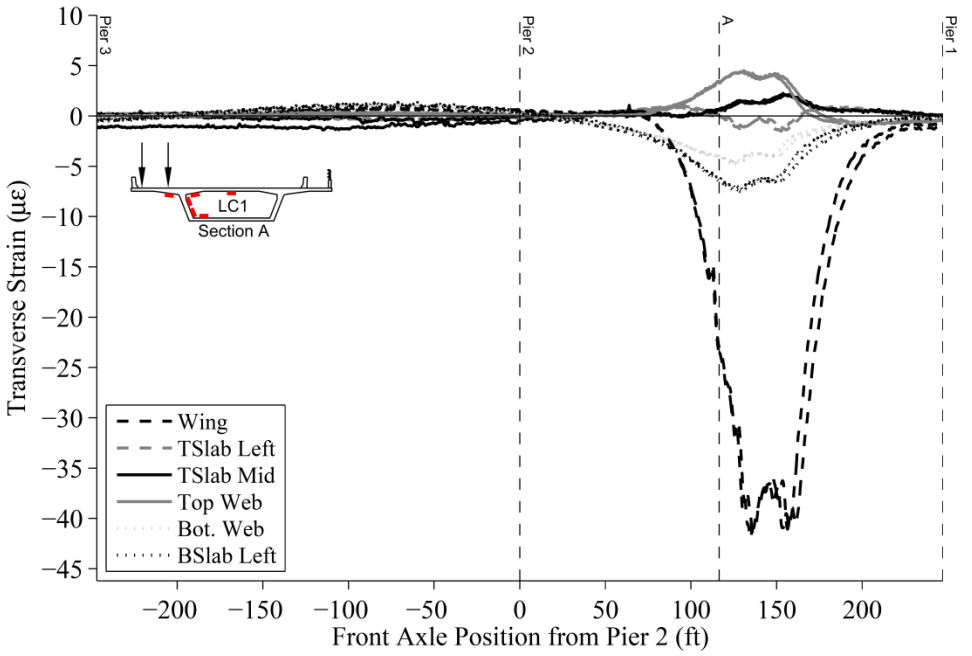

Figure 67 – Seabreeze Bridge Transverse Strains from LC1 at Section A – All Iterations

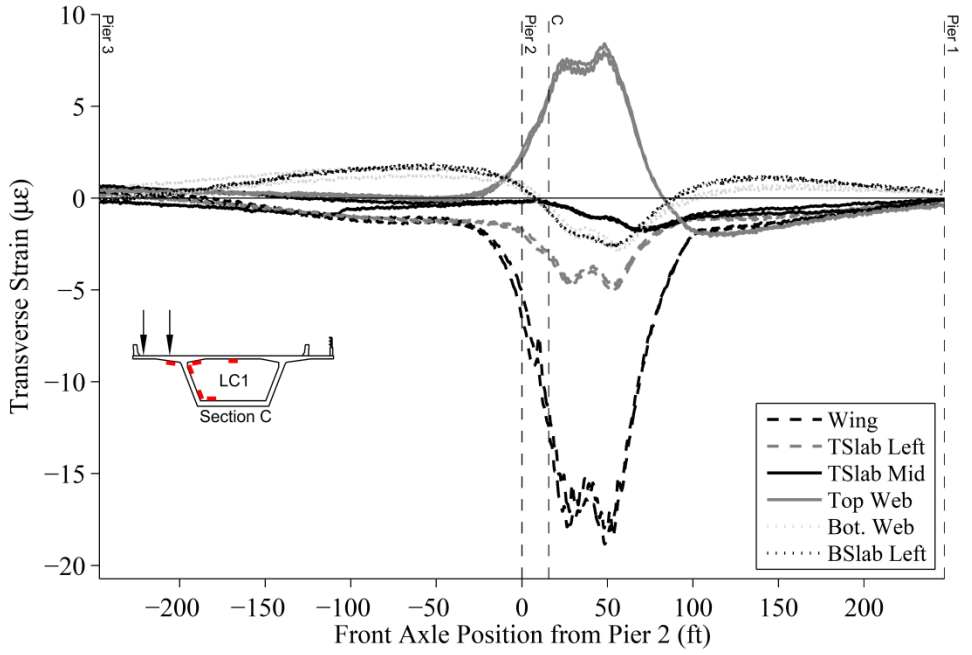

Figure 68 – Seabreeze Bridge Transverse Strains from LC1 at Section C – All Iterations

The two iterations for each load case were averaged to report the average maximum strains tabulated in Table 12 and Table 13. The maximum response at each sensor location is shown in bold. The purpose of LC1 was to induce maximum bending strains in the wing of the structure.

As expected, transverse strains in the wing were higher than any other location on the box girder during this load case. Maximum strain at the underside of the cantilever was -42 με (see Table 12) and -19 με (see Table 13) for Sections A and C, respectively. The reason for this reduction is unclear, but likely because Section C is very near the large pier diaphragm. The reason for the reduction will be discussed further in Section 5.2. The maximum measured strain away from the cantilever during LC1 was at the top web location; only +4 με at Section A (see Table 12) and +8 με at Section C (see Table 13).

The top slab left strain was smallest during LC3. The middle top slab and top web strains were maximum and minimum, during LC4 at both Section A and C, respectively. For Section C, the wing, bottom of web, and bottom left slab strains were minimum during LC1. Top slab left, top middle slab and top of web strains were all absolute maximum during LC4.

Table 12 – Section A Maximum and Minimum Transverse Strains

		Section A		
		LC1	LC3	LC4
Wing	Max (με)	1	1	1
	Min (με)	**-42**	-4	-6
Top Slab Left	Max (με)	1	1	3
	Min (με)	-1	**-19**	-18
Top Slab Middle	Max (με)	2	38	**53**
	Min (με)	-1	0	0
Top of Web	Max (με)	4	0	0
	Min (με)	-1	-5	**-7**
Bottom of Web	Max (με)	1	1	1
	Min (με)	**-5**	-3	-4
Bottom Slab Left	Max (με)	1	1	1
	Min (με)	**-7**	-2	-4

Table 13 – Section C Maximum and Minimum Transverse Strains

		Section C		
		LC1	LC3	LC4
Wing	Max (με)	1	1	1
	Min (με)	**-19**	-3	-5
Top Slab Left	Max (με)	0	0	1
	Min (με)	-5	-15	**-18**
Top Slab Middle	Max (με)	1	27	**33**
	Min (με)	-2	-1	-1
Top of Web	Max (με)	8	0	0
	Min (με)	-2	-11	**-16**
Bottom of Web	Max (με)	1	1	1
	Min (με)	**-3**	-1	-1
Bottom Slab Left	Max (με)	2	1	2
	Min (με)	**-3**	-1	-1

The highest measured strains occurred in the wing, top slab and top web locations. Consistently, the smallest strains occurred in the bottom slab and bottom web positions. This indicates that the force of the truck spreads out from the wheel loads down through the section longitudinally and transversely. Strains are consistently smallest away from the applied loads.

4.1.3 Deflections and Rotations

Strain response is a localized measurement, whereas deflection and rotation reflect an accumulation of strains over the entire bridge, offering a measure of global response. Vertical deflections were measured at midspan of Spans 2 and 3. Longitudinal and transverse rotations were measured at Pier 2, both inside the box girder and at the top of the pier (longitudinal only).

4.1.3.1 Pier Rotations

Three rotation measurements were taken at Section D: transverse and longitudinal inside the pier segment and longitudinal on the top of the pier. Figure 69 presents each of the rotation measurements at Section D versus Truck Position for LC1. Positive longitudinal rotation indicates counter clockwise rotation about the north-positive directional axis. Positive transverse rotation indicates counter clockwise rotation about the west-positive directional axis. During one truck iteration, there was signal interference as evidenced by the large noise in all three

instruments beginning near truck position 600 ft. The individual truck iterations otherwise seem to match up well. The plots for the remaining load cases can be found in Appendix A.

There were significant rotations measured for all three directions. Qualitatively, LC1 rotations followed what was expected; longitudinal box and pier rotation were of opposite sign and the pier displayed much less rotation magnitude. Longitudinal rotation magnitudes were significantly larger when the truck was on Span 2, when compared to Span 3. This was expected because the span closer to the support would be more flexible. Transverse rotation of the box girder shows that as the truck neared the pier, the transverse rotation reached its peak, which is intuitive. It is interesting to note that the double bearings at the bottom of the box do allow some rotation.

For comparison purposes, Figure 70 presents the three rotation measurements versus truck position for LC5, the load case with the right-most truck position (LC1 was left-most truck position). In Figure 70, the longitudinal rotations, inside and outside the box, are nearly identical to those from LC1 with a slightly smaller magnitude when the truck is on Span 2.

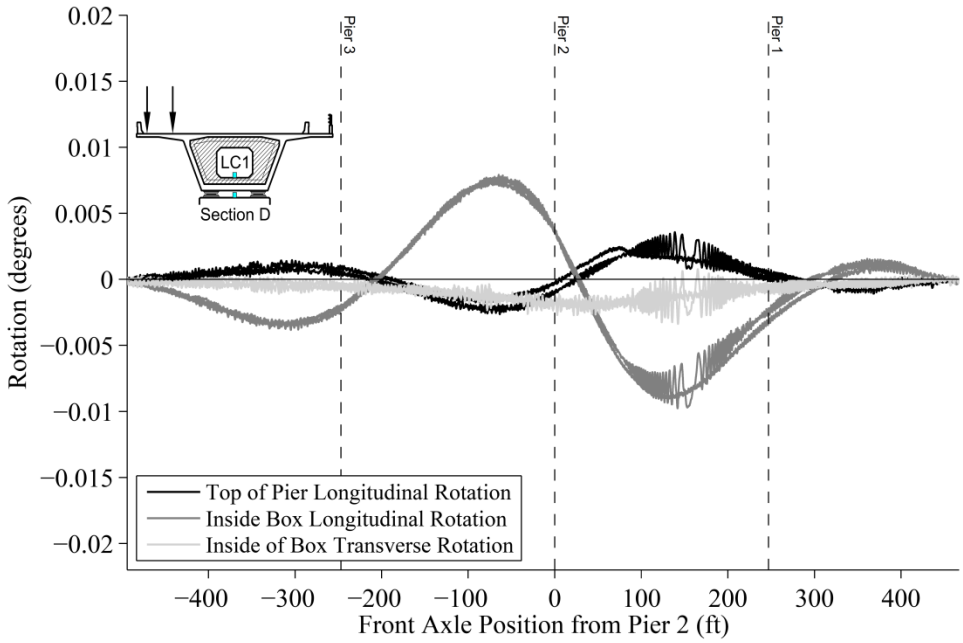

Figure 69 – Seabreeze Bridge Section D Rotations due to LC1 – All Iterations

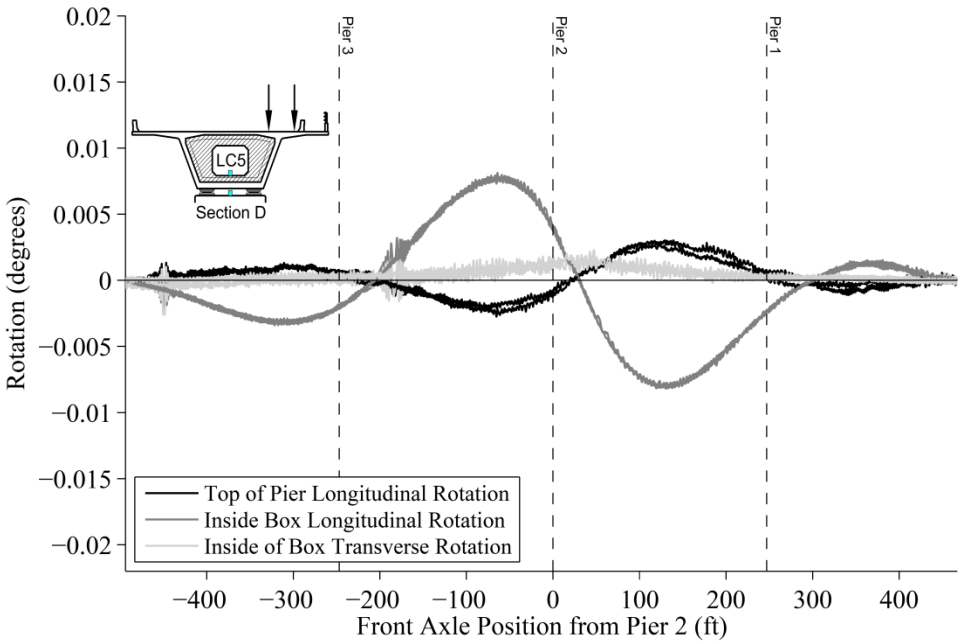

Figure 70 – Seabreeze Bridge Rotations due to LC5 – All Iterations

Table 14 presents maximum and minimum rotation values at Section D for each load case. It is evident from the table that maximum and minimum longitudinal rotations did not change much across load tests; however, there were significant differences in the transverse rotation measurements. As noted in the previous paragraph, the largest differences came between LC1 and LC5, which place the load on opposite sides (transversely) of the box (see -0.0027 deg. and +0.0021 in Table 14). The truck position in LC2 and LC5 is mirrored about the centerline and therefore, the rotations should be opposite. It is clear the rotations from LC2 and LC5 are similar magnitude, but in opposite directions. However, the LC4 and LC5 seem to be more similar, indicating the center of rotation is more closely aligned between those two load cases.

Table 14 – Section D Maximum and Minimum Rotation Measurements

		LC1	LC2	LC3	LC4	LC5
Pier Longitudinal	Max (deg.)	0.0029	0.0027	0.0029	0.0031	0.0029
	Min (deg.)	-0.0026	-0.0023	-0.0024	-0.0024	-0.0025
Box Longitudinal	Max (deg.)	0.0080	0.0081	0.0082	0.0080	0.0080
	Min (deg.)	-0.0088	-0.0080	-0.0080	-0.0079	-0.0082
Box Transverse	Max (deg.)	0.0010	0.0010	0.0014	0.0015	0.0021
	Min (deg.)	-0.0027	-0.0023	-0.0015	-0.0019	-0.0015

4.1.3.2 Global Deflections

Figure 71 presents the measured deflections at Sections A and E versus truck position for LC1. Downward (reported as negative) deflection is maximized for Section A when the truck position is on Span 2 and for Section E when the truck is on Span 3. The maximum deflection at Section A is considerably less than the maximum deflection at Section E. This indicates that Span 3 is more flexible than Span 2. The deflection plots for the remaining LCs can be found in Appendix A.

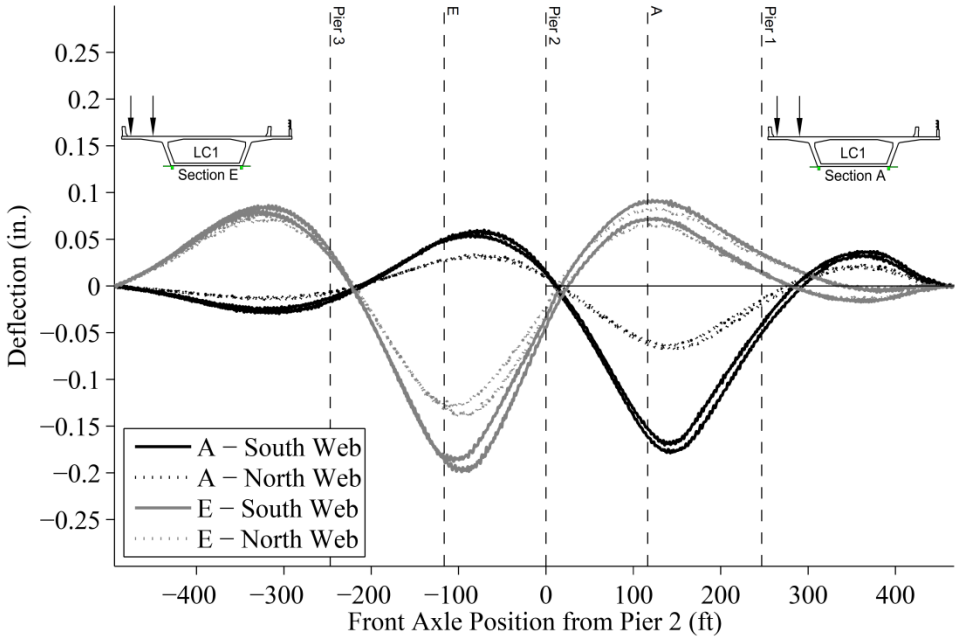

Figure 71 – Seabreeze Bridge Deflection versus Truck Position at LC1 for Sections A and E – All Iterations

Table 15 presents the maximum and minimum vertical deflection measurements taken at Sections A and E. Across load cases, the upward deflection values changed little. For instance, when the truck was on opposite sides of the roadway in LC1 and LC5, but there was little change (compare 0.83 in. at South Section E and 0.087 in Table 15). However, there did seem to be significant change during the minimums (downward), which occurred when the truck was on the span with the sensor.

Section A and E north web deflections are larger than the south web locations. This is be due to the two barrier rails nearer the north web. As the truck moves closer to the barrier rails, the deflection increases in the north web and decreases in the south web, although they do not completely reverse. It is possible the Section A north web twanger calibration was off as the deflections indicate the north web is deflecting half as much (or more) when compared to the south web. Section E deflections are more similar at each web, compared to Section A, but the north web is still behaving stiffer.

Table 15 – Seabreeze Bridge Section A and E Maximum and Minimum Deflection Values

			LC1	LC2	LC3	LC4	LC5
Section A	South Web	Max (in.)	0.058	0.060	0.063	0.062	0.066
		Min (in.)	-0.173	-0.170	-0.147	-0.157	-0.135
	North Web	Max (in.)	0.033	0.032	0.033	0.033	0.033
		Min (in.)	-0.065	-0.064	-0.069	-0.067	-0.075
Section E	South Web	Max (in.)	0.083	0.081	0.083	0.083	0.087
		Min (in.)	-0.196	-0.196	-0.171	-0.183	-0.154
	North Web	Max (in.)	0.075	0.072	0.072	0.074	0.075
		Min (in.)	-0.137	-0.139	-0.149	-0.143	-0.159

4.2 Smart Road Bridge Test Results

The Smart Road Bridge, a five span single cell segmental box girder, was instrumented at two cross sections (see Figure 38). At Section A and B, longitudinal and transverse strain were measured as shown in Figure 39 through Figure 42. The following sections describe the data from the Smart Road Bridge load test. Additional data for the Smart Road Bridge load test is presented in Appendix B.

4.2.1 Longitudinal Strains

Longitudinal strains were measured at six locations on the Smart Road Bridge each of which was on the interior of the box. Figure 72 and Figure 73 present longitudinal strain versus truck position plots for LC3. For clarity, only data from Span 2 and 3 are shown with zero indicating the location of Pier 2. Load Case 3 has a load truck on each wing away from the longitudinal

strain sensors. Beause no longitudinal strain gages are on the wings, LC3 provides the clearest measurement of global longitudinal bending strains with two load trucks.

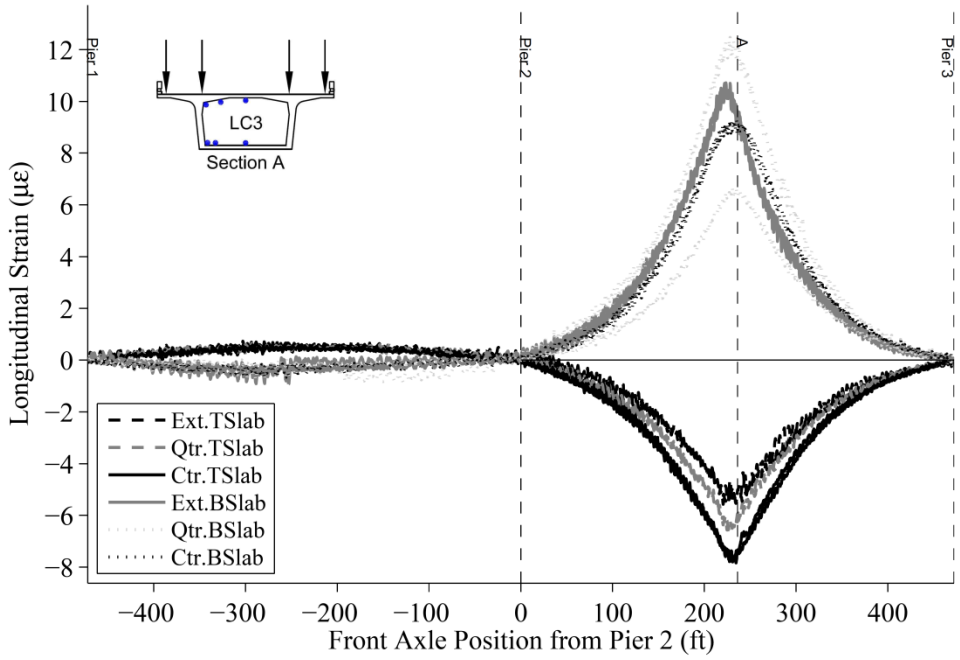

Figure 72 – Smart Road Bridge Longitudinal Strains from LC3 at Section A – All Iterations

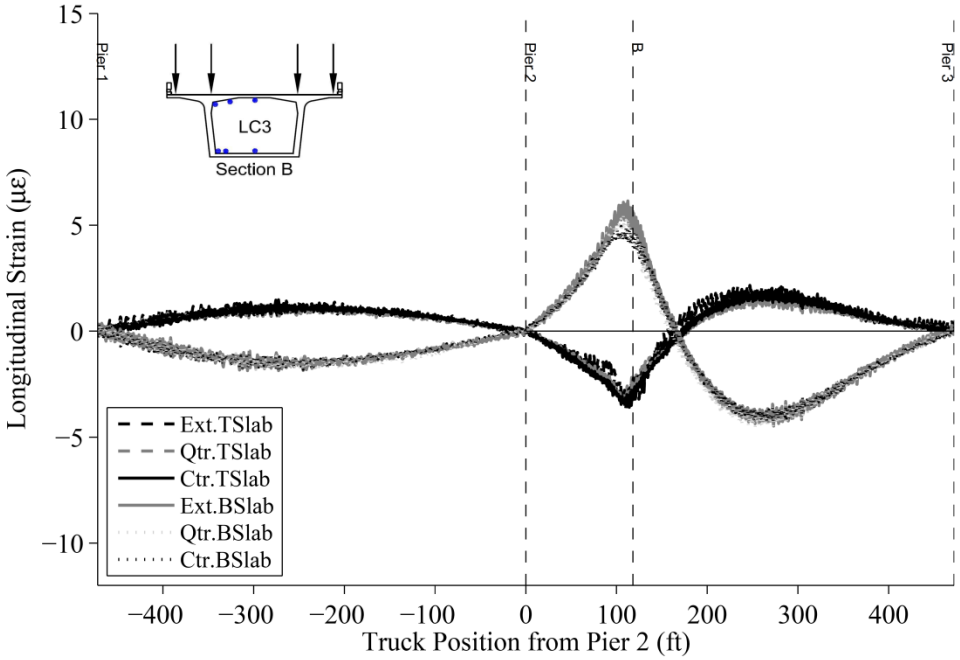

Figure 73 – Smart Road Bridge Longitudinal Strains from LC3 at Section B – All Iterations

Table 16 and Table 17 provide the maxima and minima for each load case and each longitudinal transducer at Section A and B, respectively. For each load case, the global bending effects should remain similar as the total load remains the same in the one and two truck load cases. When comparing LC1 and LC2, strains remain very similar at each longitudinal measurement location, however, strains are very small. When comparing LC3 through LC5, the two truck load cases, bottom slab strains remain relatively constant through across load cases with the exception of the quarter point on the bottom slab (compare 10 με during LC3 to 7 με during LC4 and LC5 at Section A). The reason for this difference is unclear, but upon inspection of Figure 72, strains were not very consistent across iterations. Differences are less pronounced on Section B, but measured longitudinal strains were significantly smaller.

When comparing the longitudinal strains on the top slab, during LC3 to either LC4 or LC5, there are significant differences at the center top slab location. These are caused by the local effects of the truck loads, which are not present in LC1 though LC3 because of the truck positions on the wings where there were no longitudinally oriented sensors. Additioanlly, there are very high tensile strains at the center of the top slab in a positive bending region.

Table 16 – Smart Road Bridge Section A Maximum and Minimum Strain Values

		LC1	LC2	LC3	LC4	LC5
Exterior of Top Slab	Max (με)	1	0	1	1	1
	Min (με)	-3	-3	-6	-7	**-7**
Quarter Point of Top Slab	Max (με)	1	0	1	1	1
	Min (με)	-4	-3	-7	-9	-9
Center of Top Slab	Max (με)	1	1	1	12	12
	Min (με)	-4	-4	-8	-13	**-16**
Exterior of Bottom Slab	Max (με)	7	4	11	**12**	10
	Min (με)	-1	-1	-1	-1	-1
Quarter Point of Bottom Slab	Max (με)	7	5	**10**	7	7
	Min (με)	-1	-1	-1	0	-1
Center of Bottom Slab	Max (με)	5	5	9	**10**	9
	Min (με)	-1	-1	1	-1	-1

Table 17 – Smart Road Bridge Section B Maximum and Minimum Strain Values

		LC1	LC2	LC3	LC4	LC5
Exterior of Top Slab	Max (με)	1	1	2	2	1
	Min (με)	-3	-1	-3	-6	**-7**
Quarter Point of Top Slab	Max (με)	2	1	2	3	6
	Min (με)	-3	-1	-3	-6	**-7**
Center of Top Slab	Max (με)	1	1	2	7	**12**
	Min (με)	-2	-2	-3	-7	-10
Exterior of Bottom Slab	Max (με)	1	2	6	**8**	6
	Min (με)	-2	-2	-4	-5	-4
Quarter Point of Bottom Slab	Max (με)	4	2	5	**7**	5
	Min (με)	-3	-2	-4	-5	-4
Center of Bottom Slab	Max (με)	2	2	5	**5**	5
	Min (με)	-2	-2	-4	-4	-4

Figure 74 and Figure 75 present a plot from LC5 at Section A and B, respectively, where the applied loads are near the longitudinal strain transducers. This has caused significant local effects in the top slab strain transducers, specifically at the center top slab location. These local effects are not present on the bottom slab transducers, or the exterior top slab location where the slab is thickened. It is difficult to see in Figure 74 and Figure 75, but the quarter top slab sensor also experiences these local effects, but not to the same extent, likely due to the thickend slab at that location. The shorter transverse length of the top slab on the Smart Road Bridge will not experience the magnitude of local effects as one with a longer top slab, like the Seabreeze Bridge. However, as noted in the Seabreeze Bridge test, these strains are still on the same order of magnitude and larger than the global longitudinal strains without local effects.

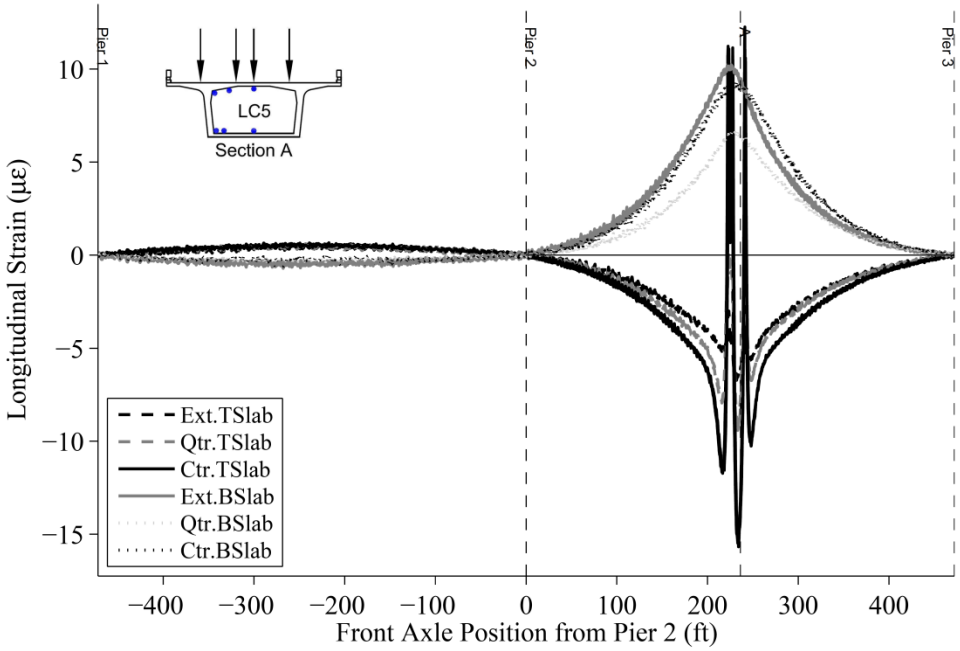

Figure 74 – Smart Road Bridge Longitudinal Strains from LC5 at Section A – All Iterations

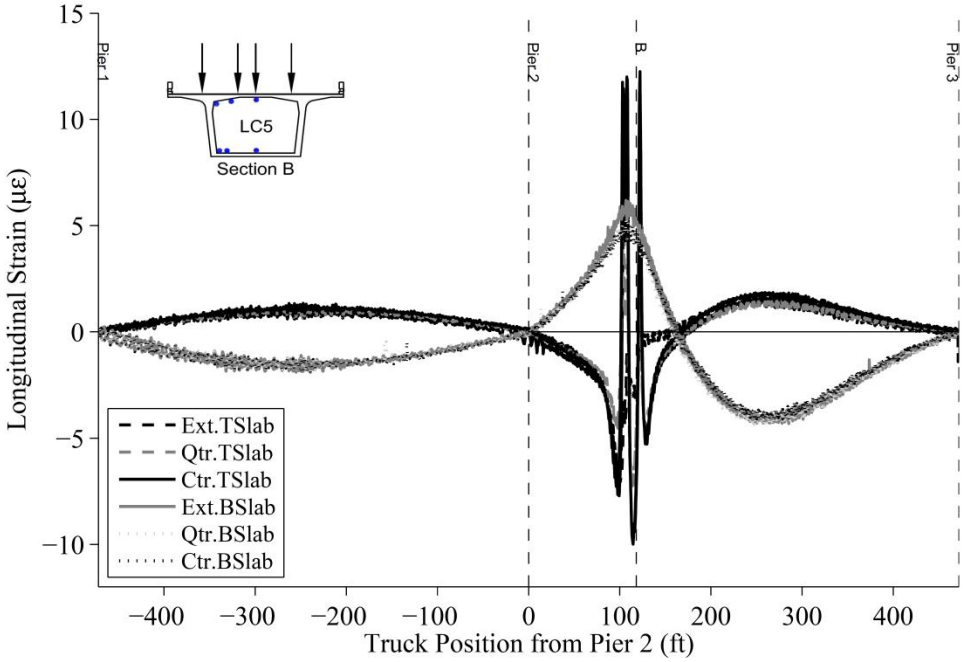

Figure 75 – Smart Road Bridge Longitudinal Strains from LC5 at Section B – All Iterations

There were three strain sensors located on the top slab to identify any significant shear lag effects. Figure 76 and Figure 77 present the absolute maximum strains observed at the same

point in time from LC3, plotted on the cross section. Because the wheel loads are far away from the longitudinal sensors, LC3 does not create the large local effects when compared to LC4 and LC5. The strains measured at the exterior slab locations do not present significantly larger strain increases when compared to the middle instrument, at either Section A or B. Interestingly, if Equation 2 is used to estimate b_e for the bottom flange at Section B (see Figure 77), b_e/b is 0.85. However, a 1με difference between the maximum and minimum strains is negligible as it is within the functional accuracy of the data acquisition system. Because of this, it is difficult to identify b_e/b accurately with so few sensors and generally small live load strains. The strains at each location on the top slab and haunches are very similar, especially when noting the haunch sensor location is closer to the neutral axis when compared to those at the middle top slab location.

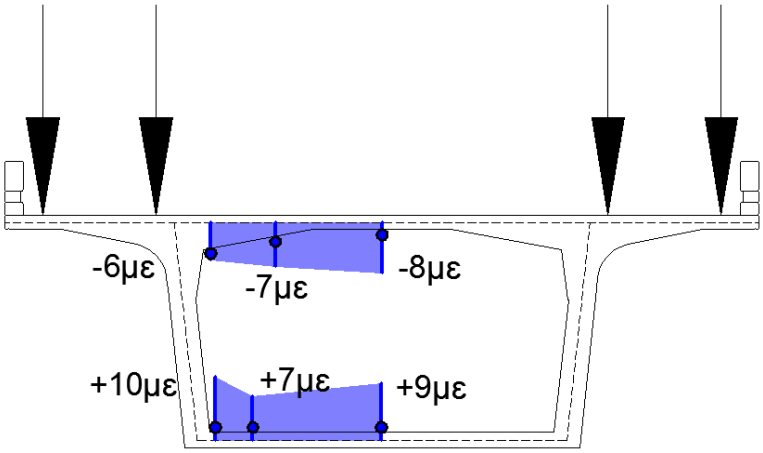

Figure 76 – Smart Road Bridge, Section A, LC3, Iteration1

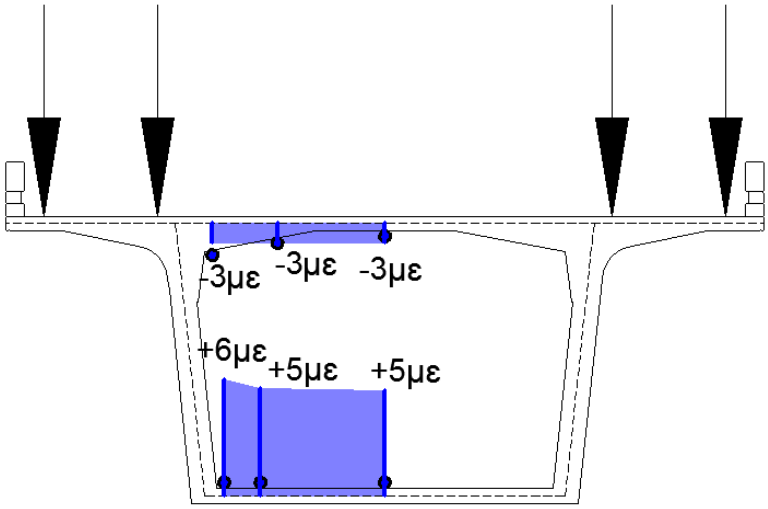

Figure 77 – Smart Road Bridge, Section B, LC3 Iteration1

Table 18 presents b_e/b predictions using the design code values outlined in the literature review. Clearly, the Smart Road Bridge has very compact components (also see Figure 16) such that there is no, or very little flange reduction (b_e/b minimum 0.96 by JRA in Table 18) according to the prediction equations. This is consistent with the results from the load tests were shear lag effects are within the accuracy of the load test.

Table 18 – Smart Road Bridge b_e/b Predictions

Bridge	Section	Member	AASHTO Standard	AASHTO Segmental	AASHTO LRFD	CSA - 00	Euro-code	JRA
Smart Road	A,B	Wing	1.00	1.00	1.00	1.00	1.00	0.97
	A,B	Top Slab	1.00	1.00	1.00	1.00	1.00	0.95
	A,B	Bottom Slab	1.00	1.00	1.00	1.00	1.00	0.96

4.2.2 Transverse Strains

Transverse strains were measured at ten locations around Sections A and B on the Smart Road Bridge as shown in Figure 40 and Figure 42. Figure 78 through Figure 81 show typical strain influence lines for most gages at Sections A and B, while the truck is between Pier 2 and Pier 3.

The full set of transverse strain versus truck position plots can be found in Appendix B. Note that the top left web location at Section B malfunctioned during the test and is not presented.

The transverse strain influence lines for the Smart Road Bridge are similar to those measured on the Seabreeze Bridge (see Figure 67 and Figure 68), with wheel loads clearly influencing the sensor measurements. The rear axle group and lighter front tire are obvious in each figure, with a smaller hump shortly before the peak for the most greatly affected top flange/wing sensors.

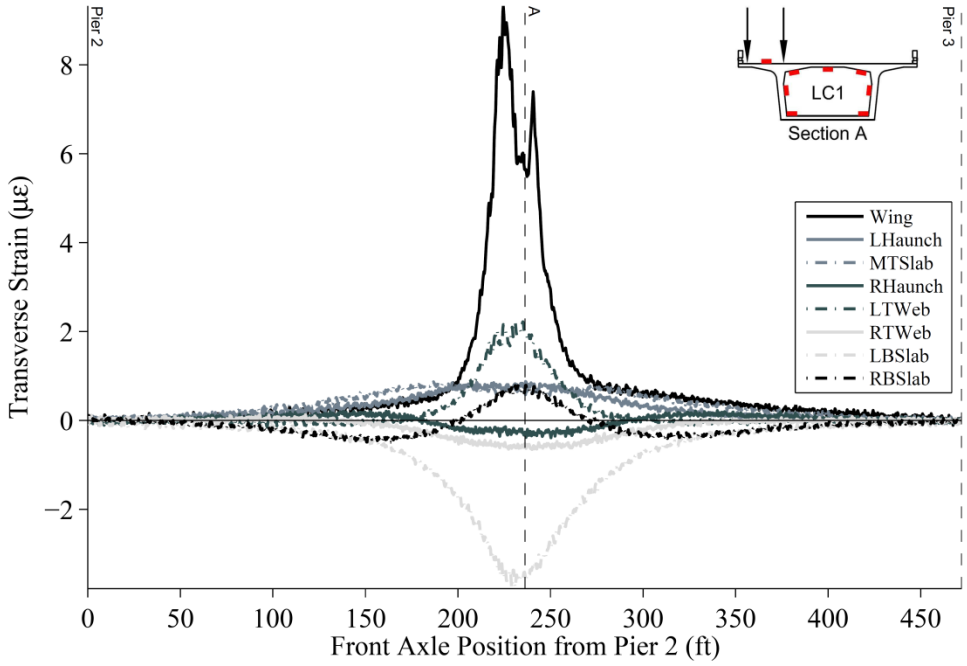

Figure 78 – Smart Road Bridge Select Transverse Strain Influence Lines – LC1 – Section A

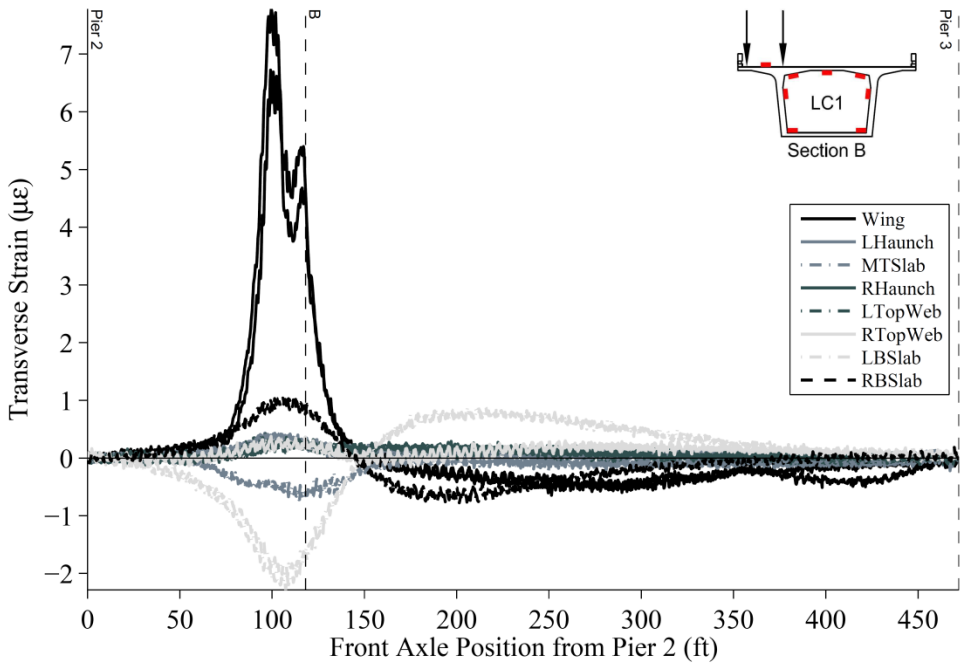

Figure 79 – Smart Road Bridge Select Transverse Strain Influence Lines – LC1 – Section B

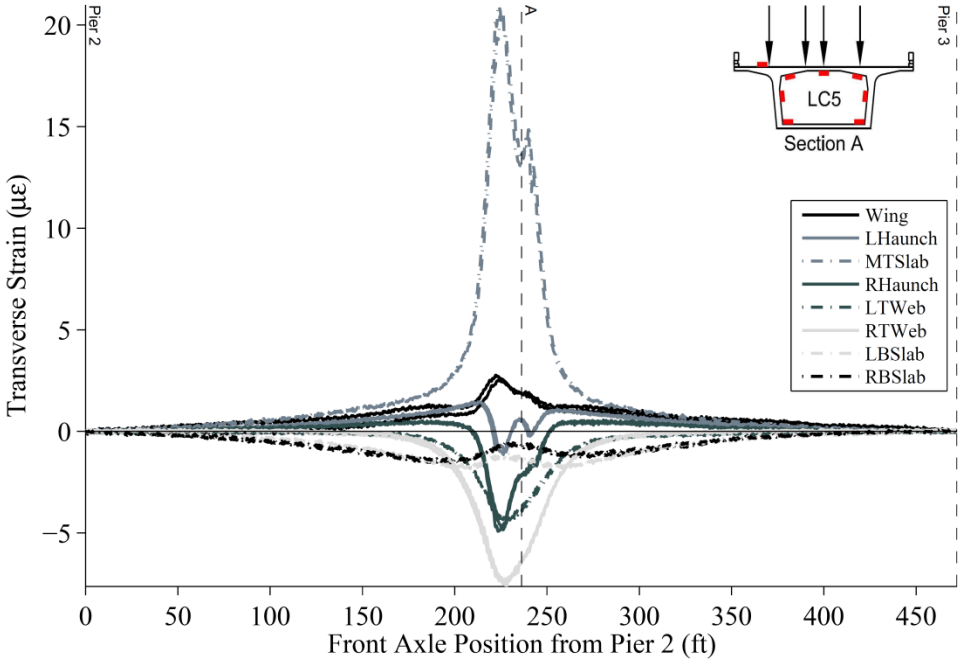

Figure 80 – Smart Road Bridge Select Transverse Strain Influence Lines – LC5 – Section A

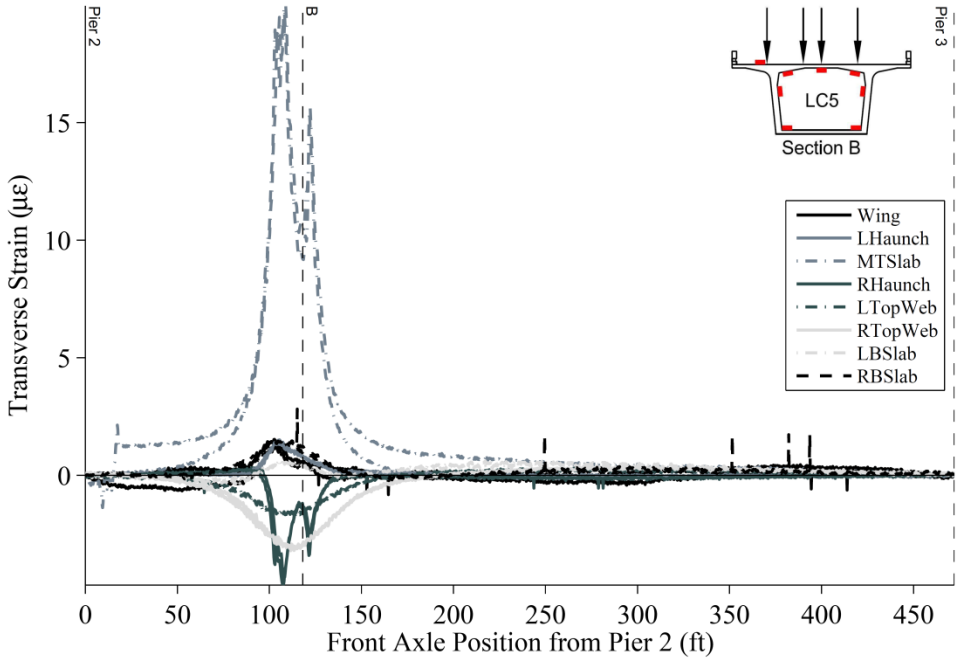

Figure 81 – Smart Road Bridge Select Transverse Strain Influence Lines– Section B – LC5 – All Iterations

The strain measurements from each iteration for each load case are averaged and reported in Table 19 and Table 20 for Section A and B, respectively. The maximum response at each sensor location is shown in bold. Unlike the Seabreeze Bridge, there is no significant difference between the midspan section and the section nearer the pier. Seabreeze Section C was significantly closer to the pier such that it was affected by the pier diaphragm, but Smart Road Section B is at quarter span. Although, Smart Road Section A and B are different depths, strains are not significantly changed. It should be noted Section B is the closest the research team could safely access the top flange due to the steep bottom flange slope.

One major difference is the significantly lower strains overall when comparing Smart Road to Seabreeze. For instance, the absolute largest observed strain on the Smart Road Bridge is +21 με versus +53 με on the Seabreeze Bridge. However, in many cases, specifically LC1 though LC3, response is very small and in most cases less than +/-2 με. Interestingly, superposition can be confirmed, to around +/- 1 με, by summing the responses from LC1 and LC2 and compared to those from LC3. Again, note that most strains are very small. LC5 was the most severe load condition for most components, including the top slab and webs.

Table 19 – Smart Road Bridge Section A Maximum and Minimum Transverse Strains

		Section A				
		LC1	LC2	LC3	LC4	LC5
Wing	Max (με)	9	1	**11**	11	3
	Min (με)	0	0	0	0	0
Left Haunch	Max (με)	1	0	1	3	2
	Min (με)	0	-1	0	0	**-5**
Middle Top Slab	Max (με)	1	1	2	17	**21**
	Min (με)	0	0	0	0	0
Right Haunch	Max (με)	0	1	1	1	1
	Min (με)	0	0	0	**-4**	-3
Top Right Web	Max (με)	0	2	2	1	0
	Min (με)	-1	0	0	-4	**-8**
Mid Right Web	Max (με)	0	0	0	0	0
	Min (με)	-1	0	-1	-4	**-7**
Right Bottom Slab	Max (με)	1	0	0	1	0
	Min (με)	0	-3	**-3**	-2	-2
Left Bottom Slab	Max (με)	0	1	0	0	0
	Min (με)	-4	-1	-3	**-5**	-2
Mid Left Web	Max (με)	2	0	1	0	0
	Min (με)	0	-1	-1	-3	**-6**
Top Left Web	Max (με)	2	0	2	0	0
	Min (με)	0	-1	0	-1	**-4**

Table 20 – Smart Road Bridge Section B Maximum and Minimum Transverse Strains

		Section B				
		LC1	LC2	LC3	LC4	LC5
Wing	Max (με)	7	0	**8**	7	1
	Min (με)	-1	-1	-1	-1	-1
Left Haunch	Max (με)	1	1	2	3	6
	Min (με)	-3	-1	-3	-6	**-7**
Middle Top Slab	Max (με)	0	0	0	14	**20**
	Min (με)	-1	0	-1	0	-1
Right Haunch	Max (με)	0	1	1	1	1
	Min (με)	0	-1	0	**-4**	-3
Top Right Web	Max (με)	0	1	1	0	0
	Min (με)	0	0	0	-2	**-4**
Mid Right Web	Max (με)	0	0	1	0	0
	Min (με)	0	-1	0	-1	**-3**
Right Bottom Slab	Max (με)	1	1	0	2	**2**
	Min (με)	-1	-2	-1	-1	0
Left Bottom Slab	Max (με)	1	1	1	1	1
	Min (με)	-2	-1	-1	**-2**	0
Mid Left Web	Max (με)	0	0	0	0	0
	Min (με)	0	0	0	-1	**-2**

4.3 Varina-Enon Bridge Test Results

The Varina-Enon Bridge, a six span single cell segmental box girder, was instrumented at four cross sections (see Figure 48 and Figure 49). At Section A, deflection was measured. At Section B, longitudinal strain was measured (see Figure 50). At Section C, transverse strains were measured (see Figure 51). At Section D, longitudinal and transverse strains were measured (see Figure 52 and Figure 53). The following sections describe the data from the Varina-Enon Bridge load test. Additional data for the Varina-Enon Bridge load test is presented in Appendix C.

4.3.1 Longitudinal Strains

Longitudinal strain versus truck location plots for the strain transducers located at Section B are presented in Figure 82 and Figure 83 for LC3 and LC6, respectively. Because the sensors are on Span 5, tension spikes caused by the local longitudinal bending from the wheel loads in Figure 82 do not coincide with the maximum global bending strains. These occur when the truck is on Span 6 (the end span). Several random strain spikes of small magnitude, caused by traffic on the left and middle lanes, can be seen in Figure 83, Figure 86 and Figure 87 and during all data from LC4 through LC6. Traffic could not be stopped during the quasi-static tests (LC4 through LC6). Interestingly, there does not seem to be significant dynamic effect from the high-speed load cases, LC1 though LC3. This is often marked by a ringing or sinusoidal shape in the transducer measurements as the truck suspension bounces on the structure, however, there are no significant signs of this in the example plots in the high speed load cases plotted in Figure 82, Figure 84 and Figure 85. This lack of visible sinusoidal motion suggests there is little or no dynamic amplification. Without comparative static testing, it is difficult to quantify dynamic amplification magnitude. Quasi-static and/or static testing in the same load paths as LC1 through LC3 was not possible due to traffic control constraints.

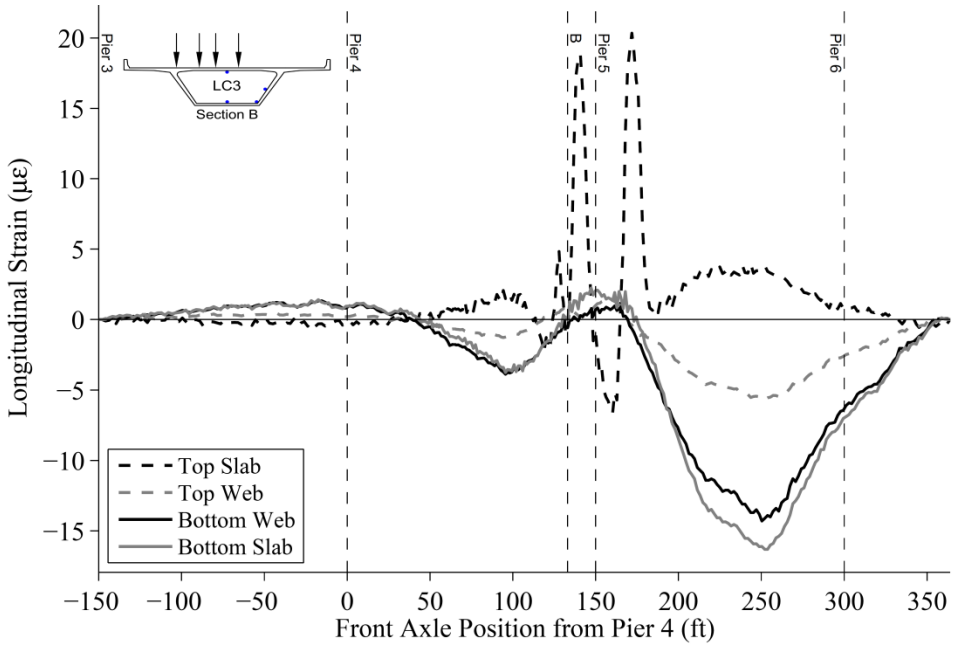

Figure 82 – Varina-Enon Bridge Longitudinal Strain Influence Lines at Section B, LC3, Iteration 1

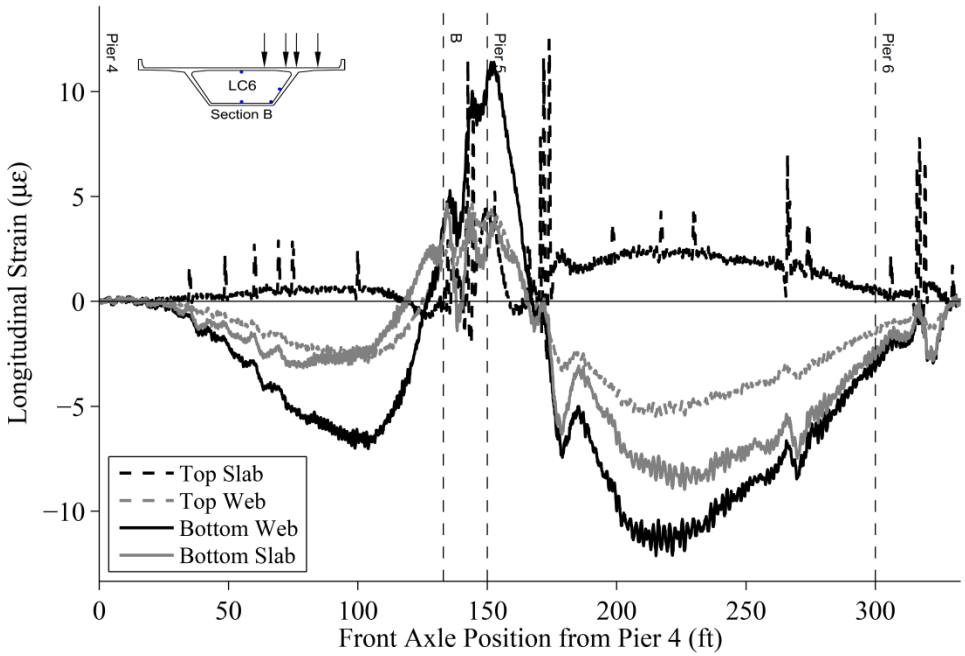

Figure 83 – Varina-Enon Bridge Longitudinal Strain Influence Lines at Section B, LC3, Iteration 1

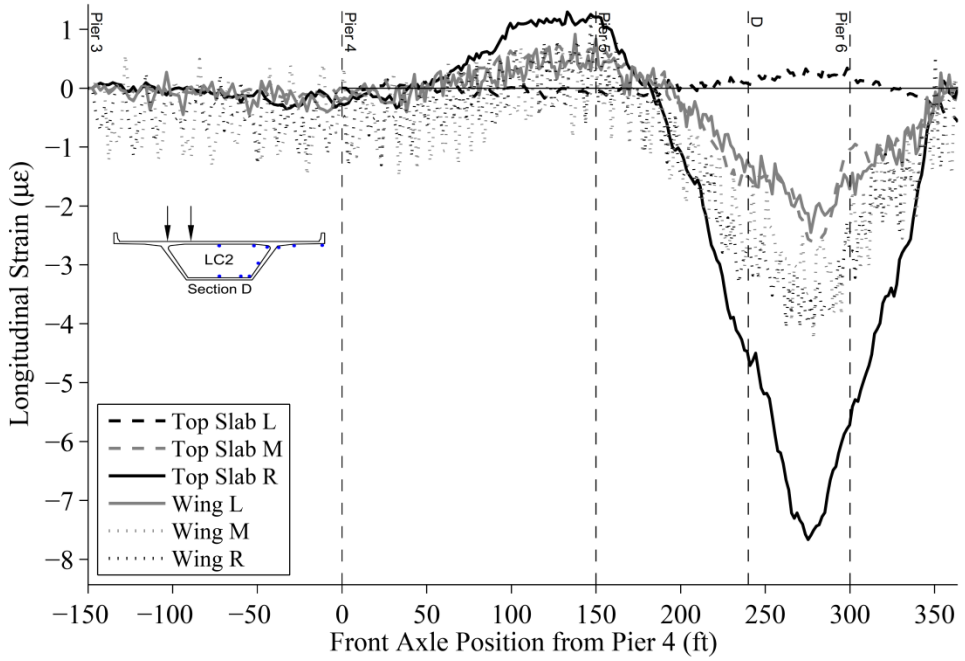

Figure 84 – Varina-Enon Bridge Longitudinal Strain Influence Lines at Section D, Top Slab and Wing, LC2, Iteration 1

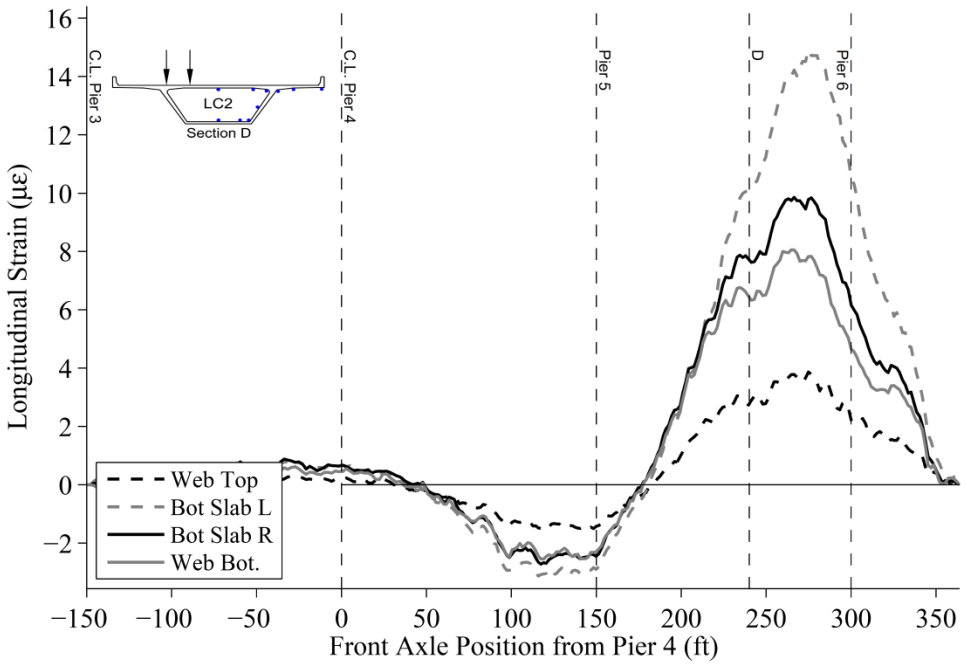

Figure 85 – Varina-Enon Bridge Longitudinal Influence Lines at Section D, Web and Bottom Slab, LC2, Iteration 1

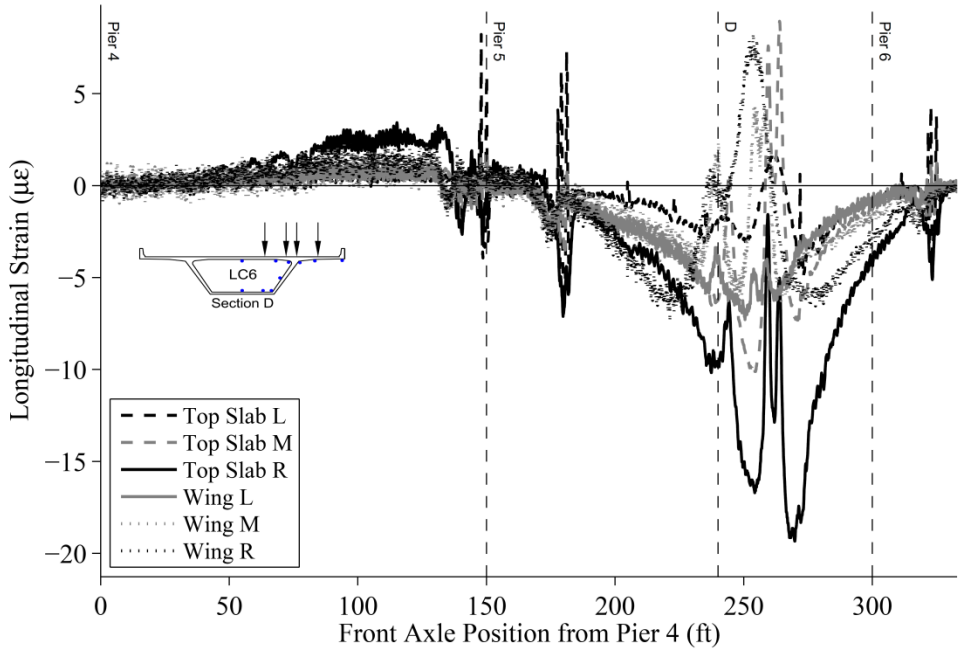

Figure 86 – Varina-Enon Bridge Longitudinal Strain Influence Lines at Section D, Top Slab and Wing, LC6, Iteration 1

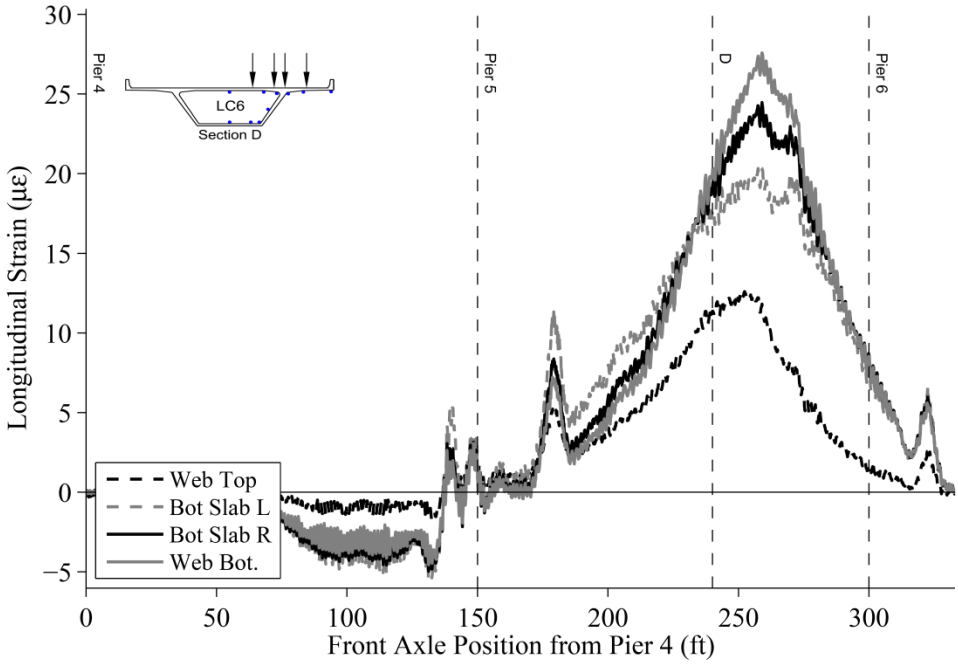

Figure 87 – Varina-Enon Bridge Longitudinal Strain Influence Lines at Section D, Web and Bottom Slab, LC6, Iteration 1

Table 21 and Table 22 present the absolute maximum strain values for LC1 though LC3 at Section B and D, respectively. Note that a wireless communication error occurred during LC1 and affected the measurements as the truck was on Span 5. Care was taken to estimate the strain caused by the load truck bending and disregard strain by the vehicular traffic. However, due to difficulty in separating strain caused by the load trucks from light vehicular traffic, there could be a small amount of traffic strain included in the reported strains. During all tests, there were no ambient large trucks, only light vehicular traffic on the instrumented spans, although exact record of the ambient traffic was not recorded. According to the the Environmental Protection Agency (EPA), the average light duty vehicle weights approximately 4 kips (EPA 2013), which is approximately 6% of the weight of a single Varina-Enon VDOT dump truck. This load could cause changes in global response depending on the number and distribution of live traffic on the bridge at during testing.

Table 21 – Varina-Enon Bridge Maximum and Minimum Recorded Longitudinal Strains at Section B

		Section B					
		LC1	LC2	LC3	LC4	LC5	LC6
Top Slab	Max (με)	20	4	**21**	2	3	4
	Min (με)	-6	-1	-6	-2	-1	-1
Top Web	Max (με)	1	1	1	3	3	4
	Min (με)	-4	-3	**-6**	-2	-5	-5
Bottom Web	Max (με)	1	1	1	7	5	10
	Min (με)	-10	-7	**-15**	-5	-10	-10
Bottom Slab	Max (με)	2	1	2	2	3	5
	Min (με)	-10	-9	**-17**	-4	-10	-8

Table 22 – Varina-Enon Bridge Maximum and Minimum Recorded Longitudinal Strains at Section D

		Section D					
		LC1	LC2	LC3	LC4	LC5	LC6
Left Top Slab	Max (με)	11	1	12	1	1	1
	Min (με)	-11	-3	**-13**	-2	-3	-3
Middle Top Slab	Max (με)	5	1	4	1	1	1
	Min (με)	-6	-3	**-10**	-3	-5	-5
Right Top Slab	Max (με)	1	1	3	1	1	1
	Min (με)	-11	-8	**-19**	-8	-13	-13
Left Wing	Max (με)	1	1	1	1	2	1
	Min (με)	-3	-3	**-5**	-5	-5	-5
Middle Wing	Max (με)	1	1	2	1	2	1
	Min (με)	-4	-4	**-6**	-5	-3	-6
Right Wing	Max (με)	2	1	2	1	2	1
	Min (με)	-4	-4	-7	-5	-3	-6
Middle Web	Max (με)	7	4	11	5	7	**12**
	Min (με)	-1	-2	-3	-2	-3	-2
Left Bot. Slab	Max (με)	13	15	**26**	11	17	20
	Min (με)	-2	-3	-6	-2	-3	-3
Mid. Bot. Slab	Max (με)	11	9	21	10	17	**23**
	Min (με)	-2	-3	-5	-2	-1	-4
Low Web	Max (με)	11	8	19	11	17	**28**
	Min (με)	-1	-3	-5	-2	-3	-4

Figure 88 and Figure 89 show the longitudinal strains in the cross section, with the magnitude of strain scaled to reflect the relative magnitudes. When comparing tensile strains in the web and bottom flange, the measurements indicate load location plays a significant role, unlike observations during the Smart Road Bridge tests. When the load is near the middle of the cross section, the right bottom flange strains are considerably larger (see Figure 88) when compared to right web longitudinal strains when the truck is in the left lane (see Figure 89). Interestingly the wing strains remain relatively constant when comparing Figure 88 and Figure 89.

In many cases, the localized wheel loads affect the top flange sensor strain distribution making it difficult to observe global longitudinal bending strains separate from local bending strains. This can be seen in Figure 88 where the -11 με at the middle top slab location is affected by the localize strain spike. Conversely, in Figure 89, with the same total load and less local affect, the top flange strain profile appears to indicate the presence of shear lag because it has higher strain near the web. Significant shear lag can be seen in Figure 89 where there is -8 με at the right top slab sensor, but only -3 με at the other locations. Using Equation 2, b_e/b is 0.6 as estimated from the top slab strains. However, it is still unclear how much the difference in load location and local effects are affecting the top slab strain measurements as wheel loads are on the top flange. Ideally, a heavy, symmetric load case, with point loads directly above the web-flange intersection should be used to measure shear lag. Smart Road LC3, shown in Figure 76 and Figure 77, is the closest load case used in this report. Longitudinal strains in the wing remain relatively constant through LC1 through LC3, when the trucks are far from the wing, and do not indicate shear lag.

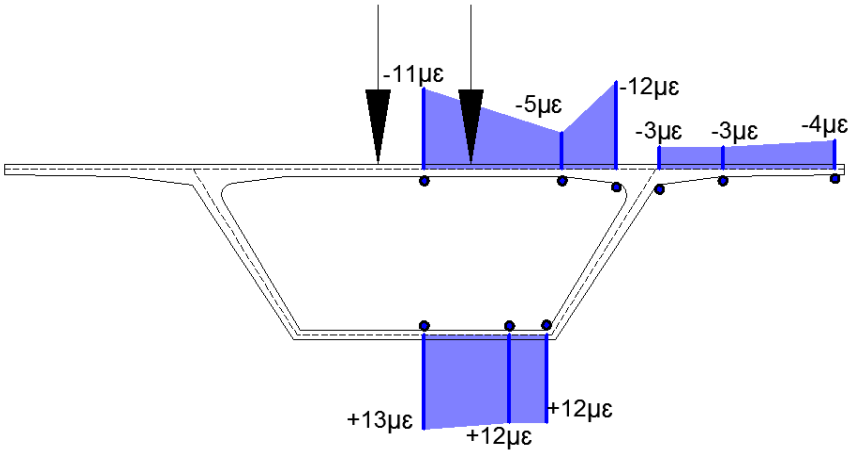

Figure 88 – Varina-Enon Bridge Maximum Longitudinal Strains LC1, Iteration 1

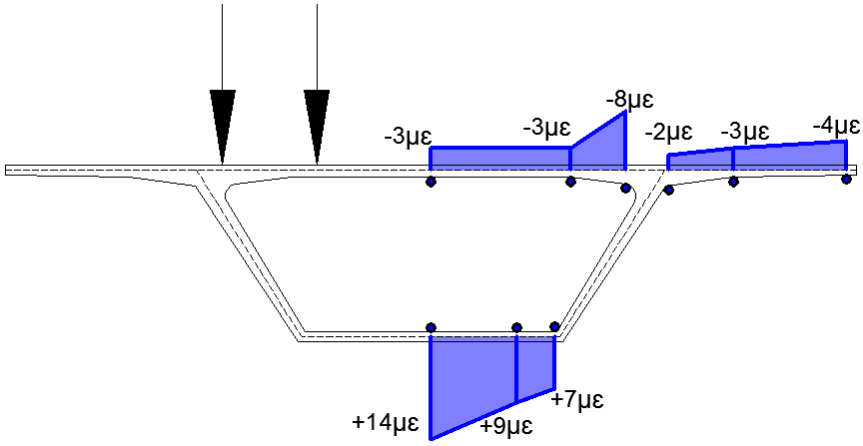

Figure 89 – Varina-Enon Bridge Maximum Longitudinal Strains, LC2, Iteration 1

Table 23 presents the predicted b_e/b using the design code provisions presented in the literature review. In most cases, the code predictions are very near full effective flange width. However, assuming the measured b_e/b for the top flange, 0.6 as calculated from measured strains using Equation 2, is free of the local effects, the standards predict unconservatively in this instance.

Table 23 – Varina-Enon Bridge b_e/b Predictions

Bridge	Section	Member	AASHTO Standard	AASHTO Segmental	AASHTO LRFD	CSA	Euro-code	JRA
Varina-Enon	D	Wing	1.00	0.92	0.92	0.95	1.00	0.89
	D	Top Slab	0.93	0.89	0.89	0.90	0.96	0.86
	D	Bottom Slab	1.00	0.84	0.84	0.99	1.00	0.95

4.3.2 Transverse Strains

Transverse strains were measured at five locations at Section C and seven locations at Section D. Example transverse strain influence lines can be found in Figure 90 through Figure 93. As discussed in the previous section traffic during LC4 through LC6 could not be stopped in the open traffic lanes. Short spikes in the data are visible and are often larger than the quasi-static results, especially from the top slab instruments, which are very near the live traffic tire loads. To estimate the transverse strain maxima at Section C and D, presented in Table 24 and Table 25, respectively, some judgment was required to separate the true quasi-static response. Because the transverse strains are localized, traffic on the bridge provides very little error, except when near the instrumentation. In some cases, like LC4, Iteration 1, shown in Figure 90, there was no traffic near the instruments, while the load trucks were inducing maximum effect.

As stated previously, LC1 through LC3 were high-speed load cases with trucks centered as close as possible within the travel lanes. During this type of loading, the accuracy of the truck position is poor and transverse strains are highly sensitive to changes in transverse truck location. Additionally, even though minimal dynamic affect was found for longitudinal strains and global deflections, it is unknown how dynamic loading affects the transverse strains and how they can be compared to static strains measured on other structures. For this reason only the static load are presented and discussed in this report.

The purpose of instrumenting Section C was to compare transverse strains in the pier diaphragm region to strains away from it. The measured transverse strains are significantly lower in comparative locations at Section C and D. For instance, at the middle top slab location, strains

are significant smaller at Section D (compare +5 με during LC6 in Table 24 to +23 με Table 25); this trend is also evident at other measurement locations. However, locations such as the haunch did not exhibit significantly different strains and the bottom slab had consistently higher strain measurements at Section C.

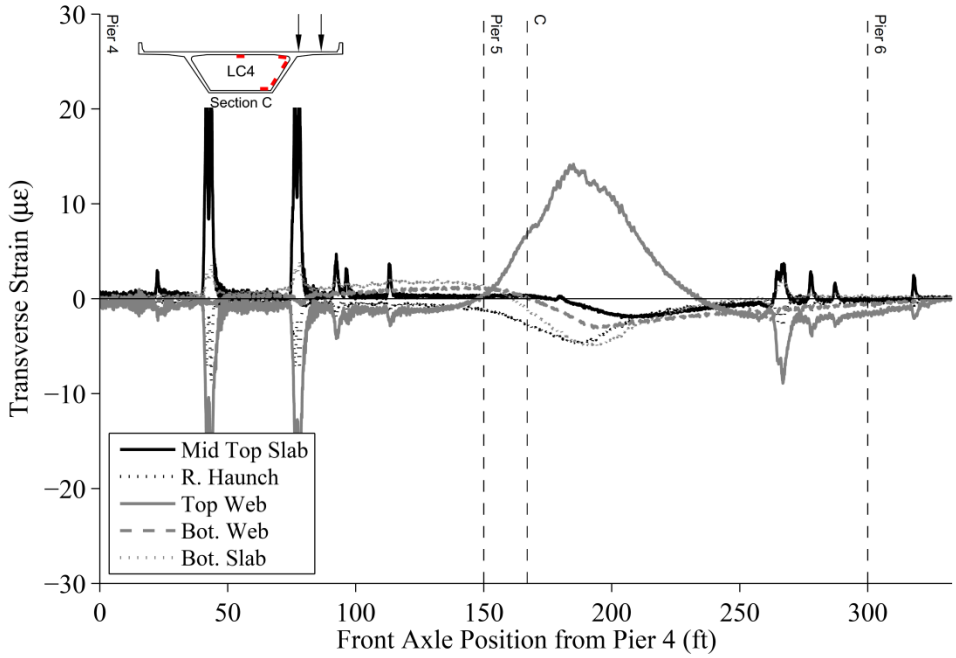

Figure 90 – Varina-Enon Bridge Transverse Strain Influence Lines at Section C, LC4, Iteration 2

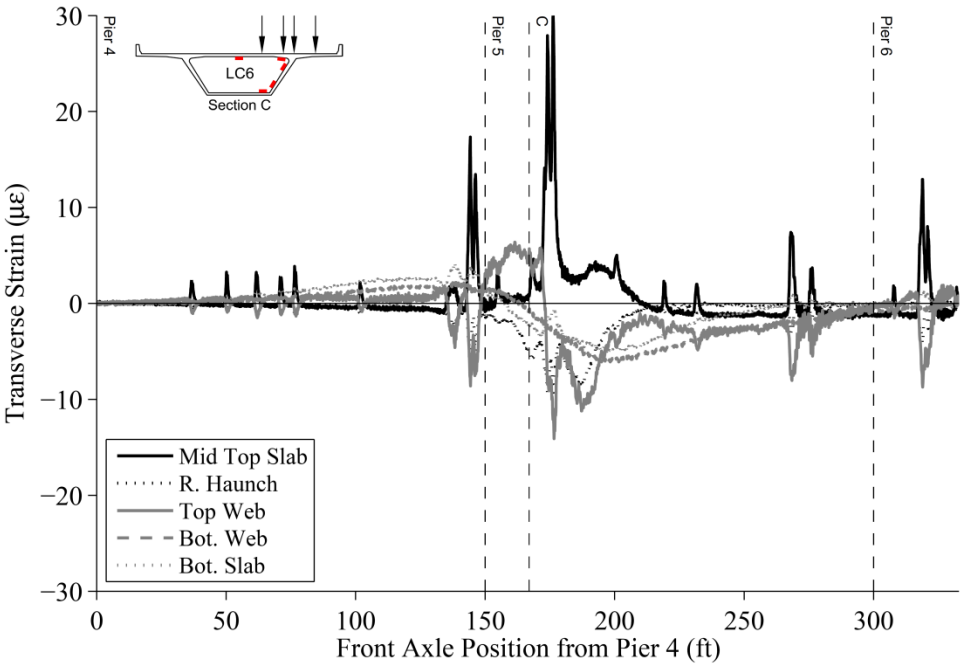

Figure 91 – Varina-Enon Bridge Transverse Strain Influence Lines at Section C, LC6, Iteration 1

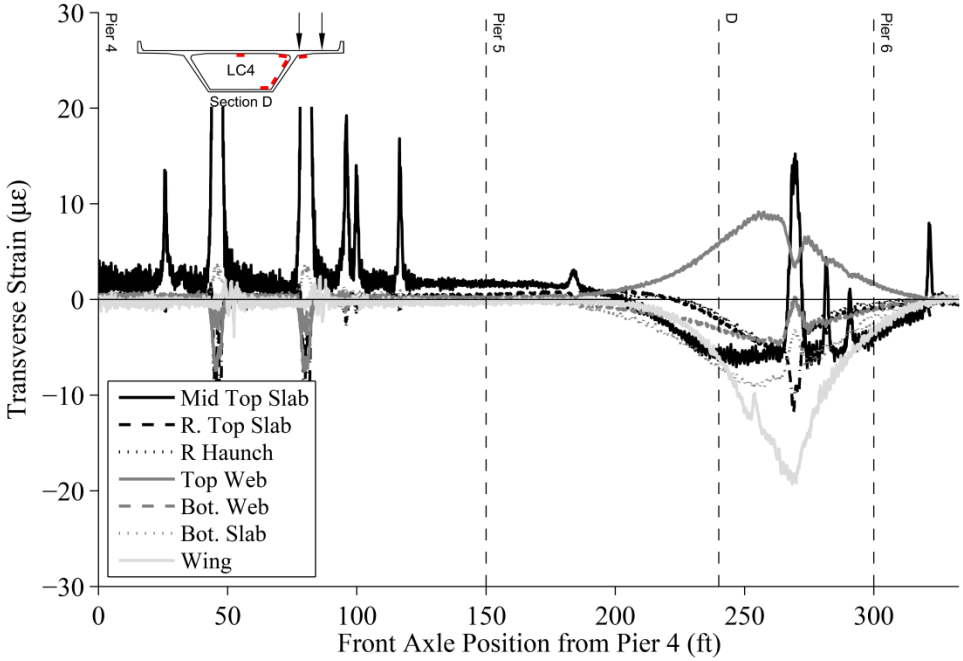

Figure 92 – Varina-Enon Bridge Transverse Strain Influence Lines at Section D, LC4, Iteration 2

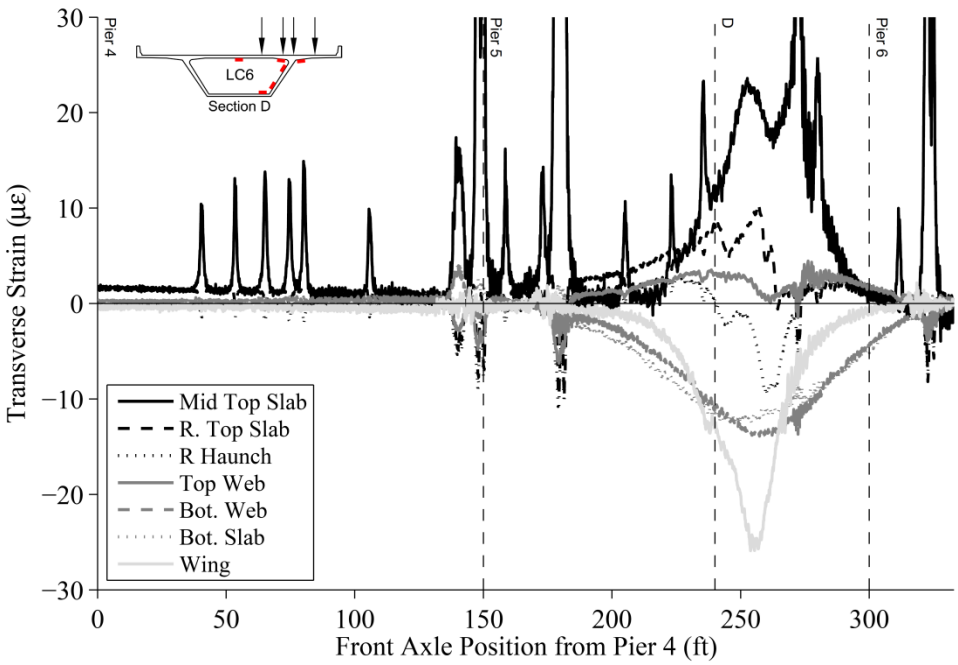

Figure 93 – Varina-Enon Bridge Transverse Strain Influence Lines at Section D, LC6, Iteration 1

Table 24 – Varina-Enon Bridge Maximum and Minimum Recorded Transverse Strains at Section C

		Section C		
		LC4	LC5	LC6
Mid Top Slab	Max (με)	1	1	**5**
	Min (με)	-2	-3	-1
Right Haunch	Max (με)	1	1	1
	Min (με)	-4	-6	**-7**
Top Web	Max (με)	14	**23**	5
	Min (με)	-1	-1	-10
Bottom Web	Max (με)	1	1	1
	Min (με)	-3	**-7**	-6
Bottom Slab	Max (με)	1	2	1
	Min (με)	-5	**-9**	-5

Table 25 – Varina-Enon Bridge Maximum and Minimum Recorded Transverse Strains at Section D

		Section D		
		LC4	LC5	LC6
Mid Top Slab	Max (με)	1	1	**23**
	Min (με)	-6	-12	-1
Right Top Slab	Max (με)	1	1	**10**
	Min (με)	-3	-7	-1
Right Haunch	Max (με)	1	1	1
	Min (με)	-3	-7	**-9**
Top Web	Max (με)	9	**13**	2
	Min (με)	-1	-1	-1
Bottom Web	Max (με)	1	1	1
	Min (με)	-5	-6	**-14**
Bottom Slab	Max (με)	1	1	1
	Min (με)	-9	**-15**	-12
Wing	Max (με)	1	1	1
	Min (με)	-19	**-26**	-25

4.3.3 Vertical Deflections

Figure 94 and Figure 95 present example vertical deflection influence lines, at Section A, for LC3 and LC5. Note that positive indicates downward deflection. The structure behaves predictably and exhibits very small deflections with the maximum deflection occurring when the truck is directly over the measured section. The high-speed load cases, LC1 through LC3, did not exhibit significant dynamic deflection response, which is often characterized by a sinusoidal amplification throughout the influence line. Although this is difficult to tell when static tests were not performed in the same load paths. As discussed previously, traffic was on the bridge during LC4 through LC6. This is evident by the apparent noise in Figure 95. The vertical deflection influence lines from the other truck crossings are presented in Appendix C.

Table 26 presents the tabulated maximum values for deflections. When combined, the response from the single truck LCs (approximately 0.03 in. each) yield the same response as the two truck load cases (approximately 0.06 in.). Furthermore, doubling the response from the single dump truck in LC4 (0.024 in. × 2 = 0.048 in.) is approximately the response for the two-trucks in LC5 (0.05 in.) and LC6 (0.048 in.). This confirms superposition is valid, suggesting the system remains globally elastic.

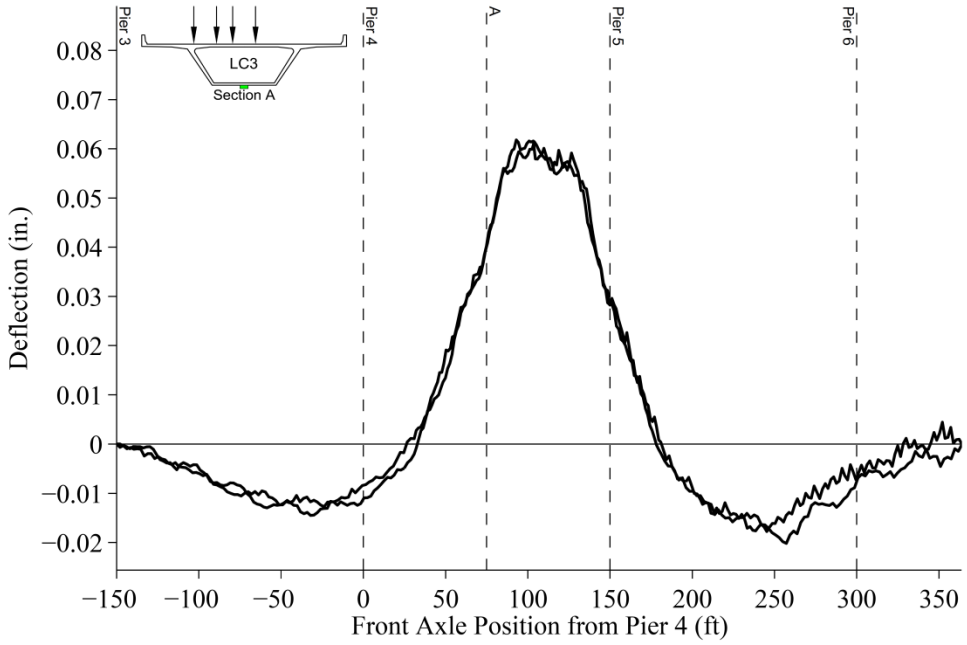

Figure 94 – Vertical Deflection Influence Lines at Section A, LC3, All Iterations

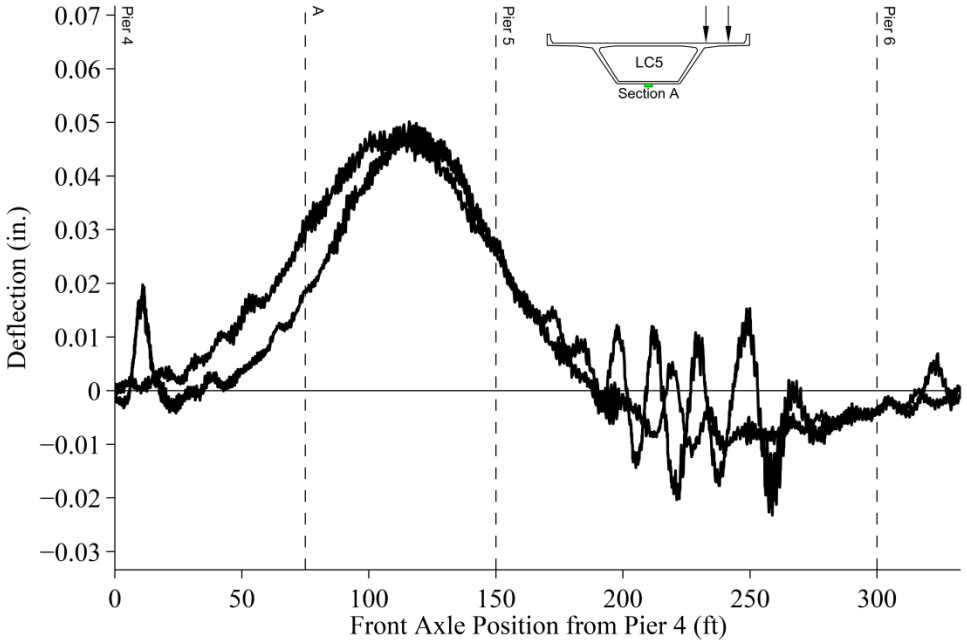

Figure 95 – Varina-Enon Bridge Deflection Influence Lines at Section A, LC5, All Iterations

Table 26 – Maximum Recorded Downward Vertical Deflection at Section A

		Section A					
		LC1	LC2	LC3	LC4	LC5	LC6
Deflection	Max (in.)	0.030	0.034	0.062	0.024	0.050	0.047
	Min (in.)	-0.010	-0.011	-0.019	-0.004	-0.012	-0.013

4.4 Results Summary

Based on the longitudinal strains, it is clear that the truck loading is creating relatively small strains (especially for the Smart Road Bridge where longitudinal strains were below ± 12 με) except when influenced by local strains (compare Figure 72 to Figure 74). Strains from the Seabreeze and Smart Road load tests indicate transverse load location does not have a large effect on the global strains. The Varina-Enon Bridge load test showed that tensile strains on the bottom flange were affected by the transverse load location, but not as significantly as the top flange compression strains were. This may affect the accuracy of some simplified longitudinal analysis methods and the estimation of shear lag.

On each structure, measured local longitudinal strains were often seen in excess of the longitudinal bending strains. The truck tires, when in close proximity to the instruments on the top slab and wing, caused high localized strains. Near midspan, where the top flange undergoes mostly compression under live and dead load, this may not cause issues. However, near the pier, the localized strains are over twice as large as the global bending strains (see Figure 59, Figure 60 and Figure 82). The observed local effects may be important at deterioration prone locations such as closure pour segments, especially those in negative moment regions. The AASHTO Segmental Commentary of Section 3.3.2 (AASHTO 1999) states that these stresses need not be designed for; however, the results indicate additional study is warranted.

On the Seabreeze and Smart Road Bridges, significant longitudinal shear lag effects were not observed at any measured location. Neither section was expected to present a large shear lag effect because they are relatively compact. On the Varina-Enon Bridge, shear lag was only observed in the top flange.

Transverse bending strains measured near midspan are significantly higher at the same transverse locations than those near the support, as investigated on the Seabreeze and Varina-Enon structures. This is likely caused by the presence of the pier diaphragms stiffening the top slab. This was not seen on the Smart Road Bridge because the closest accessible section near the pier (Section B) was at 0.25*L, over 100 ft from the pier diaphragm. Overall, top flange and wing transverse bending strains were on the same order of magnitude, but typically higher than the measured longitudinal strains.

Longitudinal pier segment rotation (Seabreeze Bridge only) and deflection measurements (Seabreeze and Varina-Enon) showed little change across load cases. Using longitudinal strains and global deflections, the principle of superposition was confirmed for each structure, indicating the bridges remained globally and locally (at strain measurement locations) elastic during load testing.

5 Longitudinal and Transverse Analysis

In the following chapter, the results from the Seabreeze, Smart Road and Varina-Enon live load tests are used to evaluate simplified longitudinal analysis techniques. Additionally these tests aided in determining, if accounting for shear lag, with an effective flange width (b_e) is necessary. It is vital to accurately estimate and/or verify the concrete elastic modulus found in these three bridges. Section 5.1 presents the methodology for the elastic modulus estimation critical for the transverse bending behavior investigation.

The literature review found longitudinal analysis techniques have been well vetted, but transverse bending observations and its comparison to analysis are lacking. Using the live load test results, two dimensional frame models are investigated with several boundary conditions including common design assumptions and a new method intended to provide support restraints that are more realistic. Because designers have often tried to take into account the stiffening of the barrier rails, spring elements are investigated as a way to add this stiffness.

Bridge engineers are increasingly using finite element software to design for localized transverse bending. Also, the simplifications involved in the two dimensional frame analyses are known to be incorrect, but conservative. A framework for creating a simple three dimensional shell model, including recommendations on mesh fineness, support conditions, and model size is presented. This model is compared to the live load test results and the simplified two dimensional frame models. The goal of these analyses is to give tools to engineers for longitudinal and transverse bending analysis that have a known accuracy.

The model evaluation in this chapter depends on two error functions commonly used to illustrate overall modeling error for model updating (Sanayei et al. 1992). Model updating was not explicitly performed; rather several longitudinal and transverse models were compared to tests results for varying design assumptions. Mean absolute error (MAE) finds the average difference in each measured response value (i.e., strain, deflection, rotation) with its predicted response:

$$MAE = \frac{1}{m}\frac{1}{n}\sum_{i=1}^{m}\sum_{j=1}^{n}\left|R_{m,i,j} - R_{p,i,j}\right| \qquad \textit{Equation 14}$$

Where:

- m is the number of measurement load cases,
- n is the number of instruments for each load case,
- $R_{m,i,j}$ is the measured response value for sensor i subjected to load case j,
- $R_{p,i,j}$ is the predicted response value from the model at the sensor i location, when subjected to load case j.

Equation 14 is mainly used, in this document, as a comparative evaluation for sensors with small recorded values relative to their accuracy. The MAE is limited when comparing multiple sensor types with different measurement types and units. In particular, the transverse bending investigation only uses strain measurements so MAE can be used effectively for comparison of these values. The results of the MAE comparator are useful as it is in the units of the measurement and therefore retains its meaning. Small MAE, near the accuracy of the measured values indicates a good prediction.

The mean absolute percent error (MAPE) finds the average percent error for each measured response value compared to its predicted response:

$$MAPE = \frac{1}{m}\frac{1}{n}\sum_{i=1}^{m}\sum_{j=1}^{n}\frac{\left|R_{m,i,j} - R_{p,i,j}\right|}{\left|R_{m,i,j}\right|} \qquad \textit{Equation 15}$$

Equation 15 provides an easily interpreted accuracy assessment, although it may provide poor comparisons for small (in relation to the measurement error) measured values because of the position of the measured response in the denominator. The MAPE comparator is reported in percent.

5.1 Simplified Longitudinal Analysis

The most common method of analysis for segmental concrete bridges is a beamline analysis. The following sections will investigate the validity of using a beamline analysis as a design tool. The Seabreeze Bridge, the Smart Road Bridge and the Varina-Enon Bridge, represent three very different segmental box girder structures. Their characteristics range in construction method,

concrete type, span length, width and post-tensioning type. Concrete properties are especially important to linear-elastic modeling, with the accuracy of the elastic modulus critical to the analysis. The transverse analyses in subsequent sections use the concrete elastic moduli verified by the longitudinal analyses.

For most segmental single cell bridge load tests, focus is on longitudinal behavior, such as longitudinal deflections, rotations and strains. A beamline model, also known as a "spline" or "spine" model, for single cell box girder bridges, is typically constructed to estimate global bridge response (e.g., bending, shear, torsion, deflection, time dependent effects). Beamline models have even been used to accurately model complex cable stayed structures like the Varina-Enon main structure (Duemmel et al. 1992, Lissenden 1988). A longitudinal beamline model approach will be used to evaluate behavior of the three subject bridges. The longitudinal beamline models use a beam offset method (Chung 2003) to represent support conditions. This offset model is presented graphically in Figure 96 and Figure 97. For each model, the beamline followed the centroid of the bridge girder, dipping near the pier supports as the cross section became deeper and the neutral axis moved down.

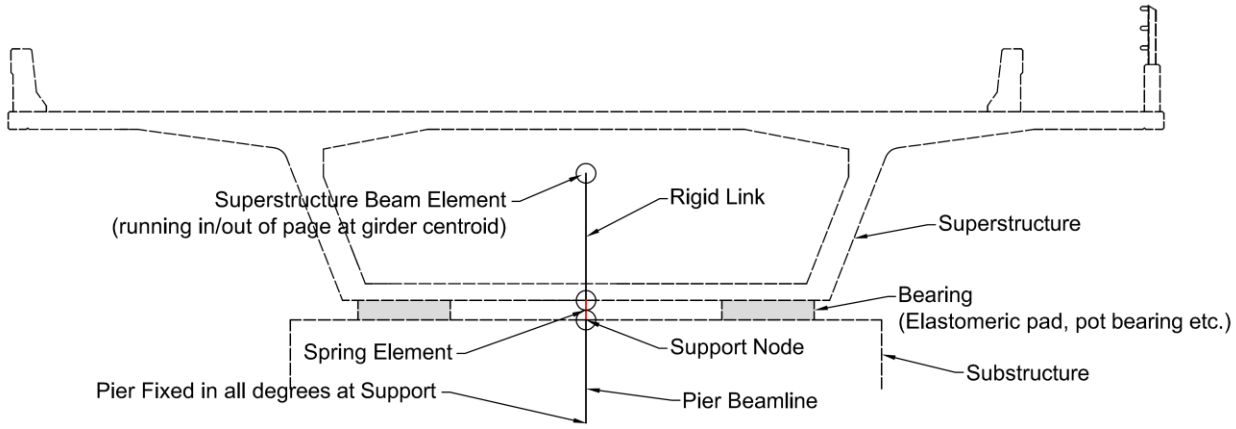

Figure 96 – Beam Offset Method for Modeling Support Conditions – Longitudinal View

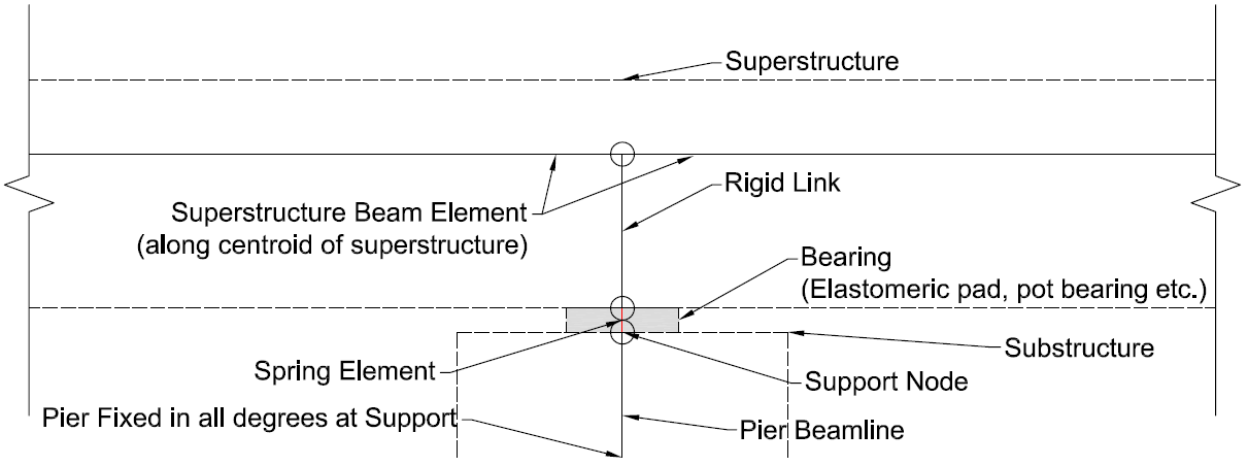

Figure 97 – Beam Offset Method for Modeling Support Conditions – Elevation View

Finite element models are often calibrated by using springs at supports to mimic support restraint conditions and/or by varying superstructure elastic modulus values to account for the highly variable elastic modulus and for differences in specified bridge dimensions. The intent of the beamline models was not to perform optimized calibrations, rather to arrive at reasonable estimations of the elastic modulus values for the transverse analysis. Based on the results in the previous chapter, only the Varina-Enon Bridge exhibited significant shear lag (top slab only), therefore shear lag effects were neglected in the beamline models. All beam elements for super and substructures used un-cracked, transformed section properties, including tendons, mild reinforcement, barrier rails, and full flange width. Beam elements were non-prismatic elements used to capture the variable stiffness segments.

5.1.1 Seabreeze Bridge

The two pot bearings at each support, one under each web, were combinations of:

- fixed (fixed in all plan directions) and fixed; or
- guided (free in plan longitudinally, fixed in plan transversely) and free (free in all plan directions).

There were two model boundary conditions used for the two pot bearing configurations. The combination of guided and free pot bearings were modeled as free to move longitudinally, fixed

transversely, and free to rotate; i.e., an idealized roller. The combination of fixed and fixed was modeled as fixed in translation in all directions, but free to rotate; i.e., an idealized pin.

Figure 98 presents a three dimensional view of the Seabreeze Bridge beamline model, using the modeling technique previously discussed. All bearings were modeled using a spring element with variable bending, shear and axial stiffness to mimic the conditions discussed in the previous paragraph. Abutment 1 through Pier 4 and Pier 8 through Abutment 2 used guided supports. The guided supports used infinite bending and axial and transverse shear stiffness, but zero shear stiffness in the guided direction. The fixed supports, Piers 5 through 7, used infinite stiffness for each. Pier 8 through Abutment 2 used guided supports rotated in plan to allow movement parallel to Pier 6, per the plans. When trying to estimate Pier 2 rotations shear stiffness was added to create partial restraint. The bottom of each pier was modeled as ideally fixed for all degrees of freedom at the ground (pile foundation).

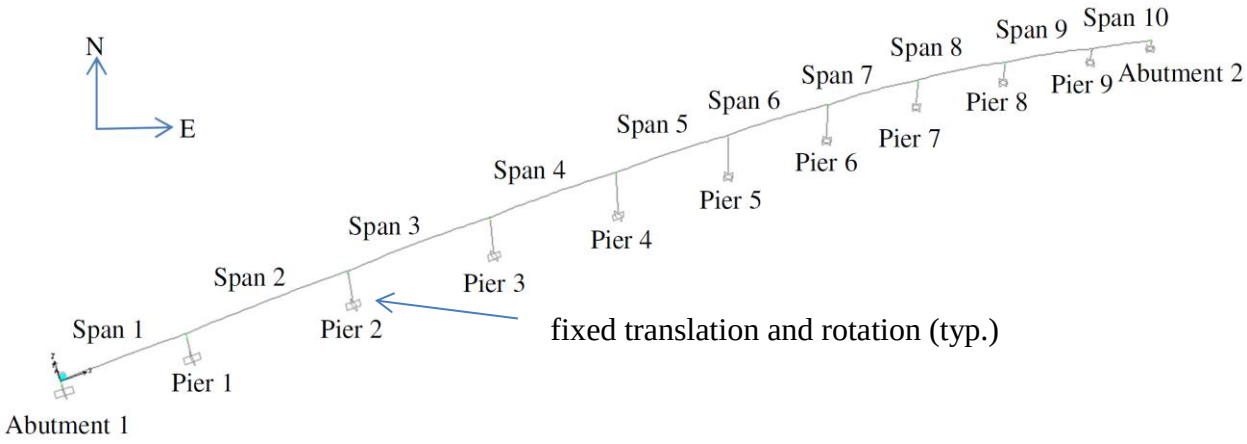

Figure 98 – Seabreeze Bridge Beamline Model – Three Dimensional View

Ultrasonic surface wave testing, performed by Rutgers University, on a 2 ft × 2 ft grid over Span 2 and Span 3 identified an average deck elastic modulus (E_c) of 5300 ksi, and similar testing on a pier identified an average pier elastic modulus of 4500 ksi. These values were used as the E_c value for the super and sub-structure components of the model.

Using these measured elastic moduli, the beamline model was able to predict all strains, rotations and deflections to an average MAPE of 20%. Example comparisons between measured and predicted influence lines for each measurement type can be found in Figure 99 through Figure 101 predicted. Girder deflections were approximately 20% larger than measured deflections as shown in Figure 99. Upon inspection, the model predictions were best when the load was near the instruments, but did not predict deflections as well when the load was away from the instruments.

Girder rotations at the bearing were predicted well, with maximum calculated rotations off by a maximum of 9%, an example of which is presented in Figure 100. One iteration from each load case is plotted on Figure 100. In Figure 100 the lines represent the measured values and are mostly indiscernible, demonstrating small variability between load cases.

Figure 101 presents typical measured and predicted influence lines for top and bottom flange strain gages. Overall, predicted strains were within 23% of measured values. This number is skewed somewhat by typically low readings. Because of this, a 1με difference, which can be considered within the functional accuracy of a load test, will create a large percent difference for the small measurements. For example, the maximum compression strain reading at Sections B and C for all load cases was less than 5 με, and a 1 με difference for these instruments will create 20% or more error.

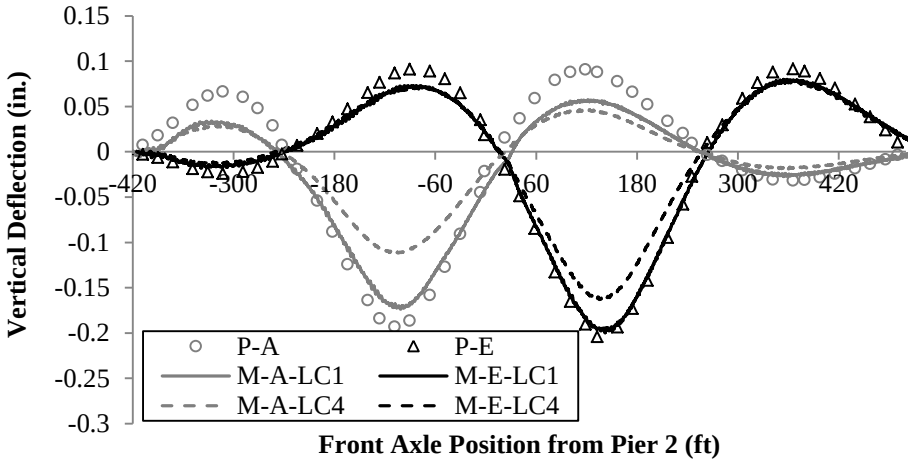

Figure 99 – Seabreeze Bridge Example Influence Line Comparison of Measured and Predicted Deflections at Section A and E (Prefixes: Measured – M; Predicted – P)

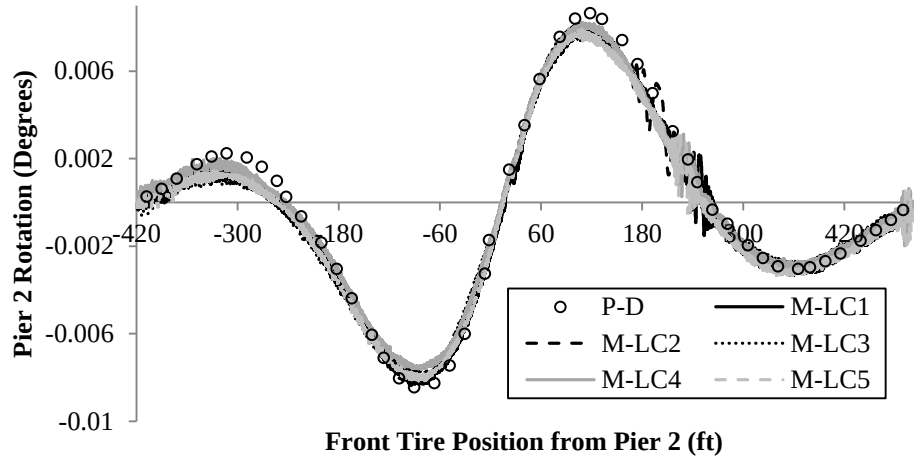

Figure 100 – Seabreeze Bridge Example Influence Line Comparison of Measured and Predicted Girder Rotations at the Pier 2 Segment (Prefixes: Measured – M; Predicted – P)

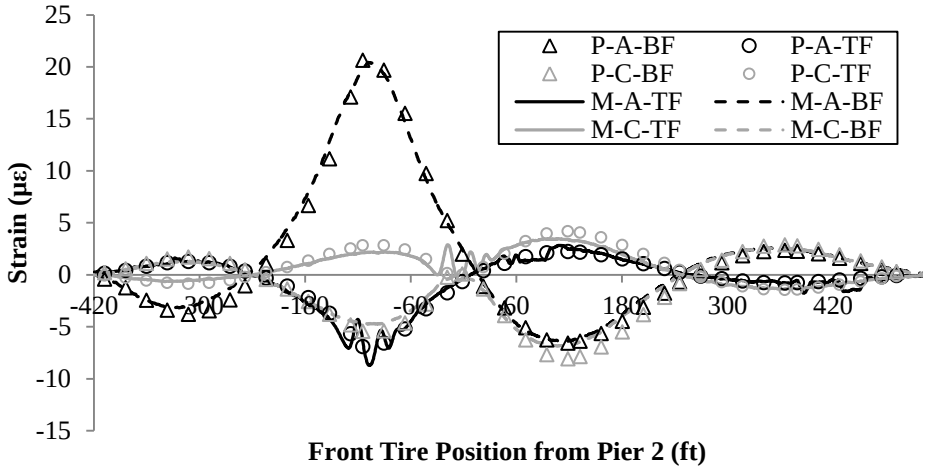

Figure 101 – Seabreeze Bridge Example Influence Line Comparison of Measured and Predicted LC2 Top Flange (TF) and Bottom Flange (BF) Strains. (Prefixes: Measured – M; Predicted – P)

Rotations at the top of Pier 2 were measured during the load test. Using the model described above, there are no predicted longitudinal rotations at the top of the pier (i.e., free longitudinal superstructure bearing movement). However, to investigate if this simple model can capture super and sub-structure interaction, the model was altered to include support springs to mimic bearing restraint at each expansion bearing in the model. All supports, which employed a fixed bearing, were modeled as pinned, as before. A spring stiffness of 3500 kip/in, applied to all guided bearings, provided enough load transfer to the pier to closely match measured top-of-pier rotations at Section D. Figure 102 presents an example comparison of girder and top of pier rotation influence lines at Section D. The additional spring stiffness improved the MAPE for the

model to 16%. Additionally, spring calibration could increase model accuracy and would have been aided with additional instrumentation. However, designers would not be able to take advantage of this without knowing spring stiffness a priori.

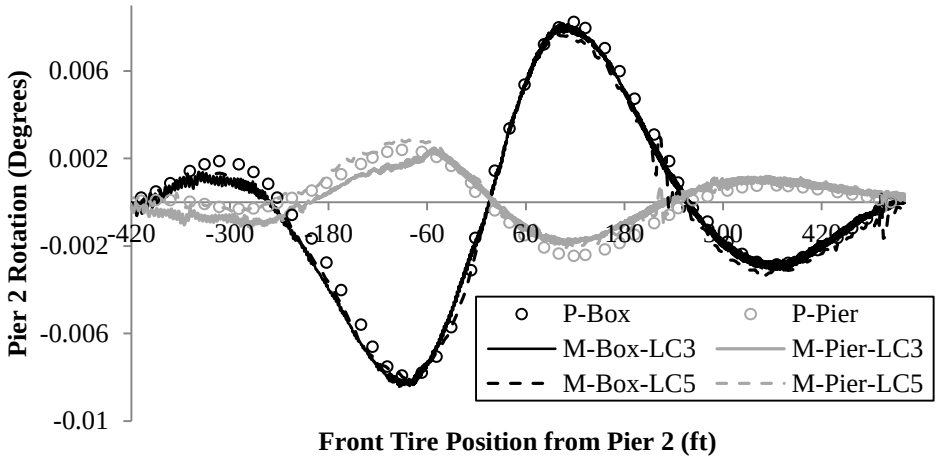

Figure 102 – Seabreeze Example Predicted and Measured Girder and Top of Pier Rotations after Adding Stiffness to Beamline Model Bearings. (Note Prefixes: Measured – M; Predicted – P)

5.1.2 Smart Road Bridge

The superstructure, which is integral with the piers for the cast-in-place Smart Road Bridge, was modeled using a rigid link offset from the centroid of the box girder beam element to the top of the pier beam element. This arrangement imposes total continuity between the super and substructures. The abutment supports were modeled as discussed for Figure 96. The variable depth superstructure and substructure were modeled using variable stiffness, non-prismatic elements. Abutment supports were modeled as link elements free to deform in shear and rigid axially (i.e. fixed vertically and free longitudinally). Pier foundations were modeled with all degrees of freedom fixed. The actual pier foundation on the Smart Road Bridge is a spread footing.

Concrete strength was specified at 8 ksi (E_c = 5100 ksi) per the plans. However, upon tracking down the concrete mixture and speaking with the concrete producer (then Marshall Concrete Products, now Chandler Concrete Company) contracted for the project in 2001, the concrete superstructure compressive strength was observed up to 15 ksi , and substructure around 12 ksi (George Kuhn, personal communication, February 18, 2013). Using the modulus prediction

values adopted by AASHTO for high strength concrete, discussed by Al-Omaishi et al. (2009), the superstructure elastic modulus was set to 7,800 ksi and substructure to 6,800 ksi.

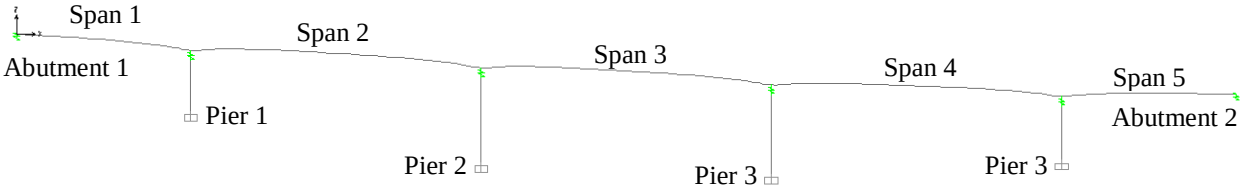

Figure 103 – Smart Road Bridge Beamline Model – Elevation View

Figure 104 and Figure 105 present plots comparing measured and predicted influence lines for strains on the top and bottom flanges at the two measurement locations. Figure 104, typical influence line comparison for Section A, LC3, shows good agreement between the model and measured values at nearly all truck locations. In this instance, the prediction is approximately 1 με higher than measured at maximum bottom slab strain location, but nearly the same for the top flange.

Figure 105 shows similar strain influence line comparisons for Section B, LC3. The data does not fit ideally when compared to Section A. However, in this case, the maximum strains are small and are still relatively well predicted to within 1 με at all local maxima.

The overall MAPE is 18% for the strain readings on the Smart Road Bridge. However, because strains are the only measurement and are typically small (with the absolute maximum strain measurement only 10 με and typical maximum strains around 4 με), mean absolute error (MAE) provides a better estimator. The Smart Road Bridge MAE is only 0.76 με indicating that the actual average difference between measured and predicted strains is less than 1 με. For comparison purposes, on the Seabreeze Bridge, MAE for the strain measurements only is 1.36 με. Because of uncontrollable factors (i.e., wind, temperature, inaccurate truck position, inaccuracy in axle weights), 1 με can be considered the maximum accuracy indicating maximum strain MAE for each structure is very good.

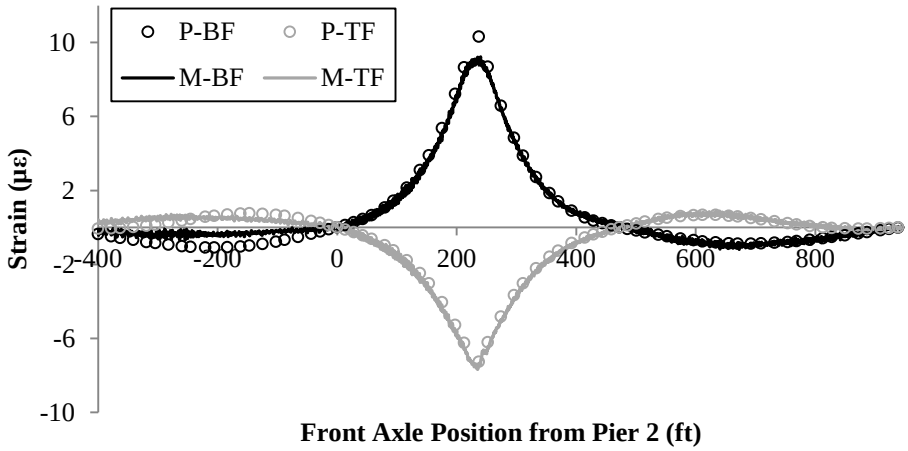

Figure 104 – Smart Road Bridge Example Average Measured and Predicted Strain Top Flange (TF) and Bottom Flange (BF) strain influence lines for Section A, LC3(Prefixes: Measured – M; Predicted – P)

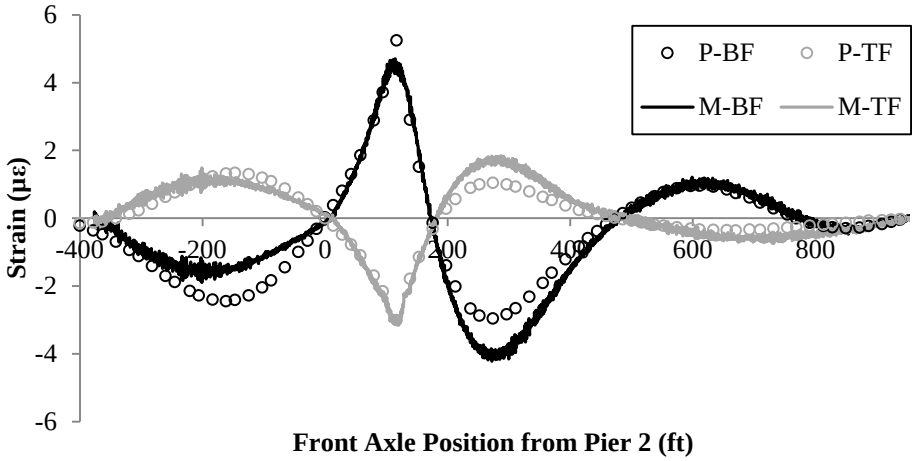

Figure 105 – Smart Road Bridge Example Average Measured and Predicted Strain Top Flange (TF) and Bottom Flange (BF) strain influence lines for Section B, LC3(Prefixes: Measured – M; Predicted – P)

5.1.3 Varina-Enon Bridge

The Varina-Enon Bridge approach structure consists of a single-cell box girder with several external tendons. Figure 106 presents the elevation view of the Varina-Enon beamline model. Each tendon was modeled as a tendon element deviated from the box girder centroid, using rigid offset elements to the actual deviation locations as shown in the detail view in Figure 107. Each tendon used nominal tendon area and an elastic modulus of 28,500 ksi. Girder concrete was specified as 5.5 ksi. Using AASHTO modulus prediction equations on the nominal strength, the

concrete modulus would be 4300 ksi. However, it is typical to have higher concrete strength than specified in design as with the structures in the preceding sections. When only varying the concrete strength, MAE and MAPE were minimized when using 5000 ksi for the concrete elastic modulus for the super and substructures. This is a reasonable assumption for elastic modulus bias (5000 ksi/4300 ksi = 1.16) based on bias factors found by Hueste et al. (2004) for 6,000 psi ±1000 psi concrete (1.31).

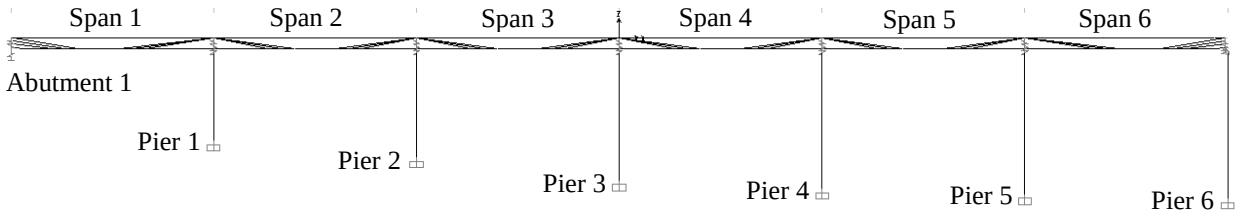

Figure 106 – Varina-Enon Bridge Beamline Model – Elevation View

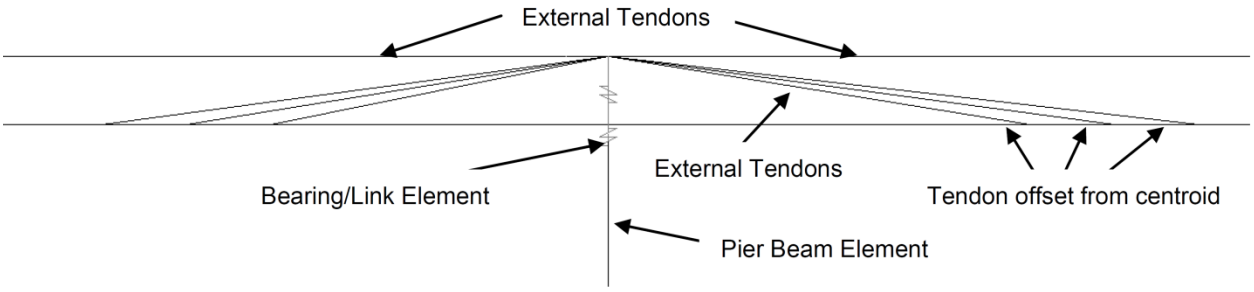

Figure 107 – Varina-Enon Beamline External Tendon Modeling Details

The abutment supports were modeled as discussed for Figure 96, but connected to ground rather than a pier beam element. The Varina-Enon Bridge bearings are elastomeric pads of varying height. Using the calculation procedure developed by Stanton et al. (2008), Appendix G, the component stiffness of each bearing set were set as presented in Table 27.

Table 27 – Varina-Enon Calculated Elastomeric Pad Support Link Stiffness

Support (S to N)	Height (in.)	Vertical Stiffness (kip/in.)	Horizontal Stiffness (kip/in.)	Rotational Stiffness (kip/rad)
1	7.6	26,000	240	1,700
2	4.3	38,500	490	2,500
3	3.0	73,600	630	4,900
4	3.0	73,600	630	4,900
5	3.0	73,600	630	4,900
6	4.3	38,500	490	2,500
7	7.6	26,000	240	1,700

The constant stiffness super and substructures used transformed section properties including all mild reinforcement and the barrier rails. Even though some shear lag was observed in the top flange, an effective width reduction was not performed for the superstructure, as is consistent with the programs in the literature. Pier foundations were modeled with all degrees of freedom fixed. The actual pier foundation on the Varina-Enon Bridge is a pile foundation.

Figure 108 through Figure 111 present plots comparing measured and predicted influence lines for deflections at Section A and longitudinal strains on the top and bottom flanges for the Varina-Enon Bridge. Figure 108 compares the predicted and measured deflections for Varina-Enon LC1-3. The prediction for LC1 and LC2 are the same because the truck was identical, but in different lanes, which the beamline model did not account for. Overall deflection values were within 25% MAPE and 0.01 in. MAE. This is significantly worse than the Seabreeze Bridge deflection MAPE (20%), however, in that case the elastic modulus was measured, whereas there is little information to guide Varina-Enon elastic modulus selection.

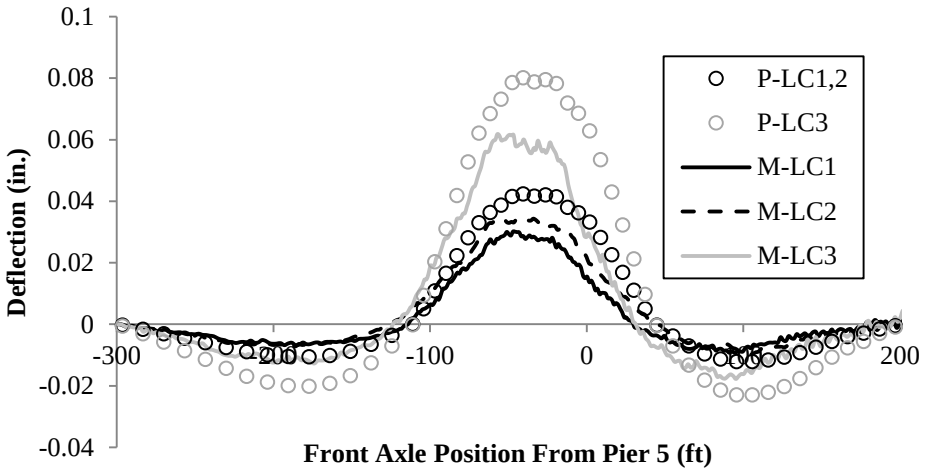

Figure 108 – Varina-Enon Bridge Example Influence Line Comparison of Measured to Predicted Deflections at Section A and E (Prefixes: Measured – M; Predicted – P

Figure 109 presents the measured and predicted strain comparisons at Section B. The plot shows good correlation between strains on the top and bottom flange, including maximum strains. The local strains in the top flange locations caused by the axles passing near the sensors, cause jumps in strain that the beamline model could not imitate.

Figure 110 and Figure 111 compare measured and predicted strains for sensors at Section D. Again, strains are very well predicted in the examples shown, often overlapping with the measured values throughout the dataset. Local strains in the top slab location (dashed, gray line) are poorly predicted because of limitations in the beam element based model. In Figure 110, strains for LC1, the web sensor prediction and measurement is poor, but predicted well for LC2. The tensile strains in the bottom flange at Section D were dependent on the transverse truck position as discussed in Section 4.3.1 and presented graphically in Figure 88 and Figure 89.

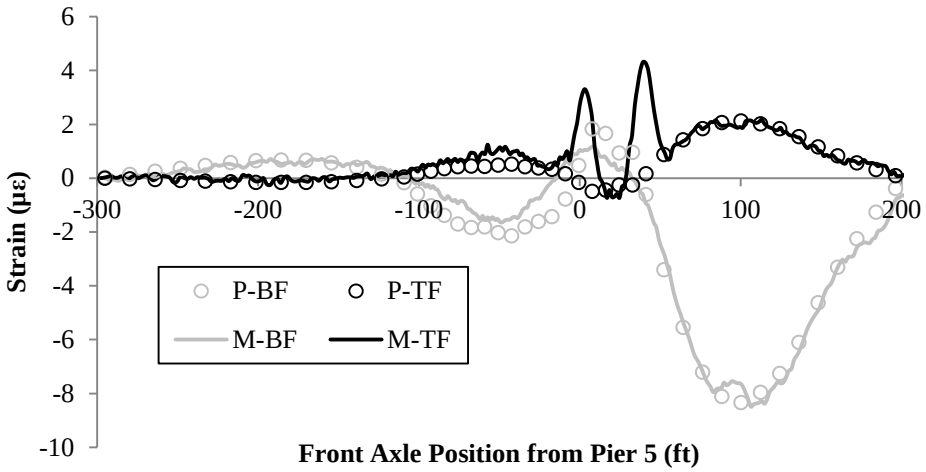

Figure 109 – Varina-Enon Bridge Example Average Measured and Predicted Strain Top Flange (TF) and Bottom Flange (BF) strain influence lines for Section B, LC2(Prefixes: Measured – M; Predicted – P)

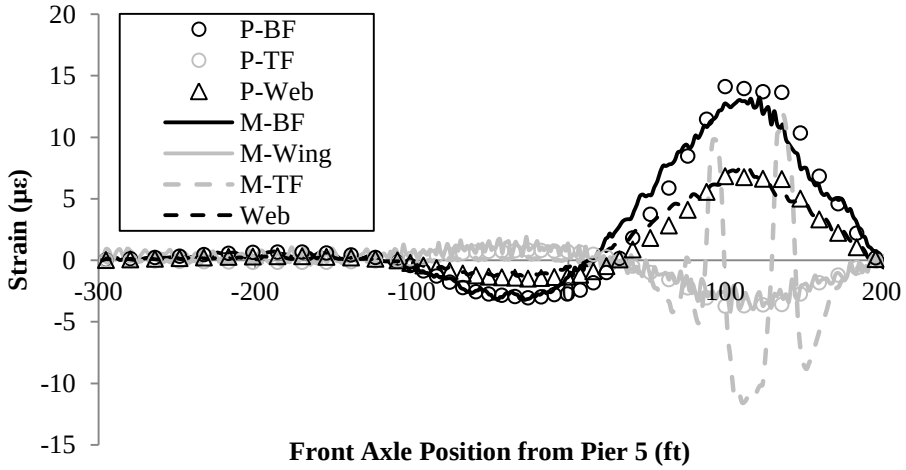

Figure 110 – Varina-Enon Bridge Example Average Measured and Predicted Strain Top Flange (TF) and Bottom Flange (BF), wing and web strain influence lines for Section B, LC1(Prefixes: Measured – M; Predicted – P)

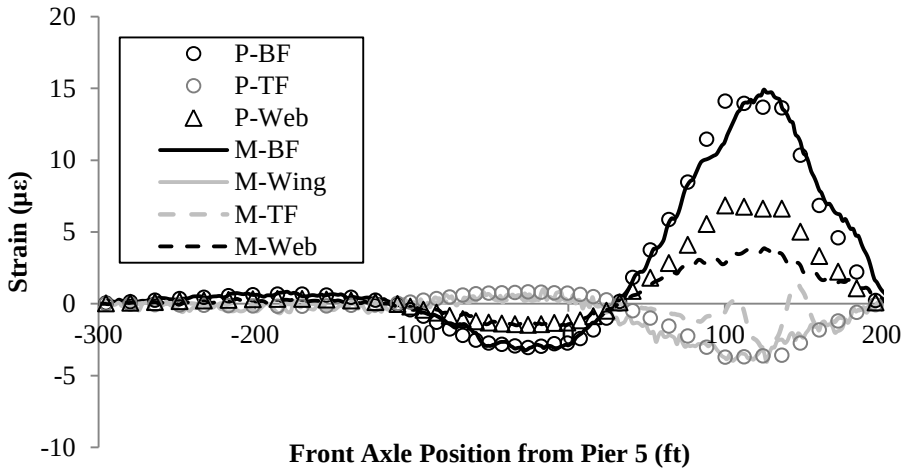

Figure 111 – Varina-Enon Bridge Example Average Measured and Predicted Strain Top Flange (TF) and Bottom Flange (BF), wing and web strain influence lines for Section B, LC2(Prefixes: Measured – M; Predicted – P)

Overall, strains were within 18% MAPE and 1.3 με APE indicating accuracy at the same level as the other tests. It may be possible to modify the modulus and bearing stiffness to obtain better comparisons. However, because these predictions are close to those found on the previous bridges, where more information is known about the material properties, they are considered good enough. One main function of the models presented here is to verify the elastic modulus values for use in the transverse analysis presented later in this report.

5.1.4 Longitudinal Analysis Summary

The purpose of the longitudinal modeling in this report was to determine the level of accuracy the simplified beamline analysis can provide and to estimate a reasonable modulus of elasticity for the transverse analysis modeling. For each structure, a beamline model was created using typical design assumptions, without calibration. Table 28 presents a summary of the statistical comparators for the longitudinal modeling, for each bridge.

Table 28 – Summary of Longitudinal Modeling Comparators

Structure	Superstructure Elastic Modulus (ksi)	MAE		MAPE		
		Deflection (in.)	Strain (με)	Global*	Strain	Overall
Seabreeze	5,300	0.03	1.36	13%	23%	20%
Smart Road	7,800	-	0.76	-	18%	18%
Varina-Enon	5,000	0.01	1.3	25%	18%	19%

*Global includes all measured deflections and/or rotations

The Seabreeze Bridge used a measured, from ultrasonic surface wave testing, modulus of elasticity of 5,300 ksi. Anecdotal evidence indicated that the Smart Road Bridge concrete was much stronger than specified at around 15 ksi at 28 days, for an elastic modulus of 7,800. The Varina-Enon Structure did not have any material testing or non-destructive evaluation to determine the elastic modulus. After trying larger superstructure elastic modulus values, the MAPE comparator was minimized using 5,000 ksi for the modulus. Using this value, the Varina-Enon Bridge model MAE, and MAPE comparators were similar to those observed on the Smart Road and Seabreeze Bridges.

The MAE and MAPE comparators indicate the simple beamline models can adequately reproduce live load test data. Several other research programs have found the same result (e.g., Roberts 1993, Davis 1999). Based on these results, designers do not need to create complex three dimensional shell or solid models to provide reasonable, conservative results. In nearly all cases, the models predicted conservatively as shown in Figure 99, Figure 104, and Figure 108. One minor shortcoming of the beamline modeling technique is the inability to predict local longitudinal stresses generated by the large tire loading on the top slab and wings.

5.2 Transverse Frame Analysis

Transverse frame analysis, detailed in the literature review, is a common simplified analysis method to estimate stresses in the transverse direction caused by localized tire loads, transverse post-tensioning, dead load, creep and shrinkage. The following section investigates different types of transverse frame analysis. The accuracy of these techniques is estimated and compared overall using the MAE and MAPE comparators. Finally, recommendations are made regarding transverse analysis practice.

Serviceability/allowable stresses typically control transverse design and rating. For this reason transverse prestressing moment, axial force and resulting strain at the sensor location are presented in Table 29 through Table 31 for the Seabreeze Section A, Smart Road Section A and Varina-Enon Section D, respectively. The presented prestressing values give the reader a reference point for the following measured and calculated live load values presented in the following sections. The prestressing effects were calculated using a SAP2000 frame model with pin and roller supports at the bottom of the webs, which is outlined in more detail in the following section. The total prestressing (primary plus secondary) strains were calculated using gross cross sectional properties and elastic modulus values shown in Table 28. Tendon and loss information was presented in the plans, which are presented in Table 32. The Grade 270 low relaxation strands in each structure were jacked to 216 ksi and were modeled using SAP2000 tendon elements.

Table 29 – Seabreeze Section A Transverse Prestressing Information After Losses

Sensor Location	M_{ps} (kip-in/ft)	P_{ps} (kips)	Prestressing Strain (με)
Wing	140	-32	19
Left Top Slab	104	-33	13
Mid Top Slab	-39	-34	-104
Top Web	4	0	-2
Bottom Web	2	0	-1
Left Bot. Slab	1	0	-2

Table 30 – Smart Road Section A Transverse Prestressing Information After Losses

Sensor Location	M_{ps} (kip-in/ft)	P_{ps} (kips)	Prestressing Strain (με)
Wing	187	-46	-93
Left Haunch	246	-49	38
Middle Top Slab	-66	-54	-115
Right Haunch	246	-49	38
Top Right Web	-28	0	6
Mid Right Web	-16	0	4
Right Bottom Slab	6	0	-4
Left Bottom Slab	6	0	-4
Mid Left Web	-16	0	4
Top Left Web	-28	0	6

Table 31 – Varina-Enon Section D Transverse Prestressing Information After Losses

Sensor Location	M_{ps} (kip-in/ft)	P_{ps} (kips)	Prestressing Strain (με)
Top Slab	-66	-54	-157
Right Top Slab	16	-54	-74
TS Haunch	160	-54	21
Wing	205	-53	34
Top Web	-3	0	2
Bot Web	0	0	0
Bot Slab	1	0	-2

Table 32 – Post-Tensioning and Loss Values

Bridge	A_{ps} (in^2/ft)	Friction Coefficient	Wobble Coefficient (1/in.)	Anchor Set (in.)
Seabreeze Bridge	0.217	0.20	0.00015	0.375
Smart Road Bridge	0.353	0.25	0.00066	0.350
Varina-Enon Bridge	0.347	0.25	0.00008	0.375

5.2.1 Simplified Frame Models

For each bridge, one transverse frame model was constructed for each cross section of different depth. Each frame model breaks up the unit length (1 ft in longitudinal direction) box girder

cross section into several transverse beam elements and rigid links, as shown in Figure 112. One model for each of Seabreeze Section A and C, Smart Road Bridge Section A and B and the Varina-Enon Bridge. The Varina-Enon Bridge has a constant depth, therefore only one frame model was necessary. Each two dimensional transverse frame model was constructed using gross concrete properties and the elastic moduli validated by the longitudinal models presented in Section 5.1. Barrier rails are included at the free ends of the wings as vertical springs and discussed in Section 5.2.1.3.

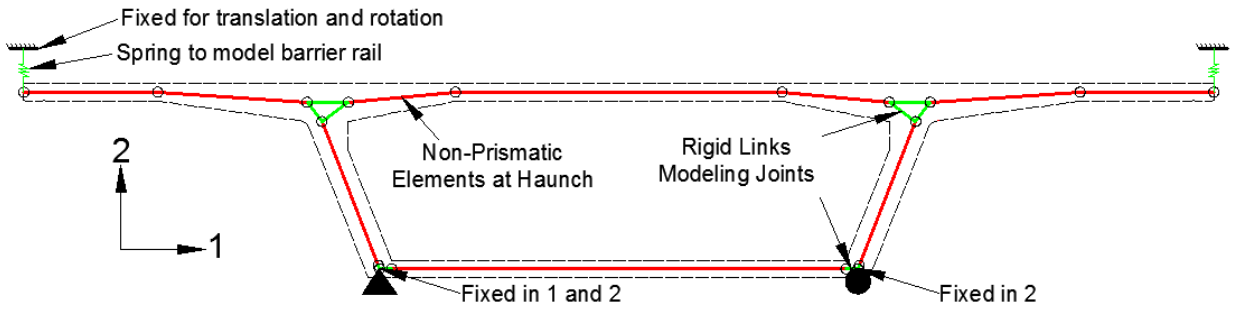

Figure 112 – Example Frame Model Setup

There is little guidance in the literature about how to construct the frame model web-flange joints. For the following models, joints were constructed by creating a joint bounding box defined by the extension of the top flange and web components, as shown in Figure 112. The points at which the beam elements intersect the bounding box are then connected using rigid links in a triangle pattern. The bounding box dimensions and location can be defined differently, but the differences will be on the order of a few inches for beam/link lengths. A similar bounding box may be constructed for the bottom flange joint, as shown in Figure 113 and Figure 114.

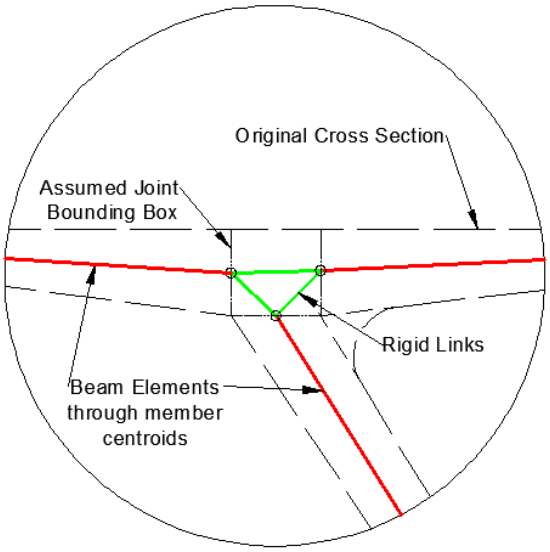

Figure 113 – Detail View of Top Flange Joint

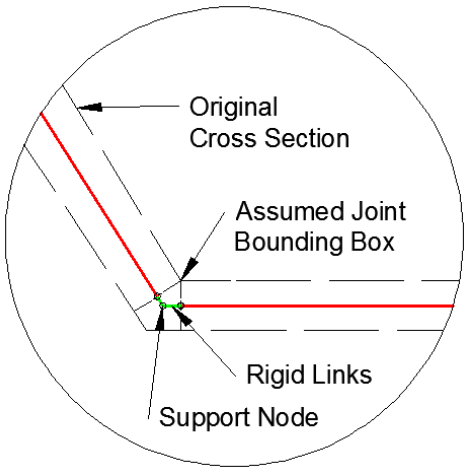

Figure 114 – Detail View of Bottom Flange Joint

In practice, engineers have reported using various support conditions. Generally, engineers assign pin and roller supports at the bottom of each web (B P-R) as shown in Figure 112. Some engineers have also tried placing pin and roller supports at the top of the webs (T P-R), although this seems to be much less common. To investigate possible frame model improvements, pin-roller supports are also substituted with pin-pin supports at the top (T P-P) and bottom of the webs (B P-P) and at both top and bottom (4P). It is unknown, but unlikely, designers have ever used any of the pin only boundary conditions in practice. Each of the B P-R, B P-P, T P-R, T P-P

and 4P boundary conditions are presented visually in Figure 115 and were investigated for each structure tested. Furthermore, designers occasionally try using springs on the wing tips (see Figure 112) to take into account the stiffening effect of the barrier rails on the cantilever wing. This technique is also investigated below for each cross section tested.

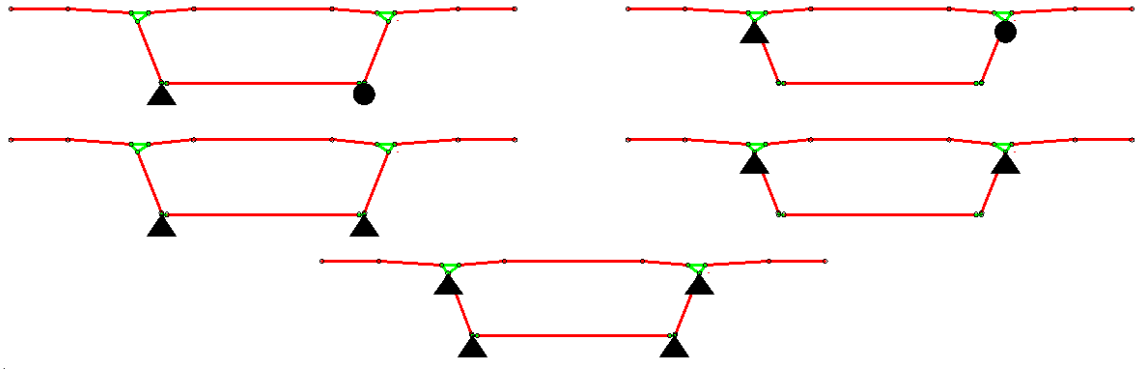

Figure 115 – Investigated Frame Model Boundary Conditions

The applied fixed-end moments, as calculated using Pucher and Homberg influence surfaces (as shown in Figure 14) are presented in Table 33 through Table 35, where positive indicates counter clockwise bending. Figure 116 presents an example of applying the fixed end moment. Determining the loads on the loaded members using the non-nodal load procedure is demonstrated in Figure 13.

Table 33 – Seabreeze Bridge Applied Joint Moments from Influence Surfaces

Seabreeze Bridge Load Case	Influence Surface	Base of Left Cantilever (kip-ft)	Left Top Slab Support (kip-ft)	Right Top Slab Support (kip-ft)
LC1	Pucher	14.00	0.00	0.00
	Homberg	15.60	0.00	0.00
LC3	Pucher	0.00	-6.30	7.70
	Homberg	0.00	-9.12	10.22
LC4	Pucher	0.00	-8.69	4.54
	Homberg	0.00	-14.18	7.16

Table 34 – Smart Road Bridge Applied Joint Moments from Influence Surfaces

Smart Road Bridge Load Case	Influence Surface	Base of Left Cantilever (kip-ft)	Left Top Slab Support (kip-ft)	Right Top Slab Support (kip-ft)	Base of Right Cantilever (kip-ft)
LC1	Pucher	5.88	0.00	0.00	0.00
	Homberg	7.05	0.00	0.00	0.00
LC2	Pucher	0.00	0.00	0.00	-5.88
	Homberg	0.00	0.00	0.00	-7.05
LC3	Pucher	5.88	0.00	0.00	-5.88
	Homberg	7.05	0.00	0.00	-7.05
LC4	Pucher	5.88	-5.26	3.61	0.00
	Homberg	7.05	-6.93	5.08	0.00
LC5	Pucher	0.00	-6.65	6.03	0.00
	Homberg	7.05	-9.35	7.63	0.00

Table 35 – Varina-Enon Bridge Applied Joint Moments from Influence Surfaces

Varina-Enon Bridge Load Case	Influence Surface	Left Top Slab Support (kip-ft)	Right Top Slab Support (kip-ft)	Base of Right Cantilever (kip-ft)
LC4	Pucher	0.00	0.00	-9.03
	Homberg	0.00	0.00	-10.40
LC5	Pucher	0.00	0.00	-9.40
	Homberg	0.00	0.00	-10.65
LC6	Pucher	-0.75	8.30	-9.03
	Homberg	-1.12	12.50	-10.40

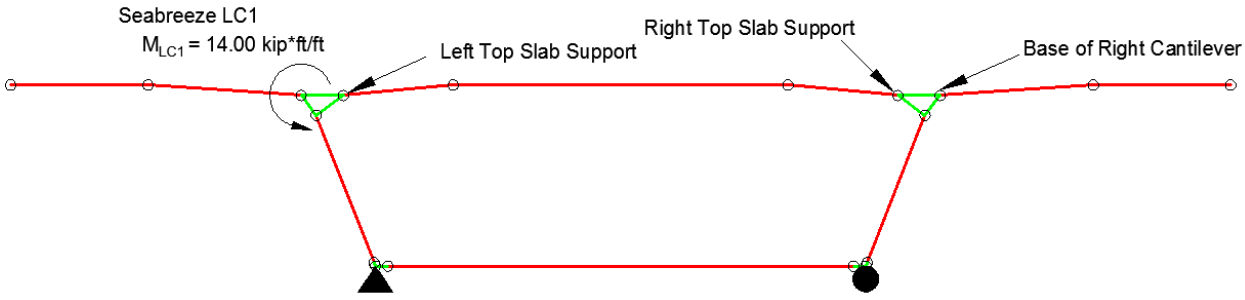

Figure 116 – Example Applied Load for Seabreeze Frame Model

Pucher influence surfaces were developed for constant thickness plates and are theoretically less accurate for haunched plate components when compared to Homberg influence surfaces. Homberg influence surfaces were developed for slabs with varying thicknesses and can be selected to closely match the real structure geometry, see Figure 117 for example using Seabreeze Bridge dimensions. For the Seabreeze and Smart Road Bridge, the Homberg parabolically varying thickness with a fixed:free thickness ratio equal to 2:1 was used to describe the real geometry. The Homberg thickness variation is not exact, but considered close enough, e.g., 19 in. : 9 in. is not the same as 2:1, nor does the parabola describe the haunch section exactly (see Figure 117). For the top slab, the fixed:middle thickness ratio was also 2:1 and varied parabolically for the Seabreeze and Smart Road Structures. For the Varina-Enon Bridge, a parabolically varying fixed:free, 2:1 thickness ratio for the wing and a parabolically varying 1.5:1 fixed:middle thickness ratio for the top slab was selected to most accurately describe the geometry.

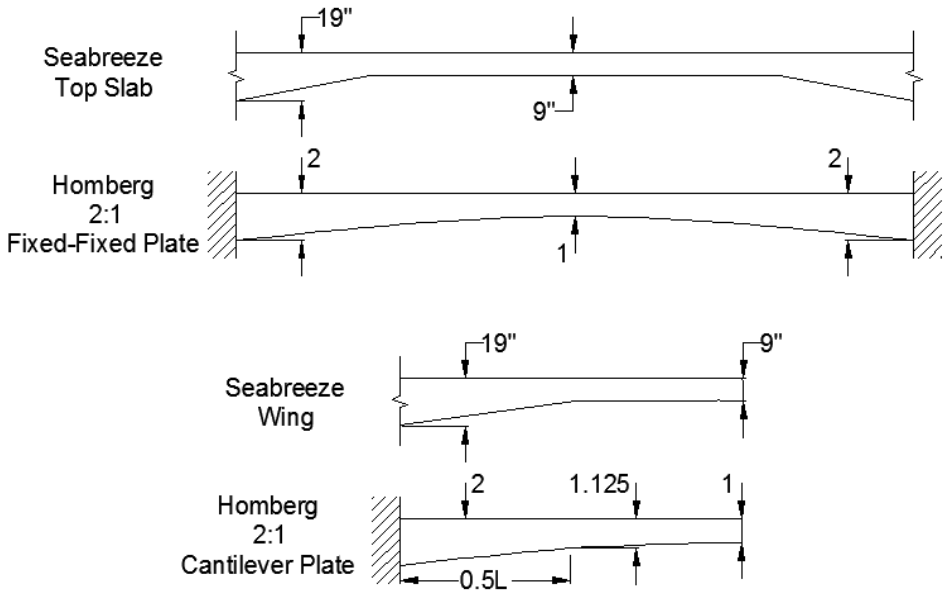

Figure 117 – Example Seabreeze Bridge and Homberg Plate Dimension Matching

Moments from the frame models were converted to outer fiber stresses at the measurement sections assuming an uncracked section (i.e., $\sigma = Mt/2I$, where $I = 1/12(1\text{ ft})t^3$ and t is the component thickness). The outer fiber stresses were converted to strains with Hooke's Law,

using the elastic modulus values determined in Table 28 and compared to measured values. The calculated strains are then compared to the measured strains.

5.2.1.1 Bottom Web Pin-Roller

The most commonly used frame model has B P-R boundary conditions. Calculated strains from the B P-R model, for each instrumented cross section, are summarized in Table 36 through Table 46. In all subsequent tables, positive strain indicates tension.

For Seabreeze LC1, with the load maximizing bending in the wing, the measured compressive strains under the cantilever wing and in the interior slab near the web are 5% and 15% lower than calculated.

Top slab predictions are overall not as accurate. For Seabreeze Bridge LC3 top slab predictions are between 18% and 114% different. For Seabreeze Bridge LC4, strains are under predicted at the left top slab location (compare -19 με to -14 με at Section A, Pucher in Table 38) and greatly over predicted at the middle slab location (compare Section A measured midspan slab +53 με to predicted +82 με in Table 38). Clearly, wheel loads are being distributed more effectively in the real structure for the top slab than the model predicts.

Measured strains in the web and bottom slab are not only smaller than predictions, but predict the incorrect bending sense for Seabreeze Bridge LC1 and LC3. For example, compare the measured -7 με at the bottom slab location to the Pucher and Homberg predicted +26 με (Pucher) and +29 με (Homberg) respectively at Seabreeze Section A (Table 36).

Evidence that the pier diaphragm is influencing transverse box girder behavior is observed in all Seabreeze LCs when comparing top slab strain magnitudes at Section A to Section C. For example, compare -42 με (Section A, Table 36) to -19 με (Section C, Table 36) under the cantilever wing and +53 με (Section A, Table 38) to +33 με (Section C, Table 38) at the middle of the interior slab. This reduction in strain near the pier is caused, at least in part, by the large pier diaphragm, which stiffens the cross-section and reduces top flange bending. The frame

model does not reflect this reduction, but it is also unlikely a designer would want to account for this reduction.

Table 36 – Seabreeze LC1 Measured and Predicted Transverse Strains

Sensor Location	LC1 - Section A (με)			LC1 - Section C (με)		
	Measured	Pucher	Homberg	Measured	Pucher	Homberg
Wing	**-42**	-46	-51	**-19**	-46	-51
Left Top Slab	**-1**	-27	-30	**-5**	-24	-27
Mid Top Slab	**1**	-3	-3	**-1**	-6	-6
Top Web	**4**	30	33	**8**	38	42
Bottom Web	**-4**	16	18	**-2**	17	19
Left Bot. Slab	**-7**	26	29	**-2**	6	6

Table 37 – Seabreeze LC3 Measured and Predicted Transverse Strains

Sensor Location	LC3 - Section A (με)			LC3 - Section C (με)		
	Measured	Pucher	Homberg	Measured	Pucher	Homberg
Wing	**-4**	0	0	**-3**	0	0
Left Top Slab	**-19**	-22	-30	**-14**	-21	-29
Mid Top Slab	**38**	55	85	**27**	58	89
Top Web	**-5**	-21	-30	**-11**	-24	-34
Bottom Web	**-2**	-4	-6	**1**	3	4
Left Bot. Slab	**-2**	7	8	**1**	8	10

Table 38 – Seabreeze LC4 Measured and Predicted Transverse Strains

Sensor Location	LC4 - Section A (μstrain)			LC4 - Section C (μstrain)		
	Measured	Pucher	Homberg	Measured	Pucher	Homberg
Wing	**-6**	0	0	**-6**	0	0
Left Top Slab	**-19**	-14	-23	**-17**	-15	-23
Mid Top Slab	**53**	82	129	**33**	84	134
Top Web	**-7**	-24	-37	**-16**	-28	-45
Bottom Web	**-3**	-8	-13	**0**	-4	-7
Left Bot. Slab	**-3**	-5	-9	**2**	3	4

Table 41 through Table 43 present measured and calculated strains from the Smart Road Bridge standard frame models. Upon inspection, the Smart Road Bridge measured strains from all LCs

are smaller overall when compared to the Seabreeze Bridge strains, even though the measurements were in similar locations. This is most evident in Table 41, where strains are often at or near the functional minimum accuracy (+/-1 με per the above discussion).

During LC3, negative bending was maximized in the wing. This was predicted using the two dimensional frame model to within 39% and 69% using the Pucher and Homberg influence surfaces for load scaling (compare measured +11 με to +15 με and +18 με in Table 41).

Predictions for LC4 and LC5 show a similar relationship. For instance, the maximally loaded middle top slab strain measurements are off by 38% and 166% for the LC4 Pucher and Homberg predictions, respectively. The LC5 predictions are less accurate at the middle top slab location; 225% for the Homberg prediction at Section C (compare +65 με to +20 με in Table 42). Similar to Seabreeze Bridge observations, bending sense is not always predicted correctly. This is noted in the asymmetric load cases, typically at the bottom slab locations.

Table 39 – Smart Road LC1 Measured and Predicted Transverse Strains

Sensor Location	LC1 - Section A (με)			LC1 - Section C (με)		
	Measured	Pucher	Homberg	Measured	Pucher	Homberg
Wing	**9**	15	18	**7**	15	18
Left Haunch	**1**	-8	-10	**-3**	-9	-11
Middle Top Slab	**1**	-2	-3	**-1**	-3	-4
Right Haunch	**0**	6	7	**0**	6	7
Top Right Web	**-1**	4	4	**0**	5	6
Mid Right Web	**-1**	2	2	**0**	3	4
Right Bottom Slab	**1**	-6	-7	**1**	-7	-8
Left Bottom Slab	**-4**	3	4	**-2**	3	3
Mid Left Web	**2**	4	5	**0**	5	6
Top Left Web	**2**	6	7	**-**	-	-

Table 40 – Smart Road LC2 Measured and Predicted Transverse Strains

Sensor Location	LC2 - Section A (με)			LC2 - Section C (με)		
	Measured	Pucher	Homberg	Measured	Pucher	Homberg
Wing	**1**	0	0	**-1**	0	0
Left Haunch	**-1**	6	7	**-1**	6	7
Middle Top Slab	**1**	-2	-3	**0**	-3	-4
Right Haunch	**1**	-8	-10	**1**	-9	-11
Top Right Web	**2**	6	7	**1**	6	8
Mid Right Web	**0**	4	5	**-1**	5	6
Right Bottom Slab	**-3**	3	4	**-2**	3	4
Left Bottom Slab	**1**	-6	-7	**1**	-6	-8
Mid Left Web	**-1**	2	2	**0**	3	4
Top Left Web	**-1**	-7	-9	**-**	-	-

Table 41 – Smart Road LC3 Measured and Predicted Transverse Strains

Sensor Location	LC3 - Section A (με)			LC3 - Section C (με)		
	Measured	Pucher	Homberg	Measured	Pucher	Homberg
Wing	**11**	15	18	**8**	15	18
Left Haunch	**1**	-2	-3	**-3**	-3	-3
Middle Top Slab	**2**	-5	-6	**-1**	-7	-8
Right Haunch	**1**	-2	-3	**1**	-3	-3
Top Right Web	**2**	9	11	**1**	11	13
Mid Right Web	**-1**	6	7	**1**	8	10
Right Bottom Slab	**-3**	-3	-4	**-1**	-4	-4
Left Bottom Slab	**-3**	-3	-4	**-1**	-4	-4
Mid Left Web	**1**	6	7	**0**	8	10
Top Left Web	**2**	9	11	**-**	**-**	**-**

Table 42 – Smart Road LC4 Measured and Predicted Transverse Strains

Sensor Location	LC4 - Section A (με)			LC4 - Section C (με)		
	Measured	Pucher	Homberg	Measured	Pucher	Homberg
Wing	**11**	15	18	**7**	15	18
Left Haunch	**3**	-7	-10	**-6**	-7	-8
Middle Top Slab	**17**	23	37	**14**	24	37
Right Haunch	**-4**	1	4	**-4**	1	1
Top Right Web	**-4**	-3	-7	**-2**	-3	-5
Mid Right Web	**-4**	-2	-5	**-1**	-3	-4
Right Bottom Slab	**-2**	-2	-4	**2**	-3	-3
Left Bottom Slab	**-5**	4	8	**-2**	4	6
Mid Left Web	**-3**	-1	-2	**-1**	-1	-3
Top Left Web	**-1**	-2	-5	-	-	-

Table 43 – Smart Road LC5 Measured and Predicted Transverse Strains

Sensor Location	LC5 - Section A (με)			LC5 - Section C (με)		
	Measured	Pucher	Homberg	Measured	Pucher	Homberg
Wing	**3**	0	0	**1**	0	0
Left Haunch	**-5**	-5	-9	**-7**	-5	-8
Middle Top Slab	**21**	54	63	**20**	56	65
Right Haunch	**-3**	-5	-8	**-3**	-4	-7
Top Right Web	**-8**	-10	-13	**-4**	-12	-16
Mid Right Web	**-7**	-6	-8	**-3**	-9	-11
Right Bottom Slab	**-2**	4	6	**2**	4	7
Left Bottom Slab	**-2**	3	3	**1**	3	4
Mid Left Web	**-6**	-6	-9	**-2**	-9	-12
Top Left Web	**-4**	-10	-14	-	-	-

Table 44 through Table 46 present measured and calculated strains from the Varina-Enon B P-R supported transverse frame model. As with the Seabreeze Bridge, the strain measurements are significantly reduced at Section C because it is near the pier diaphragm. Similarly the top web strain is more severe near the pier diaphragm. For instance, compare Seabreeze LC4, -7 με (Table 38, Section A) to -16 με (see Table 38, Section C) and Varina-Enon LC5, +13 με (Table 45, Section D) to +23 με (Table 45, Section C). The Seabreeze B P-R model predicts a small increase in some cases (compare Section A -26 με to Section C -28 με, Table 38) due to the differences in web depth. However, the Varina-Enon Bridge has a constant depth; therefore, the frame model cannot predict any difference.

During LC4 and LC5, the load trucks were placed on the wing. This was predicted using the two dimensional frame model to within 57% and 19% using the Pucher influence surfaces for LC4 and LC5, respectively (compare measured -19 με to -30 με in Table 44 and -26 to -31 με in Table 45). The difference in accuracy between the two similar load cases may indicate the wing is distributing moments further away than the influence surfaces assume or the load trucks were closer to each than intended in (LC5).

Top slab Pucher influence surface predictions for Varina-Enon LC6 are off by 20%, 150%, and 120% for the middle top slab, right top slab and the haunch locations, respectively, at Section D. These differences are similar to those seen on the Seabreeze (Section A, LC4, Pucher top slab accuracy ranges from 25% to 54%, see Table 38) and Smart Road Bridges (e.g., Section A LC4, Pucher, top slab accuracy ranges from 38% to 351%, see Table 42). Typically the mid slab measurement is more accurate than the haunch measurements because of rapidly changing moments. Moment gradients near the haunches are higher because of their proximity to inflection points, the joints and the loads are often near the sensors. As noted from the previous bridges, bottom flange bending sense is infrequently predicted correctly. For the Varina-Enon Bridge the bottom flange bending sense was not predicted correctly during any LC.

Table 44 – Varina-Enon LC4 Measured and Predicted Transverse Strains

Sensor Location	LC4 - Section D (με)			LC4 - Section C (με)		
	Measured	Pucher	Homberg	Measured	Pucher	Homberg
Top Slab	**-6**	-4	-4	**-2**	-4	-4
R Top Slab	**-3**	-31	-36	**-**	-31	-36
R Haunch	**-3**	-23	-26	**-4**	-23	-26
R Wing	**-19**	-30	-34	**-**	-30	-34
R Top Web	**9**	18	21	**14**	18	21
R Bot Web	**-5**	22	25	**-3**	22	25
R Bot Slab	**-8.75**	16	18	**-5**	16	18

Table 45 – Varina-Enon LC5 Measured and Predicted Transverse Strains

Sensor Location	LC5 - Section D (με)			LC5 - Section C (με)		
	Measured	Pucher	Homberg	Measured	Pucher	Homberg
Top Slab	**-12**	-4	-4	**-3**	-4	-4
R Top Slab	**-7**	-32	-37	**-**	-32	-37
R Haunch	**-7**	-24	-27	**-6**	-24	-27
R Wing	**-26**	-31	-35	**-**	-31	-35
R Top Web	**13**	19	21	**23**	19	21
R Bot Web	**-6**	23	26	**-7**	23	26
R Bot Slab	**-15**	16	19	**-9**	16	19

Table 46 – Varina-Enon LC6 Measured and Predicted Transverse Strains

Sensor Location	LC6 - Section D (με)			LC6 - Section C (με)		
	Measured	Pucher	Homberg	Measured	Pucher	Homberg
Top Slab	**23**	18	26	**5**	18	26
R Top Slab	**10**	25	44	**-**	25	44
R Haunch	**-9**	-20	-23	**-7**	-20	-23
R Wing	**-25**	-30	-34	**-**	-30	-34
R Top Web	**2**	0	-6	**-10**	0	-6
R Bot. Web	**-14**	3	-3	**-6**	3	-3
R Bot. Slab	**-12**	3	-1	**-5**	3	-1

5.2.1.2 Support Condition Comparison

Because comparison of frame model support conditions have rarely been studied in the past, the following section compares the load test results with five different boundary conditions, B P-R, B P-P, T P-R, T P-P, and 4P, as shown in Figure 115. Below, measurements and model predictions are compared for select instances. Appendix D contains the complete results from each frame model with the five boundary conditions.

Figure 118 and Figure 119 present an overall support condition comparison using the MAE and MAPE comparators. In these figures, the Seabreeze and Varina-Enon Bridge values are those at the midspan locations only. The diaphragm affected results near the supports were not included. Additionally, because the measured values were very small during Smart Road Bridge LC1 and

LC2 (see Table 39 and Table 40), they were also omitted from Figure 118 and Figure 119 calculations.

The MAE and MAPE comparisons are difficult to make quantitatively between structures, especially the MAE value. When comparing MAE and MAPE across structures one must keep in mind the differences between sensor numbers, locations, and load cases. For instance the Varina-Enon load trucks were limited to the right lane and shoulder, where there were no such restrictions for the Smart Road or Seabreeze Bridges. The MAE and MAPE are comparative values related to the overall error. Therefore lower MAPE and MAPE values indicate a better overall prediction.

The MAE and MAPE show similar trends. As noted in the previous section, Pucher provided more accurate predictions than Homberg in all cases. Additionally, the most common frame configuration, B P-R provides the least accurate prediction for each bridge out of all support permutations. Using the B P-P support conditions does not provide a significant change in accuracy. Interestingly, placing the supports at the top of the webs provides a significant boost on the Seabreeze and Varina-Enon Bridges, but not the Smart Road Bridge. Upon comparing Smart Road B P-P (Pucher MAPE 225% in Figure 119) to T P-R (Pucher MAPE 228% in Figure 119), there was a small decrease in accuracy. Using the T P-P support condition provided a significant increase in accuracy from all models. The 4P support conditions provided the most accurate MAE and MAPE in all cases, although only by a small amount for the Smart Road Bridge. As posited above, the real structure is continuously supported and distributes loads in three dimensions. By supporting the frame at the stiffest locations (the joints), the 4P support condition seems to provide support conditions more like the real structure.

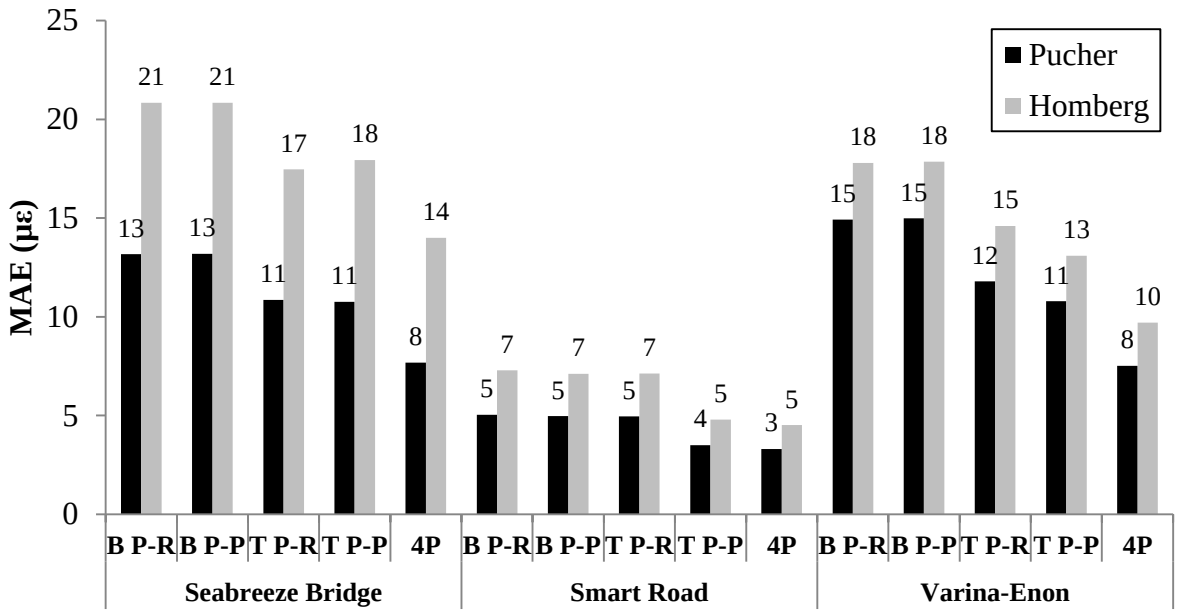

Figure 118 – Transverse Frame Model Support Comparison using MAE

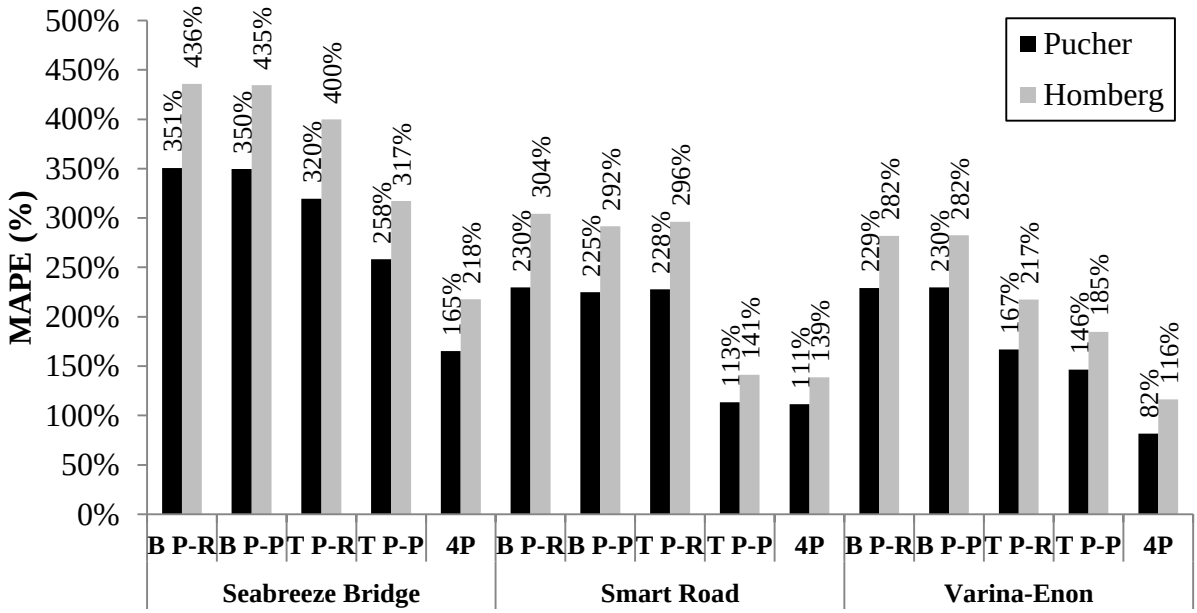

Figure 119 – Transverse Frame Model Support Comparison using MAPE

To further elaborate on the best performing frame model, Table 47 and Table 48 provide example results from the Seabreeze Bridge transverse frame model with 4P support conditions.

Across all support conditions, including 4P, the wing strains remain identical as is expected (e.g., LC1 Section A, Pucher -46 με in Table 36 and Table 47). However, at nearly every other location strains were decresed significantly. For LC1, the left haunch location decreased from by 33% and the middle top slab location changed to the correct sign although predicting higher than measured (compare Table 36 to Table 47). The largest difference came in the bottom slab prediction which was tremendously off with the B P-R supports (compare measured -7 με to Pucher +26 με in Table 36), but with the 4P supports able to predict sense and magnitude (compare measured -7 με to Pucher -6 με in Table 47). This was not the case over all LCs. The bottom slab was predicted the correct bending sense during LC4 with B P-R supports (see Table 38) but using the 4P boundary conditions did not predict bending sense correctly (see Table 48). The top web position did not register a significant change with the different support conditions at LC1, but it did during LC4. Interestingly, nearly all predictions at Seabreeze Section C were improved and, overall, predicted better than Section A.

Table 47 – Seabreeze Bridge LC1 Transverse Frame Comparisons with 4P Supports

Sensor Location	LC1 - Section A (με)			LC1 - Section C (με)		
	Measured	Pucher	Homberg	Measured	Pucher	Homberg
Wing	**-42**	-46	-51	**-19**	-46	-51
Left Top Slab	**-1**	-9	-10	**-5**	-11	-13
Mid Top Slab	**1**	5	6	**-1**	6	6
Top Web	**4**	30	34	**8**	28	32
Bottom Web	**-4**	7	7	**-2**	-4	-4
Left Bot. Slab	**-7**	-6	-6	**-2**	-7	-8

Table 48 – Seabreeze Bridge LC4 Transverse Frame Comparisons with 4P Supports

Sensor Location	LC4 - Section A (με)			LC4 - Section C (με)		
	Measured	Pucher	Homberg	Measured	Pucher	Homberg
Wing	**-6**	0	0	**-6**	0	0
Left Haunch	**-19**	-21	-33	**-17**	-20	-31
Middle Top Slab	**53**	74	118	**33**	74	117
Top Right Web	**-7**	-16	-25	**-16**	-14	-23
Mid Right Web	**-3**	-4	-6	**0**	1	2
Right Bottom Slab	**-3**	2	4	**2**	3	5

The Smart Road and Varina-Enon transverse frame models experience similar changes when using the 4P supports. For example, the middle top slab prediction decreases significantly during Smart Road LC5, but the haunch measurements remain similar. However, several locations are not much different or predicted worse. The web locations are significantly worse predicted during LC5 (e.g., compare measured -8 με to -10 με in B P-R Table 43 and -3 με in 4P Table 49). For the Smart Road Bridge, the bottom slab is predicted with more correct sense when using 4P (see Table 49), and the Varina-Enon is slightly improved, but still not conservative.

Table 49 – Smart Road Bridge LC5 Transverse Frame Comparisons with 4P Supports

Sensor Location	LC5 - Section A (με)			LC5 - Section B (με)		
	Measured	Pucher	Homberg	Measured	Pucher	Homberg
Wing	**3**	0	0	**1**	0	0
Left Haunch	**-5**	-8	-12	**-7**	-7	-12
Middle Top Slab	**21**	43	49	**20**	43	49
Right Haunch	**-3**	-7	-10	**-3**	-7	-10
Top Right Web	**-8**	-3	-3	**-4**	-3	-3
Mid Right Web	**-7**	-2	-2	**-3**	-2	-2
Right Bottom Slab	**-2**	0	0	**2**	1	0
Left Bottom Slab	**-2**	1	1	**1**	1	1
Mid Left Web	**-6**	-2	-3	**-2**	-2	-4
Top Left Web	**-4**	-8	-11	**-**	-	-

Table 50 – Varina-Enon Bridge LC6 Transverse Frame Comparisons with 4P Supports

Sensor Location	LC6 - Section D (με)			LC6 - Section C (με)		
	Measured	Pucher	Homberg	Measured	Pucher	Homberg
Top Slab	**23**	18	23	**5**	18	23
R Top Slab	**10**	28	40	**-**	28	40
R Haunch	**-9**	-18	-25	**-7**	-18	-25
R Wing	**-25**	-30	-34	**-**	-30	-34
R Top Web	**2**	2	-4	**-10**	2	-4
R Bot Web	**-14**	0	0	**-6**	0	0
R Bot Slab	**-12**	-1	1	**-5**	-1	1

Overall, the 4P boundary condition stiffens the structure and provides more accurate predictions. Note that the improved prediction does not eliminate the shortcomings of the two dimensional transverse frame model. The bottom slab and bottom web positions are still typically not

predicted well. However, when compared to the most common, B P-R model, the bottom slab was better predicted when using the 4P boundary condition. The above indicates the 4P boundary condition more accurately reflects real transverse bending support.

5.2.1.3 Barrier Springs

The barrier rail runs longitudinally on the edge of the wing and adds longitudinal and transverse stiffness to the box girder wing. Thoman (1985) and Kuhn (2009) noted the stiffening effect of the barrier rails, although neither discussed a way to apply it to a two dimensional frame model. Designers have tried placing springs at the barrier rail location on the frame models (see Figure 112) to take advantage of this stiffening effect, often without reliable test data to back up the technique. The following outlines a method used to rationally convert the longitudinal barrier rail stiffness to a one dimensional spring stiffness applied to the two dimensional transverse frame model at the barrier rail locations.

To convert the longitudinal barrier rail stiffness to one dimensional vertical spring stiffness, the barrier rail is assumed to have a deflected shape similar to a simply supported beam. This is likely not the case, as discussed below, but allows simple calculation and does not complicate the method more than is necessary. Assuming an applied load at the center of a simply supported structure, the stiffness of the system is calculated by dividing the applied load by the resulting deflection as shown in Figure 120. This spring stiffness can be applied to the model at the barrier rail locations.

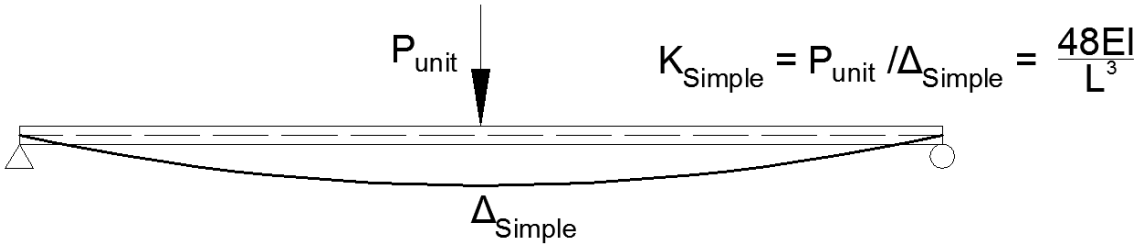

Figure 120 – Simply Supported Beam Point Load Stiffness

The uncertainty of this approach lies in selecting the appropriate length, herein called the effective barrier length, to approximate the barrier rail stiffness. Three rational ways to estimate the length are investigated to determine this spring stiffness for each structure. The first, and

simplest, method attempted is to use the entire span length (L_{SPAN}) in the simply supported beam stiffness equation in Figure 120 to calculate a spring stiffness, K_{SPAN}. This is obviously incorrect, but will guarantee a conservative estimation of the barrier rail stiffness and serve as a starting point.

The second method involves the use of a fixed-free influence surface scaled to the appropriate wing length for the structure (see Figure 121). Upon inspection of this surface, a point load will produce a negligible (1% of maximum) fixed end moment at a certain distance away from the point of interest. This is approximated from Figure 121 to be 18.5 units in each direction or 37 units centered on the point of interest, where 1 unit equals the wing length divided by five. Equation 16 estimates the effective barrier length using the methodology:

$$L_{IS} = L_{Cantilever}\frac{37}{5} \qquad \textit{Equation 16}$$

Where:

- L_{IS} is the estimated effective barrier length between 1% of the maximum response from a Pucher influence surface
- $L_{Cantilever}$ is the length of the box girder cantilever wing

For the Seabreeze, Smart Road and Varina-Enon, Equation 16 produces effective barrier lengths of 86 ft, 62 ft and 96 ft, respectively. To check the validity of this estimation, inspection of the wing transverse bending influence lines in Figure 67, Figure 78, Figure 92 yields 150 ft, 80 ft and 120 ft, respectively. The length affected by the truck in the figures, subtracted by the truck lengths, is closest to those produced by Equation 16.

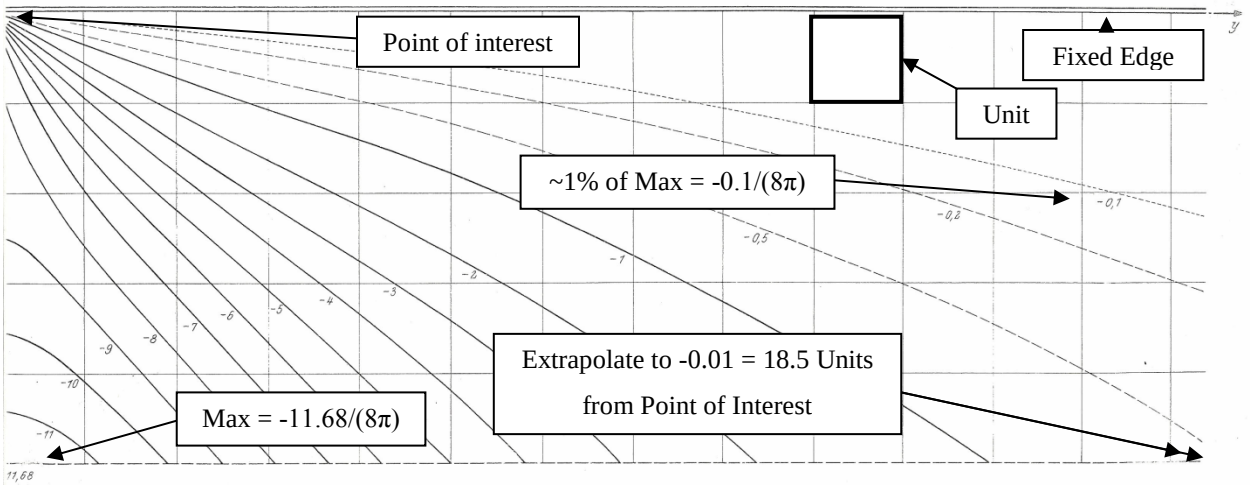

Figure 121 – Cantilever Plate Influence Surface Effective Length (Adapted from Pucher 1977)

The third method assumes the barrier rail acts similar to a beam on elastic foundation (BEF), with the wing transverse stiffness making up the foundation and the barrier rail stiffness as the beam sitting on that foundation. The BEF analogy more accurately models the deflected shape than the simply supported assumption above. However, decoupling the stiffness imparted by the beam from the elastic foundation for an infinitely long BEF is difficult. As shown in Figure 122, after applying load, at some distance on either side of the point load the beam returns to zero deflection. For the purposes of this method, the shape between these points is approximated using a simply supported beam as discussed above.

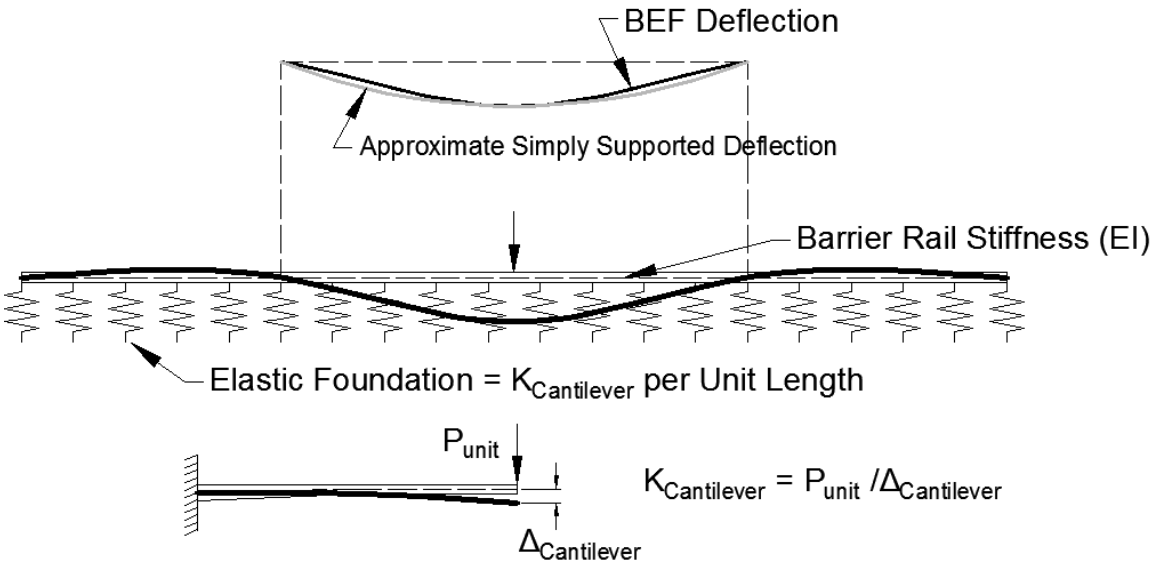

Figure 122 – BEF and Simply Supported Deflection Analogy and Definitions

Hartog (1952) approximates the length between the nearest points of zero deflection from the load as:

$$L_{BEF} = \frac{4.8}{\sqrt[4]{\frac{K_{Cantilever}}{4EI}}} \qquad \textit{Equation 17}$$

Where:

- L_{BEF} is the effective barrier length between points of zero deflection used to approximate simply supported barrier rail length
- $K_{Cantilever}$ is the cantilever stiffness calculated per Figure 122 in force per unit length per unit length
- E is the elastic modulus of the barrier rail
- I is the moment of inertia of the barrier rail

Table 51 presents the three different simply supported lengths used to calculate the spring stiffness for each transverse frame. For each structure, the K_{SPAN} stiffness is significantly lower than the others, but the L_{IS} and L_{BEF} have similar effective barrier lengths and, therefore, stiffness values. The Smart Road Bridge stiffness is much higher for the K_{IS} and K_{BEF} than K_{SPAN}, when compared to the others. This is because the Smart Road Bridge has a much longer span, but shorter wings. Intuitively this seems correct, as the wing stiffness would affect the barrier rail more than longitudinal span length.

Table 51 – Barrier Rail Spring Stiffness

Bridge	L_{SPAN} (in.)	K_{SPAN} (kip/in)	L_{IS} (in.)	K_{IS} (kip/in)	L_{BEF} (in.)	K_{BEF} (kip/in)
Seabreeze	2,800	0.28	1,036	5.59	856	9.92
Smart Road	5,640	0.03	740	15.35	654	22.19
Varina-Enon	1,800	1.07	1,147	4.12	1,058	5.26

Table 52 through Table 54 compare the measured and predicted wing strains for the B P-R and 4P support conditions with the estimated wing spring stiffness included in the models. The complete measured and predicted strains for each spring stiffness using B P-R and 4P boundary

conditions are presented in Appendix D. For each bridge and boundary condition there is a clear trend showing increasing the spring stiffness on the cantilever decreases the predicted strain.

As shown in Table 52, with the B P-R, when the spring stiffness is set to K_{BEF}, the prediction is nearly 20% unconservative (compare -42 με to Pucher -34 με in Table 52). Interestingly, when using the 4P boundary conditions, the prediction does not change significantly with increasing spring stiffness. All methods of analysis including the barrier rail are conservative except K_{IS} and K_{BEF} for the B P-R model.

Table 52 – Seabreeze LC1 Section A Wing Strain Predictions

Frame Supports	Wing Spring Stiffness	Measured Wing Strain (με)	Pucher		Homberg	
			Predicted Wing Strain (με)	%Error	Predicted Wing Strain (με)	%Error
B P-R	Zero	**-42**	-46	-10%	-51	-18%
	K_{SPAN}		-45	-7%	-50	-19%
	K_{IS}		-37	13%	-41	2%
	K_{BEF}		-34	18%	-38	9%
4P	Zero		-46	-10%	-51	-18%
	K_{SPAN}		-45	-8%	-51	-21%
	K_{IS}		-42	0%	-47	-12%
	K_{BEF}		-41	3%	-46	-9%

The Smart Road and Varina-Enon Bridges do not have unconservative predictions like the Seabreeze Bridge, when using K_{IS} and K_{BEF}. When using the Pucher loads, the wing strain is predicted to within 15% and 2 με for the Smart Road Bridge and 5% and 1 με for the Varina-Enon Bridge. There is little difference between the K_{IS} and K_{BEF} spring stiffness and the resulting predictions. This is because the methods are relatively similar in the sense that they are using the same simply supported stiffness and an effective barrier length rationally based on actual system behavior, rather than span length like K_{SPAN}. All methods of analysis where barrier rail springs are included are conservative except K_{IS} and K_{BEF} for the B P-R Seabreeze Bridge model.

Overall, the K_{SPAN} stiffness does not provide enough change in wing strain to justify its use. For the Seabreeze and Smart Road Bridges, which have very long spans, the K_{SPAN} stiffness provides

only a 1 με improvement (compare Pucher predicted zero spring -46 to K_{SPAN} -45 in Table 52) or less on the Smart Road Bridge (see Table 53). For the Varina-Enon Bridge, there was significant change using the K_{SPAN} stiffness, where the B P-R, Pucher prediction dropped 5 με. The reason for the K_{SPAN} differences between wing predictions has to do with the span lengths used in the calculations (see L_{SPAN} in Table 47). Clearly, the results indicate the L_{SPAN} length and K_{SPAN} stiffness do not describe the actual barrier rail stiffness and does not provide significant stiffness on longer span structures.

Table 53 – Smart Road Bridge LC1 Section A Wing Strain Predictions

Frame Supports	Wing Spring Stiffness	Measured Wing Strain (με)	Pucher		Homberg	
			Predicted Wing Strain (με)	%Error	Predicted Wing Strain (με)	%Error
B P-R	Zero	**9**	15	-61%	18	-93%
	K_{SPAN}		15	-61%	18	-92%
	K_{IS}		11	-23%	14	-47%
	K_{BEF}		11	-15%	13	-38%
4P	Zero		15	-61%	18	-93%
	K_{SPAN}		15	-61%	18	-93%
	K_{IS}		13	-43%	16	-70%
	K_{BEF}		11	-15%	13	-38%

Table 54 – Varina-Enon Bridge LC4 Section D Wing Strain Predictions

Frame Supports	Wing Spring Stiffness	Measured	Pucher		Homberg	
			Predicted Wing Strain (με)	%Error	Predicted Wing Strain (με)	%Error
B P-R	Zero	**-19**	-30	-59%	-34	-81%
	K_{SPAN}		-25	-32%	-29	-51%
	K_{IS}		-21	-10%	-24	-25%
	K_{BEF}		-20	-5%	-23	-20%
4P	Zero		-29	-52%	-33	-73%
	K_{SPAN}		-27	-41%	-30	-61%
	K_{IS}		-27	-41%	-30	-61%
	K_{BEF}		-26	-38%	-30	-57%

Overall, combining the 4P boundary conditions and the barrier rail springs does not provide changes in wing strain as significant as with the B P-R conditions. The reason for this is unclear, however, it indicates that the 4P boundary conditions may not describe the real behavior as correctly as the analysis results in Section 5.2.1.2 indicate.

Figure 123 through Figure 125 show the change in overall accuracy, as predicted by MAPE, for each bridge with the B P-R and the 4P boundary conditions. Interestingly, when comparing the predictions from the B P-R with and without the barrier springs there are significant gains in overall accuracy. This is caused by the overall increase in stiffness over the cross-section. However, when using the 4P boundary conditions, little overall accuracy is gained overall by applying a barrier rail spring.

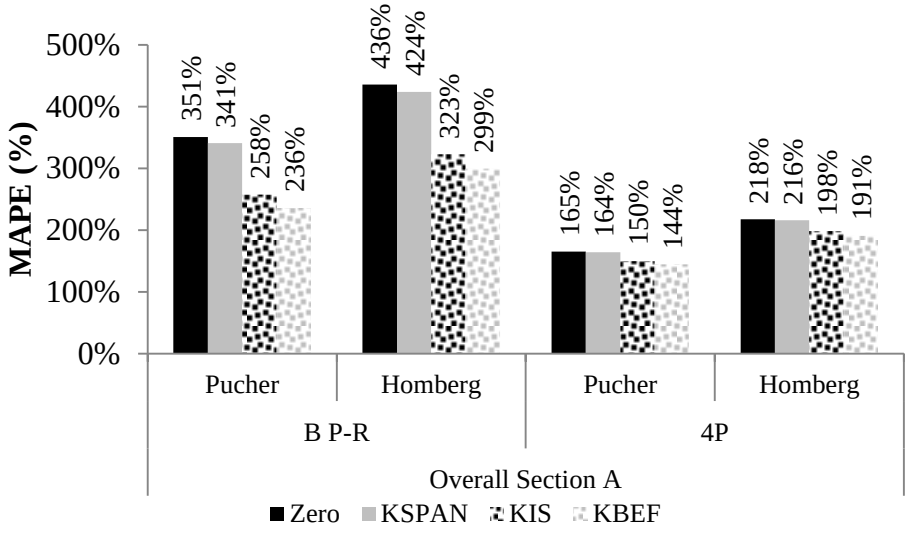

Figure 123 – Seabreeze Bridge Barrier Spring Overall Comparison at Section A

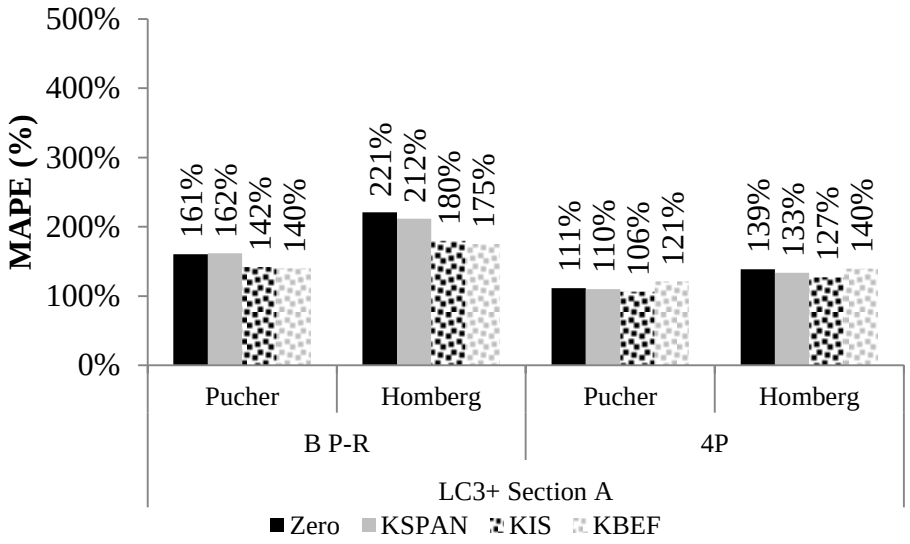

Figure 124 – Smart Road Bridge Barrier Spring Overall Comparison at Section A (LC3-LC5)

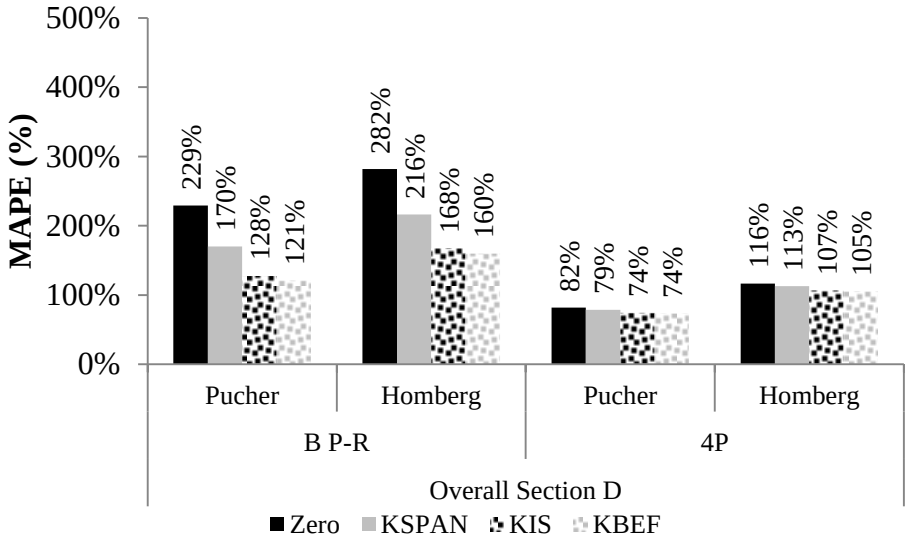

Figure 125 – Varina-Enon Bridge Barrier Spring Overall Comparison at Section D (LC4-LC6)

Table 52 indicates the Seabreeze wing strain is unconservative with K_{BEF}, but Figure 123 indicates better MAPE. To better understand how the overall MAPE accuracy increased, Table 55 presents Seabreeze LC1, Section A measurements and predictions using B P-R and K_{BEF} spring stiffness. For instance, the left haunch predictions drop significantly (compare Section A Pucher -27 με in Table 36 and Pucher -16 με in Table 55) as do web and bottom slab predictions.

Furthermore, by applying the barrier stiffness to the wing, this allows the frame model to predict bending in the wing when no load is on the wing, as is seen in the measurements (compare LC4 measured wing -6 με to Pucher and Homberg -6 με and -9 με in Table 56). In Table 38 only rigid body movement was predicted during Seabreeze LC4. Similarly, other measurement locations experience changes and produce predictions that are more accurate.

Table 55 – Seabreeze Bridge, LC1, Section A Transverse Measurements and Predictions using B P-R and K_{BEF}

Sensor Location	LC1 - Section A (με)		
	Measured	Pucher	Homberg
Wing	**-42**	-34	-38
Left Top Slab	**-1**	-16	-17
Mid Top Slab	**1**	-2	-3
Top Web	**4**	26	29
Bottom Web	**-4**	11	12
Left Bot. Slab	**-7**	11	12

Table 56 – Seabreeze Bridge, LC4, Section A Transverse Measurements and Predictions using B P-R and K_{BEF}

Sensor Location	LC4 - Section A (με)		
	Measured	Pucher	Homberg
Wing	**-6**	-6	-9
Left Top Slab	**-19**	-18	-28
Mid Top Slab	**53**	81	129
Top Web	**-7**	-21	-33
Bottom Web	**-3**	-7	-10
Left Bot. Slab	**-3**	-1	-2

Three simple and rational methods to convert the barrier rail longitudinal stiffness to an equivalent spring stiffness were attempted. The results indicate that the BEF based method produces the most accurate results, but can also provide unconservative wing results by up to 20% (see Table 52). Using the simplest K_{SPAN} method does not create enough stiffness to make changes and because it is tied to the span length rather than actual barrier rail deflection, which does not model the actual barrier rail deformation. Adding the barrier rail stiffness with 4P boundary conditions does not increase accuracy significantly, when compared to the B P-R.

5.2.1.4 Transverse Frame Model Summary and Discussion

Transverse frame analysis is a common simplified analysis method to estimate stresses in the transverse direction caused by localized tire loads. The preceding sections compare the two dimensional simplified frame model using five boundary conditions and three barrier rail spring stiffness predictions to measured tests results from the Seabreeze, Smart Road and Varina-Enon bridges.

The load scaling procedure used Pucher or Homberg influence surface approaches. In all cases, Pucher influence surfaces result in more accurate predictions because the load distribution in variable thickness plates concentrate moment at the fixed ends when compared to flat plates. Because the plate fixed end moments are used on the frame models, the resulting frame model predictions will always be smaller and therefore more accurate because the frame model cannot actually predict three dimensional behavior.

Several boundary conditions were investigated. The boundary condition that most accurately predicted measured strains was the 4P supports. The 4P supports were intended to simulate a more continuous support condition like the real structure. This model produced MAPE between 82% (Pucher, Varina-Enon) and 218% (Homberg, Seabreeze). The most widely used frame model boundary conditions used pin and roller supports at the top and bottom flanges. This model produced MAPE between 229% (Pucher, Varina-Enon Bridge) and 436% (Homberg, Seabreeze Bridge). The pin and roller supported model often produced incorrect bending sense at the bottom web and flange locations. Not only were the 4P supports more accurate, but reduced instances of incorrect bending sense prediction.

Designers have reported taking advantage of the barrier rail stiffness. Three simplified methods for estimating barrier rail stiffness were attempted. For the Seabreeze Bridge, the influence surface based and BEF based spring stiffness were unconservative, however, these methods produced accurate results for the other structures. When combined with the B P-R boundary conditions, the spring stiffness improved the overall MAPE prediction, but was negligible overall when using the 4P supports. The barrier springs are not recommended because they could produce unconservative results for the wing location.

The frame model produces generally conservative analysis predictions with all boundary conditions. All boundary conditions produce errors, including inaccurate bending sense. However, the 4P boundary condition gives the most accurate MAPE and reduces the occurrence of incorrect bending sense predictions.

5.3 Three Dimensional Shell Analysis

Transverse analysis using a three dimensional approach is relatively new to segmental concrete bridge design. Additionally, some state departments of transportation still recommend frame analysis for design and rating. The purpose of the modeling discussed in this section is to lay out a clear three dimensional analysis procedure, including meshing techniques and element type. The following section outlines the development of a standardized transverse analysis box girder three dimensional shell modeling methodology, validated based on three field tests of significantly different bridges. As outlined in the literature review, there has been very little research regarding transverse bending, specifically with comprehensive load tests on contemporary and realistic box girder cross sections.

5.3.1 Constructing the Model

Designers need an easy to construct model with reasonable computational time. For this reason, shell elements were selected rather than solid elements to model the three dimensional cross section. Solid elements have several nodes, require complex meshing and considerable computational time when compared to shells. Shell elements are often easier for post-processing as many design programs integrate the stresses automatically and can output design forces. Beam elements were selected to model the barrier rail due to ease of use and computational economy.

The shell models were constructed using SAP2000 four node, variable thickness, shell elements with six nodal degrees of freedom (Imbrahimbegovic and Wilson 1991). The shell elements in SAP2000 were not verified using another finite element program, but were assumed to represent a basic element that would be available in many finite element packages. The transverse shell connectivity is shown in Figure 126, where the shell elements were connected at mid thickness

of the wings webs and slabs. Barrier rails were modeled using a beam element running into the page at the barrier rail centroid. The beam element was connected to a node located on the wing directly below the barrier element using a body constraint. This method is similar to the beam-offset model outlined graphically in Figure 96 and Figure 97. Barrier rail gross cross sectional properties and nominal elastic modulus were used for the beam elements.

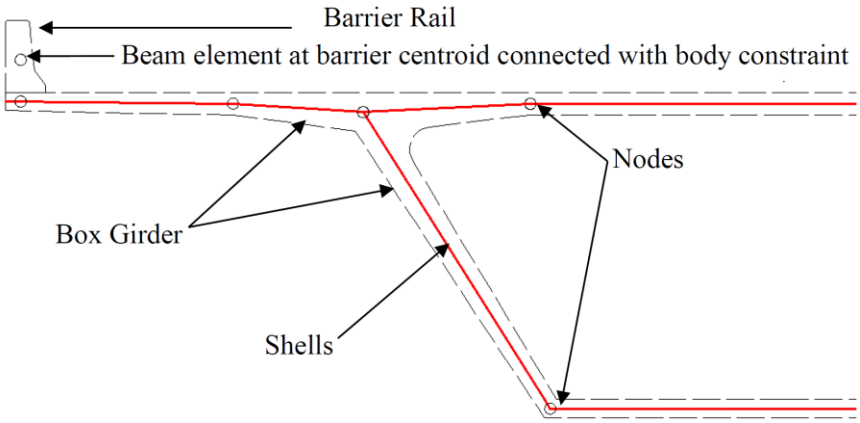

Figure 126 – Half Cross Section Shell Transverse Connectivity

Shell elements were used to approximate the variable depth box girder as shown in Figure 127. Diaphragms were placed in the model by connecting a shell element to each node to fill the interior of the box girder. Diaphragms were sized based on gross thickness and assigned the same elastic modulus as the superstructure.

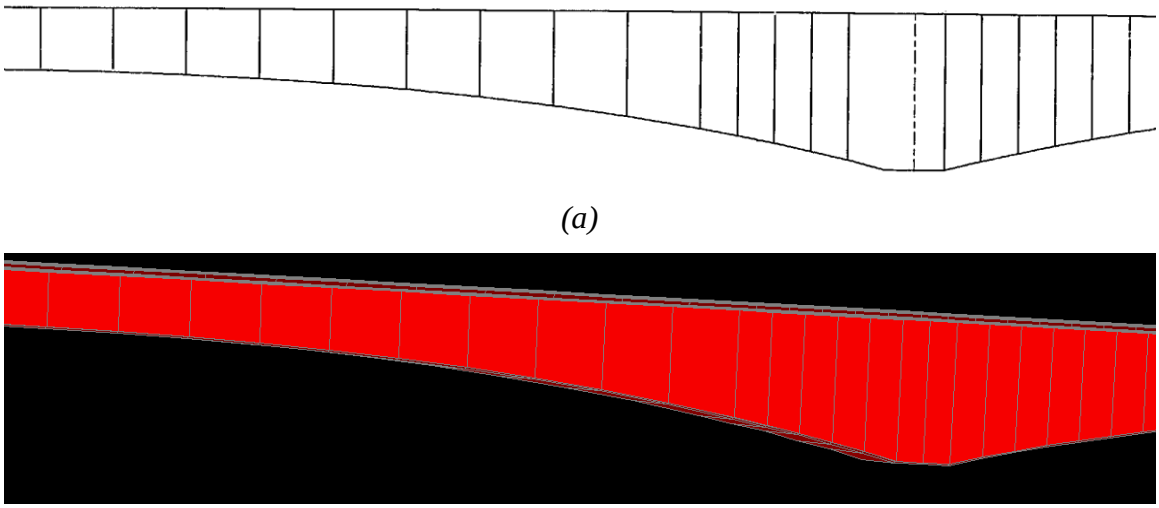

(a)

(b)

Figure 127 –Plan Superstructure Segment Layout (a) and Example Shell Model Segment Layout (b)

Determining the proper mesh size, a priori, is important to accurately modeling transverse behavior without several iterations. By using patch loading, rather than point loads, the stresses directly under the load points will converge as the mesh size decreases. Each structure was modeled and meshed with shell elements of approximately square (dimensions 2 in, 5 in., 10., and 20 in.). The mesh sizes were selected because they are multiples of the AASHTO LRFD 10 in. × 20 in. tire contact area (AASHTO LRFD Section 3.6.1.2.5), which simplified load application to the mesh. Distribution of the tire contact area from the face to the center of the shell was ignored. This configuration allowed for relatively easy patch load placement closely approximated the AASHTO LRFD specified contact area.

Figure 128 presents the results of the mesh fineness investigation for each structure. During this investigation, a contact pressure equivalent to a 15 kip tire load was placed at the transverse center of the top flange, and at midspan of each structure. The transverse stress directly under the load, on the bottom of the top flange, is shown in Figure 128 for the four approximately square mesh sizes. Note that meshing was applied to the entire structure, including both flanges and webs, not just the top flange. In Figure 128, the stress converges quickly at 10 in. and only experiences a change as the applied surface stress decreased for the 20 in. loading. Note that the 20 in. × 20 in. mesh, is twice as large as the AASHTO tire load, which reduced the stress

intensity. Based on these results, a 10 in. × 10 in. mesh fineness was selected for the transverse shell models.

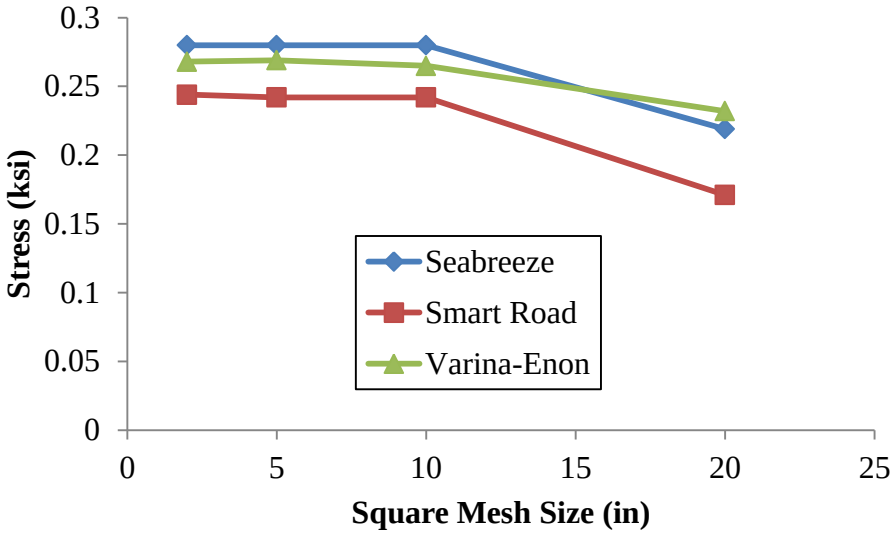

Figure 128 – Local Top Flange Transverse Shell Model Stress versus Mesh Size

Meshing an entire bridge structure with 10 in. square shell elements is inefficient and requires considerable computation time. Because the transverse model is only concerned with determining the stresses localized at a single cross section, the fine mesh is unnecessary away from the load. In this situation, a transition mesh can be used between coase and fine mesh areas. Another option is the use of an edge constraint at the transition between the fine and coarse mesh. In this case, to provide standardized and expedited meshing for the designer an edge constraint was used between fine and coarse meshed areas. An example of the edge constraint is shown in Figure 129. Note that the entire cross section is meshed and constrained as described, not only the top flange.

The edge constraint, also known as a line constraint, identifies and connects all nodes along an edge of a shell to the adjacent corner joints. The displacements at the intermediate joints along the edge are interpolated from the displacements of the corner joints. There is a slight discontinuity along the edge, however, it is small with respect to other deformations. (CSI 2010)

This edge constraint allows mis-matched meshes to perform as if connected properly at the nodes. By using this constraint, a transition mesh is not needed, which may require distorted elements and additional effort. Near this constraint, just like with any transition, the effect of the coarser elements propagates into the finer meshed region. This effect is no longer present a distance equal to one of the larger element sizes from the transition. (CSI 2010)

An approximately 50 in. square, element size was arbitrarily selected for the coarse meshed region. This coarse mesh size requires the edge constraint boundary to be, at least 50 inches away, i.e. the maximum mesh length, from the applied loads. This was the rule abided by the shell models in the remainder of this report.

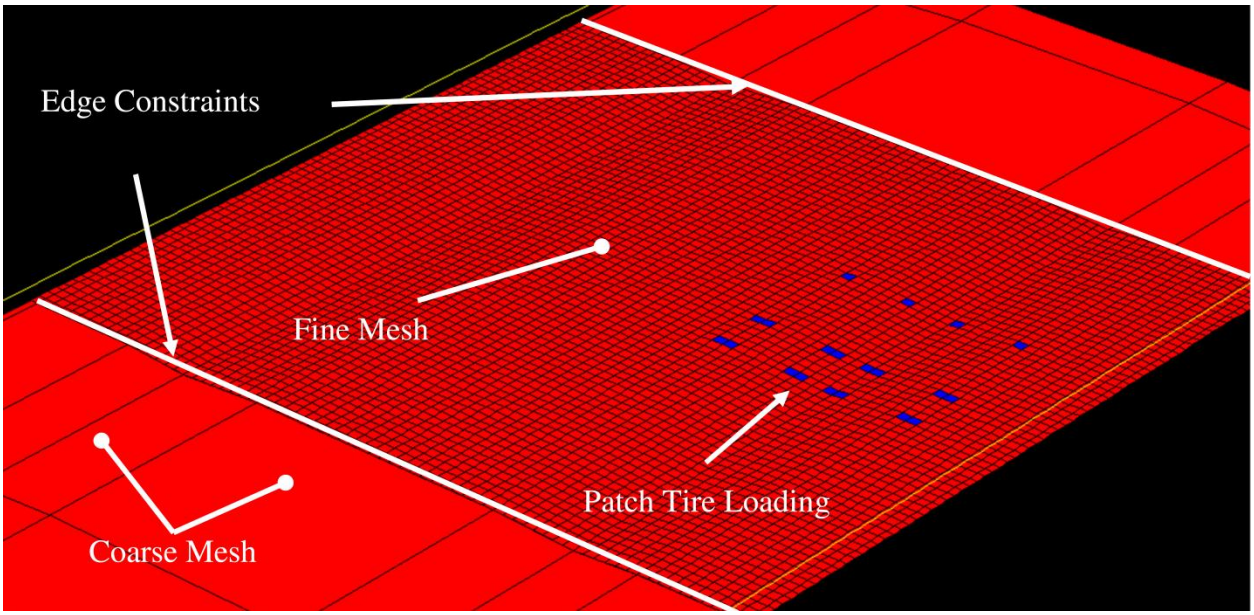

Figure 129 – Edge Constraint Description

Modeling multiple spans of a bridge at the recommended mesh sizes is tedious and may be unnecessary. Transverse response is relatively insensitive to longitudinal geometry. To investigate this effect, multiple spans were modeled for each of the three subject bridges. Loads were applied and top flange transverse stresses were tracked using the same loading scenario as used to generate data for Figure 128. The analyses were performed for each bridge with numbers of spans modeled (one to five). Figure 130 presents the results of this study and shows the transverse stresses at the bottom of the top flange at midspan are insensitive to the number of

spans modeled. For this reason each bridge is subsequently modeled using two spans so stresses near the Pier diaphragm could be modeled as accurately as possible. For design it would be sufficient to model a single span for a constant depth bridge (e.g., Varina-Enon) or two spans for a variable depth bridge (e.g., Seabreeze, Smart Road) . Modeling multiple spans for a variable depth bridge allows the designer to determine design loads for the changing geometry near the piers.

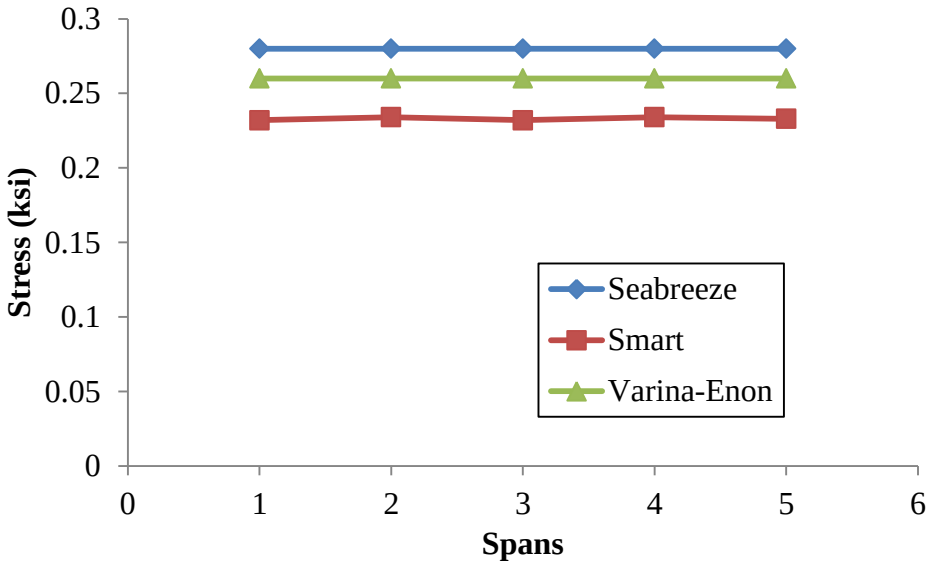

Figure 130 – Transverse Stress versus Number of Spans Modeled

Boundary conditions at the supports greatly affect longitudinal stresses. To investigate boundary condition effect on transverse stresses, the two span models used to generate data for Figure 130 were modified. Idealized Roller-Pin-Roller (RPR), Pin-Pin-Pin (PPP) and Fixed-Fixed-Fixed (FFF) supports were placed at the bottom of the webs, at the piers of each two span model. Transverse stresses directly under the 15 kip applied patch load, with a 10 in. × 10 in. mesh are plotted, in Figure 131. Similar to the previous investigation (Figure 130), stresses remained essentially constant throughout the range of support conditions. Because the support condition has no discernible effect, RPR supports were selected for all transverse shell models in the following investigation.

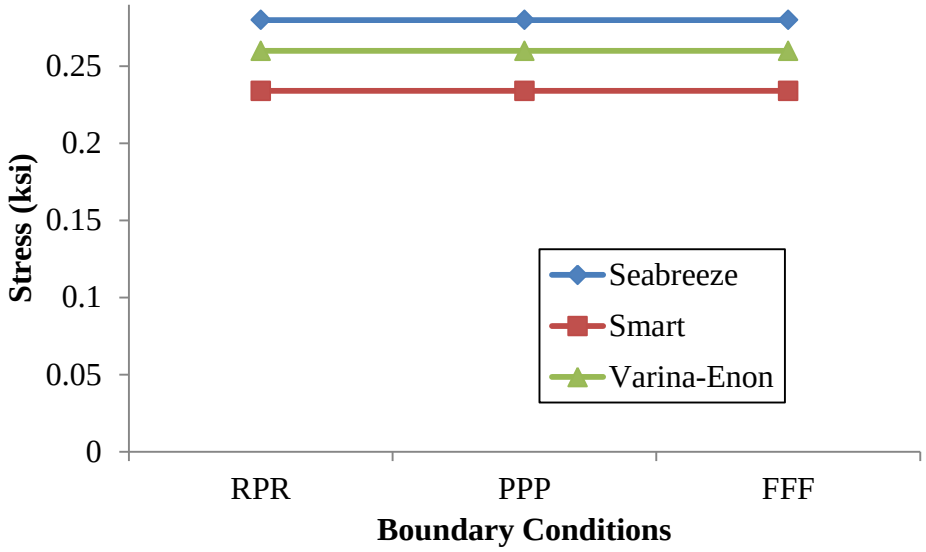

Figure 131 – Transverse Stress for Various Boundary Conditions

5.3.2 Transverse Shell Model Results without Barrier Rail

Table 57 through Table 67 present the shell model results for the transverse strain measurements from the Seabreeze, Smart Road, and Varina-Enon Bridges. These models do not include the barrier rails. The shell model over-predicts response at the wing location for the Seabreeze Bridge by 17% at Section A (compare -42 με to -49 με in Table 57), but over predicts the top web strain by 550% (compare +4 με to +26 με in Table 57). The strain in the Seabreeze Bridge top web is poorly predicted, however, upon inspection of the results from the other load cases and the frame models, top web strains are always predicted very low. There are other instances of poor top web predictions in the other bridges (e.g. Varina-Enon compare +2 με to -14 με at Section D in Table 67), but overall top web predictions are not poor in the other structures (e.g. compare -8 measure to -6 predicted at Section A in Table 64). The gross difference across the Seabreeze top web measurements may indicate that the sensor position was too close to the top of the web and localized effects are causing differences in measured strains. The same difficulty is not found in the bottom web measurements, which is often predicted with much greater accuracy for the all bridges investigated. This is in contrast to the results from the frame models, which had significant differences when predicting web and bottom slab strains. The most severe differences is the top slab prediction at Seabreeze LC3, Section A, where the strains are under-predicted by nearly 30% (compare +38 με to +27 με in Table 58).

Table 57 – Seabreeze Bridge LC1 Transverse Shell Model Comparisons, no Barriers

Sensor Location	LC1 - Section A (με)		LC1 - Section C (με)	
	Measured	Thin Shells	Measured	Thin Shells
Wing	-42	-49	-19	-47
Left Top Slab	-1	-5	-5	-14
Mid Top Slab	1	-1	-1	-1
Top Web	4	26	8	27
Bottom Web	-4	-5	-2	-6
Left Bot. Slab	-7	-15	-2	-9

Table 58 – Seabreeze Bridge LC3 Transverse Shell Model Comparisons, no Barriers

Sensor Location	LC3 - Section A (με)		LC3 - Section C (με)	
	Measured	Thin Shells	Measured	Thin Shells
Wing	-4	-4	-3	-4
Left Haunch	-19	-25	-14	-27
Middle Top Slab	38	27	27	24
Top Right Web	-5	-17	-11	-18
Mid Right Web	-2	-3	1	2
Left Bot. Slab	-2	8	1	5

Table 59– Seabreeze Bridge LC4 Transverse Shell Model Comparisons, no Barriers

Sensor Location	LC4 - Section A (με)		LC4 - Section C (με)	
	Measured	Thin Shells	Measured	Thin Shells
Wing	-6	-5	-6	-6
Left Haunch	-19	-17	-17	-23
Middle Top Slab	53	49	33	45
Top Right Web	-7	-19	-16	-24
Mid Right Web	-3	-5	0	1
Left Bot. Slab	-3	-1	2	5

The Smart Road Bridge shell model seems to accurately predict strains for the single truck load cases (see Table 60 and Table 61). However, because the measured strains are so low, small

changes (±1 με) can produce relatively large percent errors. Similar conclusions can be made for LC3, presented in Table 62, which was a two truck load case, but still had very small measured strains. The frame model, with load cases where there are trucks on the top slab (see Table 63 and Table 64) do not accurately predict the strains in the haunches, particularly under the load. At these locations, there are large moment gradients where the supports and wheel loads are near the sensors. Because of this, small differences in truck or sensor location from those specified could cause relatively large differences in measurements and predictions.

Table 60 – Smart Road Bridge LC1 Transverse Shell Model Comparisons, no Barriers

Sensor Location	LC1 - Section A (με)		LC1 - Section B (με)	
	Measured	Thin Shells	Measured	Thin Shells
Wing	9	16	7	16
Left Haunch	1	1	-3	-1
Middle Top Slab	1	-1	-1	-1
Right Haunch	0	-2	0	0
Top Right Web	-1	0	0	0
Mid Right Web	-1	0	0	1
Right Bottom Slab	1	3	1	4
Left Bottom Slab	-4	-6	-2	-4
Mid Left Web	2	3	0	2
Top Left Web	2	4	-	-

Table 61 – Smart Road Bridge LC2 Transverse Shell Model Comparisons, no Barriers

Sensor Location	LC2 - Section A (με)		LC2 - Section B (με)	
	Measured	Thin Shells	Measured	Thin Shells
Wing	1	0	-1	0
Left Haunch	-1	-2	-1	0
Middle Top Slab	1	-1	0	-1
Right Haunch	1	0	1	-1
Top Right Web	2	4	1	5
Mid Right Web	0	2	-1	2
Right Bottom Slab	-3	-5	-2	-4
Left Bottom Slab	1	4	1	4
Mid Left Web	-1	0	0	1
Top Left Web	-1	0	-	-

Table 62 – Smart Road Bridge LC3 Transverse Shell Model Comparisons, no Barriers

Sensor Location	LC3 - Section A (με)		LC3 - Section B (με)	
	Measured	Thin Shells	Measured	Thin Shells
Wing	11	16	8	16
Left Haunch	1	-1	-3	-1
Middle Top Slab	2	-2	-1	-2
Right Haunch	1	-1	1	-2
Top Right Web	2	4	1	5
Mid Right Web	-1	3	1	3
Right Bottom Slab	-3	-1	-1	0
Left Bottom Slab	-3	-1	-1	0
Mid Left Web	1	3	0	3
Top Left Web	2	4	-	-

Table 63 – Smart Road Bridge LC4 Transverse Shell Model Comparisons, no Barriers

Sensor Location	LC4 - Section A (με)		LC4 - Section B (με)	
	Measured	Thin Shells	Measured	Thin Shells
Wing	11	16	7	16
Left Haunch	3	7	-6	-8
Middle Top Slab	17	9	14	11
Right Haunch	-4	-12	-4	-7
Top Right Web	-4	-6	-2	-7
Mid Right Web	-4	-4	-1	-2
Right Bottom Slab	-2	6	2	8
Left Bottom Slab	-5	-4	-2	-1
Mid Left Web	-3	-2	-1	-2
Top Left Web	-1	-2	-	-

Table 64 – Smart Road Bridge LC5 Transverse Shell Model Comparisons, no Barriers

Sensor Location	LC5 - Section A (με)		LC5 - Section B (με)	
	Measured	Thin Shells	Measured	Thin Shells
Wing	3	0	1	0
Left Haunch	-5	-2	-7	-13
Middle Top Slab	21	27	20	31
Right Haunch	-3	-10	-3	-9
Top Right Web	-8	-8	-4	-9
Mid Right Web	-7	-5	-3	-4
Right Bottom Slab	-2	4	2	6
Left Bottom Slab	-2	1	1	3
Mid Left Web	-6	-6	-2	-4
Top Left Web	-4	-8	-	-

The Varina-Enon Bridge shell model strains are significantly closer to the measured strains when compared to the other structures. The slender components of the Varina-Enon structure produce larger strains, especially at the bottom web and slab locations is a contributing factor to the better prediction. The top web strain measurements were estimated somewhat accurately at Section D (compare +9 με to +13 με in Table 65 and +13 με to +16 με in Table 66). However, near Section

C, strains were not well predicted, most commonly in the web (e.g. compare +23 με measured to +12 με predicted in Table 66 and +2 με measured to -14 με predicted at Section D in Table 67).

Seabreeze Section C and Varina-Enon Section C are very near the large pier diaphragms. The test results showed significant differences in the transverse bending behavior near the piers. The results at these two sections indicate the shell model can predict some aspects of this behavior. For instance, the top slab response reduction was predicted for the Varina-Enon and Seabreeze Bridges when comparing the near pier to the midspan measurements (e.g., compare Varina-Enon Section D measured +23 με to predicted +19 near midspan and Section C measured +5 to predicted +11 near pier in Table 67). Conversely, the top web measurements were often amplified near the pier, but the model rarely indicated an increase (e.g., compare Seabreeze, LC3, Section A measured -5 to predicted -17 and Section C measured -11 to predicted -18)

Typically, designers do not account for the differences near the pier and only use calculations at the midspan sections. Using the midspan predictions (Section D for the Varina-Enon Bridge) provides an adequate and often more conservative prediction of transverse bending response than trying to model the complex pier behavior using shell elements.

Table 65 – Varina-Enon Bridge LC4 Transverse Shell Model Comparisons, no Barriers

Sensor Location	LC4 - Section D (με)		LC4 - Section C (με)	
	Measured	Thin Shells	Measured	Thin Shells
Top Slab	-6	-1	-2	0
R Top Slab	-3	-3	-	-
R Haunch	-3	-3	-4	-5
R Wing	-19	-28	-	-
R Top Web	9	13	14	10
R Bot Web	-5	-4	-3	-1
R Bot Slab	-9	-11	-5	-7

Table 66 – Varina-Enon Bridge LC5 Transverse Shell Model Comparisons, no Barriers

Sensor Location	LC5 - Section D (με)		LC5 - Section C (με)	
	Measured	Thin Shells	Measured	Thin Shells
Top Slab	-12	-2	-3	-1
R Top Slab	-7	-5	-	-
R Haunch	-7	-2	-6	-5
R Wing	-26	-31	-	-
R Top Web	13	16	23	12
R Bot Web	-6	-7	-7	-2
R Bot Slab	-15	-15	-9	-10

Table 67 – Varina-Enon Bridge LC6 Transverse Shell Model Comparisons, no Barriers

Sensor Location	LC6 - Section D (με)		LC6 - Section C (με)	
	Measured	Thin Shells	Measured	Thin Shells
Top Slab	23	19	5	11
R Top Slab	10	8	-	-
R Haunch	-9	-6	-7	-7
R Wing	-25	-34	-	-
R Top Web	2	-14	-10	-14
R Bot Web	-14	-13	-6	-5
R Bot Slab	-12	-10	-5	-2

5.3.3 Transverse Shell Model Results with Barrier Rail

Barrier rails were included in the three dimensional shell models in order to investigate their effect on transverse behavior. Pertinent results are presented in Table 68 through Table 71; the remainder are contained in Appendix D. For the Seabreeze Bridge, the addition of the barrier rails to the shell models reduced the predicted strain to 20% lower (unconservative) than measured at Section A.

Conversely, for the Smart Road and Varina-Enon Bridges, adding the barriers to the model improved the accuracy of the model. Under a single truck on the wing, the Smart Road Bridge wing strain decreased by 37% (compare LC1, Section A, +10 με in Table 70 to +16 με in Table

60) and was only 1 με higher than measured. Under similar loading, the Varina-Enon Bridge wing strain decreased by 18% (compare LC4, Section D, -23 με in Table 71 to -28 με in Table 65). Additionally, adding the barrier rail did not significantly affect predictions at the non-wing measurement locations.

Table 68 – Seabreeze Bridge LC1 Transverse Shell Model Comparisons with Barrier Rails

Sensor Location	LC1 - Section A (με)		LC1 - Section C (με)	
	Measured	Thin Shells	Measured	Thin Shells
Wing	-42	-34	-19	-33
Left Top Slab	-1	-3	-5	-11
Mid Top Slab	1	1	-1	0
Top Web	4	17	8	23
Bottom Web	-4	-3	-2	-5
Left Bot. Slab	-7	-11	-2	-7

Table 69 – Seabreeze Bridge LC4 Transverse Shell Model Comparisons with Barrier Rails

Sensor Location	LC4 - Section A (με)		LC4 - Section C (με)	
	Measured	Thin Shells	Measured	Thin Shells
Wing	-6	-4	-6	-8
Left Top Slab	-19	-16	-17	-23
Mid Top Slab	53	49	33	45
Top Web	-7	-15	-16	-23
Bottom Web	-3	-3	0	1
Left Bot. Slab	-3	-2	2	4

Table 70 – Smart Road Bridge LC1 Transverse Shell Model Comparisons with Barrier Rails

Sensor Location	LC1 - Section A (με)		LC1 - Section B (με)	
	Measured	Thin Shells	Measured	Thin Shells
Wing	9	10	7	11
Left Haunch	1	2	-3	0
Middle Top Slab	1	1	-1	-1
Right Haunch	0	-1	0	-1
Top Right Web	-1	-1	0	-1
Mid Right Web	-1	0	0	0
Right Bottom Slab	1	4	1	1
Left Bottom Slab	-4	-5	-2	4
Mid Left Web	2	2	0	-3
Top Left Web	2	3	-	-

Table 71 – Varina-Enon Bridge LC4 Transverse Shell Model Comparisons with Barrier Rails

Sensor Location	LC4 - Section D (με)		LC4 - Section C (με)	
	Measured	Thin Shells	Measured	Thin Shells
Top Slab	-6	0	-2	0
R Top Slab	-3	-1	-	-
R Haunch	-3	-2	-4	-4
R Wing	-19	-23	-	-
R Top Web	9	11	14	8
R Bot Web	-5	-4	-3	-1
R Bot Slab	-9	-10	-5	-6

Table 72 presents the MAE and MAPE for the transverse shell model at the wing sensor location, with and without barrier rails. In all cases, adding the barrier rails decrease the wing sensors MAE; the Smart Road and Varina-Enon structures MAE decreased by over half. As discussed above, the Seabreeze wing calculated strain was unconservative when the barrier rail is included in the shell model. Overall, including the barrier rails in the model provides a better prediction of the measured values, with the exception of the Seabreeze Bridge. Note that the values in Table 72 include the load cases in which no load was applied to the wing.

Table 72 – Wing Sensor MAE and MAPE, Shell Model Barrier Rail Comparison

Structure	Wing Sensors with Barriers		Wing Sensors without Barriers	
	MAE	MAPE	MAE	MAPE
Seabreeze	5	43%	6	38%
Smart Road	2	53%	5	86%
Varina-Enon	4	16%	8	34%

5.3.4 Uniform Surface Loading Shell Model Comparison

The final comparison for the uniform surface loading shell models is the effect of thin or thick shell formulations. Thin shell elements are based on the Kirchhoff plate formulation, which neglect shearing deformations. Thick shell elements, based on the Mindlin/Reissner formulation, include shear deformations. Note that shell thickness has no effect on the membrane stiffness/behavior, only bending.

A priori, it can be difficult to determine which element formulation will give a better prediction. Common rules of thumb indicate a span-to-depth ratio of 20 to 1 or smaller should be formulated with thick shell elements as shear deformations become larger with respect to bending (CSI 2010). At the flange-to-web joint, the span-to-depth ratio ranges from 20 to 1 to 2 to 1 for the Seabreeze top slab and Smart Road cantilever, respectively.

Upon inspection of the thin and thick shell results, there are only small differences. Typically, the differences are only ±1 με. The results indicate that for the investigated bridges thick shells are unnecessary. More compact structures than those investigated in this report may require the thick shell formulation. Individual thick shell element results are presented in Appendix D.

Figure 132 and Figure 133 present an overall comparison of the MAE and MAPE for each structure, with and without barriers, and with thin and thick shells. The Varina-Enon shell models were most accurate evidenced by the small MAE (3 με) and MAPE (57%). The Smart Road Bridge has similar MAE to the Varina-Enon, but a larger MAPE. The Smart Road Bridge maximum recorded strains were typically very small. As discussed previously, small changes

(e.g., ±1 με) due to testing error, sensor repeatability and/or accuracy can produce large percent changes when the measurements are small. Interestingly the Smart Road Bridge has higher overall MAE and MAPE when the barriers are included in the shell model.

The MAE values for the Seabreeze Bridge were worse than for the other structures. Previously, the location of the top web sensor location on the Seabreeze Bridge was discussed. If the top web sensor data is omitted from the MAE and MAPE calculations, MAE decreases by 1 με and MAPE decreases to 94% and 111% for the with and without barriers cases, respectively. Thick shell formulations do not present significant changes in MAE or MAPE. The difference between thick and thin shells is negligible as evidenced by no change in Figure 132 MAE values and small changes in the MAPE values in Figure 133.

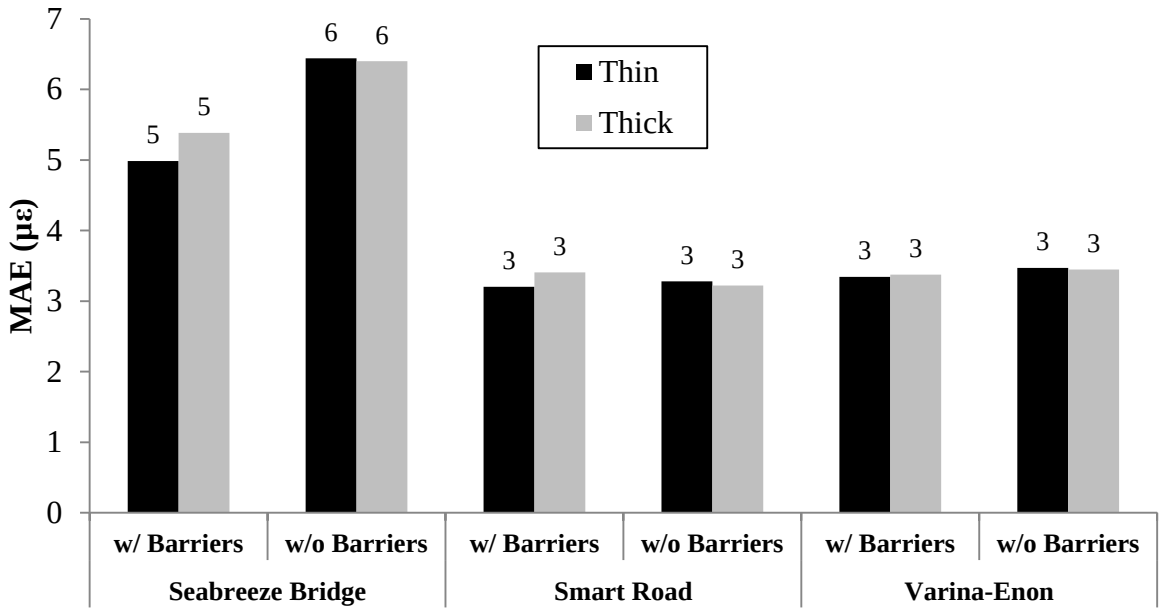

Figure 132 – Transverse Shell Model Support Comparison using MAE

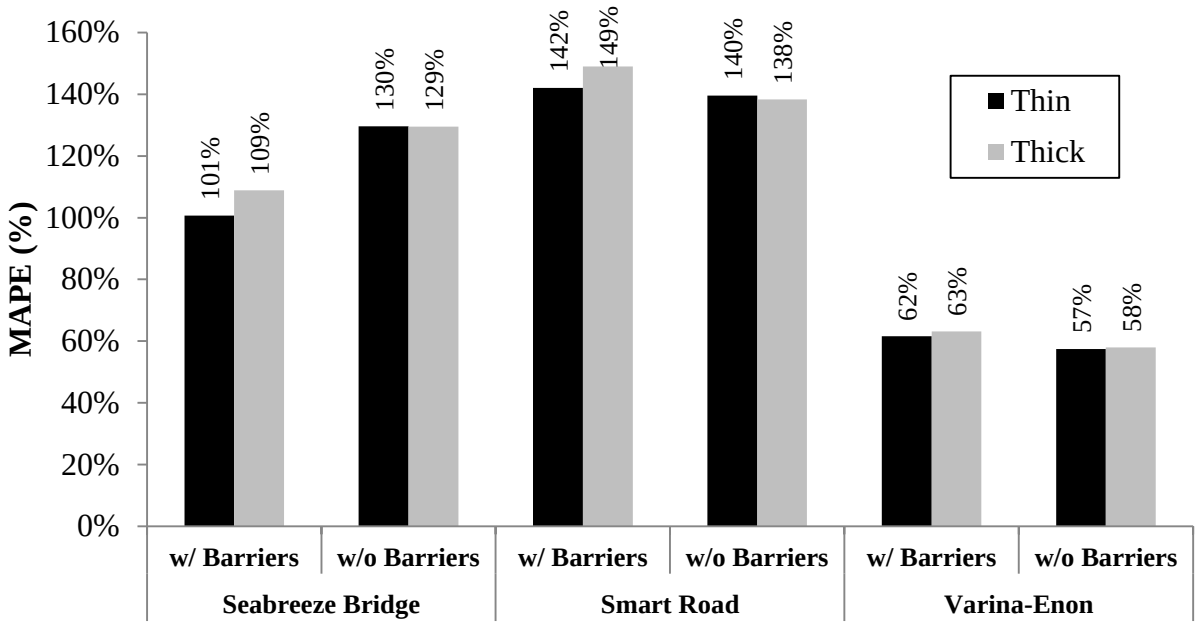

Figure 133 – Transverse Shell Model Support Comparison using MAPE

5.3.5 Structure Specific Influence Surface

Using the previously outline method of creating a three dimensional model is not ideal for design. As implied above, the engineer must manually place surface loading for multiple trucks in multiple locations to induce worst-case response for a structure. This process is time consuming and tedious. A solution to this problem is to construct a program generated influence surface. Many finite element packages, typically those used by practicing engineers (e.g., SAP2000, Midas Civil, LARSA 4D), can generate structure specific influence surfaces.

To create a structure specific influence surface, a set of nodes are defined as the loading surface and the program places a unit load at each node, or on a predefined grid, and saves the responses at each node and each loading. The program then outputs a table or matrix of data for any node of interest similar to the Pucher and Homberg influence surfaces. However, the program generated surfaces include the influence of the entire structure rather than a fixed-fixed or fixed-free plate as for the Pucher and Homberg influence surfaces. The engineer can then post-process these tables using a computer program (Mathcad, Matlab, etc.) to place any axle configuration and location on the loading surface to create maximum response at each critical location.

Because the influence surface approach uses point loads rather than surface loading, as used in the previous sections, results will not be identical near the loading points. Applying point loads to a finite element model will be more severe than applying surface loading. For instance, the stress under a load applied to a finite element mesh will increase, rather than converge, as mesh density increases. This is because the stress under an idealized point load is infinite. Therefore, applying point loads using the same mesh that was found accurate for surface loading should result in conservative predictions near the loads on the top slab.

Another drawback to using the influence surface approach is the time required to perform the analysis. Placing hundreds of point loads over a surface and solving the entire structure for this loading requires significant computational time and memory. However, if the procedure outlined above is followed and model debugging is performed prior to the influence surface generation, the engineer may only need to perform the analysis once.

Figure 134 through Figure 136 compare the results from the program generated influence surface analysis versus the uniform surface loading results from the Section 5.3.3. These plots use the data from thin shells with attached barrier rails, including all load cases and sensors for the Seabreeze, Smart Road and Varina-Enon Bridges, respectively. In each of these plots, a heavy diagonal line represents perfect correlation and a trendline is plotted for the analysis data. The Seabreeze and Varina-Enon Bridges show good correlation with R^2 values, over 0.97. Furthermore, the slope of the trendline is above 1.0 indicating the program generated influence surface values are typically more severe/conservative.

The Smart Road Bridge comparison, found in Figure 135, shows relatively poor correlation with an R^2 value of 0.81 and the scatter is obvious. Part of the issue has been a common theme, where the measurement values are typically small. This combined with the point loads applied very near the sensors during Smart Road Bridge LC4 and LC5 are the reasons for the poor correlation in this case. The Seabreeze and Varina-Enon LCs did have as many point loads very near the measurement locations.

Overall, Figure 134 through Figure 136 show that using the program generated influence method provides similar results and therefore comparable accuracy when determining transverse strains. Furthermore, the program generated influence surface method requires less tedious and hands on work than the surface loading model. The complete results of the program generated influence surface analysis at each measurement location are presented in Appendix D.

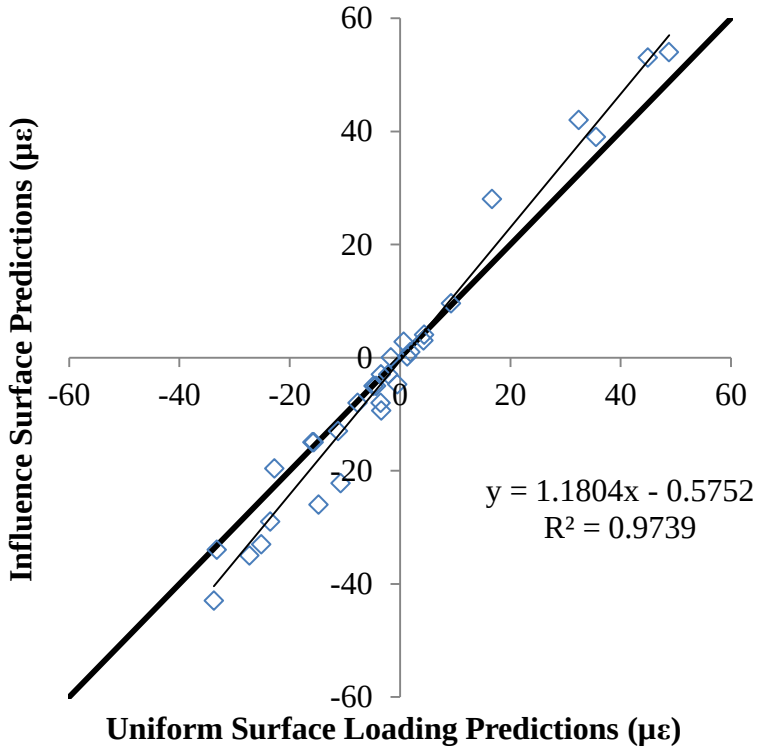

Figure 134 – Seabreeze Bridge Influence Surface Loading versus Uniform Loading

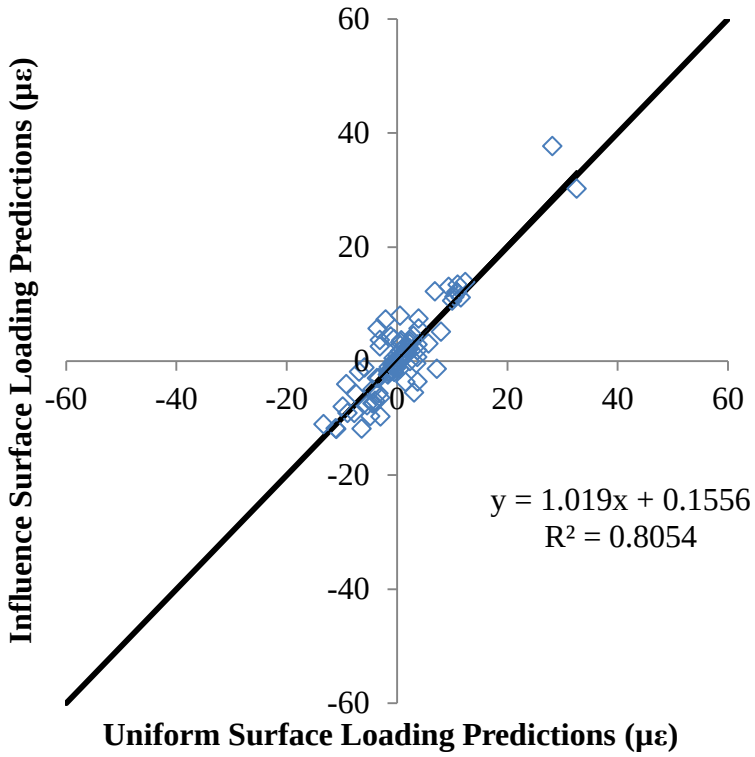

Figure 135 – Smart Road Bridge Influence Surface Loading versus Uniform Loading

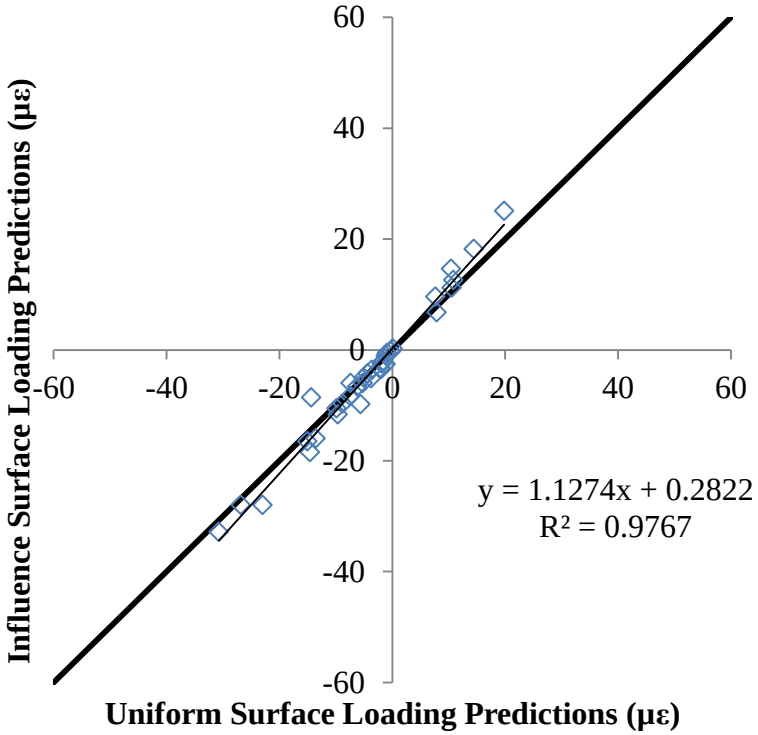

Figure 136 – Varina-Enon Bridge Influence Surface Loading versus Uniform Loading

5.4 Transverse Bending Model Comparisons

The common B P-R frame model and the best predicting 4P frame model were selected for comparison to the three dimensional shell models. Figure 137 and Figure 138 present the MAE and MAPE values for the B P-R and 4P frame models and the uniform surface loading and influence surface loading shell models with barrier rails. The three dimensional models with the barrier rails were selected for comparison because they provided overall a more accurate model. Note that it is difficult to use the MAE and MAPE to quantitatively compare across bridges, because there were different load cases and sensor configurations. For instance, the Varina-Enon Bridge only had three load cases on the right hand side of the bridge that are not directly comparable to those of the other structures and there were more transverse strain sensors on the Smart Road Bridge than the other bridges. The MAE and MAPE comparators are primarily intended to compare the different levels of modeling for a single bridge. However, the comparators maybe used to compare across bridges in a more qualitative sense.

The Seabreeze and Varina-Enon Bridges MAPE values indicate the three dimensional shell model reduces MAPE by a factor of three, when compared to the commonly used B P-R frame model. However, the Varina-Enon Bridge three dimensional shell models are only slightly more accurate when compared to the 4P frame. The magnitudes of MAE and MAPE values for the Seabreeze Bridge are inflated due to instances of small measured strains, the top web strain in particular, as discussed previously, and the inclusion of the barrier rails.

Interestingly, MAE and MAPE indicate that the 4P supported frame model and the three dimensional models provide a similar level of accuracy for each bridge. The Smart Road Bridge MAPE indicates the 4P frame model provides slightly better accuracy than the other modeling techniques, where the MAE indicates they provide the same accuracy. This is because of the generally smaller measured values for the Smart Road Structure.

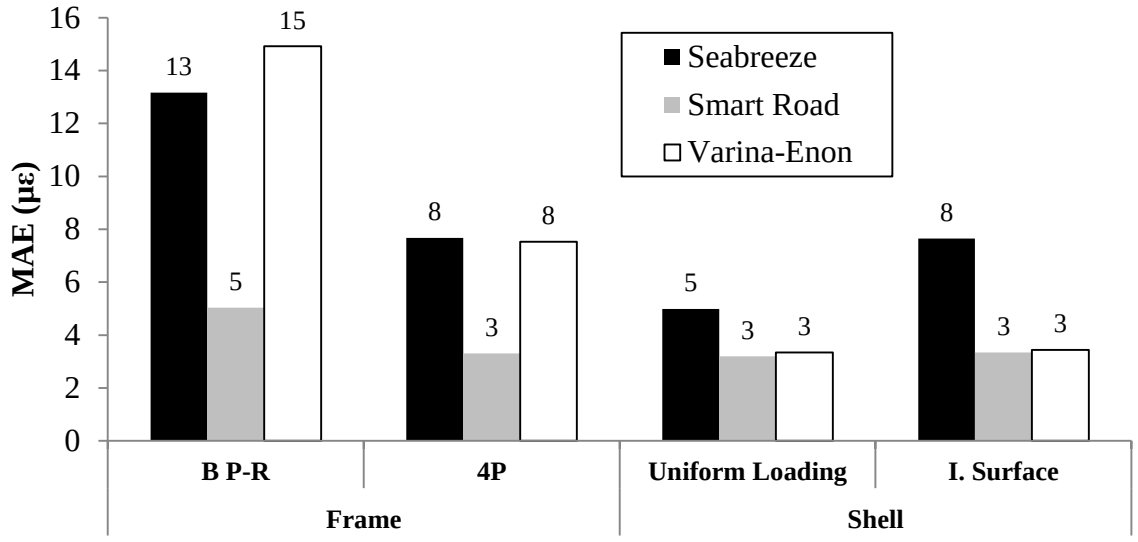

Figure 137 – Frame and Shell Model MAE Statistics

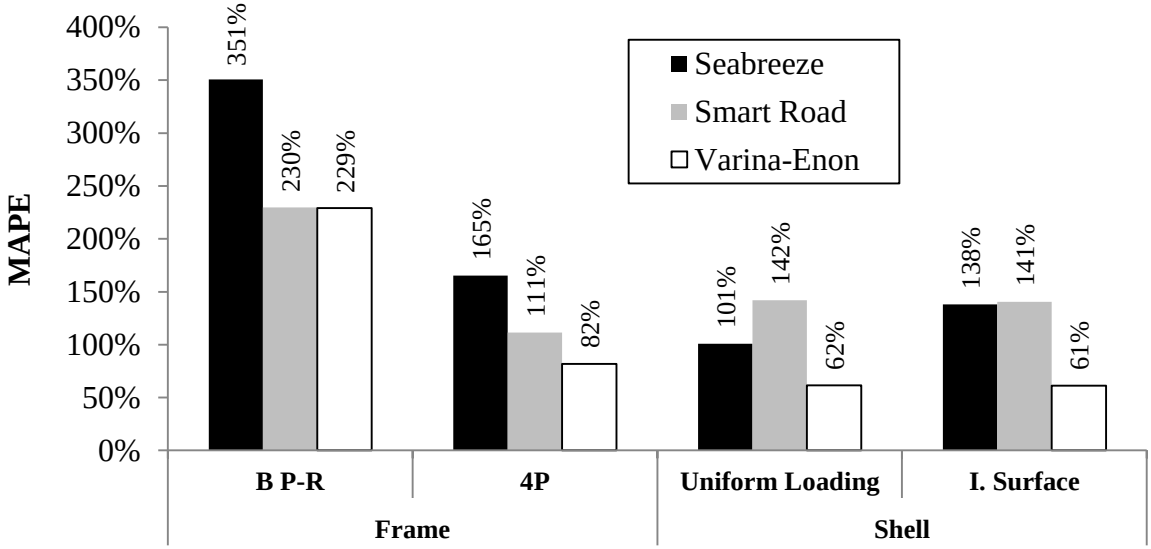

Figure 138 – Frame and Shell Model MAPE Statistics

The B P-R supported two dimensional frame model provides the poorest prediction of measured behavior. By employing the 4P or the shell models the MAPE is reduced, in most cases, by over 100%. Many engineers have adopted a three dimensional shell modeling approach and the above results indicate this will be advantageous.

Quantitatively, using the MAE and MAPE comparators, the 4P supported frame offers similar accuracy to the three dimensional shell models. Qualitatively, the 4P boundary condition, gives the impression that the additional supports are more accurate. This is similar to the reduction caused by using the Pucher influence surfaces instead of the Homberg surfaces to get more accurate results, even though the Pucher plates to not account for the clear differences in geometry. Using the Pucher influence surfaces and applying the 4P boundary conditions both provide a blanket decrease in overall predicted moments and appear to be more accurate.

Figure 139 through Figure 141 compare the transverse bending moment diagrams for the Homberg, B P-R, frame model and the patch loading thin shell model with barrier rails. The shell bending moments are along a single cross section at the point of maximum bending in the top slab for the given load case. Because the shell model is three dimensional, the moments in the cross sections presented may not represent the maximum or minimum response, as the tabulated results did. Clearly, the distribution of bending moments in the top slab is significantly different when comparing the shell to frame moment distributions. Often the web moments are similar (see Figure 140), but the frame model predicts more bending. The measured results are plotted as discrete red lines with circles and drawn to scale. Converting a single strain measurement to a bending moment requires the assumption of no axial force. This is a good assumption for the slab components, but not as good for the vertical webs. The strains were converted to stresses and stresses converted to moment using the component thickness and moment of inertia, assuming a 12 in. width. The shell models clearly provide predictions closer to the measured results.

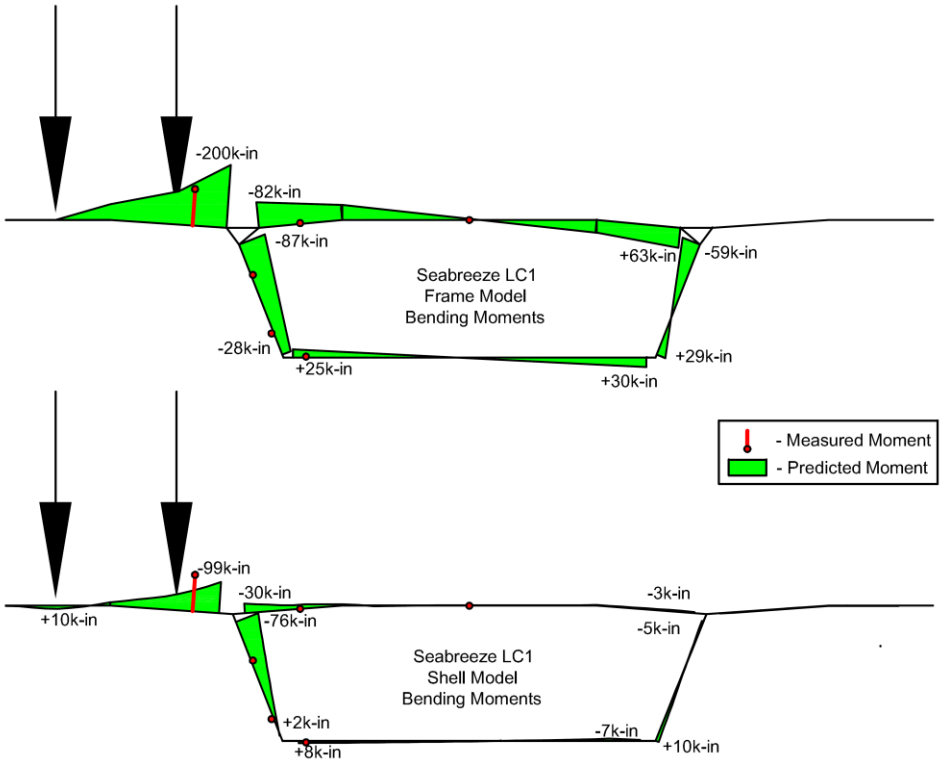

Figure 139 – Seabreeze LC1 Shell and Frame Model Transverse Bending Moment Comparison

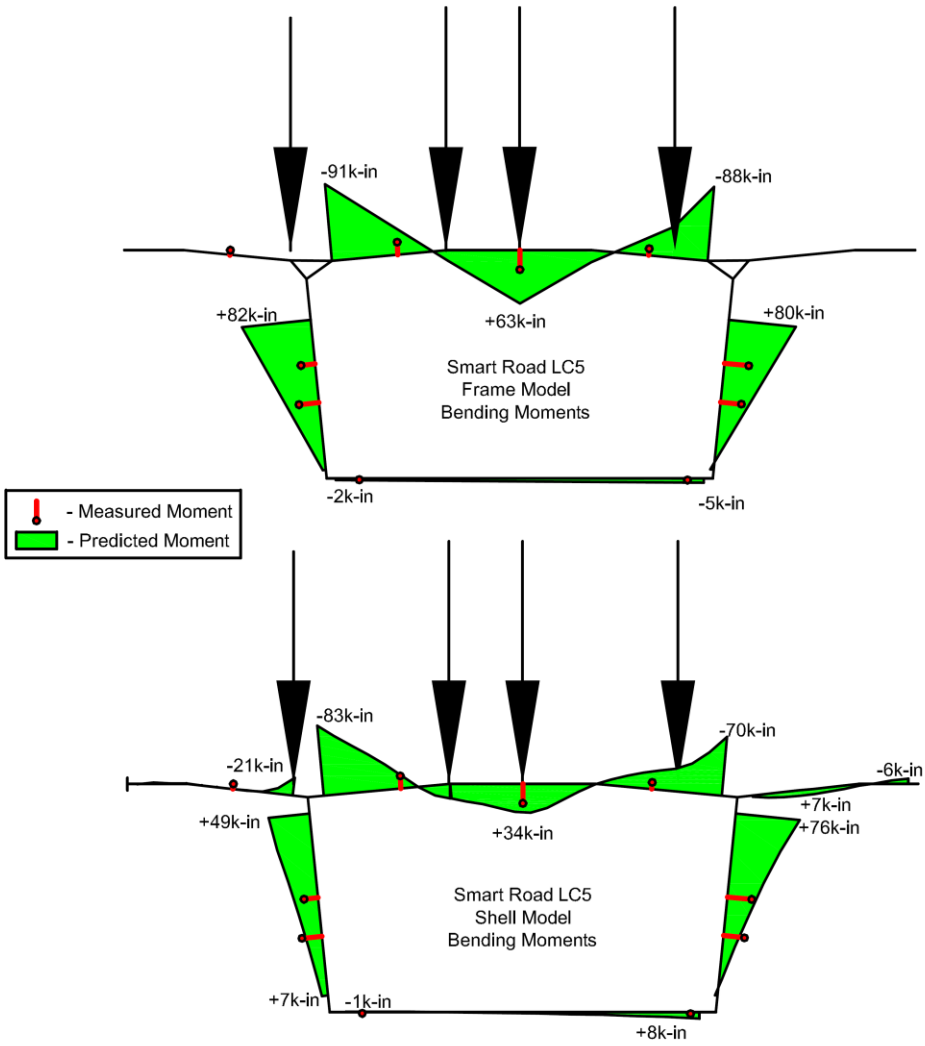

Figure 140 – Smart Road LC5 Shell and Frame Model Transverse Bending Moment Comparison

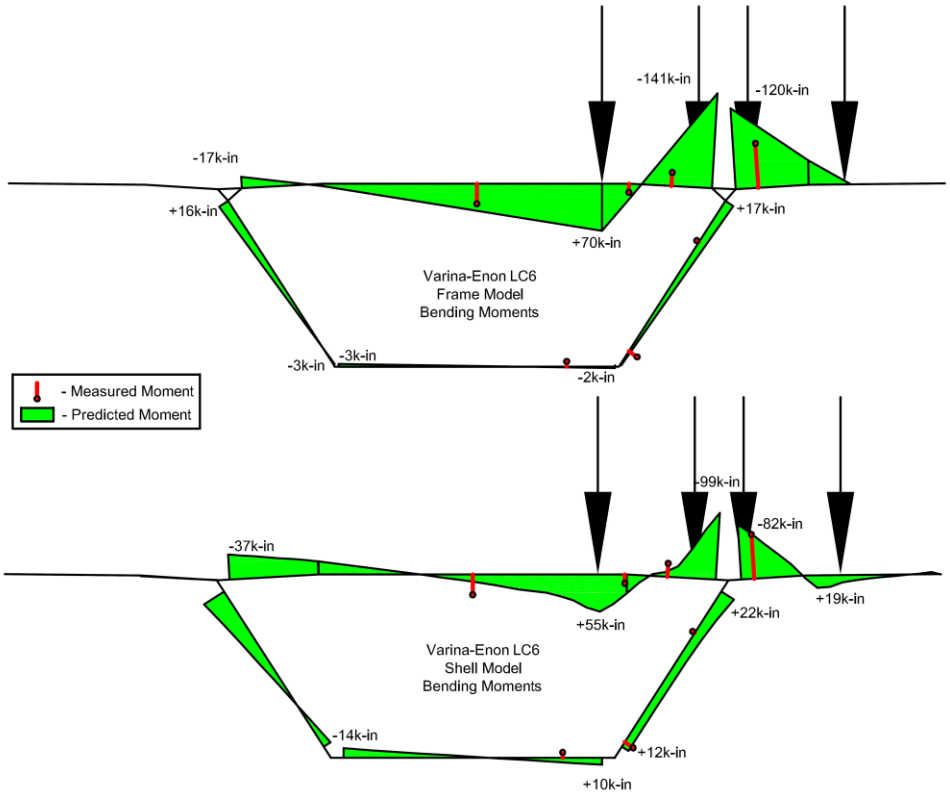

Figure 141 – Varina-Enon LC6 Shell and Frame Model Transverse Bending Moment Comparison

Modeling using the frame and three dimensional shell uniform surface loading approaches requires the engineer significant hands on time to apply loads to the model to find the worst case scenarios. Furthermore, the frame model, using the influence surfaces requires significant hand calculations and is the most time consuming even though it uses many behavior simplifying assumptions. Because of the time required by the engineer and the number of simplifying assumptions involved with all two dimensional frame models, three dimensional shell modeling is recommended. Specifically the shell model program generated influence surface method is the least time consuming and provides a similar and conservative level of accuracy when compared to the shell model uniform surface loading procedure.

5.5 Modeling Summary and Conclusions

Three beamline models were created and compared to the longitudinal and global response for the Seabreeze, Smart Road and Varina-Enon load tests presented in Section 4. Two statistical

comparators, MAE and MAPE showed the simple beamline models could adequately reproduce live load test data, even when not considering shear lag effects.

Several other research programs have found similar accuracy when comparing load test longitudinal response to beamline models (e.g., Roberts 1993, Davis 1999). Based on these results, designers do not need to create complex three dimensional shell or solid models to provide reasonable, conservative results. Additionally, in nearly all cases, the models predicted conservatively. One minor shortcoming of the beamline modeling technique is the inability to predict local longitudinal stresses generated by the large tire loading on the top slab and wings. The final purpose of the longitudinal modeling was to confirm the elastic modulus to be used for the transverse analysis.

Several transverse analysis techniques were presented and investigated through changing boundary conditions and considering the barrier rails. Common two dimensional frame models were investigated, including the effects of changing boundary conditions and adding springs to simulate barrier rail stiffness. Furthermore three rational methods for estimating barrier rail stiffness to the two dimensional frame model were investigation. The results from the two dimensional frame analysis indicate the common boundary conditions provide MAPE in excess of 250%. Clearly, the common B P-R supported two dimensional frame model provides un-acceptable error overall. For this reason, the two dimensional frame model is not recommended for use in design. On the other hand a new support configuration (4P) was introduced, which was shown to reduce MAPE to at best 82%.

A three dimensional shell modeling procedure, tailored for transverse local bending analysis, was developed. It was found the three dimensional shell models were insensitive to several changes including mesh fineness, which was found to be controlled by uniform load application, number of spans modeled, and support conditions. Using surface loading, the transverse modeling procedure was shown to provide significantly more accurate results than the common two dimensional frame models. Often MAPE was below 100%. Similarly MAE was often around 3 με for the three dimensional shell models, meaning the model predictions were was within 3 με, on average, of the test results.

Quantitatively, using the MAE and MAPE comparators, the 4P supported frame offers similar accuracy to the three dimensional shell models. Using the Pucher influence surfaces and applying the 4P boundary conditions both provide a blanket decrease in overall predicted moments and appear to be more accurate.

Modeling using the frame and three dimensional shell uniform surface loading approaches requires the engineer significant hands on time to apply loads to the model to find the worst case scenarios. Furthermore, the frame model, using the influence surfaces require significant hand calculations and is the most time consuming even though it uses many behavior simplifying assumptions. Because of the time required by the engineer and the number of simplifying assumptions involved with all two dimensional frame models, three dimensional frame modeling is recommended. Specifically the shell model program generated influence surface method is the least time consuming and provides a similar and conservative level of accuracy when compared to the shell model uniform surface loading procedure.

Applying barrier rails to the frame or shell models should be done at the risk of the engineer. For the Smart and Varina-Enon Bridges, the barrier rails improved wing strain predictions significantly when using the frame or shell models. However, upon implementing barrier rails into the Seabreeze models unconservative wing strains were found when using gross properties and assuming full continuity.

The biggest limitation to this research was the very small strains measured. While is not ideal, in each bridge test, the results were skewed by small measured values to varying degrees. Longitudinal and transverse strains were often measured at or near the accuracy of a load test strain measurement, cited above as approximately ± 1 με. Concrete load test strains are often small and difficult to work with. Because of this, experienced load testers often prefer displacement measurements on concrete structures (Brett Commander, Personal Communication, March 30, 2012). However, strains were the only option for direct transverse bending measurements presented above and often displacement measurements are more difficult logistically.

Clearly, longitudinal behavior (rotation, strain, and deflections) is predicted somewhat accurately using only common design assumptions with simplified analysis techniques. However, two dimensional and three dimensional transverse analysis techniques are typically inaccurate and highly variable. The equations defining the limit states outlined by AASHTO LRFD Specifications and other design codes, are based on idealizations. By combining the statistical distribution of truck loadings, several research programs (e.g., Kwon et al. 2011, Pelphrey et al. 2008) have developed state specific load factors, typically assuming slab-on-girder style bridges. However, in all cases the uncertainty associated with the modeling error assumed deterministic or built into the girder distribution factor uncertainty (Zureick et al. 2010). With single cell concrete segmental bridges the girder distribution factor is ignored or set to 1.0. Furthermore, the transverse analysis is highly variable and depends greatly on the level of analysis. Because of this, changing the level of analysis is also changing the real probability of failure. It is obvious through three bridge tests that there is uncertainty regarding the longitudinal and transverse analysis. Obviously several more data points would be needed for serious recalibration based on modeling analysis uncertainties.

Using the data contained in this report and others like it, the analysis procedure variability can be included in the overall live load factor calibration (Puckett et al. 2011). This would be implemented through a model analysis factor applied to the ultimate load, analogous to the professional factor, P, for resistance (Zureick et al. 2010). By deriving different load factors dependent on the level of analysis, bridge engineers will be able to maintain a constant probability of failure.

6 Summary, Conclusions and Recommendations

6.1 Summary and Conclusions

To quantify and understand longitudinal and transverse behavior, the results from three live load tests of single cell segmental concrete box girder bridges are presented. The first bridge, tested in April 2011 was the Seabreeze Bridge in Daytona, Florida. The second bridge was the Smart Road Bridge, located in Blacksburg, Virginia and tested in May 2012. The final bridge tested was the Varina-Enon Bridge approach structure, in Richmond, Virginia tested in August 2012. In the past, there has been few experimental investigations into post-tensioned segmental box girder bridges. The main contribution of this research is the collection and analysis of a large body of transverse bending experimental data. Furthermore, the modeling results presented indicate designers should use three dimensional analysis techniques to determine transverse bending demand.

Each bridge was instrumented with longitudinal and transverse strain gages on at least two cross sections. The longitudinal strain sensors were intended to identify the distribution of strains in the flanges to investigate if shear lag was present in each structure. The purpose of the transverse strain sensors was to investigate transverse behavior. Additionally, rotation and deflection sensors were placed around the structures when possible. The biggest limitation to this research was the very small strains measured and the inability to obtain strain measurements through the depth, or on both sides, of the slab and web components. While not ideal, in each bridge test, the results were skewed by small measured values to a varying degrees. Longitudinal and transverse strains were often measured at or near the functional accuracy of a load test strain measurement (± 1 $\mu\varepsilon$).

Longitudinal analysis techniques found in the literature have been somewhat well vetted, but transverse bending observations and their comparison to analysis are lacking. Using the live load test results, two dimensional frame models are investigated. Several boundary conditions, including common design assumptions and a new support scheme, were investigated along with a rational method for introducing barrier rail stiffness to the frame model. Furthermore, bridge engineers are increasingly using finite element software to design for localized transverse

bending. A framework for creating a simple three dimensional shell model, including recommendations on mesh fineness, support conditions, and model size is presented. This model is compared to the live load test results and the simplified two dimensional frame models.

The goal of these analyses is to give designers tools for longitudinal and transverse bending analysis that have an accepted level of accuracy. Their comparison to the experimental results give designers insight into how the analysis tools perform when compared to field test data.

6.1.1 Shear Lag

On the Seabreeze and Smart Road Bridges, significant longitudinal shear lag effects were not observed at any measured location. Neither bridge was expected, based on the design code predictions for b_e/b, to present a large shear lag effect at the measured locations. On the Varina-Enon Bridge, shear lag was observed in the top flange, but not the other components. The identification of shear lag was hindered by the small number of sensors employed, local longitudinal strains and limitations on loading. Larger live load strains and denser spatial distribution of sensors on each flange component, especially on the Seabreeze Bridge would have yielded better results. Because of this, conclusions regarding shear lag effect are limited.

6.1.2 Local Longitudinal Strains

On each structure, measured local longitudinal strains were often larger than the longitudinal bending strains. Near midspan, where the top flange is generally in compression under live and permanent loads, this may not cause issues. However, near the pier, the localized strains are over twice as large as the global bending strains and the bottom of the top flange is in tension from global and local longitudinal loading. The observed local effects may be important at deterioration prone locations such as closure pour segments, especially those in negative moment regions.

6.1.3 Longitudinal Analysis

Three beamline models were created and compared to the longitudinal and global response for the Seabreeze, Smart Road and Varina-Enon load tests. The main purpose of the longitudinal modeling was to validate reasonable elastic moduli used for the transverse analysis. Two statistical comparators, MAE and MAPE showed the simple beamline models could reproduce live load test data to within 20%. Shear lag effects were neglected in all models.

Several other researchers have found similar accuracy when comparing load test longitudinal response to beamline models (e.g., Roberts 1993, Davis 1999). Based on these results, designers do not need to create complex three dimensional shell or solid models to provide reasonable, conservative results. Additionally, in nearly all cases, the models yielded conservative predictions of concrete surface strains. As expected the beamline modeling technique is unable to predict local longitudinal stresses generated by the large tire loading on the top slab and wings.

6.1.4 Transverse Analysis

Several transverse analysis techniques were presented and investigated, including changing boundary conditions and considering the barrier rails using both two and three dimensional techniques. The results from the two dimensional frame analyses indicate the common bottom web pin and roller (B P-R) boundary conditions provide MAPE in excess of 250%. Conversely, the pin support on top and bottom of the webs (4P) support condition was introduced to provide a more distributed and realistic support condition. The 4P support modification was shown to reduce MAPE to 82%, which is on the same order of magnitude of the longitudinal analysis MAPE. In light of the considerable differences between the B P-R and 4P boundary conditions, the common B P-R supported two dimensional frame model provides unacceptable level of accuracy.

A three dimensional shell modeling procedure, tailored for transverse local bending analysis, was developed. It was found the three dimensional shell models were insensitive to several changes including mesh fineness (controlled by ease of uniform surface loading application), number of spans modeled, and support conditions. Using uniform surface loading, the transverse modeling procedure was shown to provide significantly more accurate results than the common two dimensional frame models. Often MAPE was below 100%. Similarly, MAE was often around 3 με for the three dimensional shell models, meaning the model predictions were within 3 με, on average, of the test results. A faster and more convenient analysis method using a program generated, structure specific, influence surface was also outlined. This method produced similar results when compared to the uniform surface loading method, while allowing additional automation for easier load application. The structure specific influence surface method is especially convenient for load rating, where often several trucks outside of the design trucks must be used.

Quantitatively, using the MAE and MAPE comparators, the 4P supported frame offers similar accuracy to the three dimensional shell models. Using the Pucher influence surfaces and applying the 4P boundary conditions both provide a blanket decrease in overall predicted moments and appear to be more accurate.

Modeling using the frame and three dimensional shell uniform surface loading approaches requires the engineer significant hands on time to apply loads to the model to find the worst case scenarios. Furthermore, the frame models, using the Pucher and Homberg influence surfaces require significant hand calculations and are the most time consuming even though the method employs many simplifying assumptions. Because of the time required by the engineer and the number of assumptions involved with all two dimensional frame models, three dimensional frame modeling is recommended. Specifically the shell model program generated influence surface method is the least time consuming and provides a similar and conservative level of accuracy when compared to the shell model uniform surface loading procedure.

For the Smart and Varina-Enon Bridges, adding the barrier rail longitudinal stiffness to the frame and shell models improved wing strain predictions significantly. However, upon introducing the barrier rails into the Seabreeze two and three dimensional models, unconservative wing strains were predicted when using the modeling techniques presented.

6.2 Recommendations

The following recommendations are based on the presented experimental and analytical results:

6.2.1 Shear Lag

- Without additional research, the AASHTO LRFD Bridge Design Specifications should continue to be used to predict shear lag, because the predictions were in most cases conservative.

6.2.2 Local Longitudinal Strains

- The AASHTO Segmental Specifications (Commentary Section 3.3.2) state that these stresses need not be designed for; however, the results indicate additional study is warranted, especially near deterioration prone closure pours.

6.2.3 Longitudinal Analysis

- A longitudinal beamline analysis, also known as a “spline” or “spine” analysis for segmental bridges can provide longitudinal response with reasonable accuracy (within 20% on average) using common design assumptions.

6.2.4 Transverse Analysis

- Two dimensional analysis should not be used to predict transverse bending response. The simplifications involved sacrifice accuracy and do not improve total analysis time.
- The 4P boundary conditions provide the most accurate live load predictions for the two dimensional frame model.
- Three dimensional methods should be used to predict transverse bending response. Specifically, the program generated, structure specific influence surface method produces accurate results and reduces the hands-on time of the engineer.
- Taking advantage of the longitudinal stiffness of the barrier rail when considering transverse bending should be done at the risk of the engineer. The results indicate that using either two or three dimensional analysis techniques with barrier rails can yield unconservative transverse wing bending predictions when using the techniques presented.

6.3 Future research

The following recommendations for future research are based on the presented experimental results:

- The effective width predictions from several design specifications provide very different answers, even for the bridges investigated. Several researchers have performed analytical shear lag studies using classical mechanics and finite element analysis and found many factors which contribute to shear lag that are not accounted for by the design codes. By placing a larger emphasis on shear lag, future load tests could have dense longitudinal strain sensor distribution. Furthermore, a targeted study that investigates slender structures prone to shear lag, preferably with large live load response would be ideal.
- As discussed in the body of the report, the AASHTO Segmental Bridge Specifications do not require designers to account for local longitudinal strains. These strains were measured larger than those caused by the global longitudinal bending strains. The worst case scenario is when the top flange is in tension from global longitudinal strains

(negative moment regions), and is then also subject to high local longitudinal tension. These strains may need to be investigated as a cause of closure pour deterioration, most likely near piers, but also at midspan closure pours as well.

- In a fully calibrated, reliability based, design code, the statistical parameters of both load and resistance need to be quantified. Many resistance and load characteristics have been accounted for, but there is still a need to include the variability associated with the analysis proceedures themselves. The data contained in this report represents information that can be used for this purpose, although additional data must be accumulated for statistical relevance. . It is obvious that there is uncertainty regarding the longitudinal and transverse analysis. Specifically, the transverse analysis is highly variable and depends greatly on the level of analysis. Because of this, changing the level of analysis (two versus three dimensional) is also changing the probability of failure. Obviously several more data points would be needed for serious recalibration based on modeling analysis uncertainties. Using the data contained in this report and others like it, the analysis procedure variability can be included in the overall live load factor calibration. By deriving different load factors dependent on the level of analysis, bridge engineers will be able to maintain a constant probability of failure.

7 References

AASHTO (1977). *Standard Specifications for Highway Bridges*, 12th Edition, American Association of State Highway and Transportation Officials. Washington, DC.

AASHTO (1999) Guide Specifications for Design and Construction of Segmental Concrete Bridges, Interim Provisions. Washington, DC.

AASHTO. (2010) Load and Resistance Factor Design (LRFD) Specifications. 5th edition. Washington DC.

Akinci, N.O., Liu, J., and Bowman, M.D. (2008). "Parapet Strength and Contribution to Live Load Response for Superload Passages". *Journal of Bridge Engineering*, 13(1), 55-63.

American Concrete Institute (ACI). (2008). Building Code Requirements for Structural Concrete (ACI318-08) and Commentary. Farmington Hills, MI.

Barker R. M. and Puckett, J. A. (2007). *Design of Highway Bridges: An LRFD Approach*. Second Edition. John Wiley & Sons. Hoboken, New Jersey.

Barker, J. M., (1978). *Post-Tensioned Box Girder Bridge Manual*. Post-Tensioning Institute. Phoenix, AZ.

Batala, F. A. (1976). *Finite Element Analysis of Prestressed Concrete Box Girders*. PhD Dissertation, Perdue University, Lafayette, IN.

Breen, J. E. and Kashima, S. (1991). "Verification of load distribution and strength of segmental post-tensioned concrete bridges." *Eng. Sruct*., 13(5), 113-127.

Campbell Scientific Incorporated (CSI). (2012*). CR9000X Measurement and Control System Instruction Manual*. CSI, Logan, UT.

Canadian Standards Association (CSA) International. (2000) Canadian Highway Bridge Design Code. CSA-S6-00, Toronto.

Chen, S. S., Aref, A. J., Ahn, I. S., Chiewanichakorn, M. Carpenter, J. A., Nottis, A., Kalpakidis, I. (2005) *Effective slab width for composite steel members*. NCHRP Report 543. Transportation Research Board. Washington, DC.

Cheung, M. S. and Chan, M. Y. T. (1978). "Finite strip evaluation of effective flange width of bridge girders." *Canadian Journal of Civil Engineering*, 5, 174-185.

Chou, P. C. and Pagano, N. J. (1967). *Elasticity: Tensor, Dyadic and Engineering Approaches*. Dover Publications, Inc. New York.

Collins, W. N., (2010). "Live Load Testing and Analysis of the Southbound Span of U.S. Route 15 Over Interstate-66." Master's Thesis, Virginia Tech., Blacksburg, VA.

Computers and Structures, Inc. (1998). *SAP2000, Integrated Finite Element Analysis and Design of Structures, Detailed tutorial including pushover analysis*. Computers and Structures, Inc., Berkeley, CA.

Computers and Structures, Inc. (2010), CSI Analysis Reference Manual. Computers and Structures, Inc., Berkeley, CA.

Davis, R. T., Thompson, M. K., Wood, B. A., Breen, J. E. and Kreger, M. E. (1999). *Measurement Based Performance Evaluation of a Segmental Concrete Bridge*. Report to Texas Department of Transportation.

Dezi, L. and Mentrasti, L. (1985). "Non-uniform Bending-Stress Distribution (Shear Lag)." *Journal of Structural Engineering*, 111(12), 2675-2690.

Duemmel, P. S., Baber, T. T., Barton, F. W. and McKeel, W. T. (1992). *Field Instrumentation and Measured Response of the I-295 Cable-Stayed Bridge: Part 1 – Field Study of Live Load Responses*. Report to Virinia Department of Transportation. Richmond, VA.

Environmental Protection Agency (2013). Light-Duty Automotive Technology, Carbon Dioxide Emissions, Fuel Economy Trends: 1975 through 2012. Transportation and Climate Division Report: EPA-420-R-13-001, Washington DC.

Eurocode 2 (1992) Design of concrete structures. DD ENV 1992-1-1:1992

Evans, H. R. and Taherian, A. R. (1977), "The prediction of the shear lag effect in box girders." *Proceedings of the Institution of Civil Engineers*. 63(March), 69-92.

Evans, H. R. and Taherian, A. R. (1980), "A design aid for shear lag calculations." *Proceedings of the Institution of Civil Engineers*, 69(June), 403-424.

Floyd D. and Sutton, C. D. (1985). *Study of the segmental box girder bridge at Turkey Run: Summary Report*. Final Report to the Indiana State Highway Commission. Indianapolis, IN.

Hadji-Argyris, J. and Cox, H. L., (1944). "Diffusion of Load into Flat Stiffened Panels of Varying Cross-Section", *Reports and Memoranda*, 1969, 1-30.

Hartog, J. P. D., (1952). *Advanced Strength of Materials*. Dover Publications, Inc., New York.

Hawkins, N. M. and Clark, J. H. (1983). *Investigation of thermal and live load stresses in Denny Creek Viaduct.* Report to Washington State Department of Transportation. Olympia, WA.

Holman, R. J. (1977) *Development of an instrumentation program for studying behavior of a segmental concrete box girder bridge*. Report to Indiana State Highway Commission. Indianapolis, IN.

Homberg, H. (1968). *Fabrhahn Platten mit Veranderlicher Dicke*. Springer-Verlag, New York.

Horie, Y., Usuki, S., Watanabe, N. (1984). "A few remarks on the shear lag analysis and the effective width of box girder bridge." *Civil Engineering for Practicing and Design Engineers*, 3(6), 569-586.

Hueste, M. B., Chompreda, P., Trejo, D., Cline, D. B. H., Keating, P. B. (2004). "Mechanical Peroperties of High-Strength Concrete for Prestressed Members". *ACI Structural Journal*, 101(4), 457-465.

Imbrahimbegovic, A., Wilson, E. L., (1991). "A unified formuation for triangular and quadrilateral flat shell finite elements with six nodal degrees of freedom." Communications in Applied Numerical Methods, 7,1-9.

Kristek, V., Evans, H. R., Ahmad, M. K. M. (1990). "A Shear Lag Analysis for Composite Box Girders." *Journal of Construction Steel Research*, 16, 1-21.

Kuhn, D. (2008) *Transverse analysis and field measurements of segmental box girder bridges*. Master's Thesis. The Florida State University. Tallahassee, Florida.

Kuhn, P. (1937). "Stress Analysis of Beams with Shear Deformations of the Flanges." *National Advisory Committee for Aeronautics*, Report No. 608, 669-686.

Kumar, M. (2010). "Influence of box girder geometry on shear lag in RC box-girder bridges." *The Indian Concrete Journal*, January, 15-20.

Kurian, B. and Menon, D. (2008). "Transverse bending analysis of concrete box girder bridges with flange overhangs." *Journal of Structural Engineering*, 35(3), 173-1979

Kuzmanovic, F. and Graham, H. J. (1981). “Shear Lag in Box Girders.” *Journal of the Structural Division*. 107(9). 1701-1712.

Kwon, O., Kim, E., Orton, S. (2011). “Calibration of Live-Load Factor in LRFD Bridge Design Specifications Based on State-Specific Traffic Environments.” *ASCE Journal of Bridge Engineering*. 16(6), 812-819.

Libby, J. R. (1976). “Segmental Box Girder Bridge Design.” *ACI Journal*, 73(5). 278-290.

Lissenden, C. J. (1988). “Dynamic Modeling of a Cable Stayed Bridge During Construction” Master’s Thesis, University of Virginia, Charlottesville, Virginia.

Mabsout, M. E., Tarhini, K. M., Frederick, G. R., and Kobrosly, M. (1997). “Influence of sidewalks and railings on wheel load distribution in steel girder bridges.” *J. Bridge Eng.*, 2(3), 88-96.

Maisel, B. I. and Roll, F. (1974). *Methods of analysis and design of concrete box beams with side cantilevers: Technical report*. Cement and Concrete Association. London.

McClure, R. M. and West, H. H. (1980). *Field Testing of an Experimental Segmental Bridge*. Report to the Pennsylvania Department of Transportation. Harrisburg, PA.

McClure, R. M. and West, H. H. (1984). “Full-scale testing of a prestressed concrete segmental bridge.” *Canadian Journal of Civil Engineering*, 11, 505-515.

McClure, R. M., Anderson, D. B., McDevitt, T. E. (1980) *An Experimental Segmental Bridge at the Pennsylvania Transportation Research Facility*. Interim Report to the Pennsylvania Department of Transportation.

Miller, A. B. (1920). “The Effective Width of a Plate supported by a Beam.” *The Institution of Civil Engineers: Selected Engineering Papers*, 83, 1-30.

Moffatt, K. R. and Dowling, P. J. (1975). “Shear lag in steel box girder bridges.” *The Structural Engineer*, 10(53), 439-448.

Moffatt, K. R. and Dowling, P. J. (1978). “British Shear Lag Rules for Composite Girders.” *Journal of the Structural Division*, 104(7), 1123-1130.

Moreton, A. J. (1998). “Segmental Analysis and Design Fundamentals.” *Recommended Practice for Design and Construction of Segmental Concrete Bridges*. American Segmental Bridge Institute, Phoenix, AZ.

Pelphrey, J., Higgens, C., Sivakumar, B., Groff, R. L., Hartman, B. H., Charbonneau, J. P., Rooper, J. W. and Johnson, B. V. (2009). “State Specific LRFR Live Load Factors Using Weigh-in-Motion Data.” *ASCE Journal of Bridge Engineering*. 13(4), 339-350.

Potisuk, T., and Higgins, C. (2007). “Field Testing and Analysis of CRC Deck Girder Bridges.” *Journal of Bridge Engineering*, 12(1), 53-63.

Pucher, A. (1977). *Influence Surfaces of Elastic Plates*. Springer-Verlag, New York.

Puckett, J. A., Huo, S.X., Jablin, M. and Mertz, D. R. (2011). “Framework for Simplified Live Load Distribution-Factor Computations.” *ASCE Journal of Bridge Engineering*, 16(6), 777-791.

Reissner E. (1938). “On the Problem of Stress Distribution in Wide-Flanged Box-Beams.” *Journal of the Aeronautical Sciences*, 5(8), 295-299.

Reissner, E. (1941). “Least Work Solutions of Shear Lag Problems.” *Journal of the Aeronautical Sciences*, 8(7), 284-291.

Reissner, E. (1946). “Analysis of Shear lag in Box Beams by the Principle of Minimum Potential Energy.” Quarterly of Applied Mathmatics, 4(3), 268-278.

Roberts C. L. (1993). “Measurement Based Revisions for Segmental Bridge Design and Construction Criteria.” PhD Dissertation, University of Texas at Austin., Austin, TX.

Sanayei, M., Onipede, O., B, R. (1992). “Selection of Noisy Measurement Locations for Error Reduction in Static Parameter Identification.” *American Institute of Aeronautics and Astronautics Journal*, 30(9), 2299-2309.

Sa-nguanmanasak, J., Chaisomphob, T. Yamaguchi, E. (2006). “Stress Concentrations due to shear lag in continuous box girders” *Engineering Structures*, 29, 1414-1421.

Schlaich, J. and Sheef, H. (1982). *Concrete Box Girder Bridges*. International Association for Bridge and Structural Engineering. Zurich, Switzerland.

Sennett, R. E. (2000). *Matrix Structural Analysis*. Waveland Press, Long Grove, IL.

Song , Q. and Scordelis, A. C., (1990). “Shear-Lag Analysis if T- I- and Box Beams.” *Journal of Structural Engineering*, 116(5), 1290-1305.

Stanton, J. F., Roeder, C. W., White, C., Kuester, C., Craig, B. (2008). “Rotation Limits for Elastomeric Bearings.” *NCHRP Report 596*, National Research Council, Washington DC.

Tahan N, Pavlovic MN. (1997). “Shear lag revisited: The use of single Fourier series for determining the effective breath in plated structures.” *Computer and Structures*, 63, 759–67.

Takebayashi, T., Deeprasertwong, K., Leung, Y. W. (1994). “A full-scale destructive test of a precast segmental box girder bridge with dry joints and external tendons.” *Proc. Instn. Civ. Engrs. Structs & Bldgs*. 104, 297-315.

Tassin, D. M. (1998). “Design of Precast Segmental Bridges Build Span-by-Span.” *Recommended Practice for Design and Construction of Segmental Concrete Bridges*. American Segmental Bridge Institute, Phoenix, AZ. 1998.

Tenchev, R. T. (1996). “Shear lag in orthotropic beam flanges and plates with stiffeners.” *International Journal of Solids Structures*, 33(9), 1317-1334.

Thoman, S. J., Redfield, C. M. and Hollenbeck, R. E. (1984). Load Test of Single-Cell Box Girder Bridge Cantilever Deck. Journal of Structural Engineering, 110(8), 1773-1785.

v. Karman, T. (1924) “Die Mittragende Breite.” *Föppl Festschrift*, August, 114-127.

Williams, D. (1960). *An Introduction to the Theory of Aircraft Structures*. Edward Arnold LTD. London.

Winter, G. (1940). “Stress distribution in an equivalent width of flanges of wide, thin-wall steel beams.” *National Advisory Committee for Aeronautics, Technical Note No. 784*, 1-26.

Younger, J. E. (1930). *Metal Wing Construction Part II*. U.S. Army Air Corps. A.C.T.R. Series No. 3288, Material Division.

Zureick, A., Ellingwood, B. R., Nowak, A. S., Mertz, D. R., Triantafillou, T. C. (2010) “Recommended Guide Specification for the Design of Externally Bonded FRP Systems for Repair and Strengthening of Concrete Bridge Elements” *NCHRP Report 655*. National Research Council, Washington DC.

8 Appendix A: Seabreeze Bridge Test Results

The following appendix presents the results from the Seabreeze Bridge load test. Figure A1 through Figure A15 present the measured longitudinal strain versus truck position plots for Sections A, B and C under LC1 though LC5. Figure A16 through Figure A21 present the measured transverse strain versus truck position plots for Section A and C under LC1, LC3 and LC4. Figure A22 through Figure A26 present the measured rotations versus truck position plots for Section D under LC1 though LC5. Figure A27 through Figure A31 present the vertical deflections versus truck position plots for Sections A and E under LC1 though LC5.

8.1 Seabreeze Bridge Longitudinal Strains

8.1.1 Seabreeze Bridge Section A

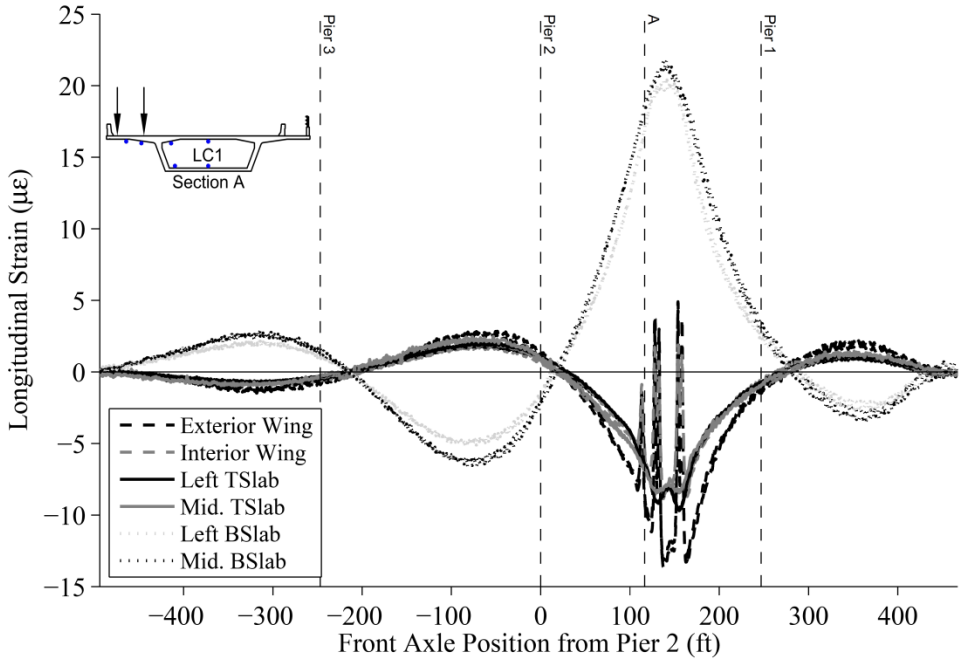

Figure A1 – Seabreeze Bridge Longitudinal Strains from LC1 at Section A – All Iterations

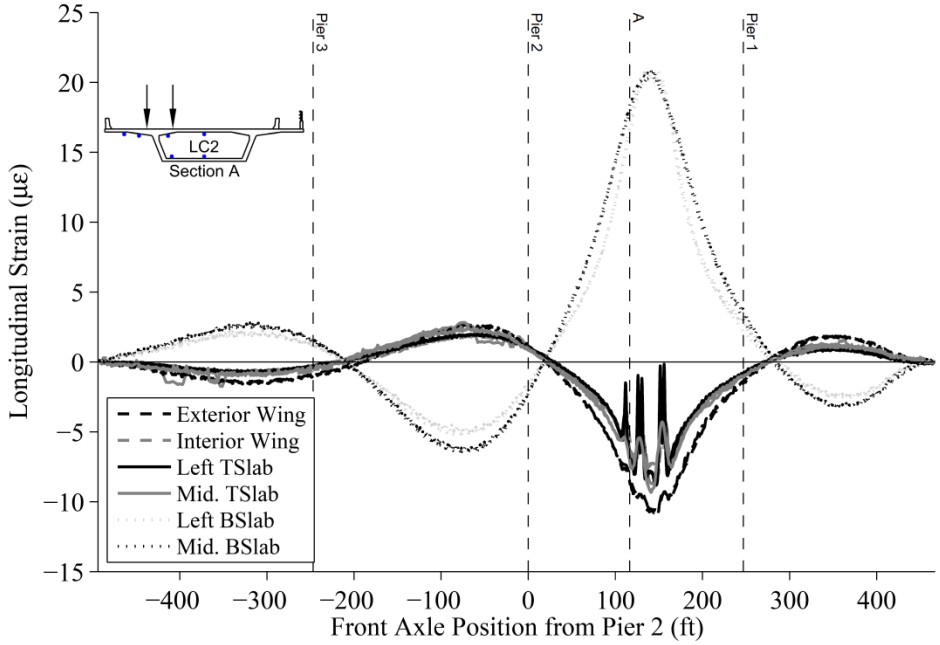

Figure A2 – Seabreeze Bridge Longitudinal Strains from LC2 at Section A – All Iterations

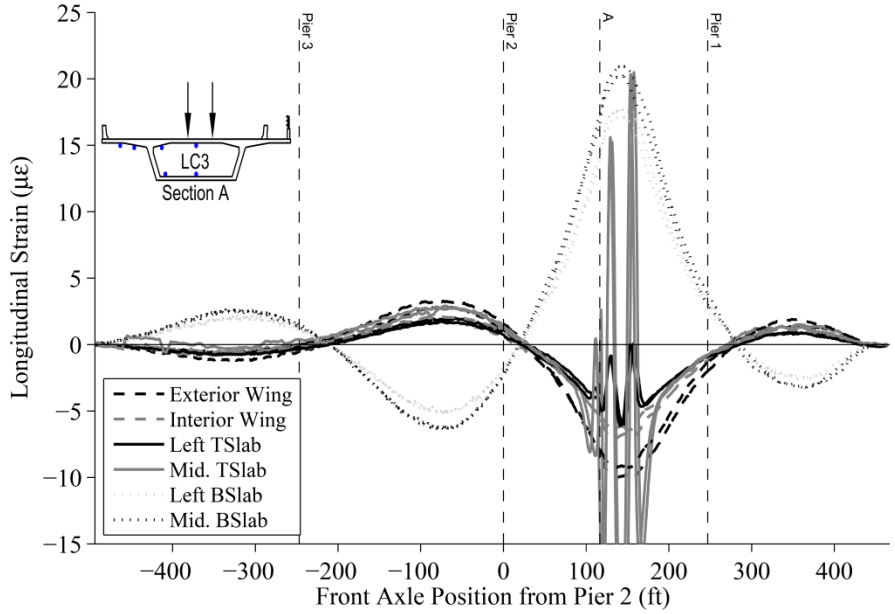

Figure A3 – Seabreeze Bridge Longitudinal Strains from LC3 at Section A – All Iterations

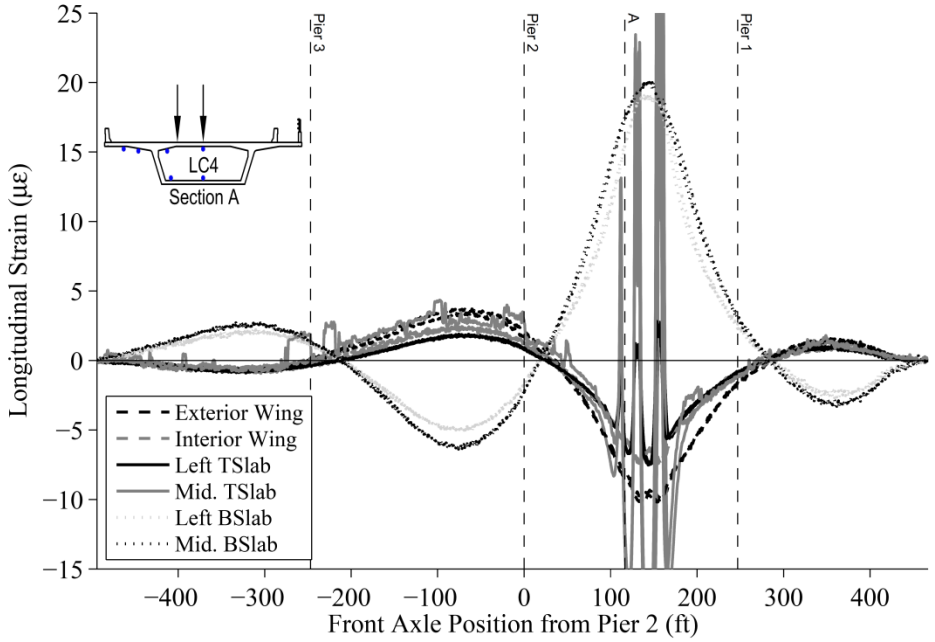

Figure A4 – Seabreeze Bridge Longitudinal Strains from LC4 at Section A – All Iterations

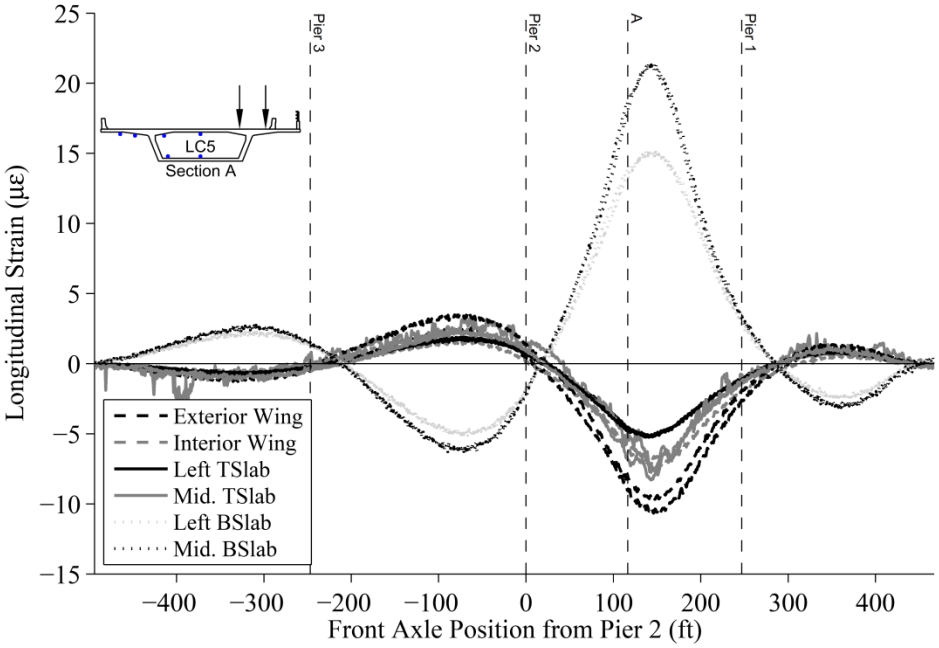

Figure A5 – Seabreeze Bridge Longitudinal Strains from LC5 at Section A – All Iterations

8.1.2 Seabreeze Bridge Section B

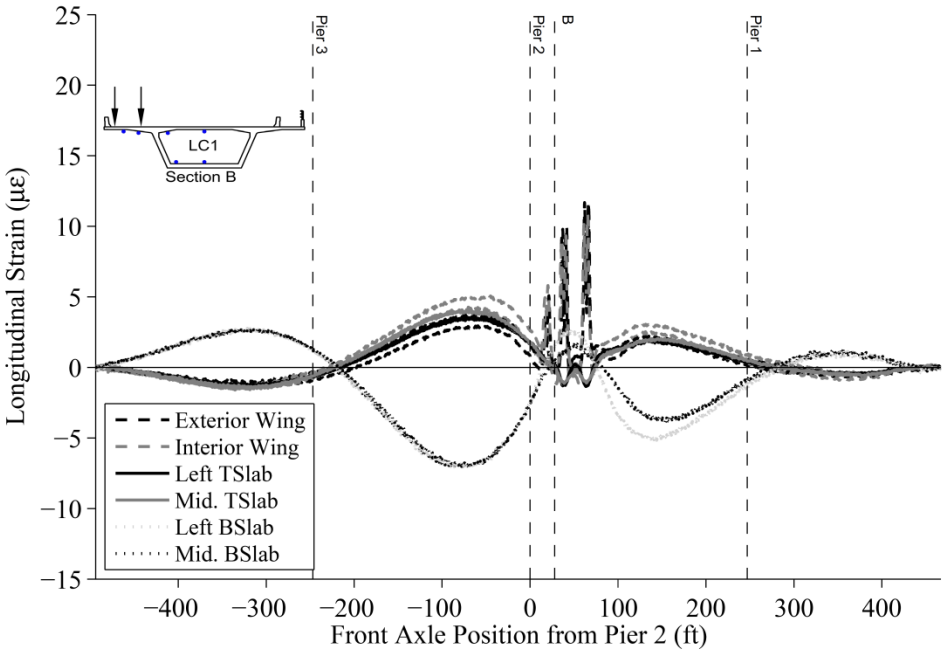

Figure A6 – Seabreeze Bridge Longitudinal Strains from LC1 at Section B – All Iterations

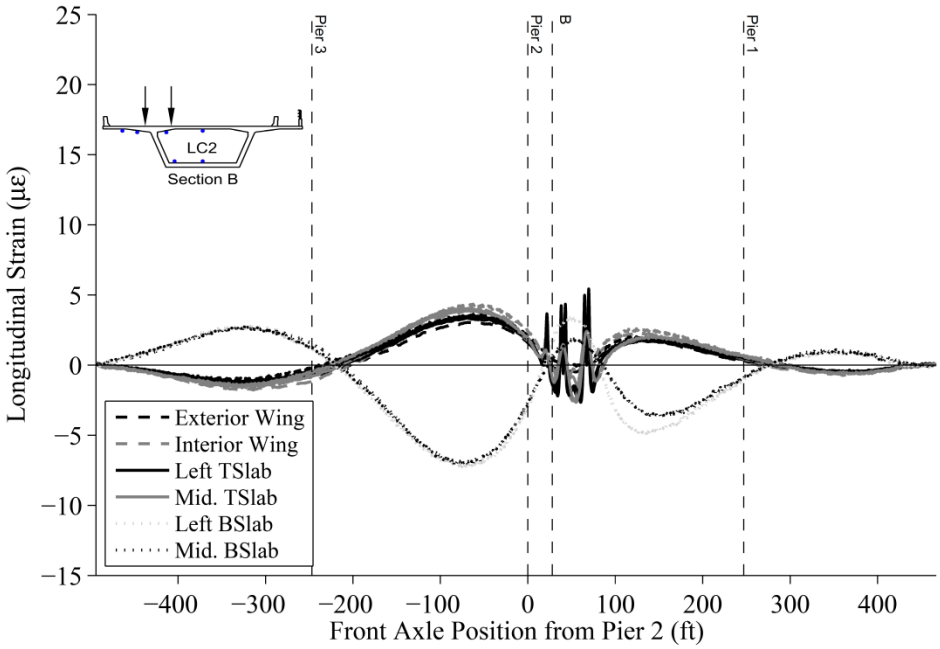

Figure A7 – Seabreeze Bridge Longitudinal Strains from LC2 at Section B – All Iterations

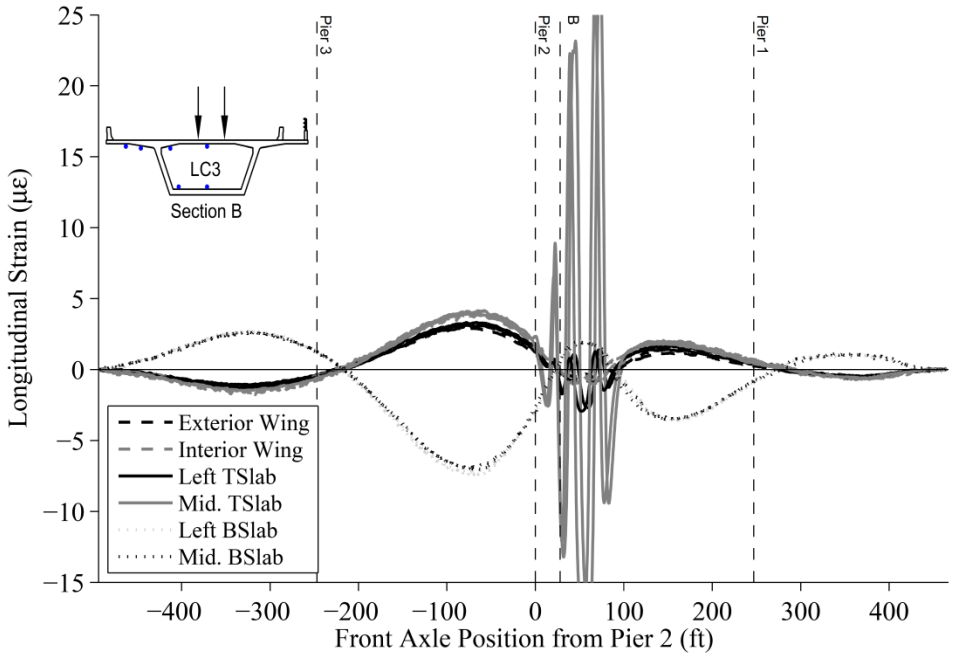

Figure A8 – Seabreeze Bridge Longitudinal Strains from LC3 at Section B – All Iterations

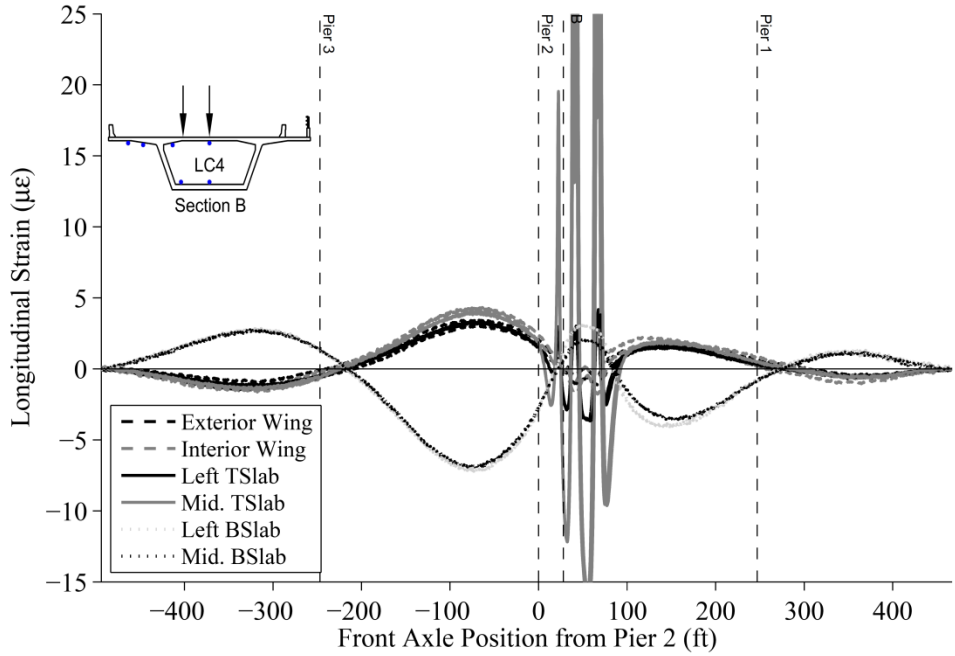

Figure A9 – Seabreeze Bridge Longitudinal Strains from LC4 at Section B – All Iterations

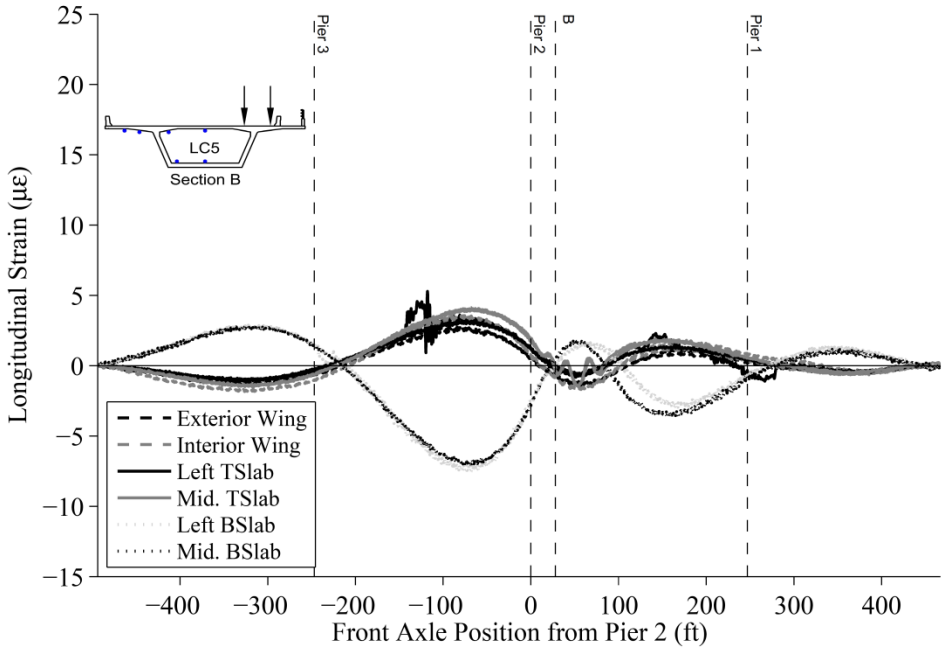

Figure A10 – Seabreeze Bridge Longitudinal Strains from LC5 at Section B – All Iterations

8.1.3 Seabreeze Bridge Section C

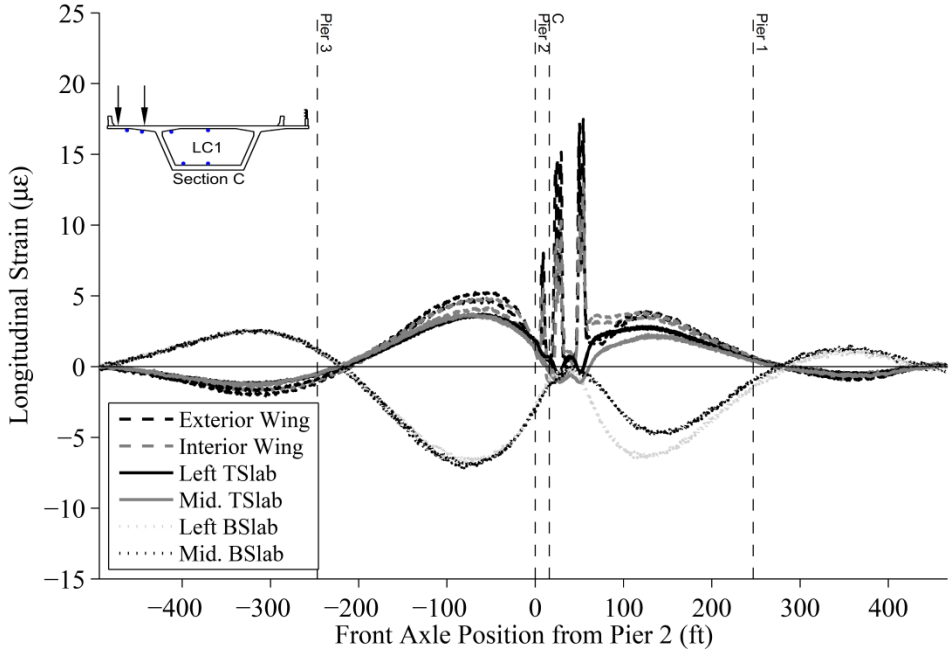

Figure A11 – Seabreeze Bridge Longitudinal Strains from LC1 at Section C – All Iterations

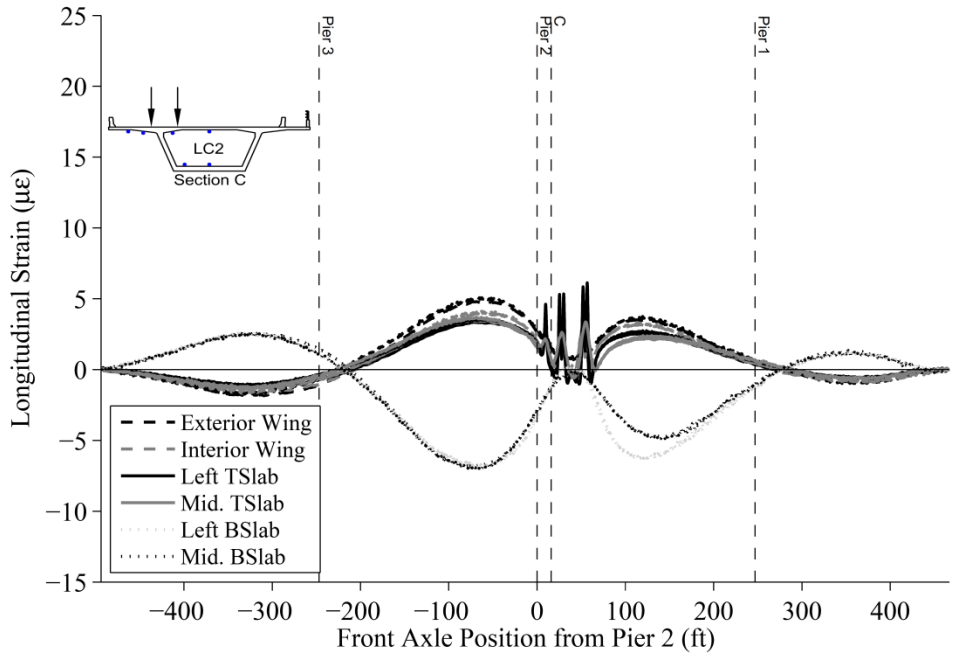

Figure A12 – Seabreeze Bridge Longitudinal Strains from LC2 at Section C – All Iterations

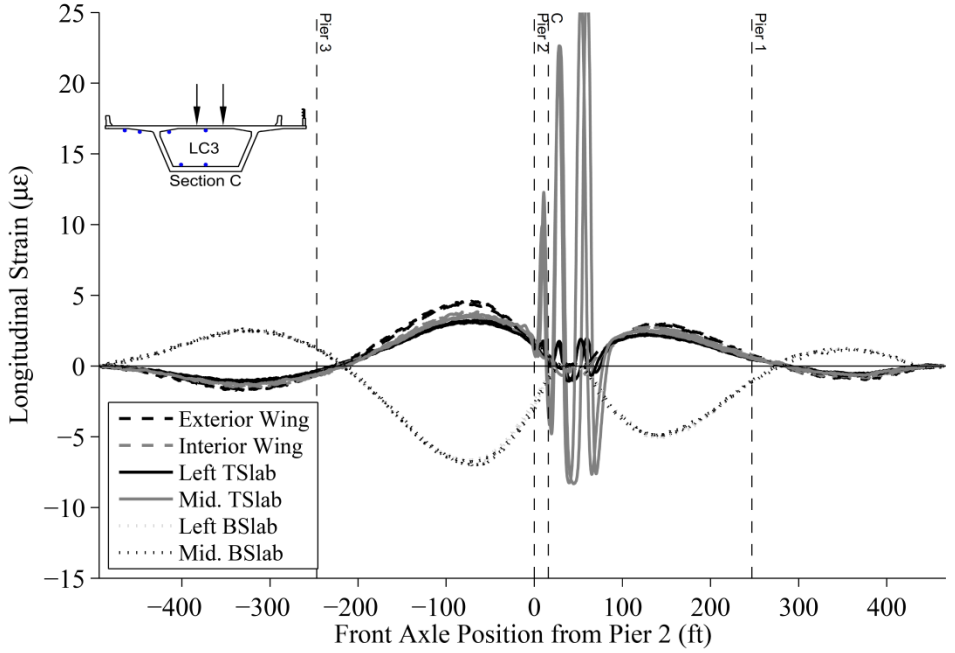

Figure A13 – Seabreeze Bridge Longitudinal Strains from LC3 at Section C – All Iterations

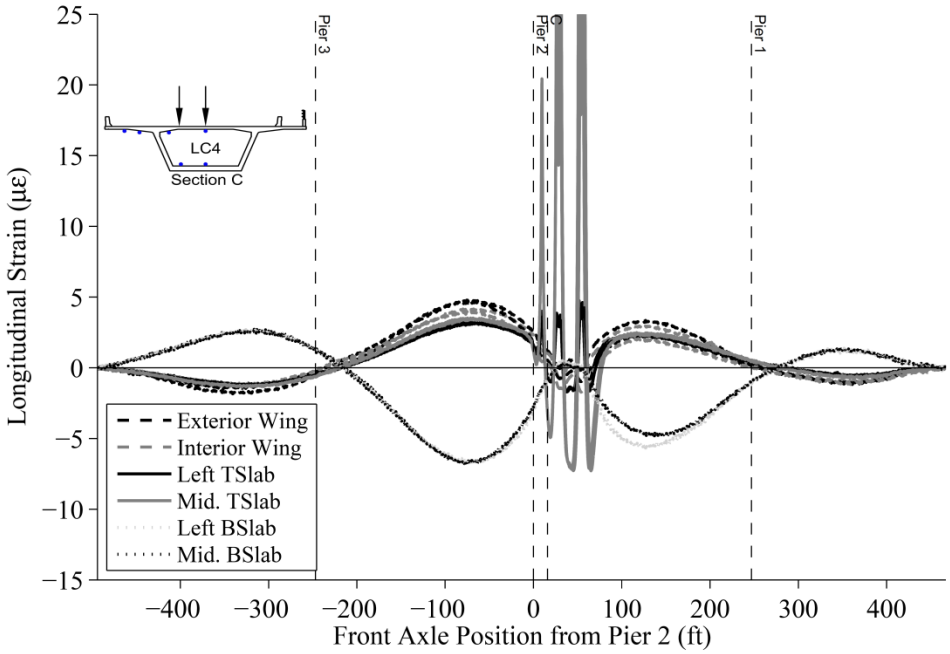

Figure A14 – Seabreeze Bridge Longitudinal Strains from LC4 at Section C – All Iterations

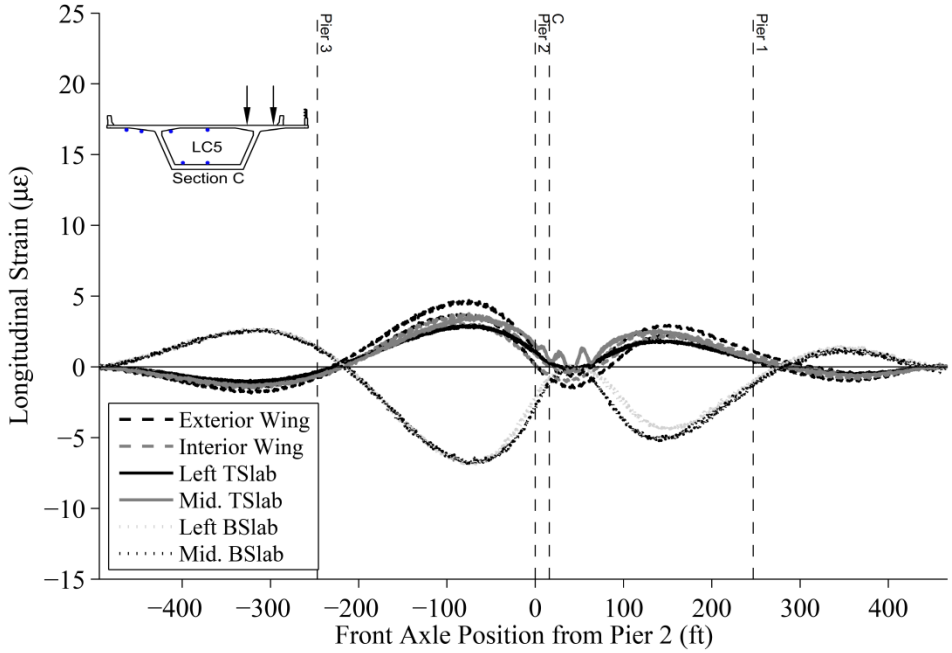

Figure A15 – Seabreeze Bridge Longitudinal Strains from LC5 at Section C – All Iterations

8.2 Seabreeze Bridge Transverse Strains

8.2.1 Seabreeze Bridge Section A

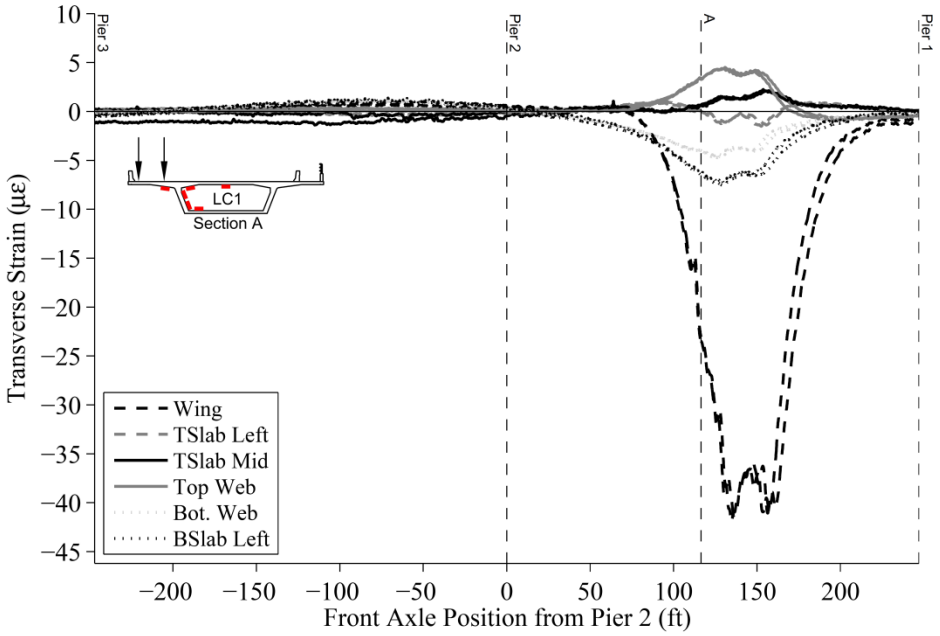

Figure A16 – Seabreeze Bridge Transverse Strains from LC1 at Section A – All Iterations

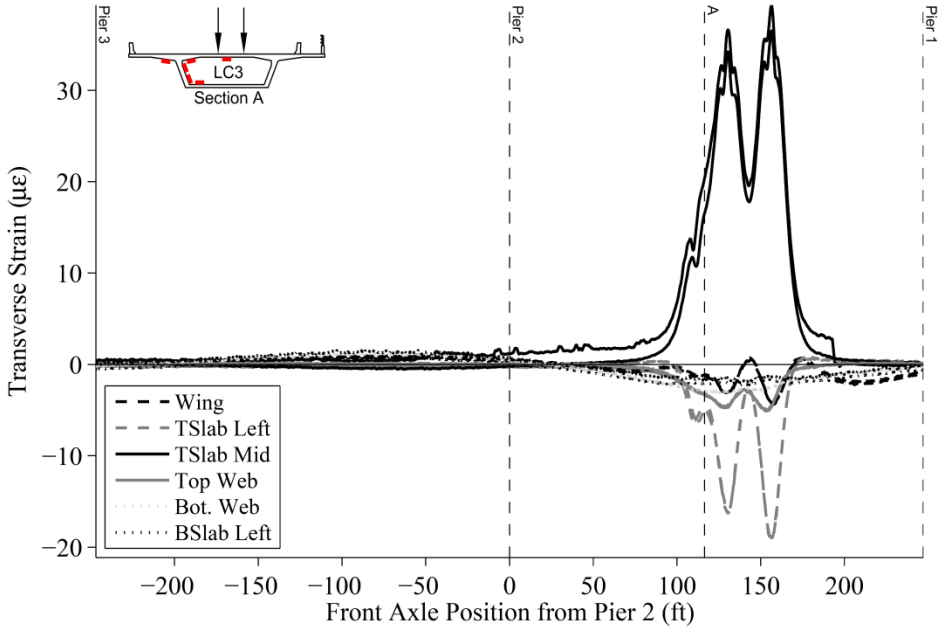

Figure A17 – Seabreeze Bridge Transverse Strains from LC3 at Section A – All Iterations

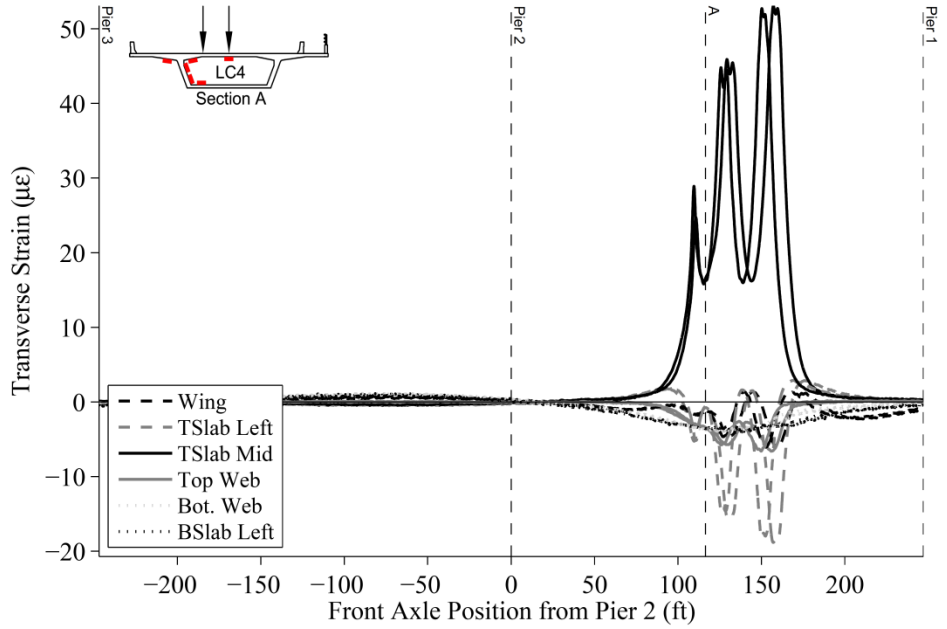

Figure A18 – Seabreeze Bridge Transverse Strains from LC4 at Section A – All Iterations

8.2.2 Seabreeze Bridge Section C

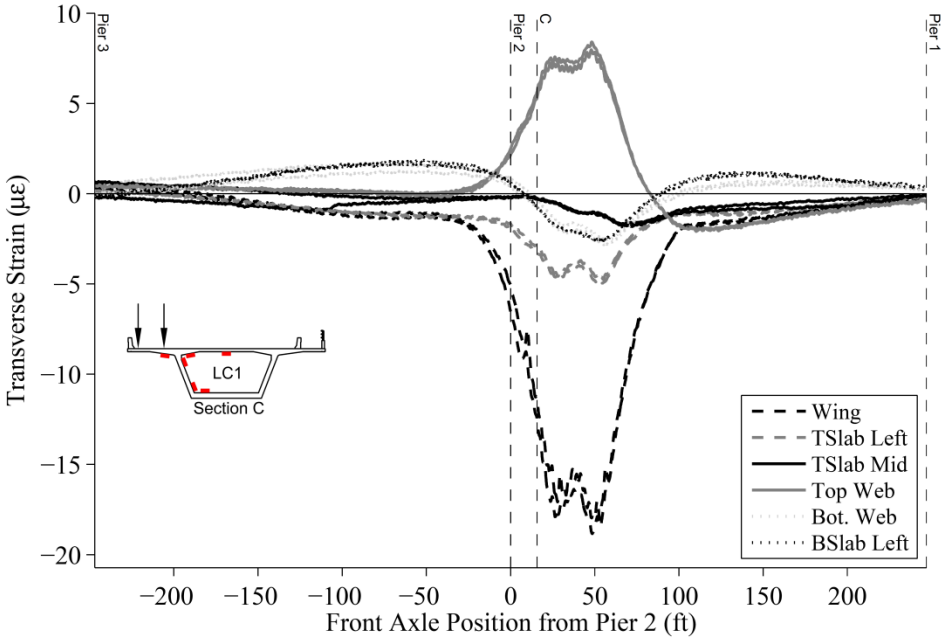

Figure A19 – Seabreeze Bridge Transverse Strains from LC1 at Section C – All Iterations

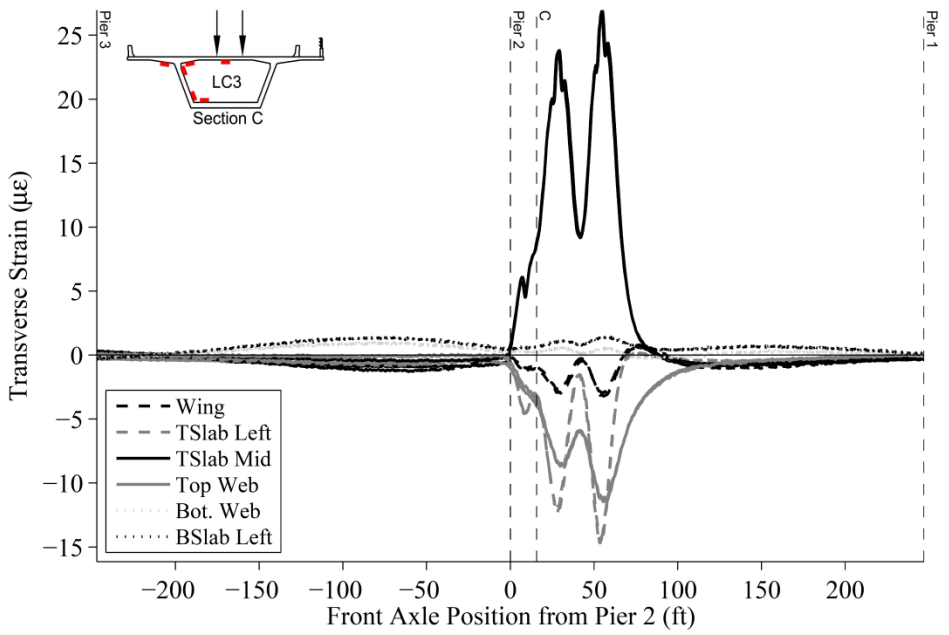

Figure A20 – Seabreeze Bridge Transverse Strains from LC3 at Section C – All Iterations

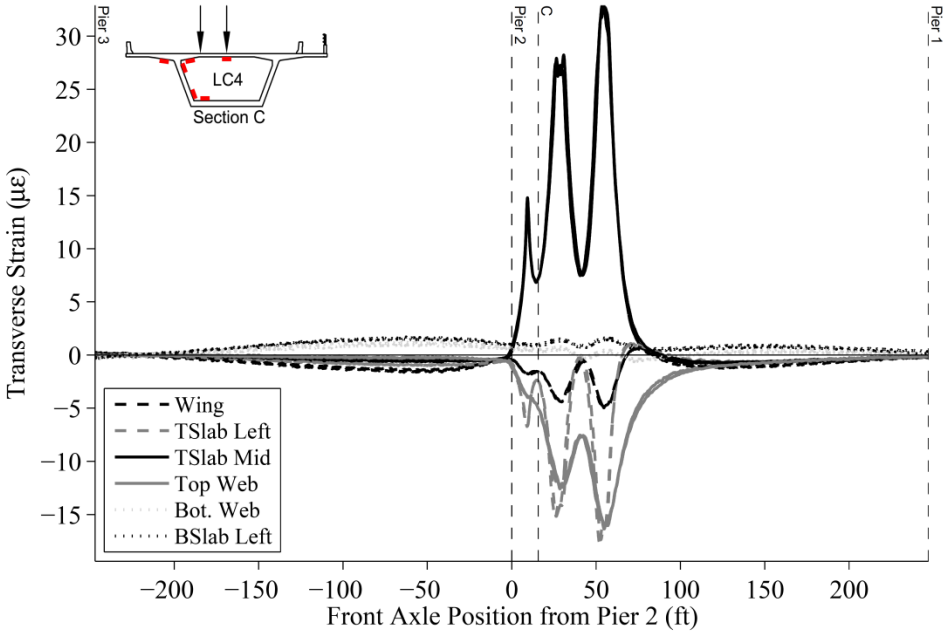

Figure A21 – Seabreeze Bridge Transverse Strains from LC4 at Section C – All Iterations

8.3 Seabreeze Bridge Rotations

8.3.1 Seabreeze Bridge Section D

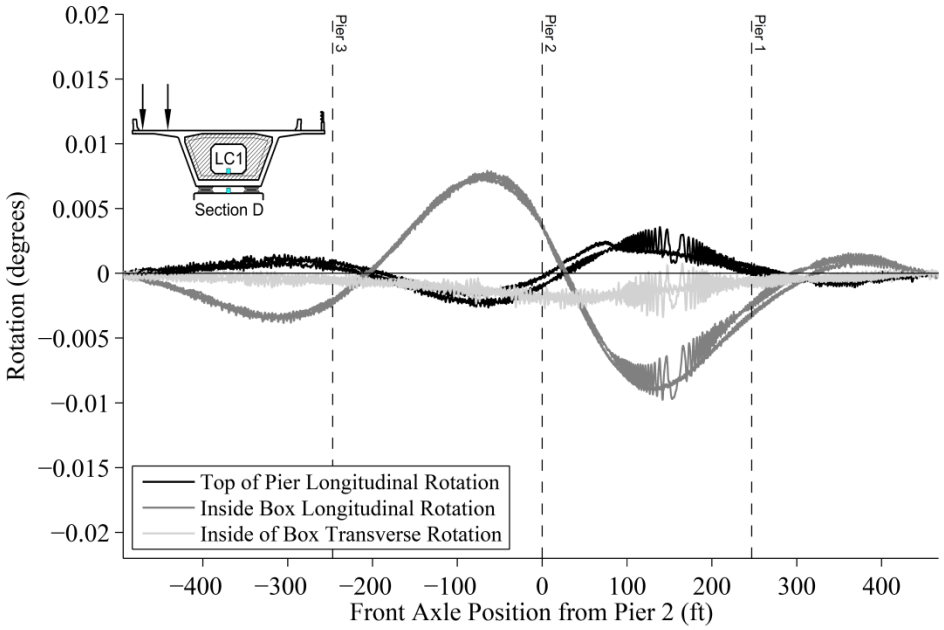

Figure A22 – Seabreeze Bridge Rotation from LC1 at Section D – All Iterations

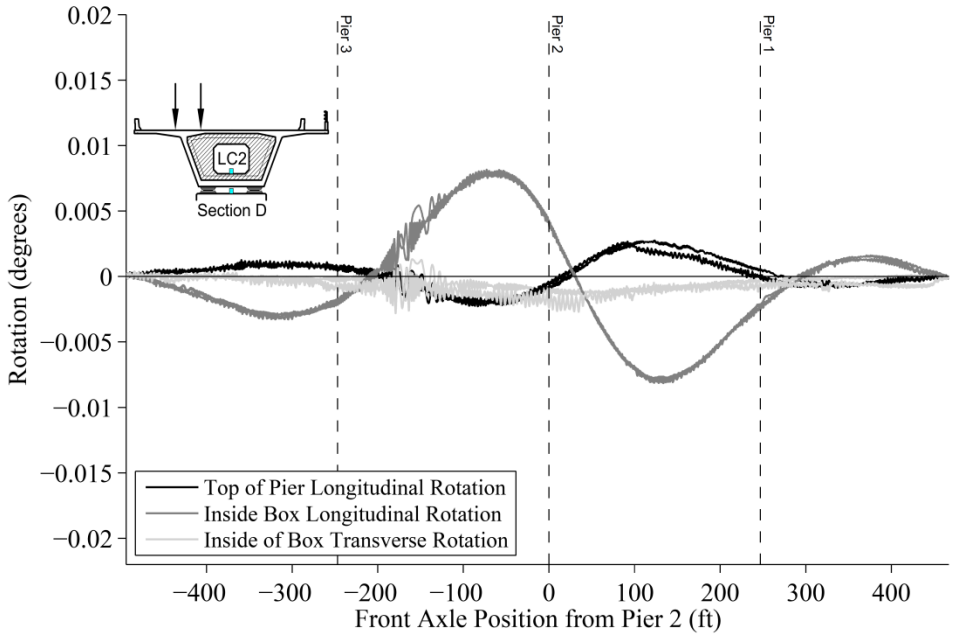

Figure A23 – Seabreeze Bridge Rotation from LC2 at Section D – All Iterations

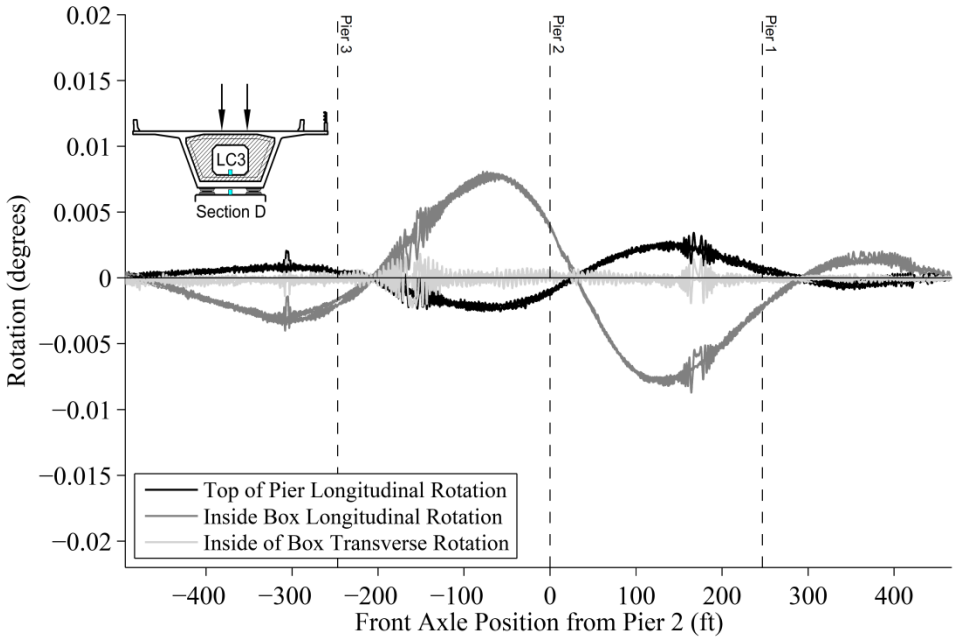

Figure A24 – Seabreeze Bridge Rotation from LC3 at Section D – All Iterations

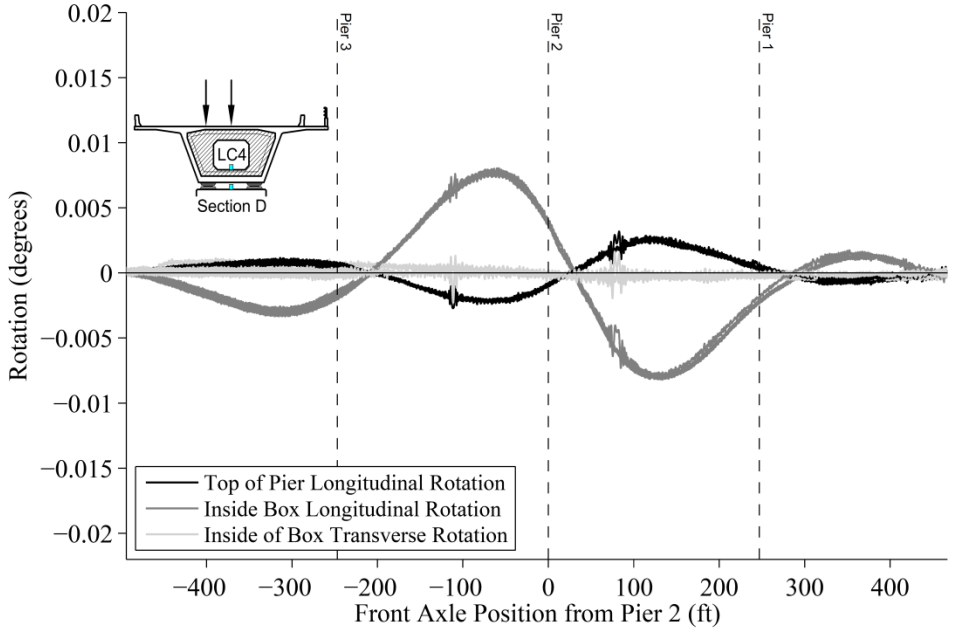

Figure A25 – Seabreeze Bridge Rotation from LC4 at Section D – All Iterations

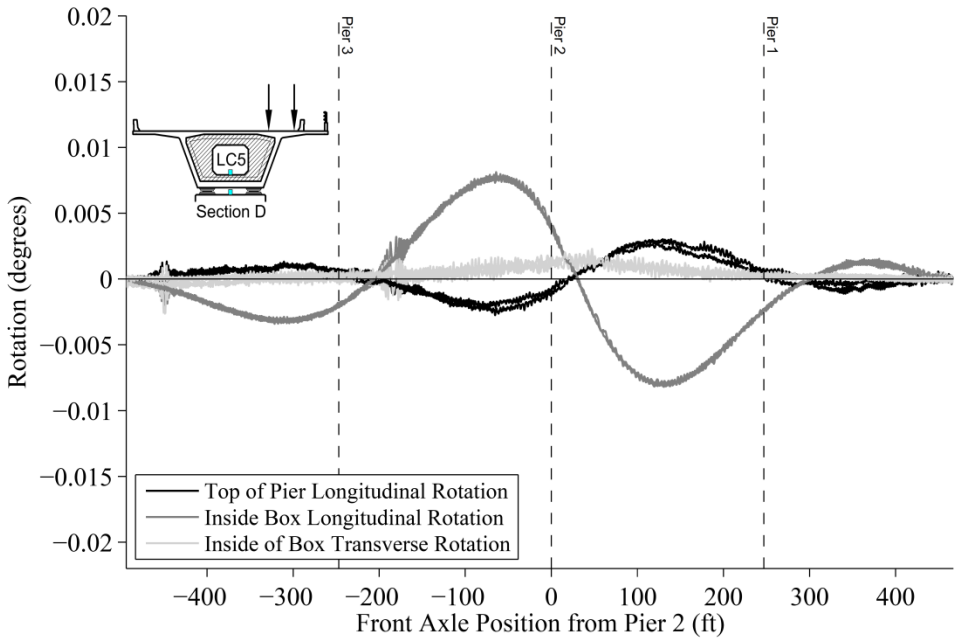

Figure A26 – Seabreeze Bridge Rotation from LC5 at Section D – All Iterations

8.4 Seabreeze Bridge Vertical Deflections

8.4.1 Seabreeze Bridge Section A and E

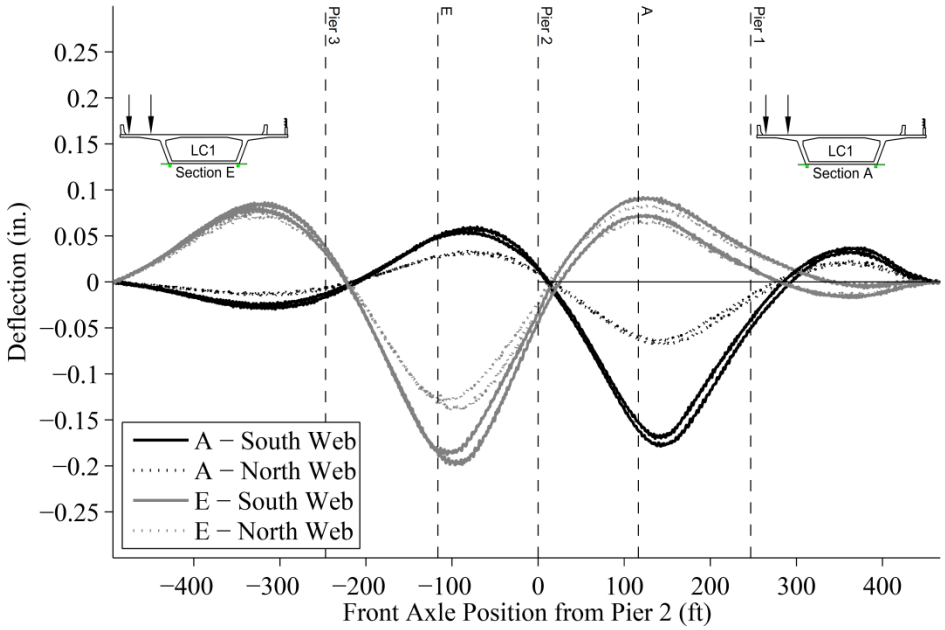

Figure A27 – Seabreeze Bridge Deflection from LC1 at Sections A and E – All Iterations

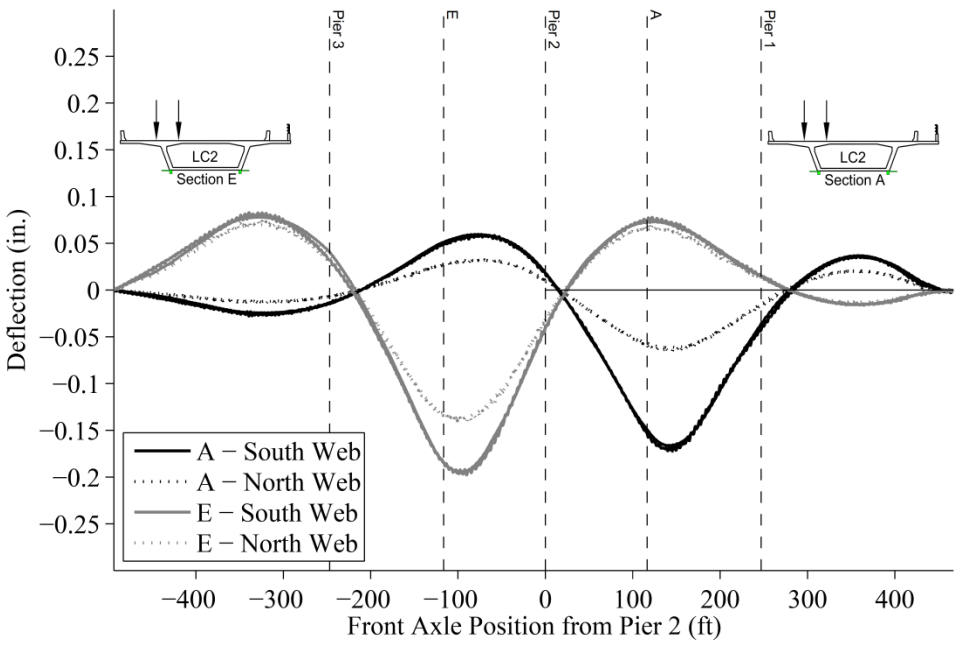

Figure A28 – Seabreeze Bridge Deflection from LC2 at Sections A and E – All Iterations

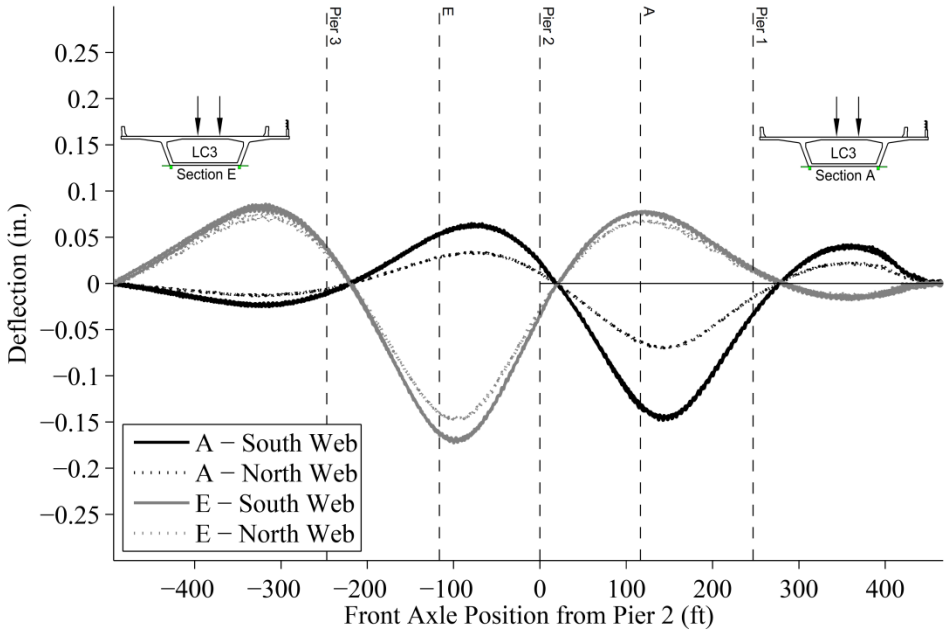

Figure A29 – Seabreeze Bridge Deflection from LC3 at Sections A and E – All Iterations

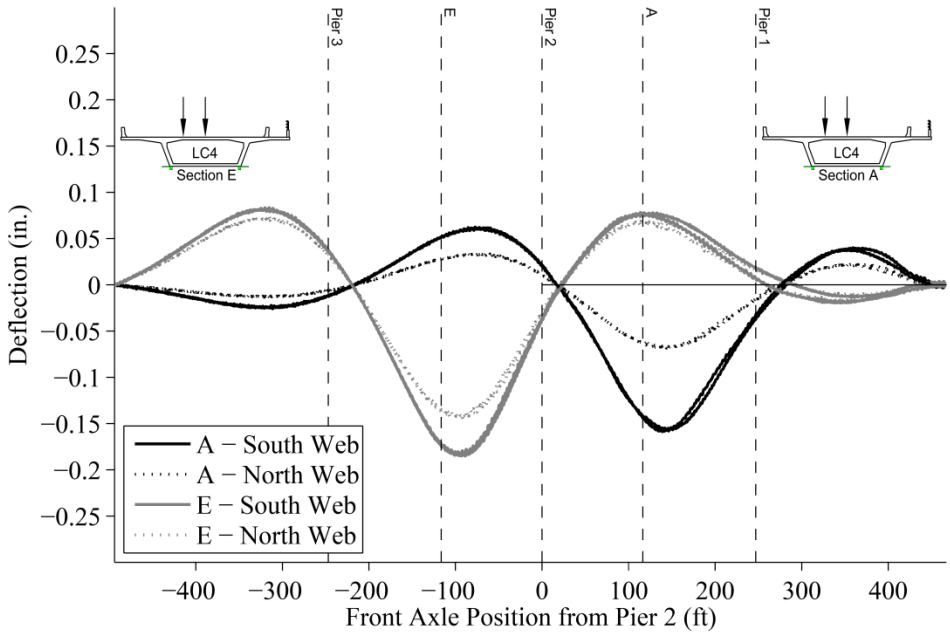

Figure A30 – Seabreeze Bridge Deflection from LC4 at Sections A and E – All Iterations

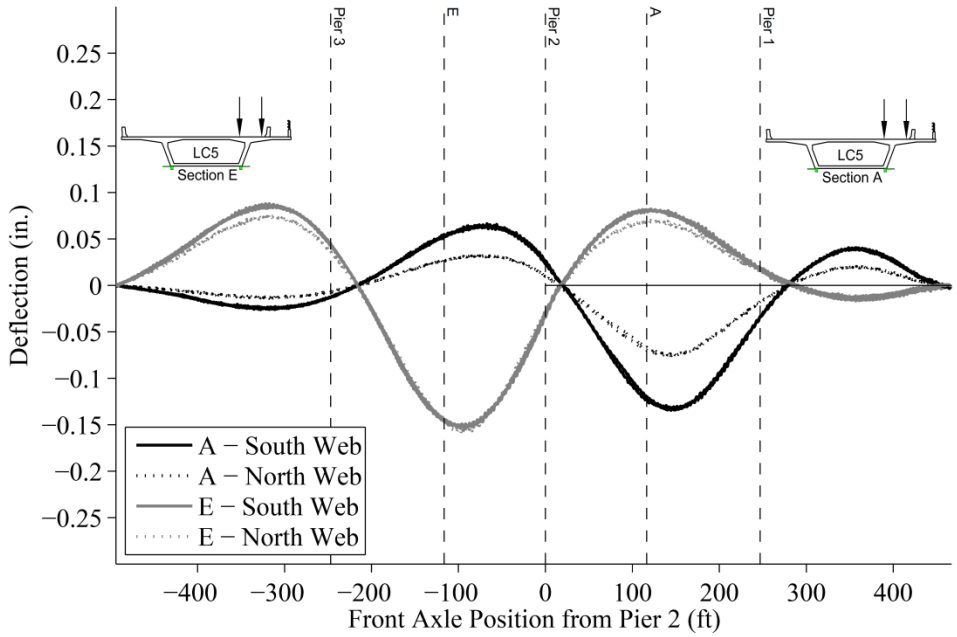

Figure A31 – Seabreeze Bridge Deflection from LC5 at Sections A and E – All Iterations

9 Appendix B: Smart Road Bridge Test Results

The following appendix presents the results from the Smart Road Bridge load test. Figure B1 through Figure B10 present the measured longitudinal strain versus truck position plots for Sections A and B under LC1 through LC5. Figure B11 through Figure B20 present the measured transverse strain versus truck position plots for Section A and B under LC1 through LC5.

9.1 Smart Road Bridge Longitudinal Strains

9.1.1 Smart Road Bridge Section A

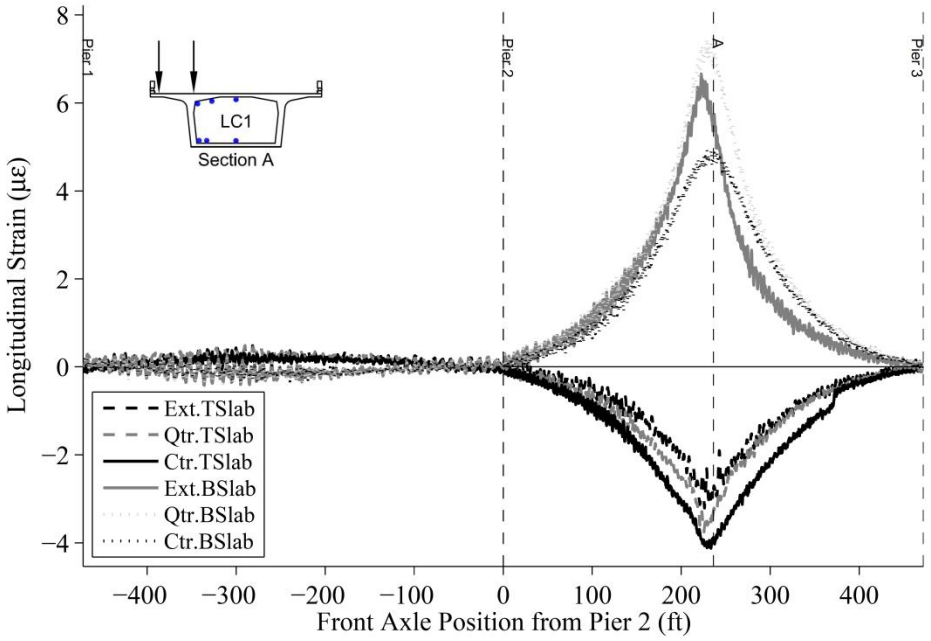

Figure B1 – Smart Road Bridge Longitudinal Strains from LC1 at Section A – All Iterations

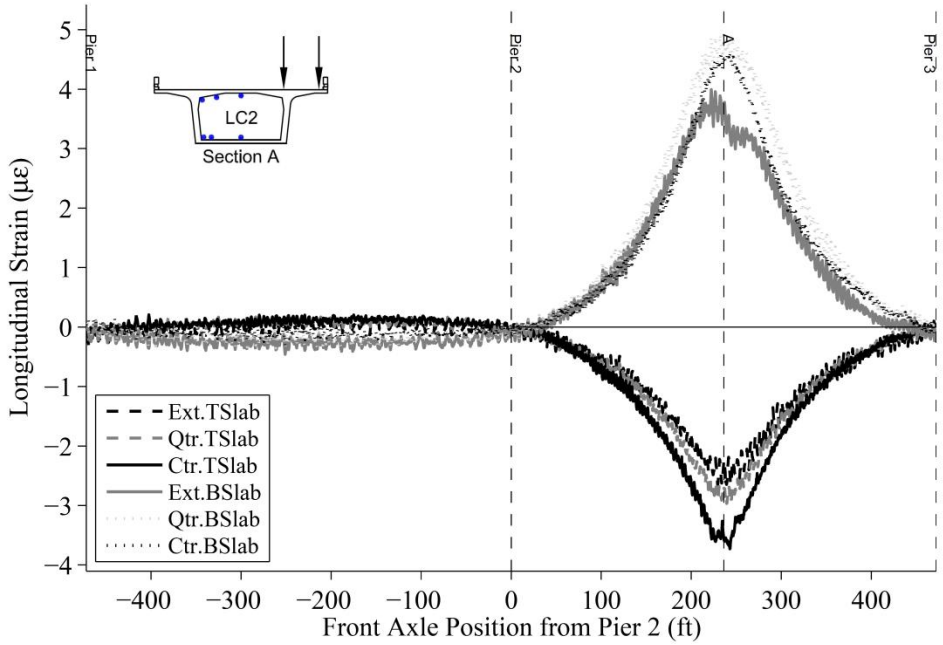

Figure B2 – Smart Road Bridge Longitudinal Strains from LC2 at Section A – All Iterations

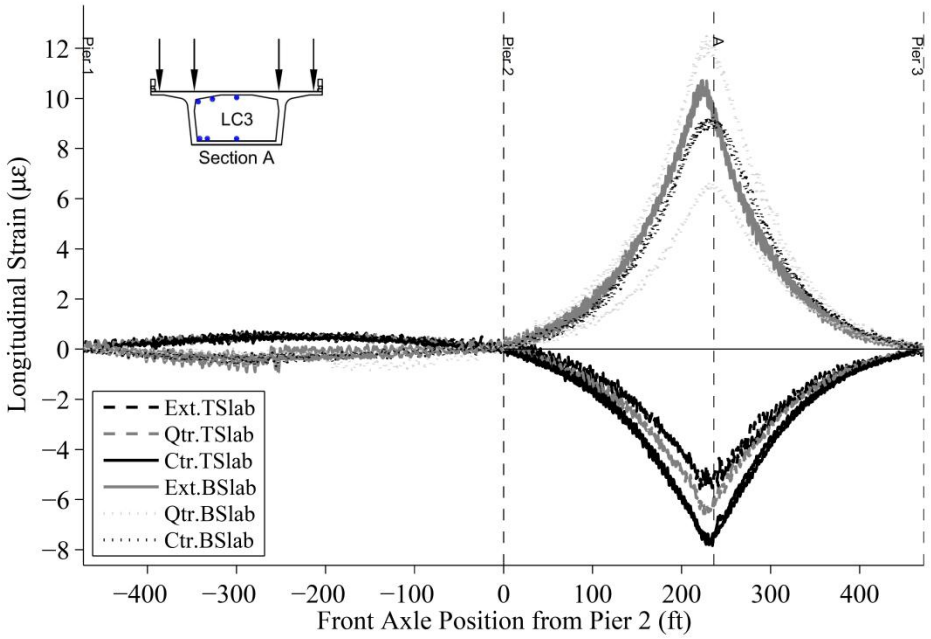

Figure B3 – Smart Road Bridge Longitudinal Strains from LC3 at Section A – All Iterations

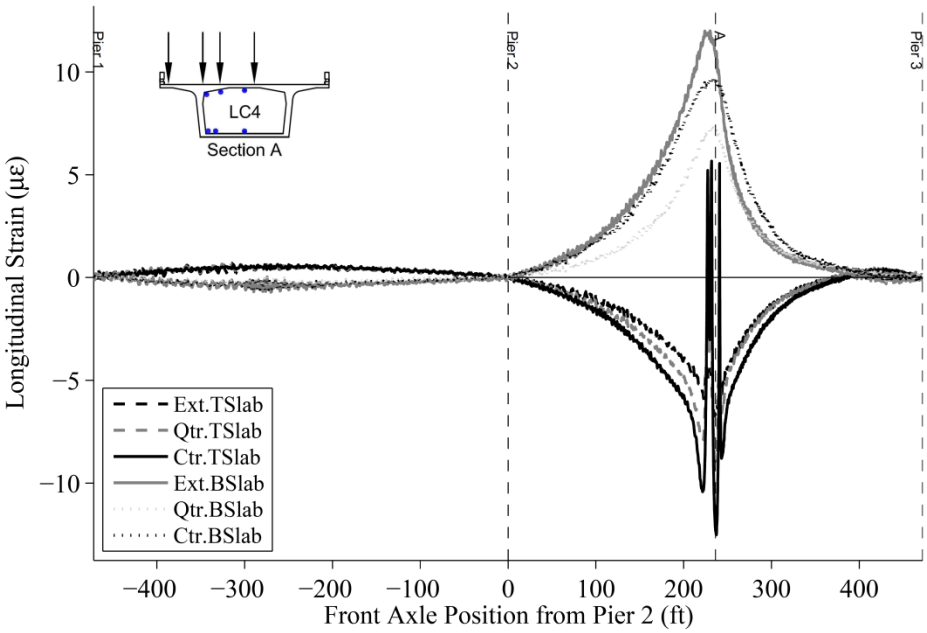

Figure B4 – Smart Road Bridge Longitudinal Strains from LC4 at Section A – All Iterations

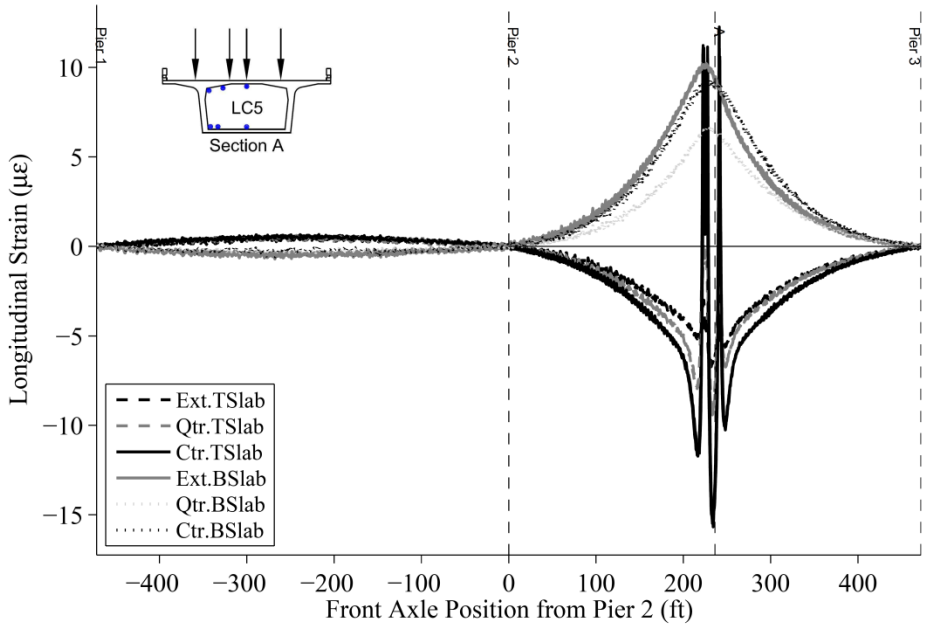

Figure B5 – Smart Road Bridge Longitudinal Strains from LC5 at Section A – All Iterations

9.1.2 Smart Road Bridge Section B

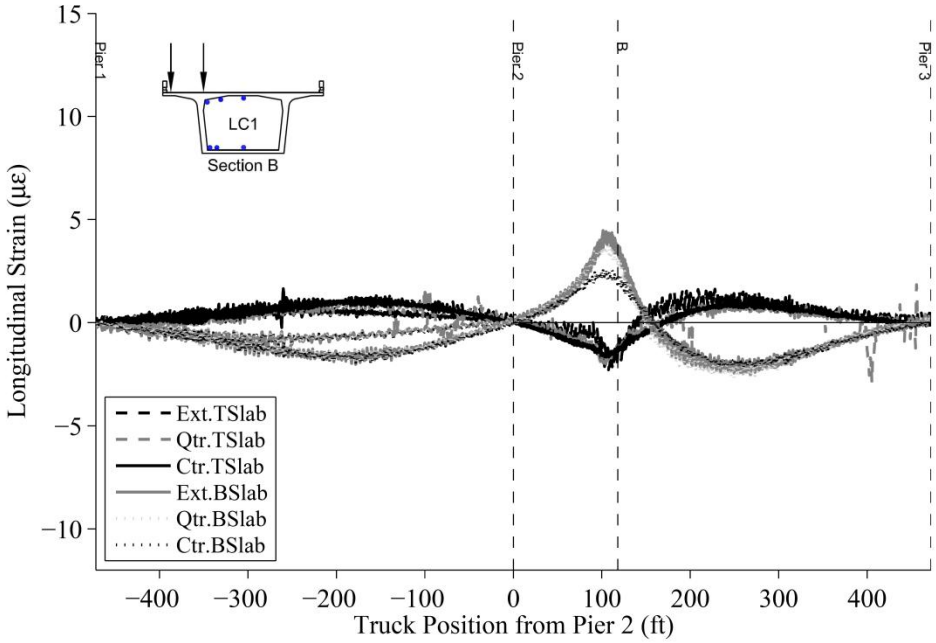

Figure B6 – Smart Road Bridge Longitudinal Strains from LC1 at Section B – All Iterations

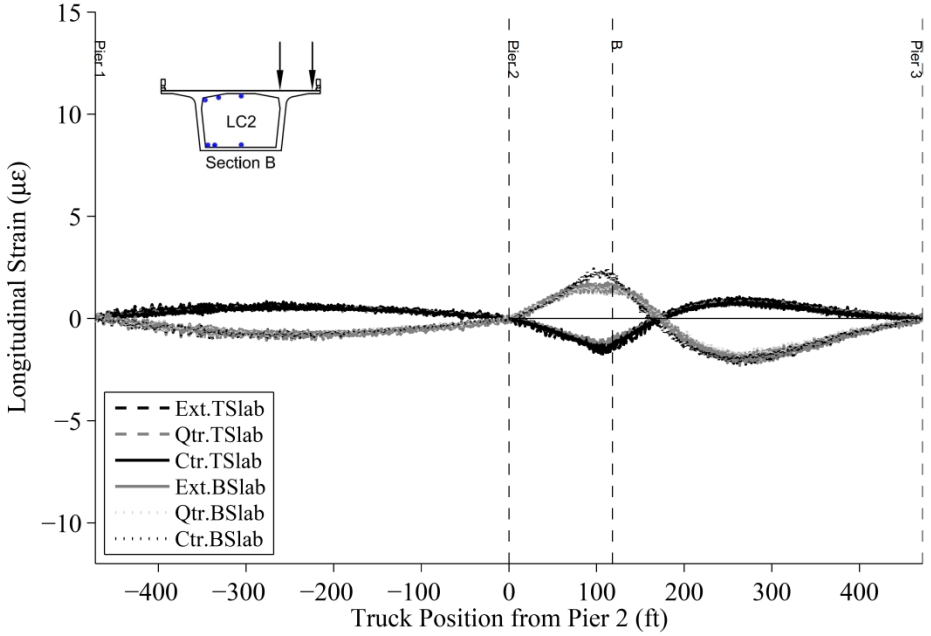

Figure B7 – Smart Road Bridge Longitudinal Strains from LC2 at Section B – All Iterations

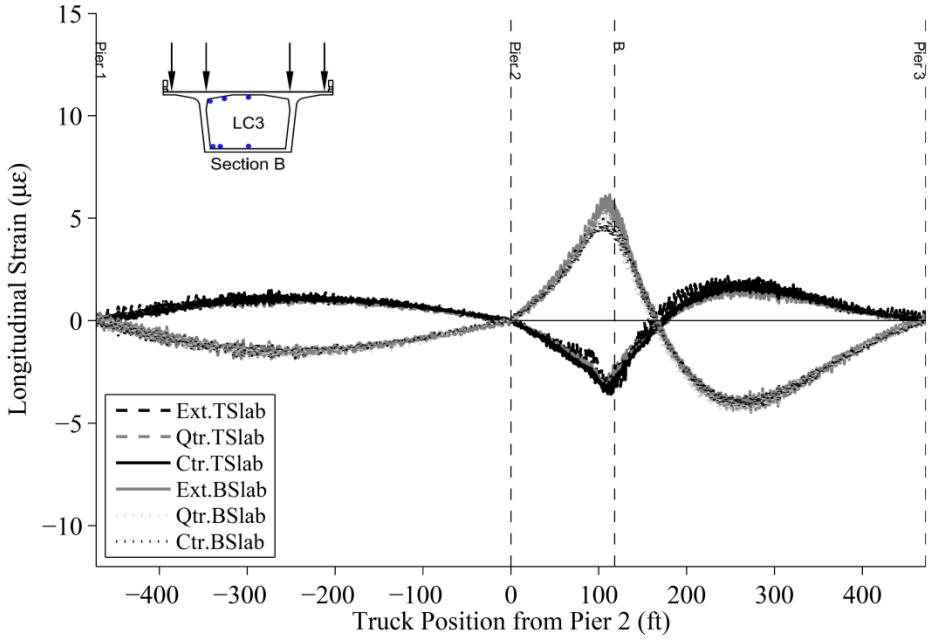

Figure B8 – Smart Road Bridge Longitudinal Strains from LC3 at Section B – All Iterations

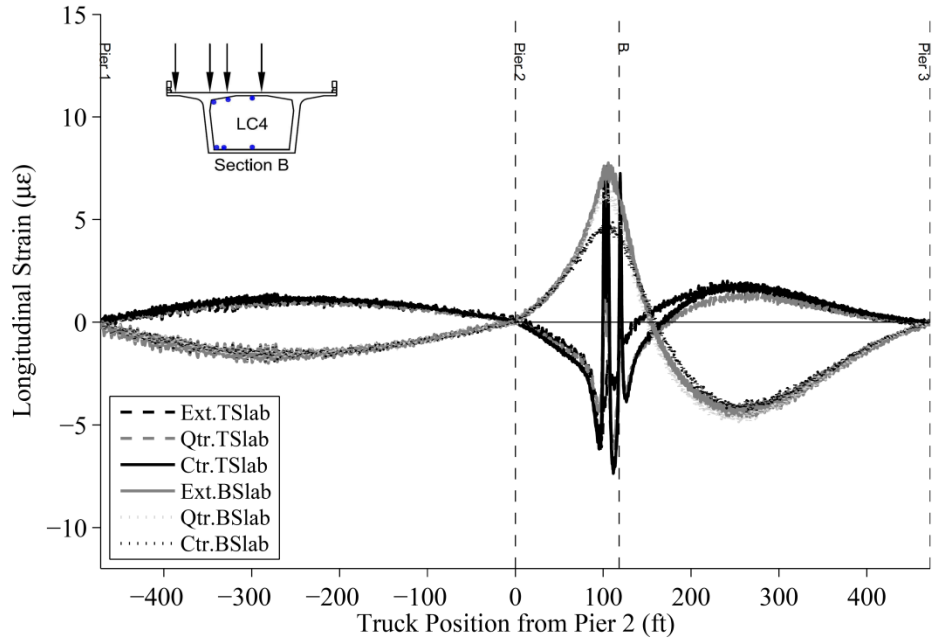

Figure B9 – Smart Road Bridge Longitudinal Strains from LC4 at Section B – All Iterations

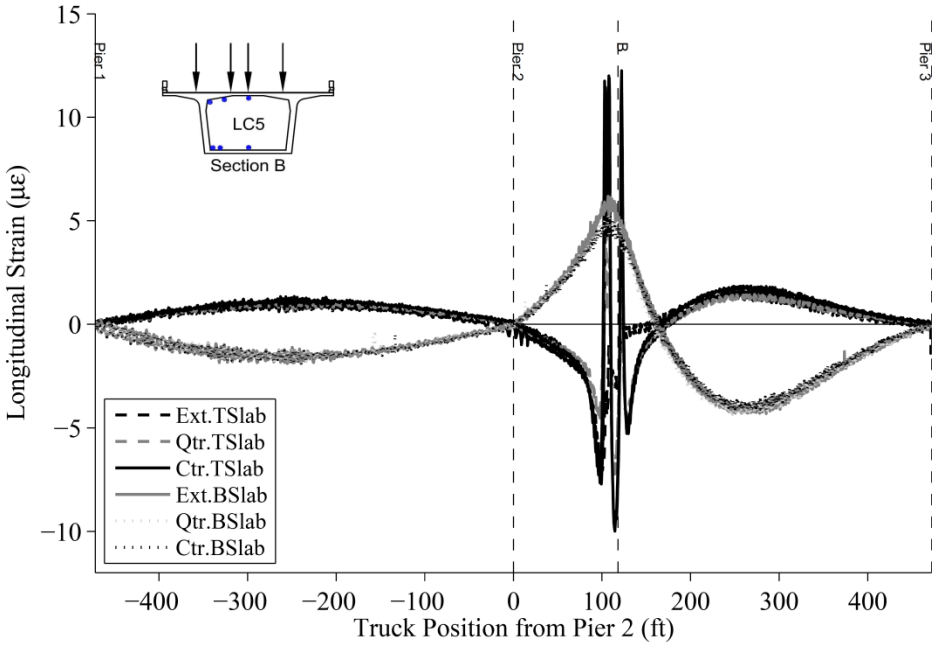

Figure B10 – Smart Road Bridge Longitudinal Strains from LC5 at Section B – All Iterations

9.2 Smart Road Bridge Transverse Strains

9.2.1 Smart Road Bridge Section A

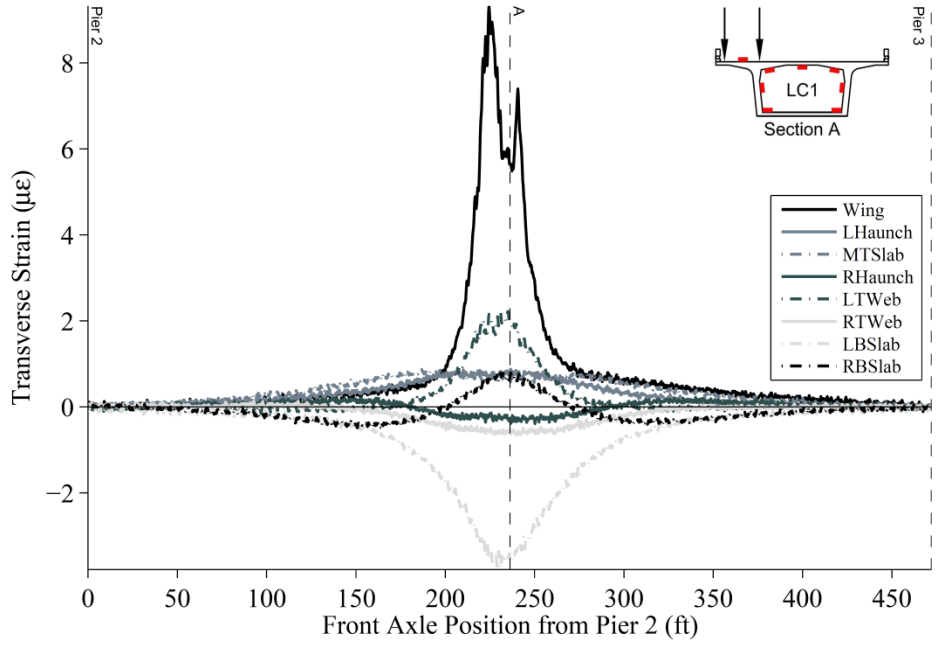

Figure B11 – Smart Road Bridge Transverse Strains from LC1 at Section A – All Iterations

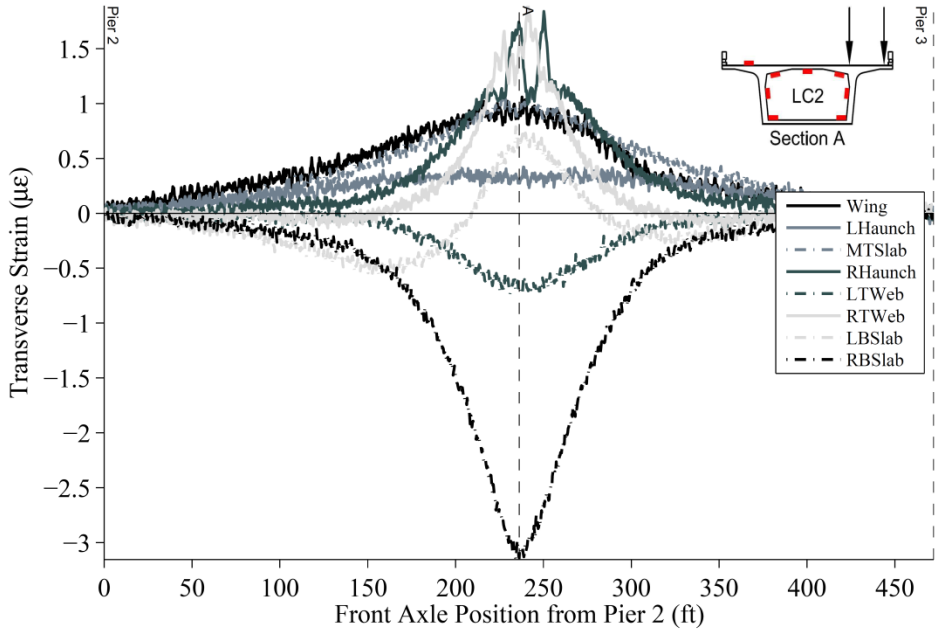

Figure B12 – Smart Road Bridge Transverse Strains from LC2 at Section A – All Iterations

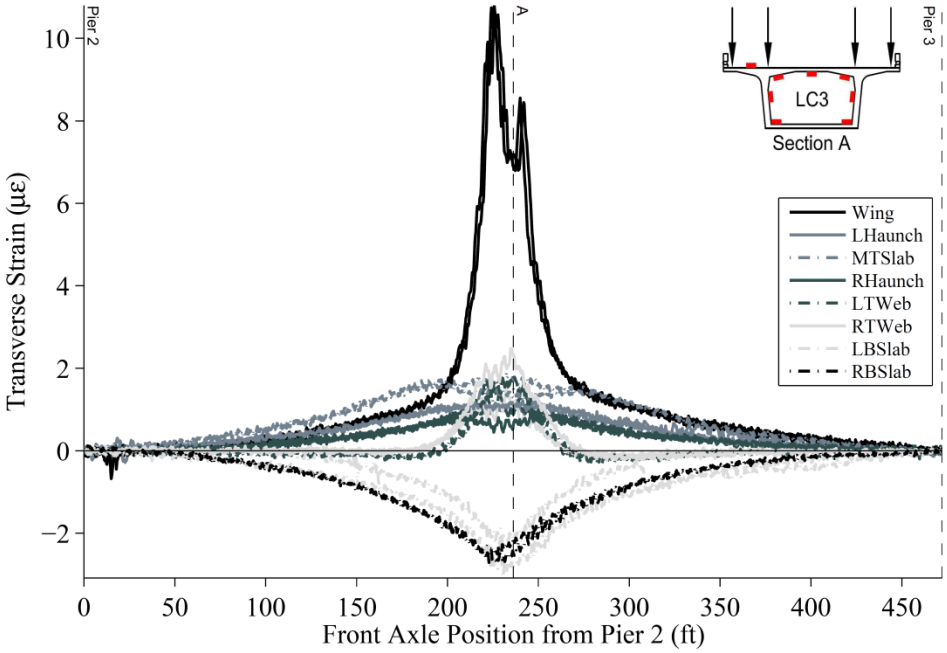

Figure B13 – Smart Road Bridge Transverse Strains from LC3 at Section A – All Iterations

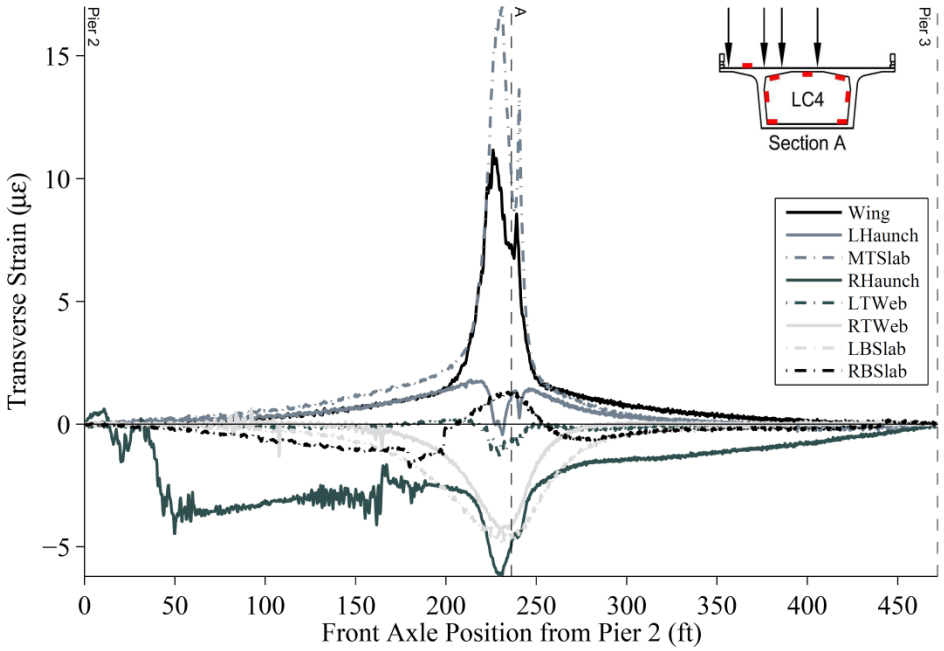

Figure B14 – Smart Road Bridge Transverse Strains from LC4 at Section A – All Iterations

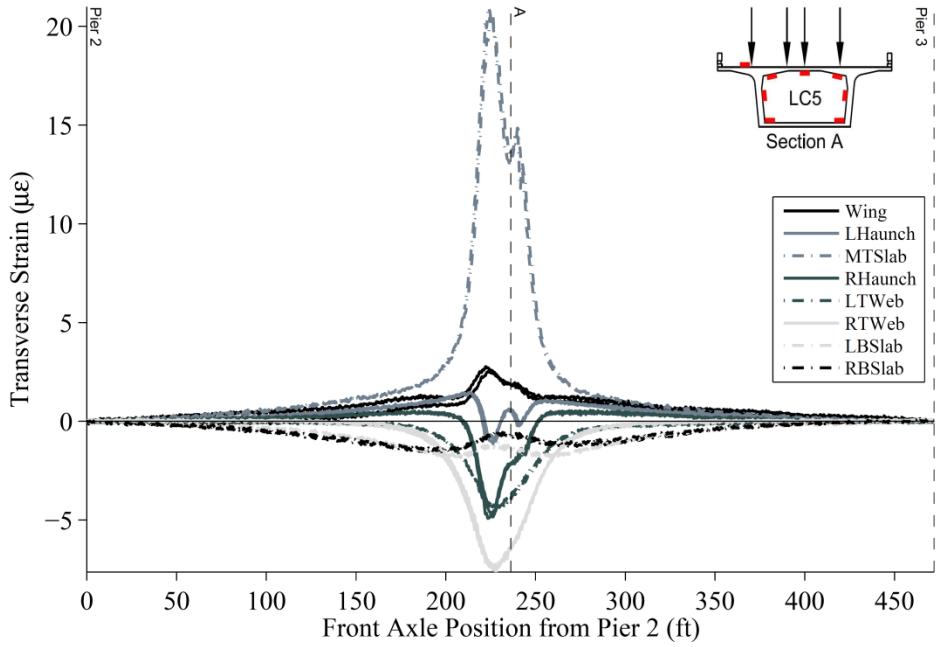

Figure B15 – Smart Road Bridge Transverse Strains from LC5 at Section A – All Iterations

9.2.2 Smart Road Bridge Section B

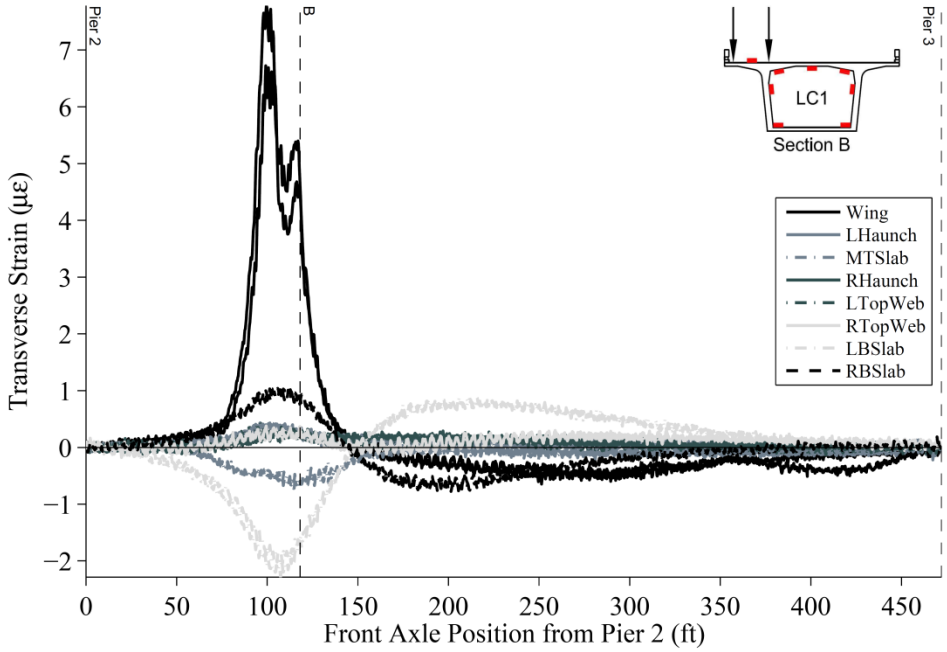

Figure B16 – Smart Road Bridge Transverse Strains from LC1 at Section B – All Iterations

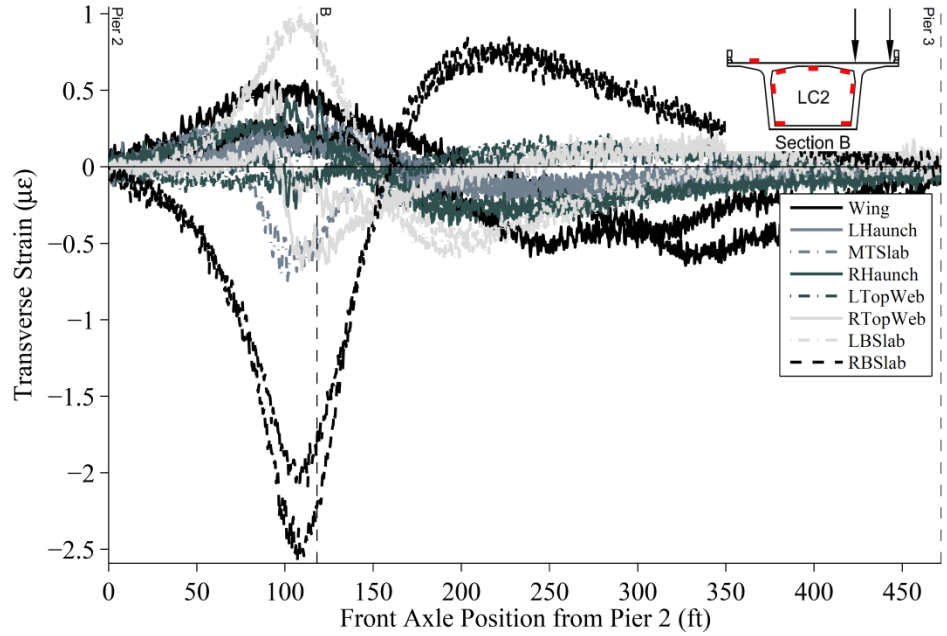

Figure B17 – Smart Road Bridge Transverse Strains from LC2 at Section B – All Iterations

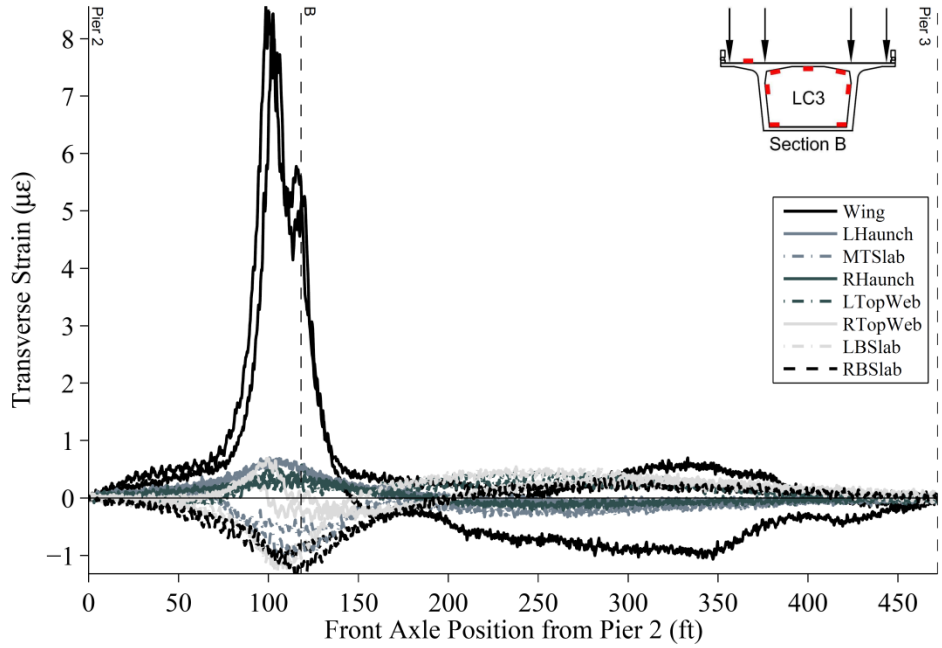

Figure B18 – Smart Road Bridge Transverse Strains from LC3 at Section B – All Iterations

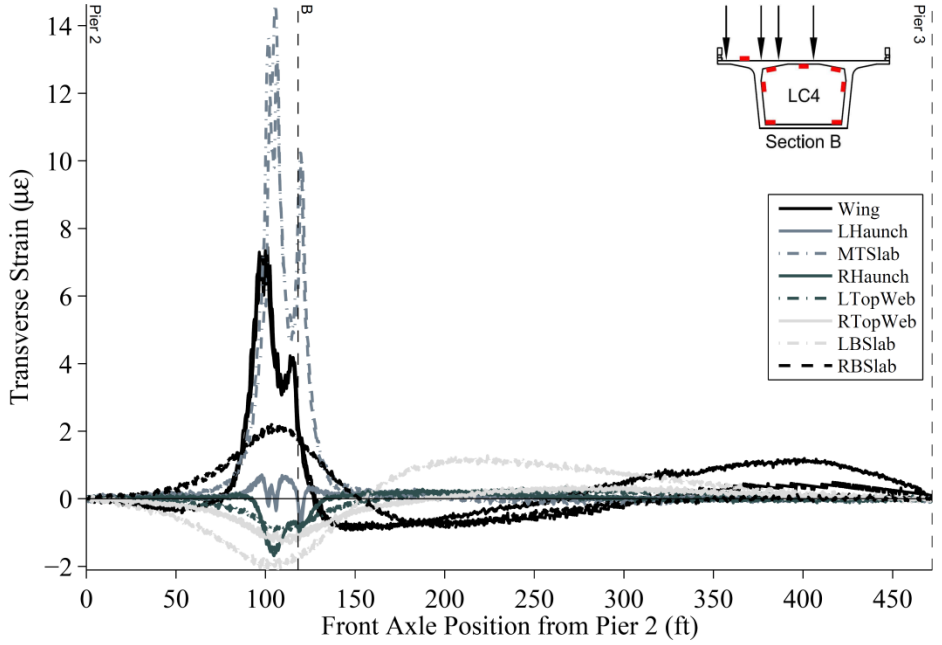

Figure B19 – Smart Road Bridge Transverse Strains from LC4 at Section B – All Iterations

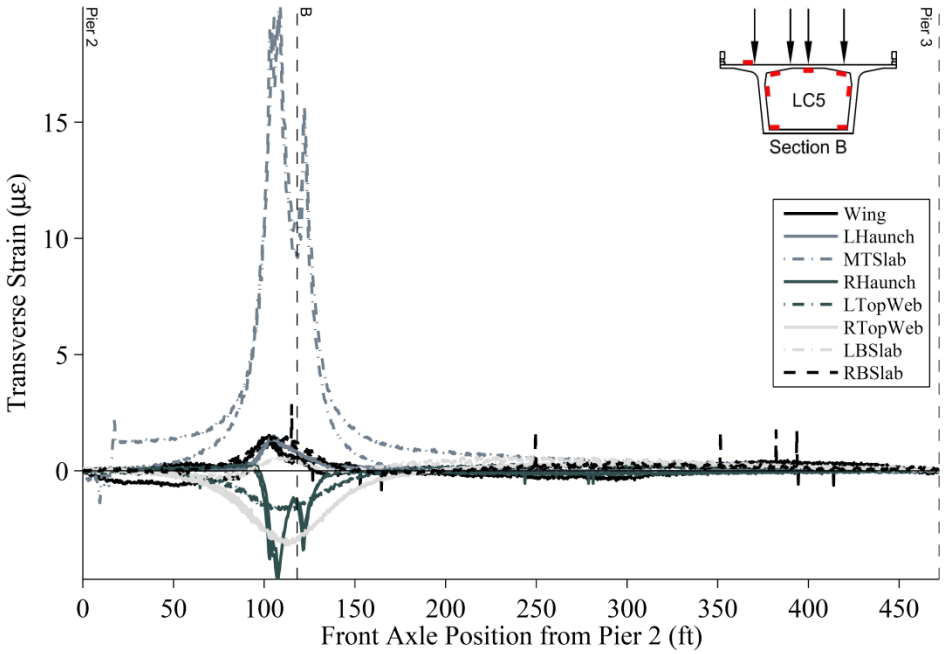

Figure B20 – Smart Road Bridge Transverse Strains from LC5 at Section B – All Iterations

10 Appendix C: Varina-Enon Bridge Test Results

The following appendix presents the results from the Varina-Enon Bridge load test. Figure C1 through Figure C33 present measured longitudinal strains at Section B and Section D under LC1 though LC5 with each iteration. Figure C34 and Figure C43 present measured transverse strains at Section D and C under LC4 through LC6 with each iteration. Figure C44 and Figure C49 present vertical deflections at Section A under LC1 through LC6 with each iteration.

10.1 Varina-Enon Bridge Longitudinal Strains

10.1.1 Varina-Enon Bridge Section B

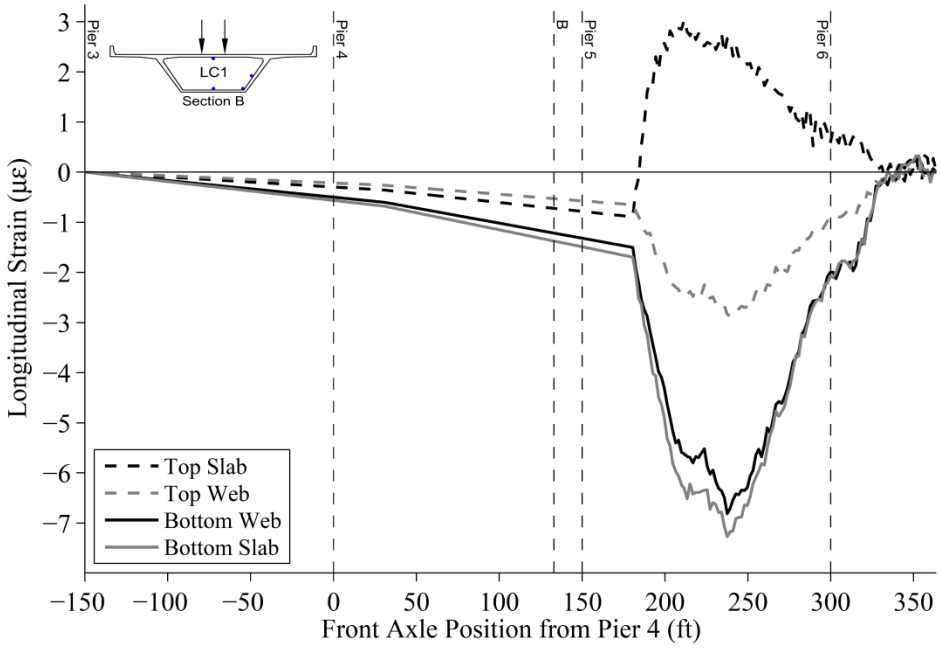

Figure C1 – Varina-Enon Bridge Longitudinal Strains from LC1 at Section B – Iteration 1

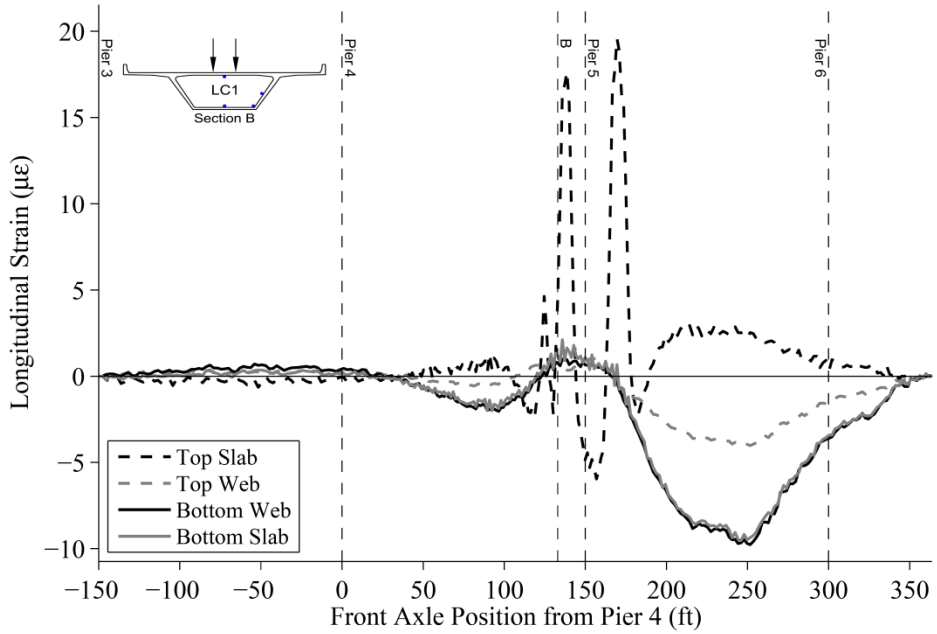

Figure C2 – Varina-Enon Bridge Longitudinal Strains from LC1 at Section B – Iteration 2

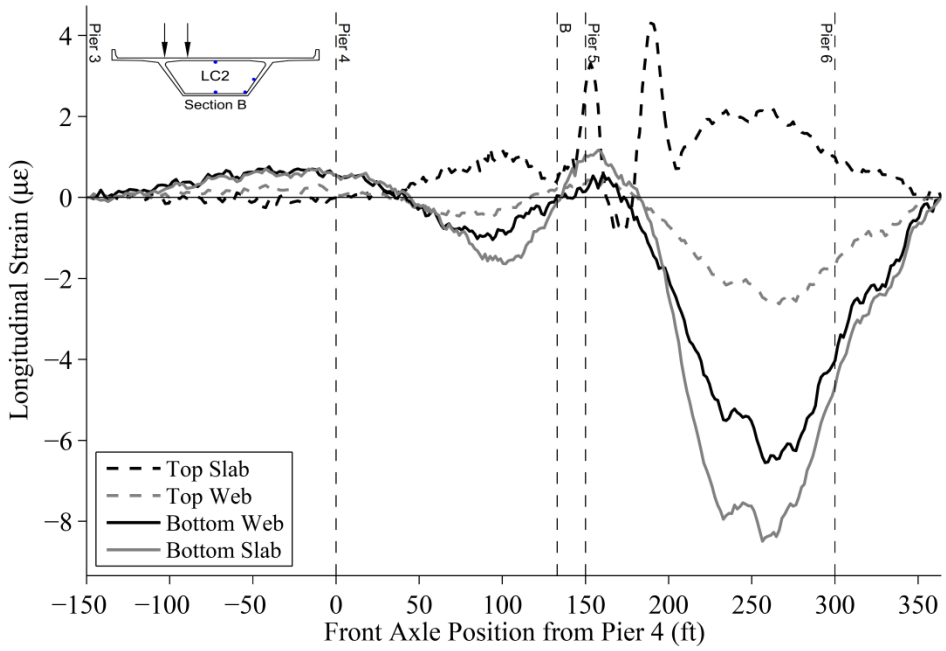

Figure C3 – Varina-Enon Bridge Longitudinal Strains from LC2 at Section B – Iteration 1

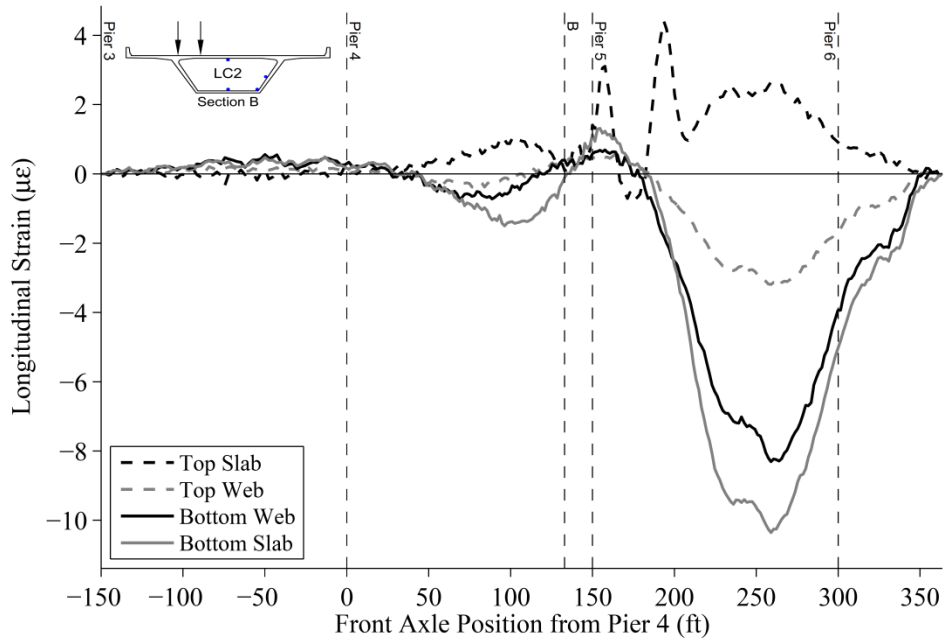

Figure C4 – Varina-Enon Bridge Longitudinal Strains from LC2 at Section B – Iteration 2

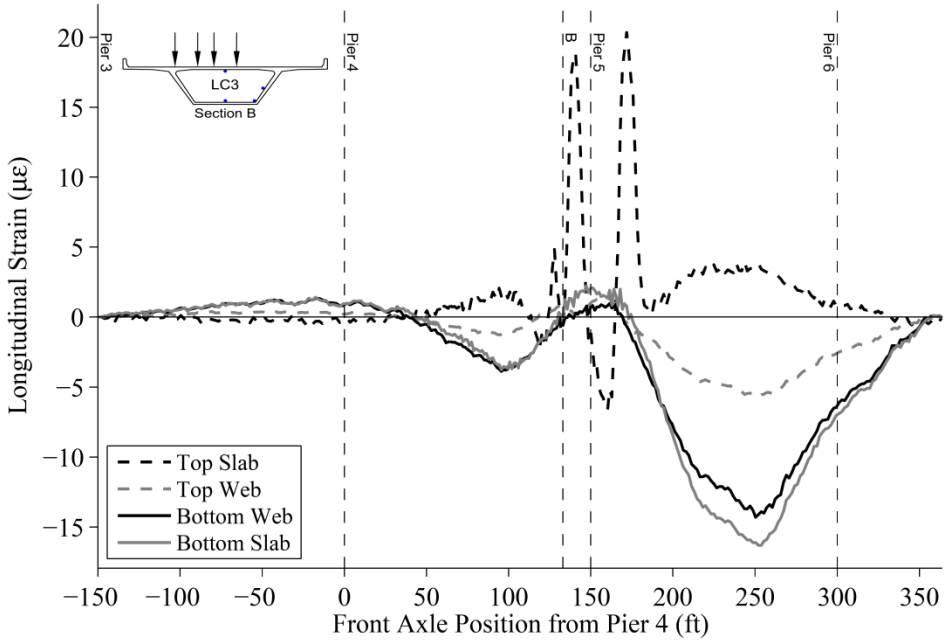

Figure C5 – Varina-Enon Bridge Longitudinal Strains from LC3 at Section B – Iteration 1

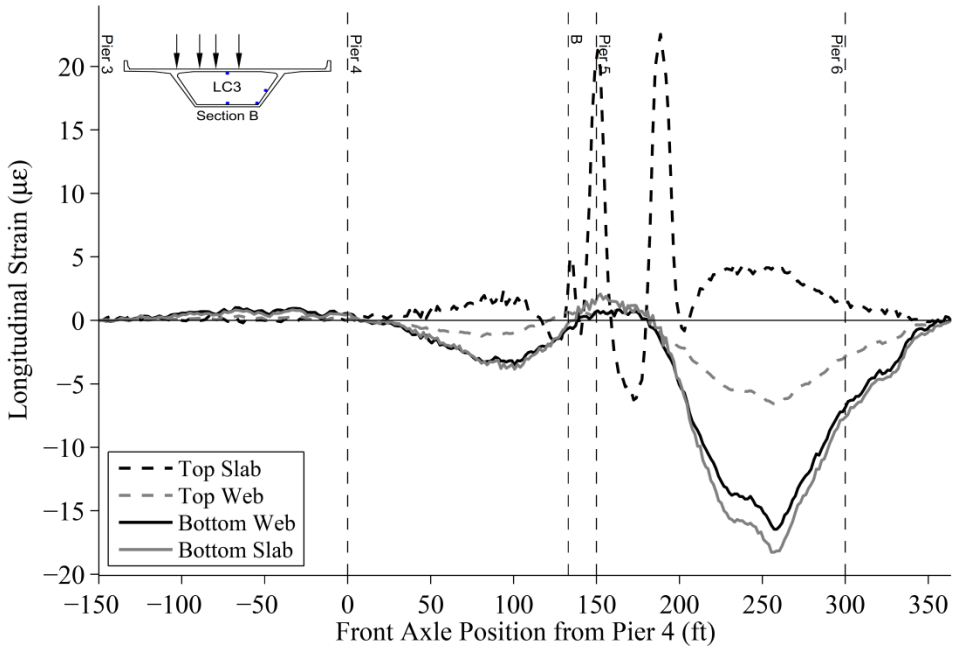

Figure C6 – Varina-Enon Bridge Longitudinal Strains from LC3 at Section B – Iteration 2

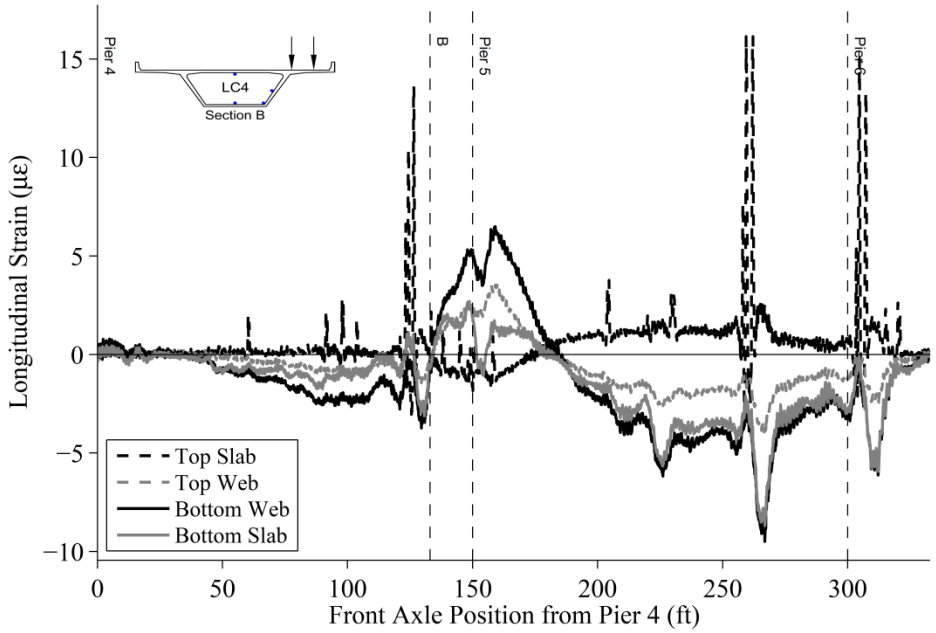

Figure C7 – Varina-Enon Bridge Longitudinal Strains from LC4 at Section B – Iteration 1

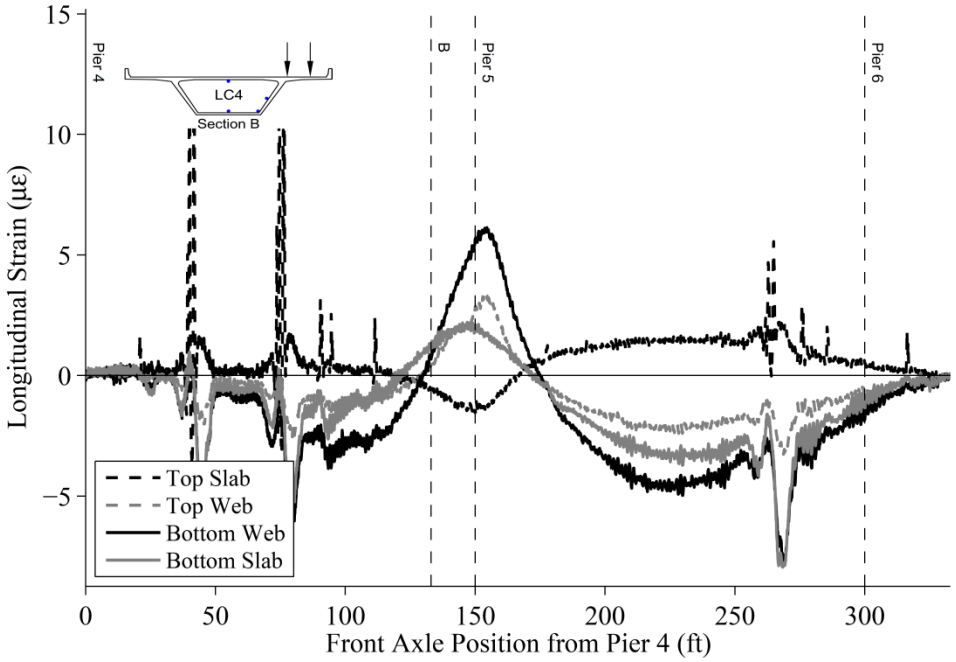

Figure C8 – Varina-Enon Bridge Longitudinal Strains from LC4 at Section B – Iteration 2

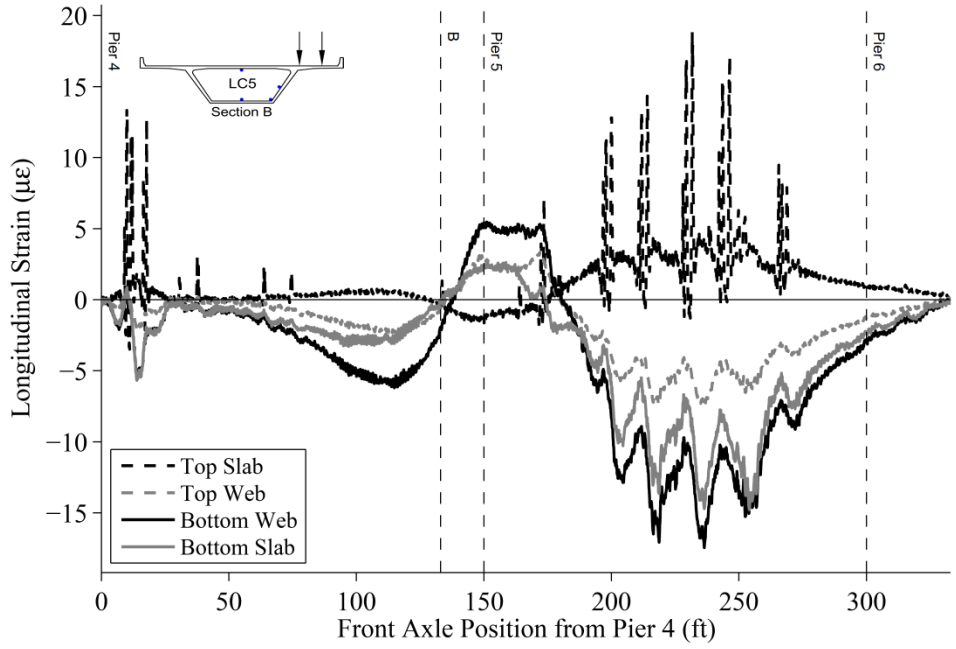

Figure C9 – Varina-Enon Bridge Longitudinal Strains from LC5 at Section B – Iteration 1

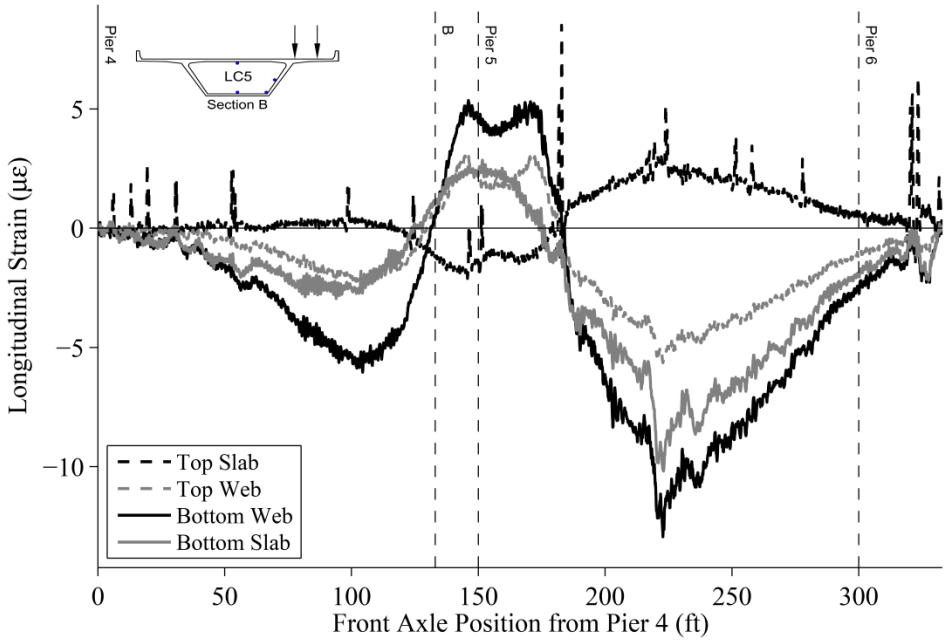

Figure C10 – Varina-Enon Bridge Longitudinal Strains from LC5 at Section B – Iteration 2

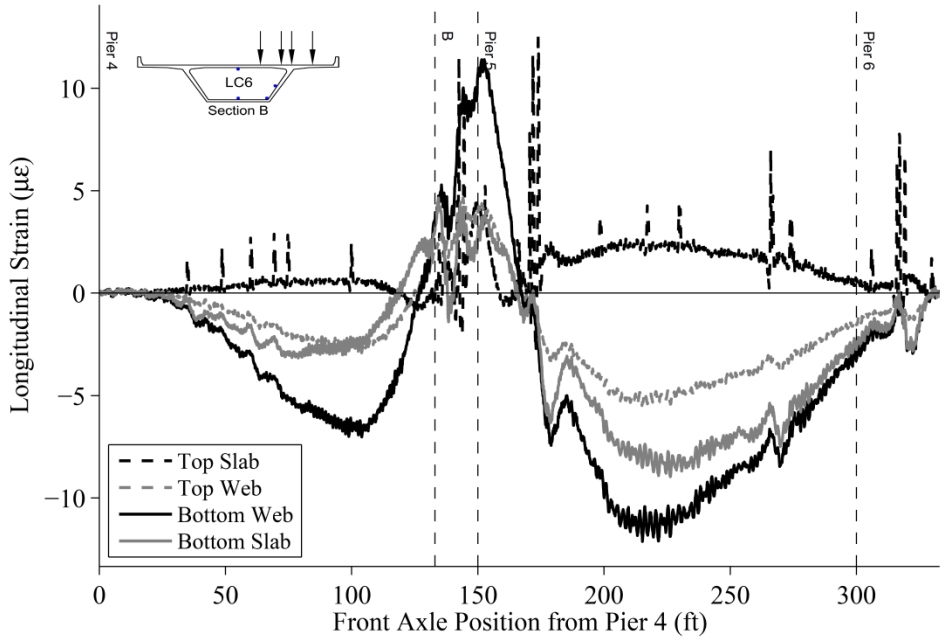

Figure C11 – Varina-Enon Bridge Longitudinal Strains from LC6 at Section B – Iteration 1

10.1.2 Varina-Enon Bridge Section D

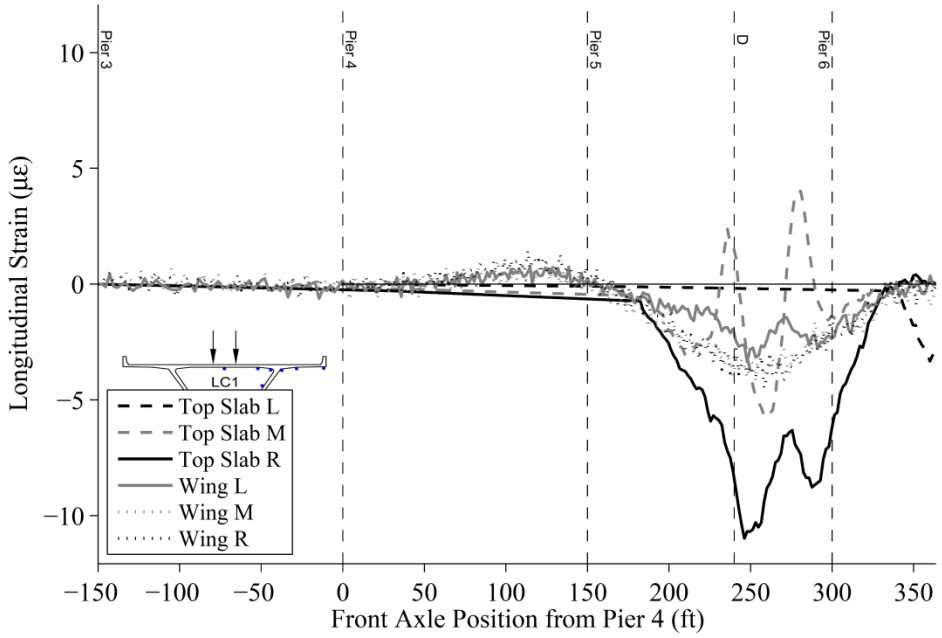

Figure C12 – Varina-Enon Bridge Top Slab and Wing Longitudinal Strains from LC1 at Section D – Iteration 1

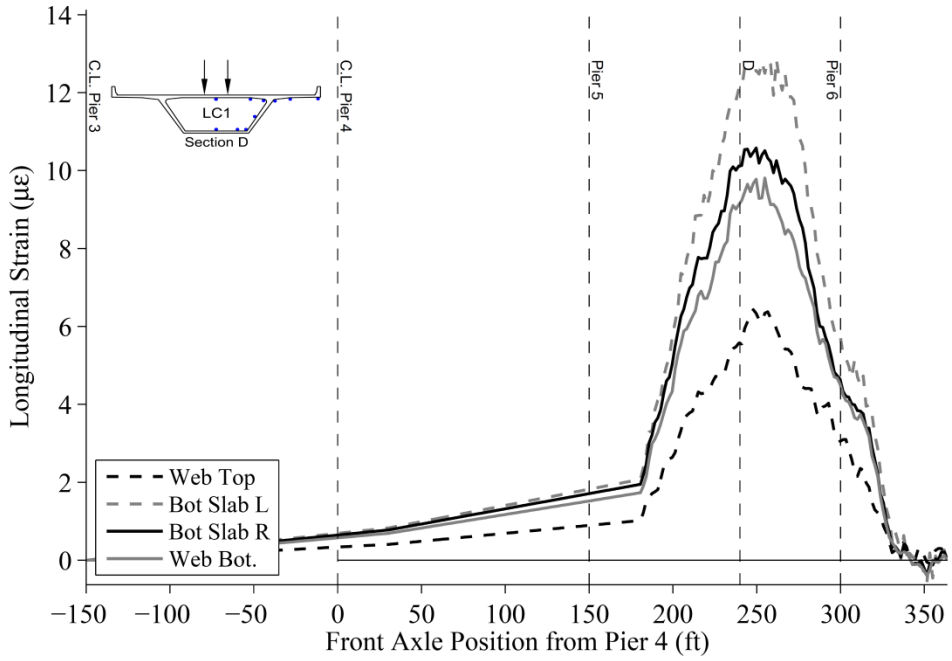

Figure C13 – Varina-Enon Bridge Bottom Slab and Web Longitudinal Strains from LC1 at Section D – Iteration 1

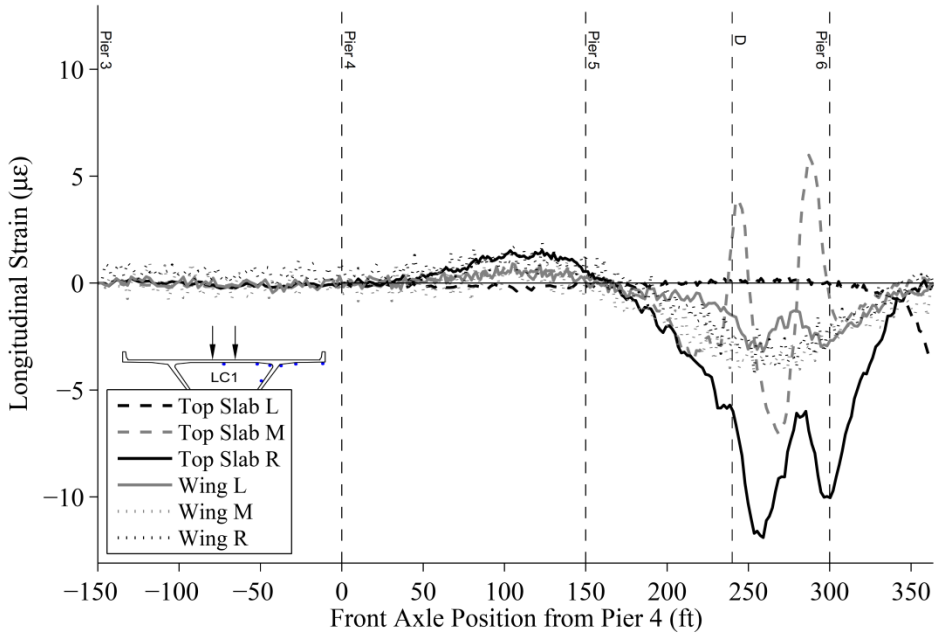

Figure C14 – Varina-Enon Bridge Top Slab and Wing Longitudinal Strains from LC1 at Section D – Iteration 2

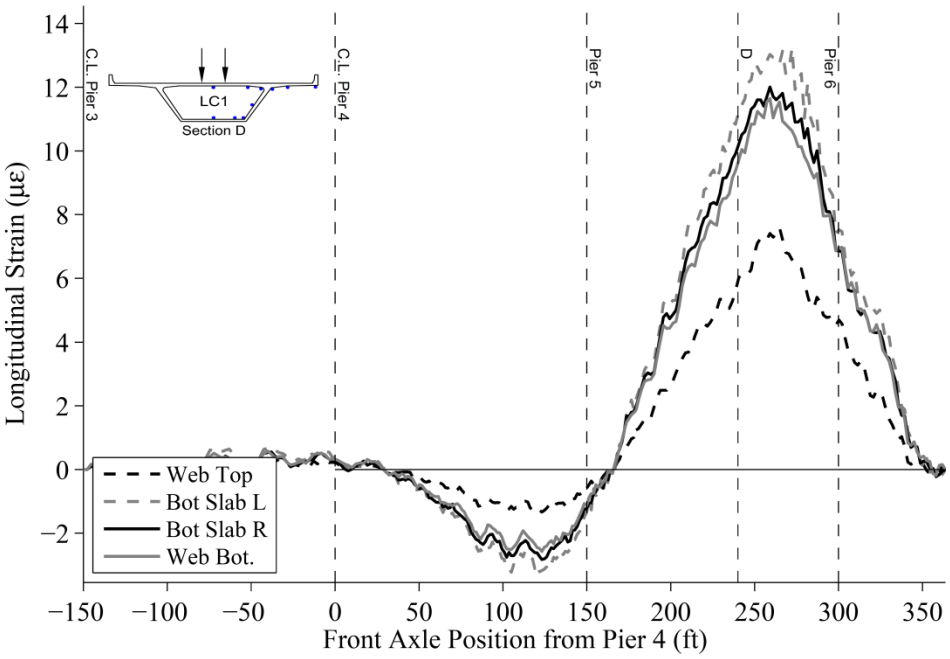

Figure C15 – Varina-Enon Bridge Bottom Slab and Web Longitudinal Strains from LC1 at Section D – Iteration 2

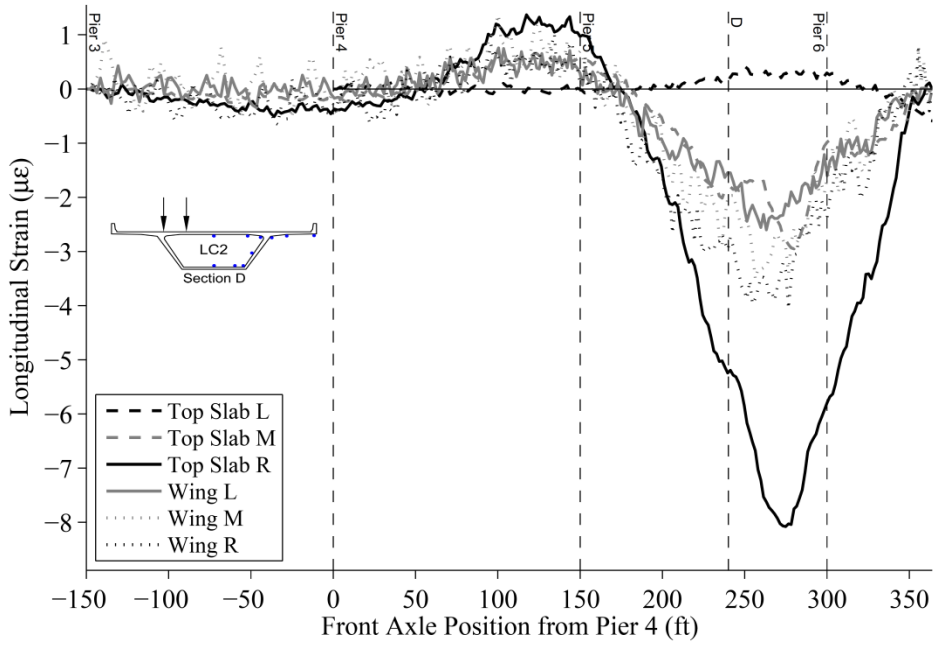

Figure C16 – Varina-Enon Bridge Top Slab and Wing Longitudinal Strains from LC2 at Section D – Iteration 1

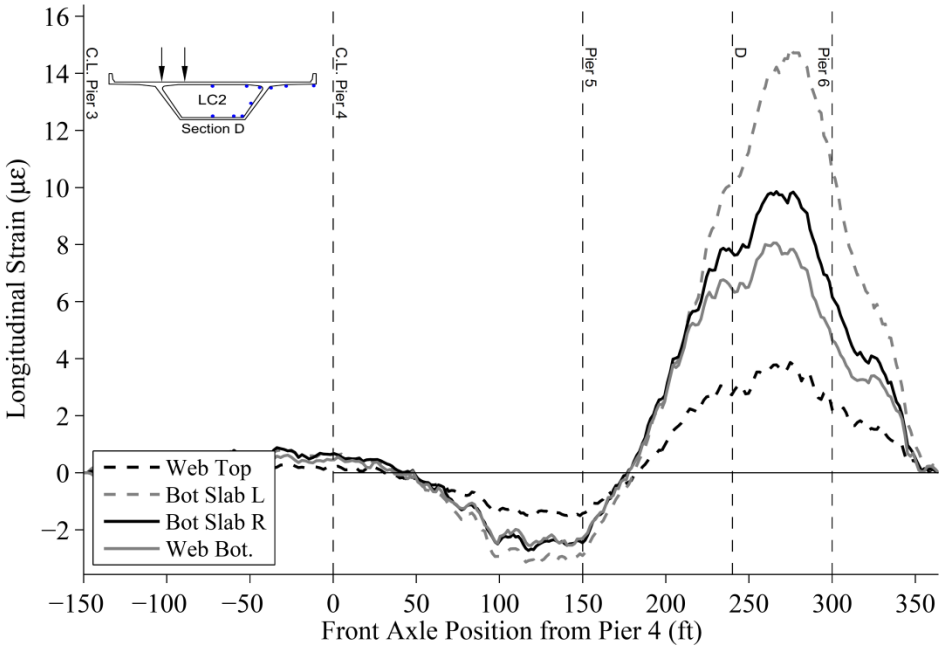

Figure C17 – Varina-Enon Bridge Bottom Slab and Web Longitudinal Strains from LC2 at Section D – Iteration 1

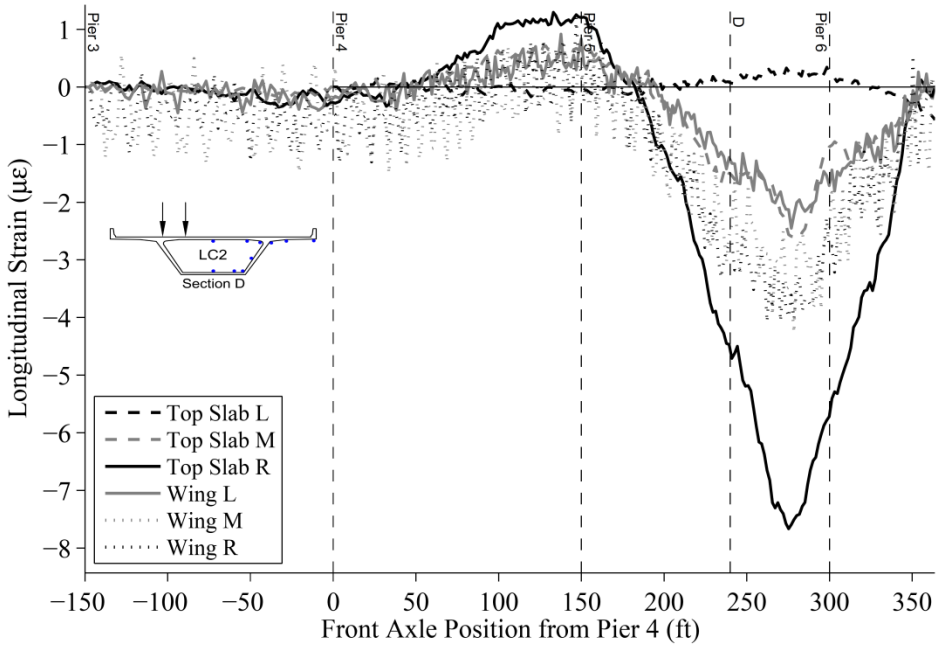

Figure C18 – Varina-Enon Bridge Top Slab and Wing Longitudinal Strains from LC1 at Section D – Iteration 2

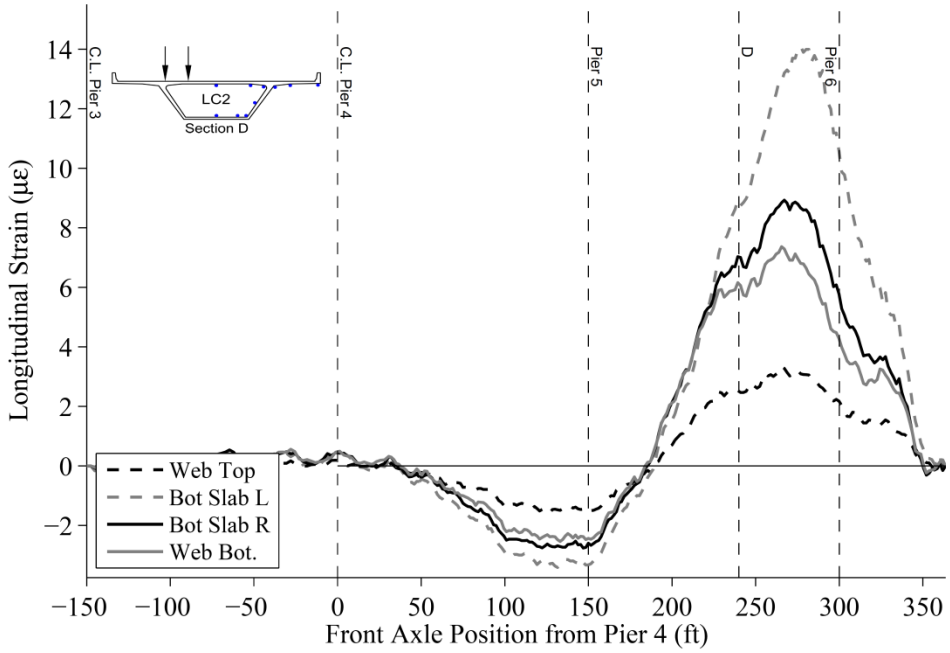

Figure C19 – Varina-Enon Bridge Bottom Slab and Web Longitudinal Strains from LC2 at Section D – Iteration 2

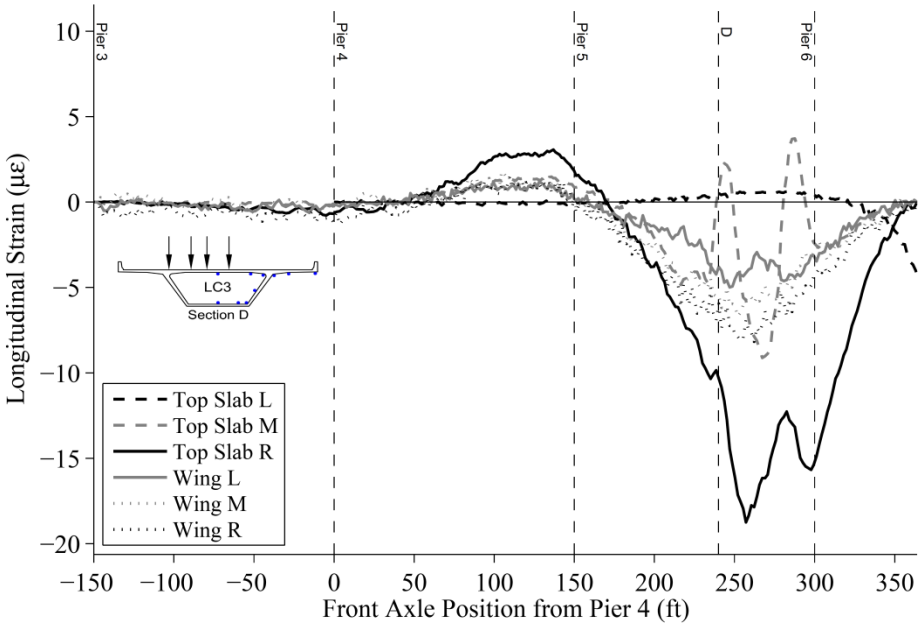

Figure C20 – Varina-Enon Bridge Top Slab and Wing Longitudinal Strains from LC3 at Section D – Iteration 1

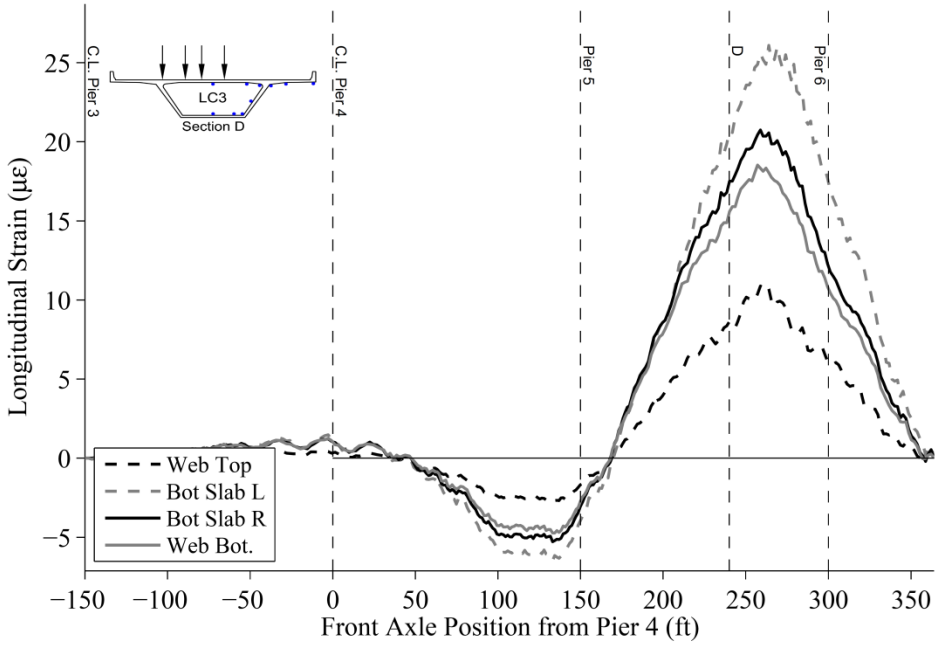

Figure C21 – Varina-Enon Bridge Bottom Slab and Web Longitudinal Strains from LC3 at Section D – Iteration 1

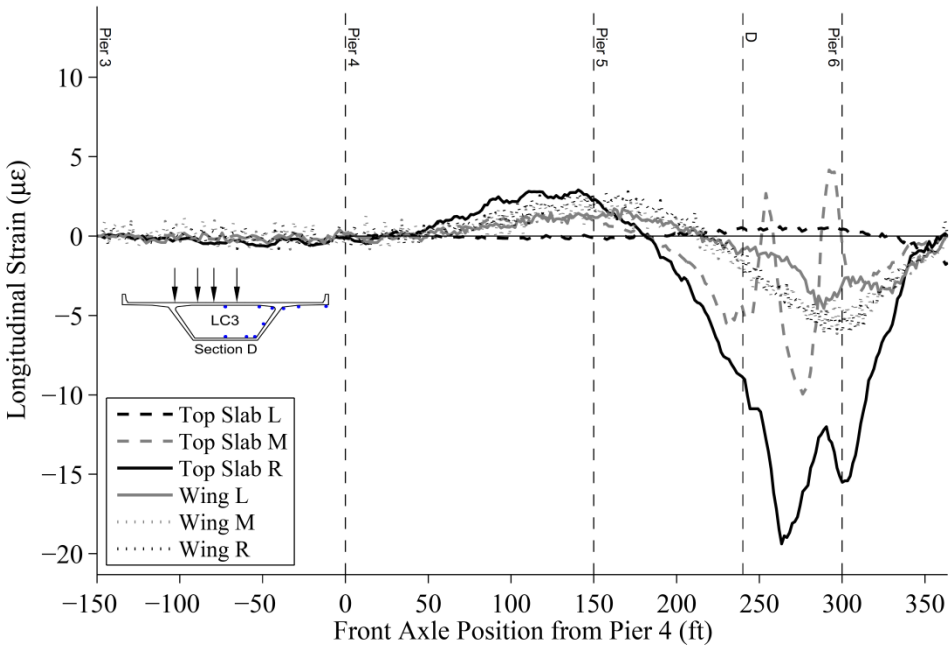

Figure C22 – Varina-Enon Bridge Top Slab and Wing Longitudinal Strains from LC3 at Section D – Iteration 2

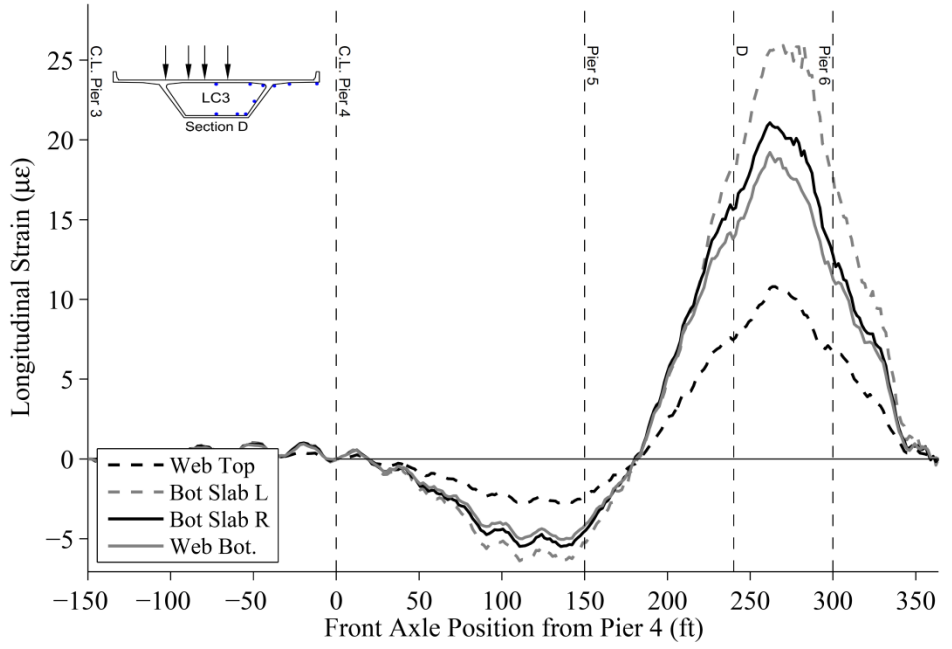

Figure C23 – Varina-Enon Bridge Bottom Slab Slab and Web Longitudinal Strains from LC3 at Section D – Iteration 2

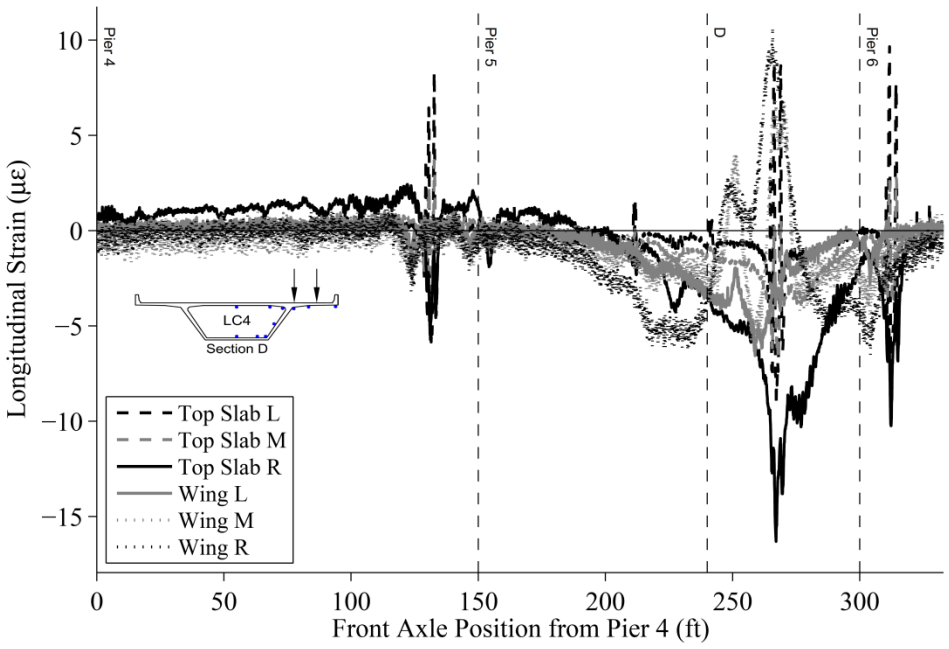

Figure C24 – Varina-Enon Bridge Top Slab and Wing Longitudinal Strains from LC4 at Section D – Iteration 1

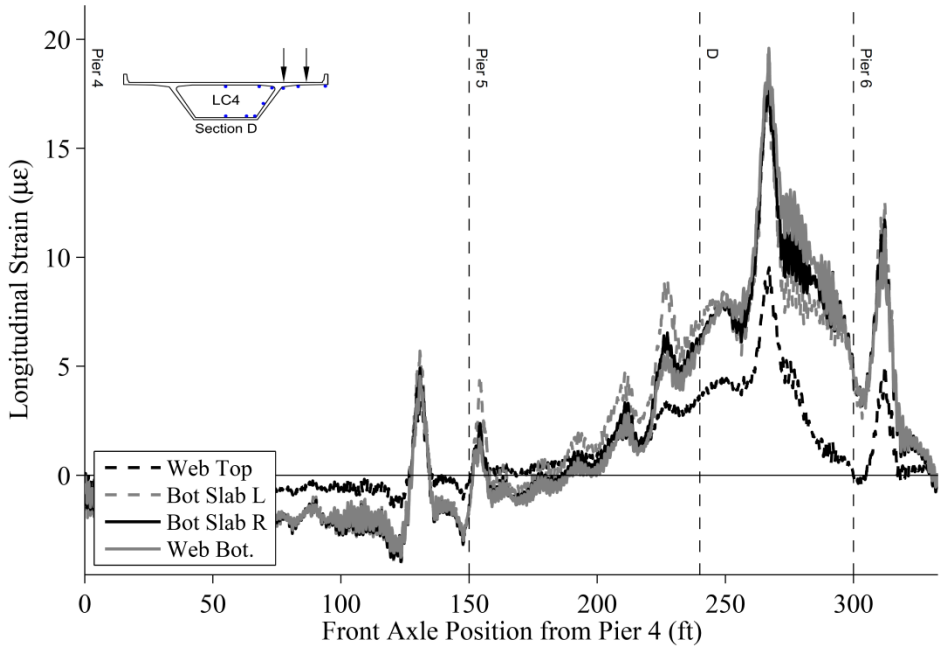

Figure C25 – Varina-Enon Bridge Bottom Slab and Web Longitudinal Strains from LC4 at Section D – Iteration 1

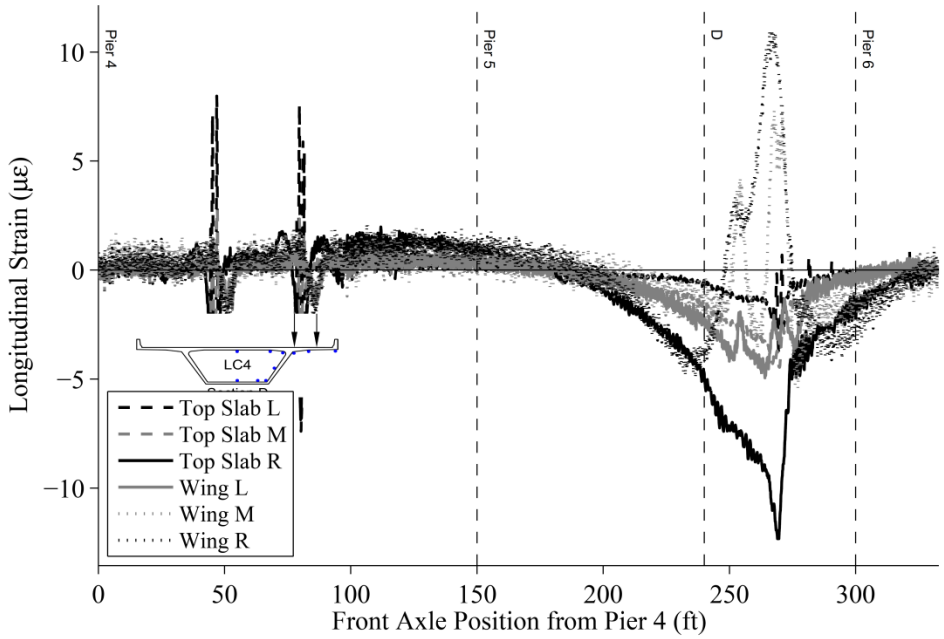

Figure C26 – Varina-Enon Bridge Top Slab and Wing Longitudinal Strains from LC4 at Section D – Iteration 2

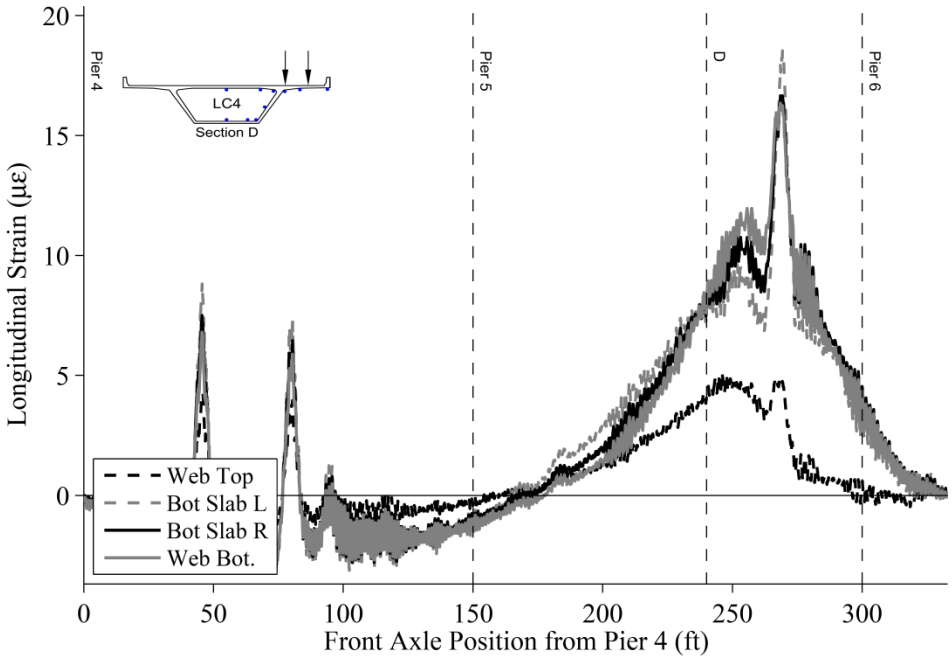

Figure C27 – Varina-Enon Bridge Bottom Slab and Web Longitudinal Strains from LC4 at Section D – Iteration 2

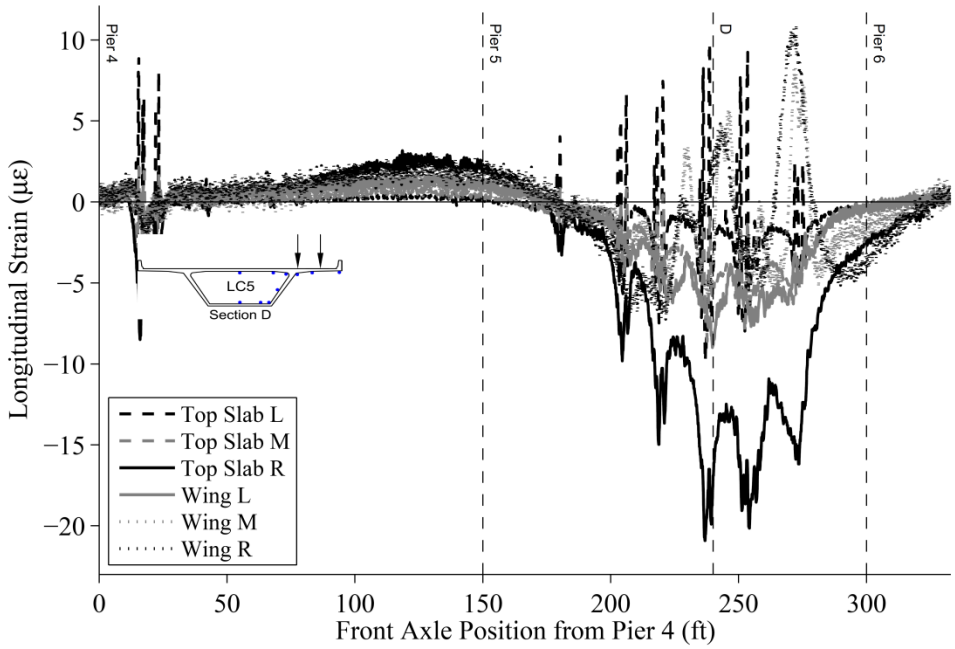

Figure C28 – Varina-Enon Bridge Top Slab and Wing Longitudinal Strains from LC5 at Section D – Iteration 1

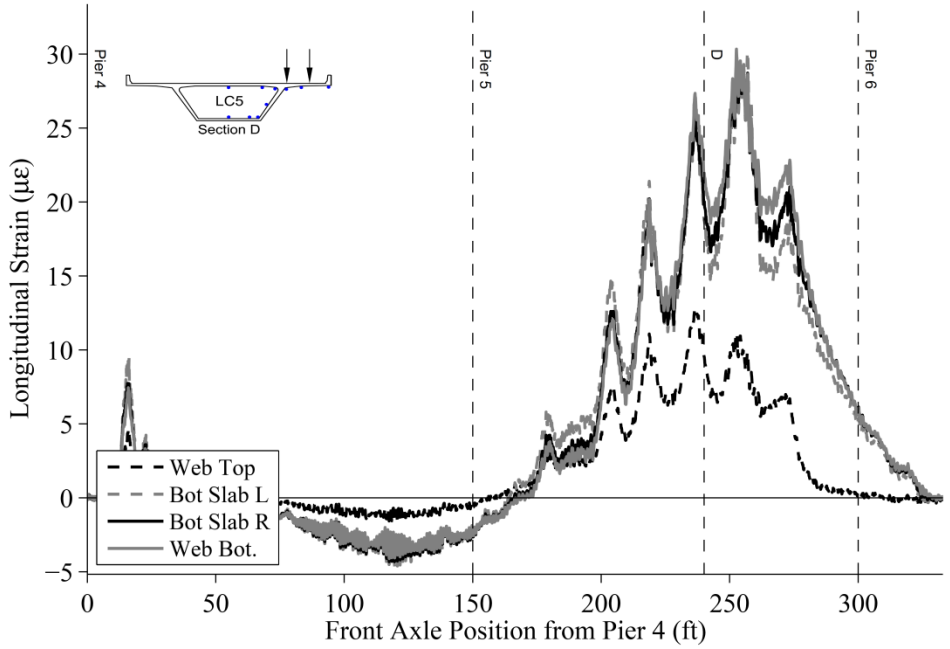

Figure C29 – Varina-Enon Bridge Bottom Slab and Web Longitudinal Strains from LC5 at Section D – Iteration 1

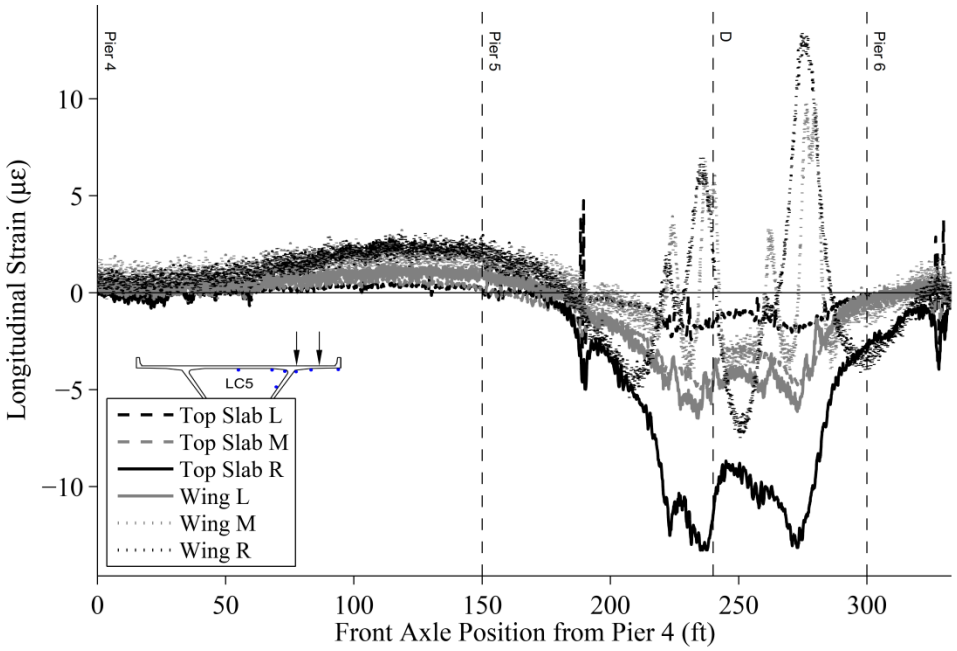

Figure C30 – Varina-Enon Bridge Top Slab and Wing Longitudinal Strains from LC5 at Section D – Iteration 2

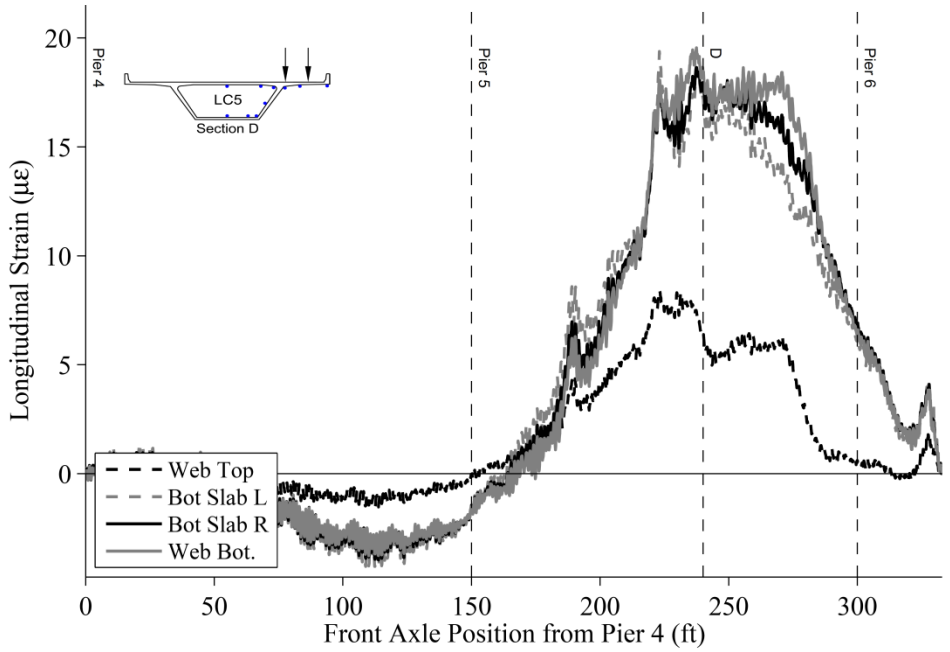

Figure C31 – Varina-Enon Bridge Top Slab and Wing Longitudinal Strains from LC5 at Section D – Iteration 2

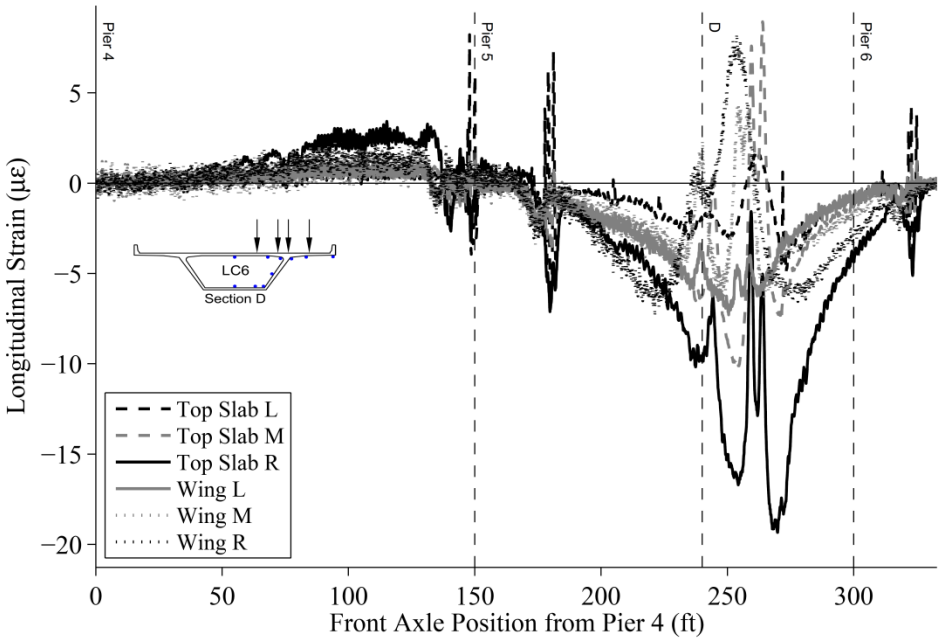

Figure C32 – Varina-Enon Bridge Top Slab and Wing Longitudinal Strains from LC6 at Section D – Iteration 1

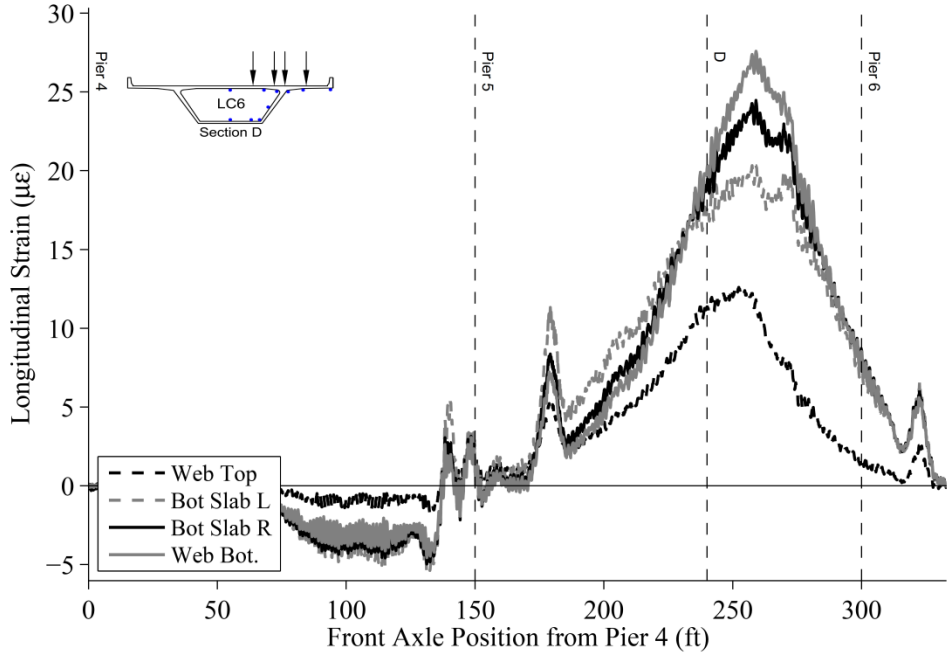

Figure C33 – Varina-Enon Bridge Bottom Slab and Web Longitudinal Strains from LC6 at Section D – Iteration 1

10.2 Varina-Enon Bridge Transverse Strains

10.2.1 Varina-Enon Bridge Section D

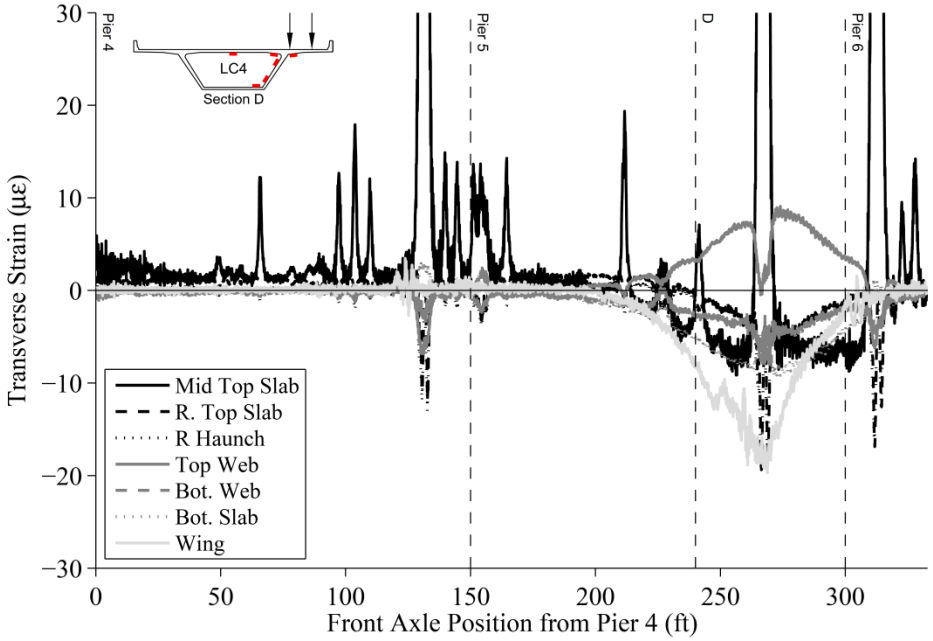

Figure C34 – Varina-Enon Bridge Transverse Strains from LC4 at Section D – Iteration 1

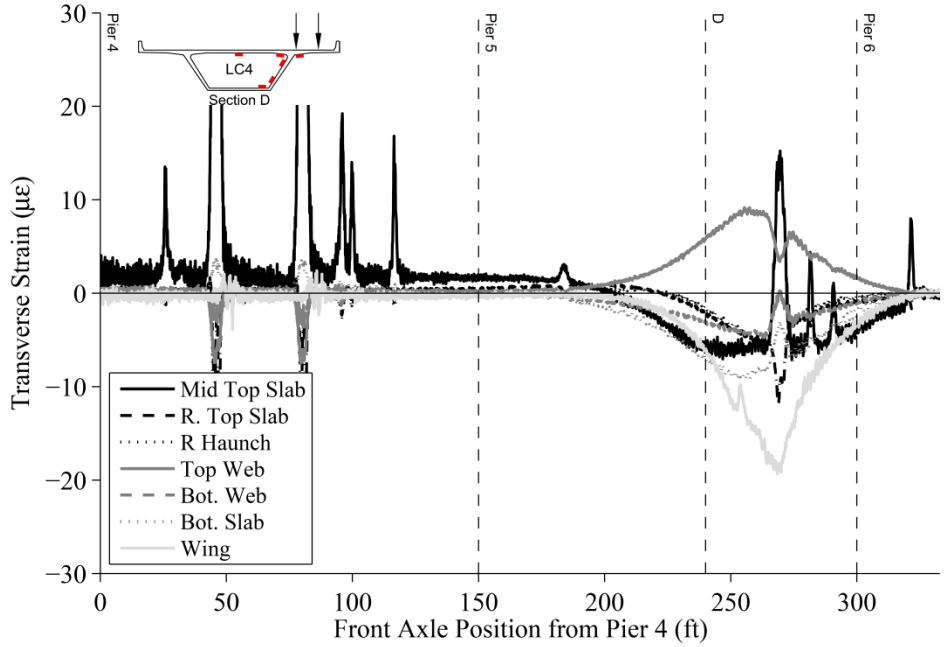

Figure C35 – Varina-Enon Bridge Transverse Strains from LC4 at Section D – Iteration 2

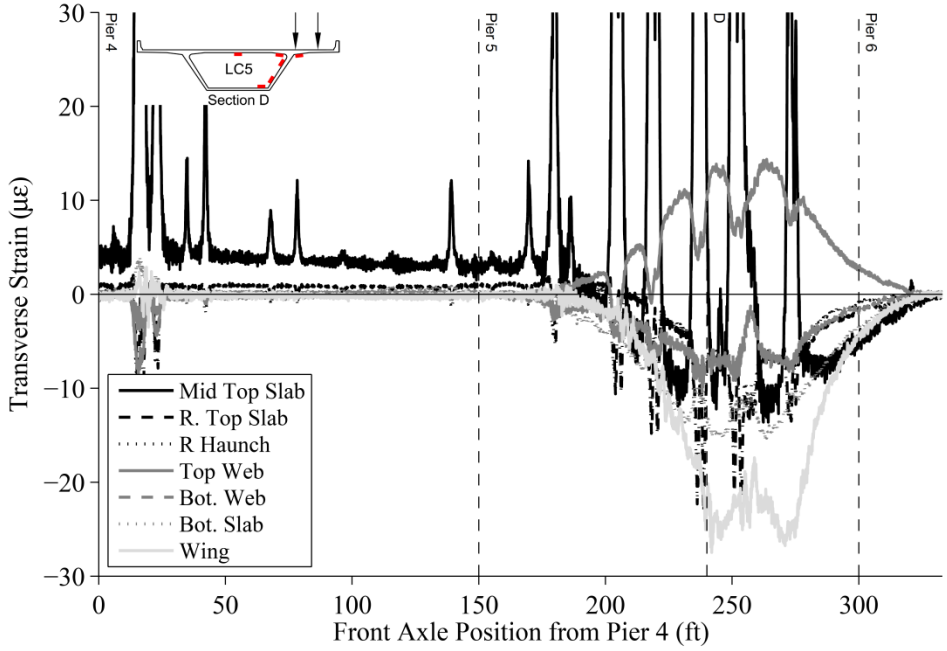

Figure C36 – Varina-Enon Bridge Transverse Strains from LC5 at Section D – Iteration 1

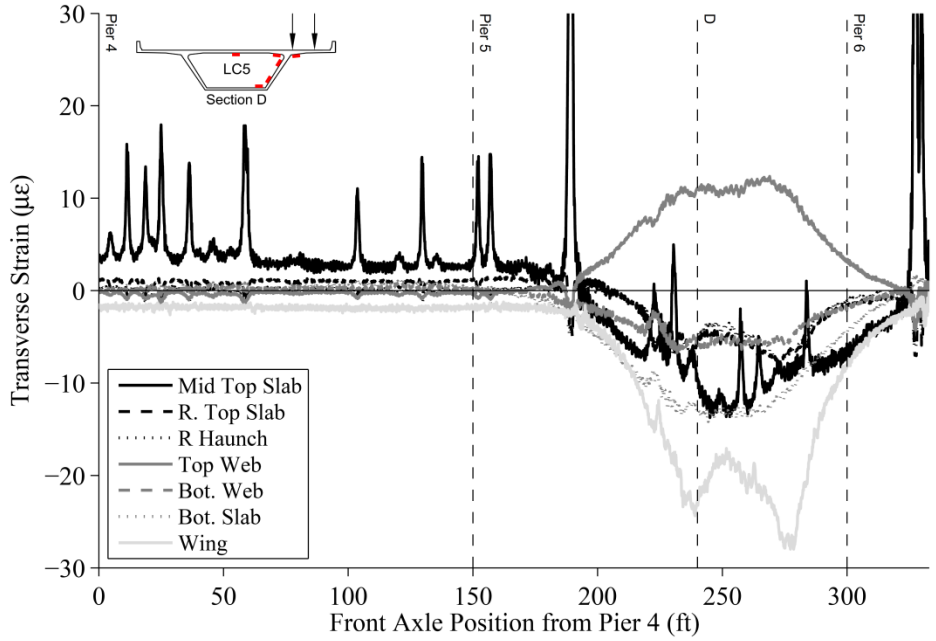

Figure C37 – Varina-Enon Bridge Transverse Strains from LC5 at Section D – Iteration 2

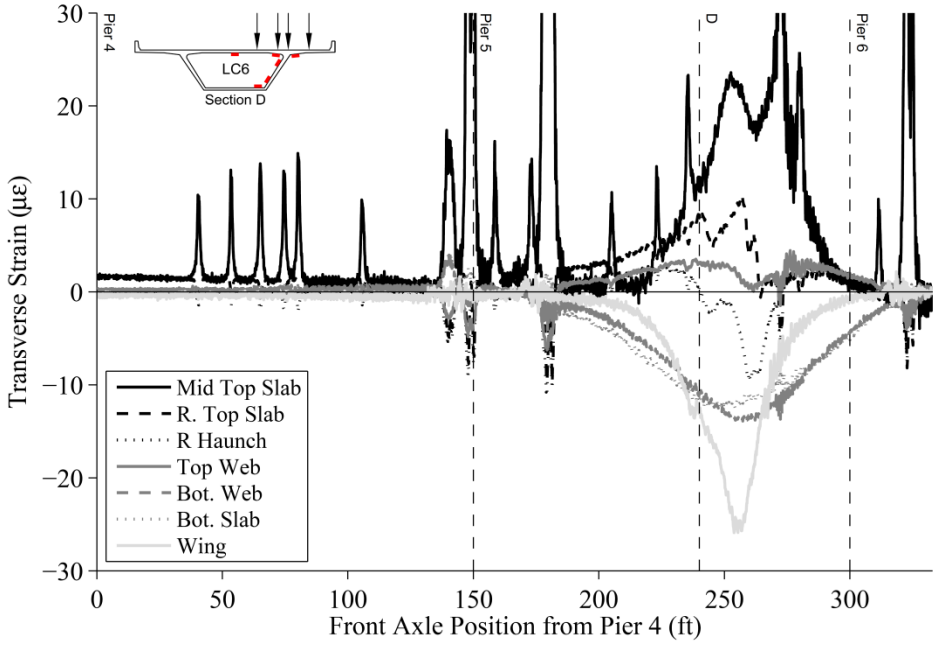

Figure C38 – Varina-Enon Bridge Transverse Strains from LC6 at Section D – Iteration 1

10.2.2 Varina-Enon Bridge Section C

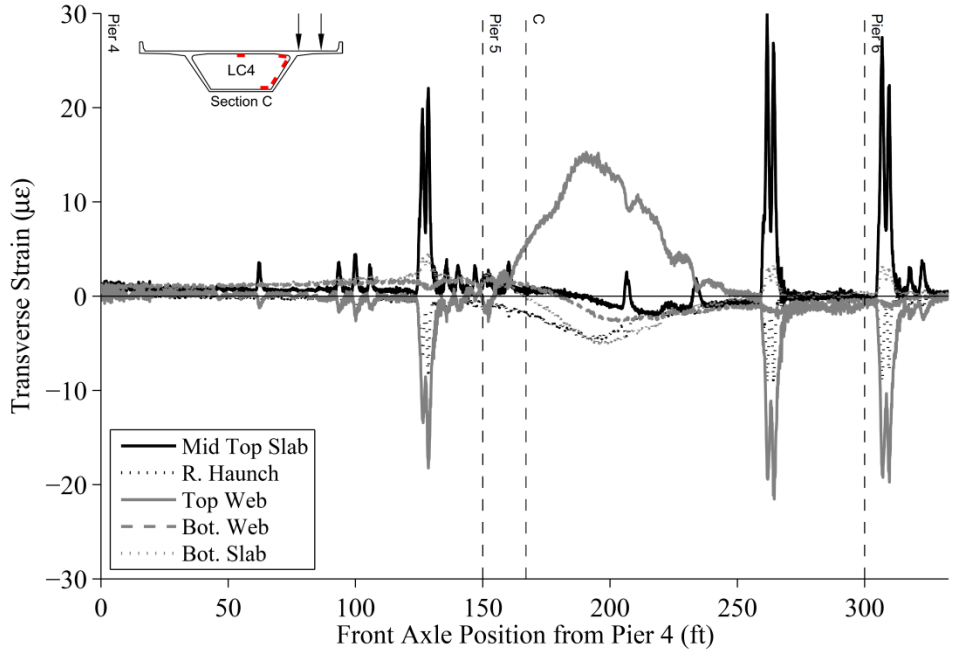

Figure C39 – Varina-Enon Bridge Transverse Strains from LC4 at Section C – Iteration 1

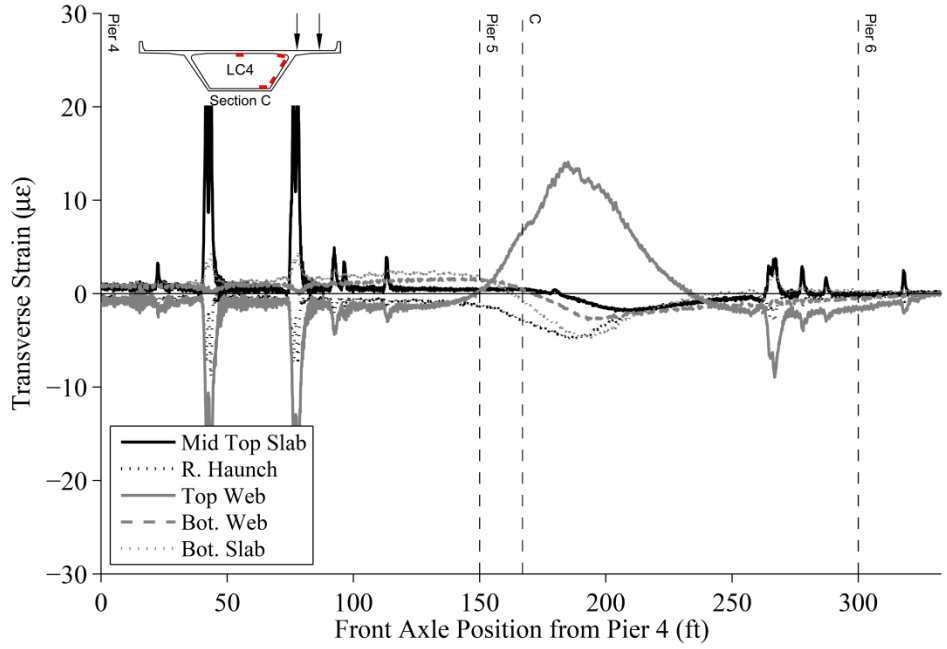

Figure C40 – Varina-Enon Bridge Transverse Strains from LC4 at Section C – Iteration 2

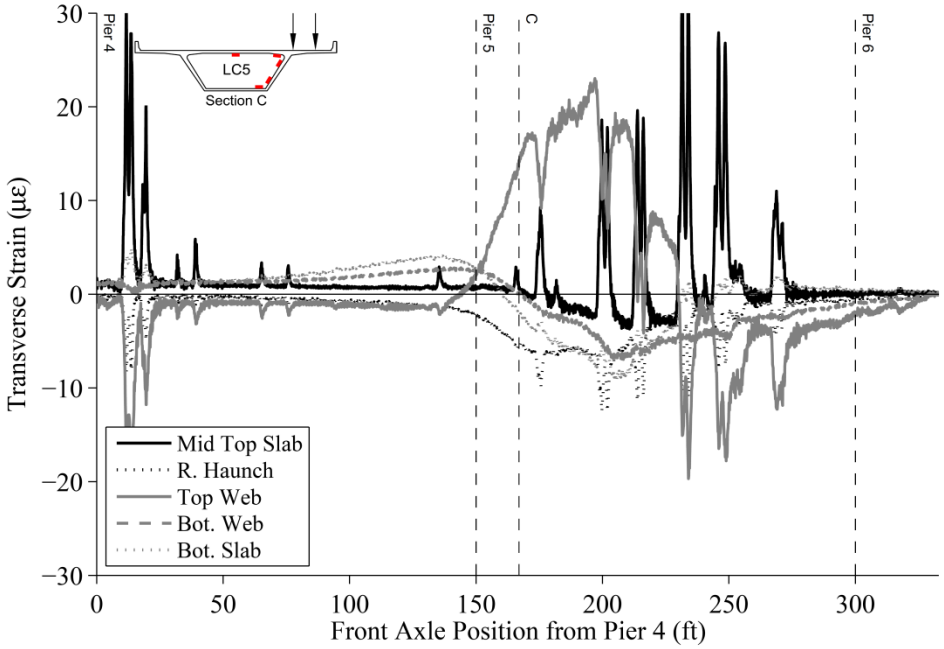

Figure C41 – Varina-Enon Bridge Transverse Strains from LC5 at Section C – Iteration 1

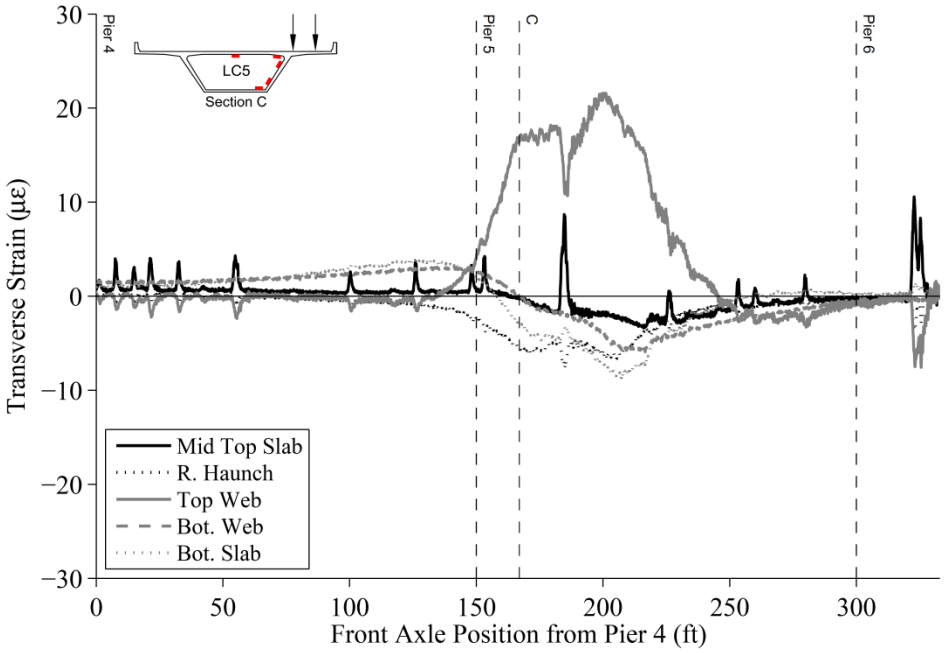

Figure C42 – Varina-Enon Bridge Transverse Strains from LC5 at Section C – Iteration 2

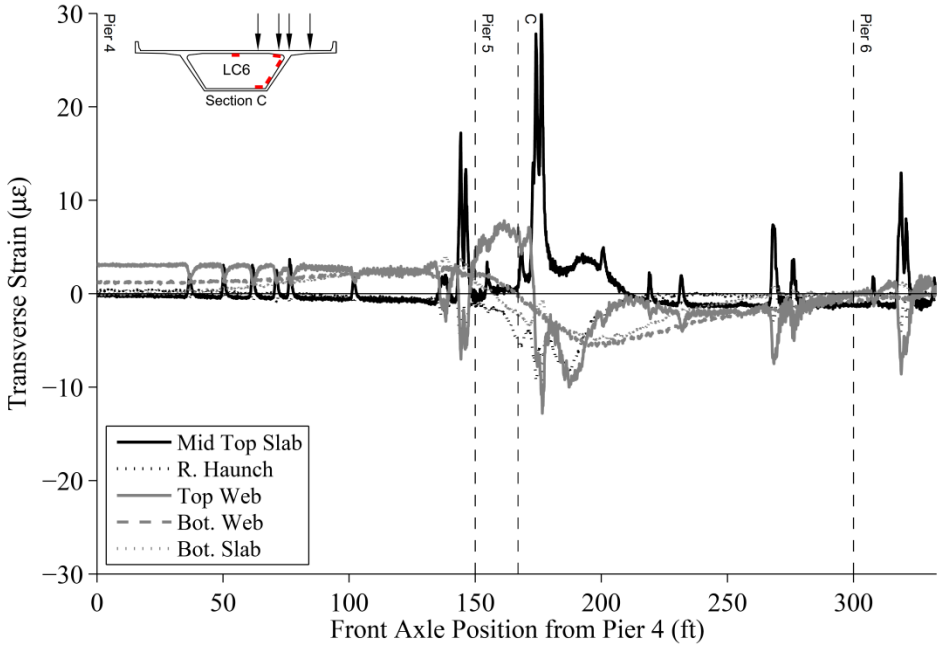

Figure C43 – Varina-Enon Bridge Transverse Strains from LC6 at Section C – Iteration 1

10.3 Varina-Enon Bridge Vertical Deflections

10.3.1 Varina-Enon Bridge Section A

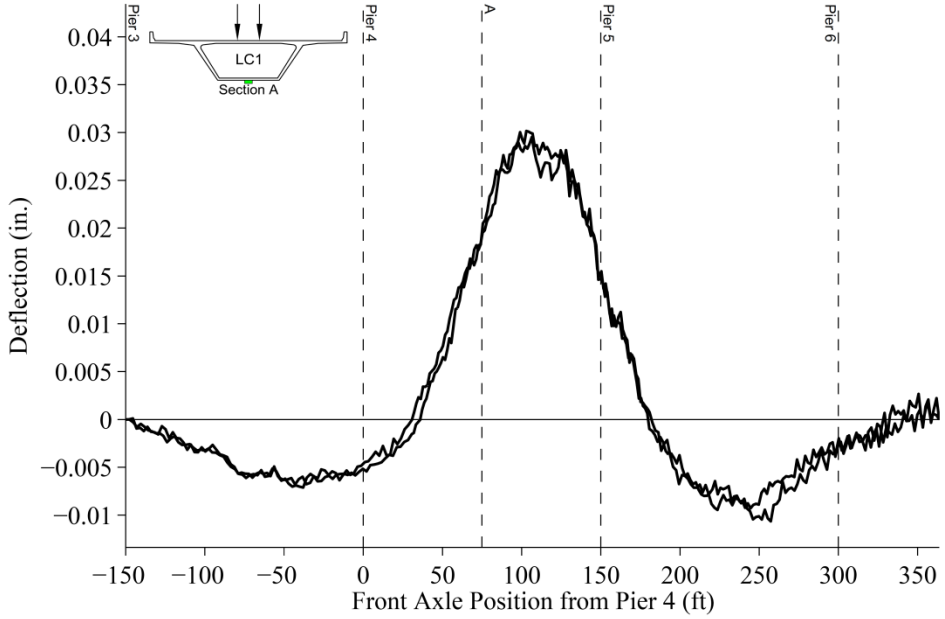

Figure C44 – Varina-Enon Bridge Vertical Deflection from LC1 at Section A – All Iterations

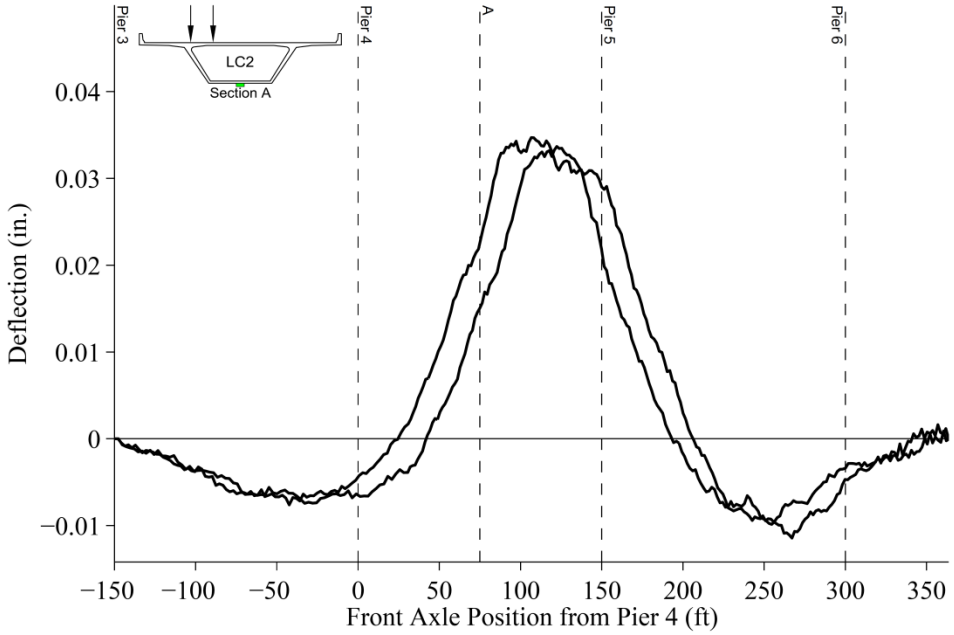

Figure C45 – Varina-Enon Bridge Vertical Deflection from LC2 at Section A – All Iterations

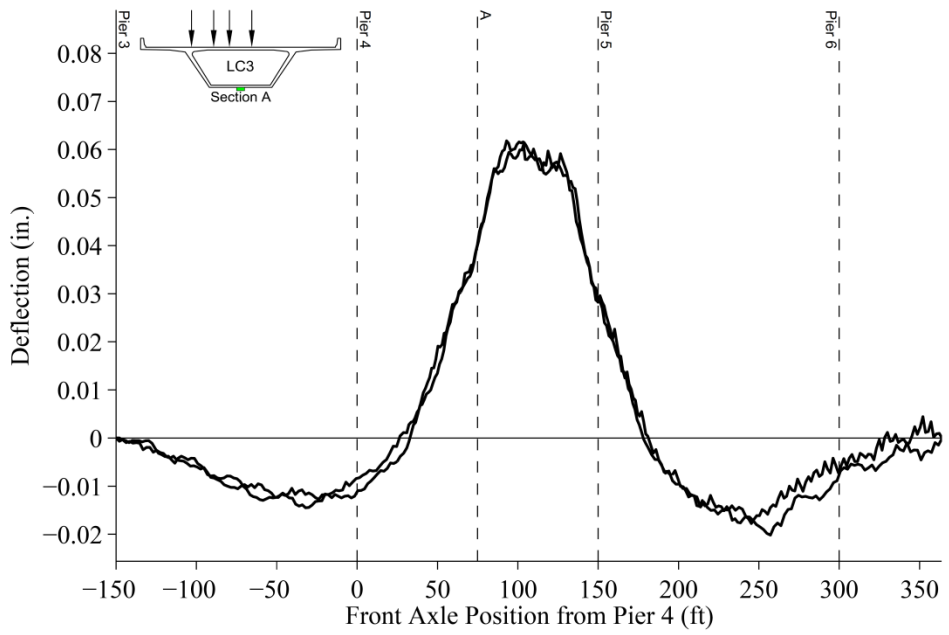

Figure C46 – Varina-Enon Bridge Vertical Deflection from LC3 at Section A – All Iterations

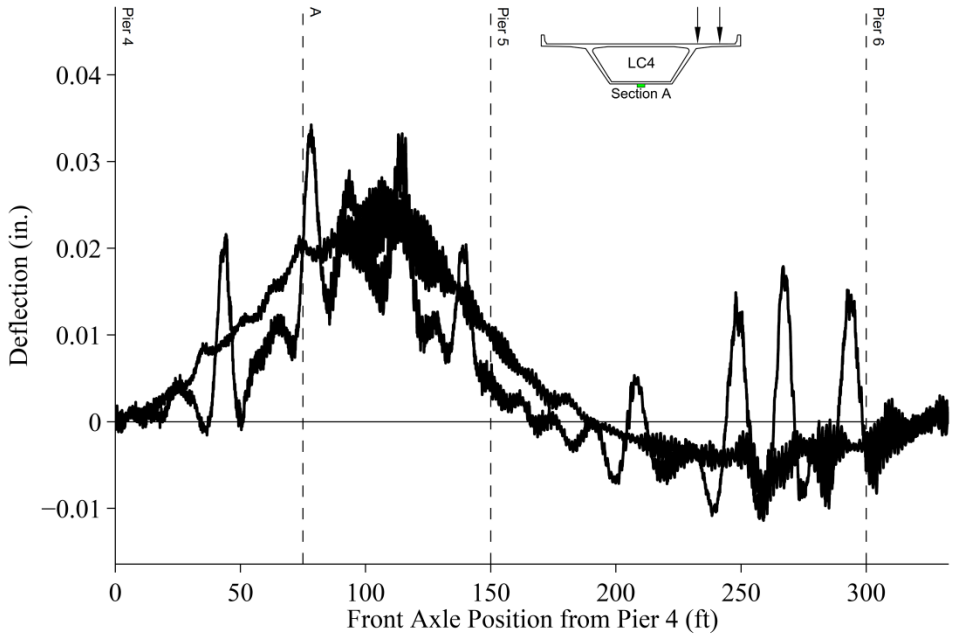

Figure C47 – Varina-Enon Bridge Vertical Deflection from LC4 at Section A – All Iterations

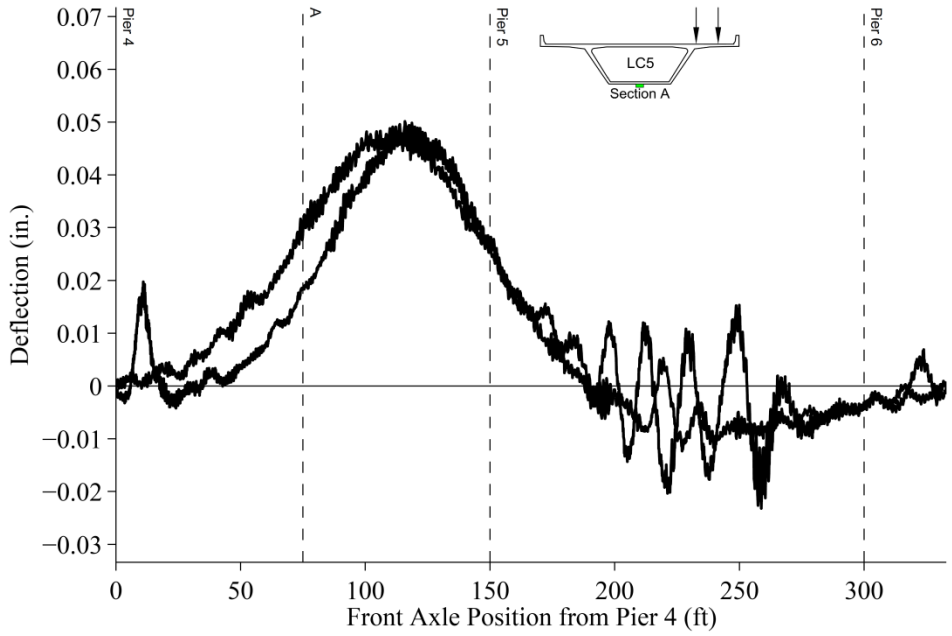

Figure C48 – Varina-Enon Bridge Vertical Deflection from LC5 at Section A – All Iterations

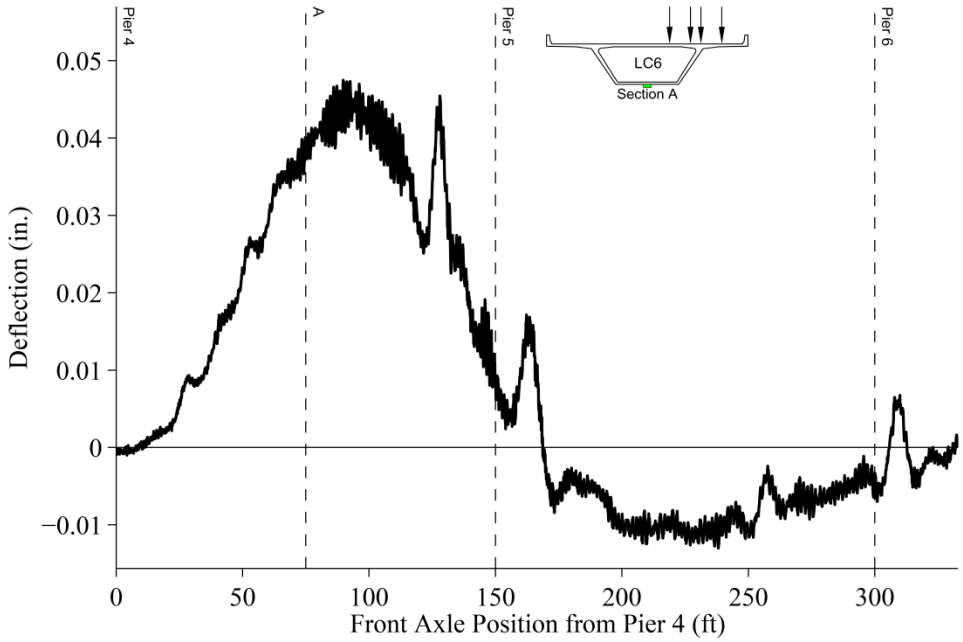

Figure C49 – Varina-Enon Bridge Vertical Deflection from LC6 at Section A – All Iterations

11 Appendix D: Tabulated Transverse Model Results

The following appendix presents the results from the two dimensional frame models and three dimensional shell models. Table D1through Table D55 present the frame model results include the five different support conditions (B P-R, B P-P, T P-R, T P-P and 4P). Table D56 through Table D121 present the results from the frame model with three different wing spring stiffness (K_{SPAN}, K_{IS} and K_{BEF}) using the B P-R and 4P support conditions. Table D122 through Table D132 present the shell model results with barrier rails. Table D133 through Table D143 present the shell model results with barrier rails. Table D144 through Table D154 present the program generated influence surface loaded shell model results.

11.1 Bottom Pin-Roller (B P-R) Frame Model Results

11.1.1 Seabreeze Bridge

Table D1 – Seabreeze Bridge LC1 Measured and Predicted Transverse Strains – B P-R

Sensor Location	LC1 - Section A (με)			LC1 - Section C (με)		
	Measured	Pucher	Homberg	Measured	Pucher	Homberg
Wing	-42	-46	-51	-19	-46	-51
Left Top Slab	-1	-27	-30	-5	-24	-27
Mid Top Slab	1	-3	-3	-1	-6	-6
Top Web	4	30	33	8	38	42
Bottom Web	-4	16	18	-2	17	19
Left Bot. Slab	-7	26	29	-2	6	6

Table D2 – Seabreeze Bridge LC3 Measured and Predicted Transverse Strains – B P-R

Sensor Location	LC3 - Section A (με)			LC3 - Section C (με)		
	Measured	Pucher	Homberg	Measured	Pucher	Homberg
Wing	-4	0	0	-3	0	0
Left Top Slab	-19	-22	-30	-14	-21	-29
Mid Top Slab	38	55	85	27	58	89
Top Web	-5	-21	-30	-11	-24	-34
Bottom Web	-2	-4	-6	1	3	4
Left Bot. Slab	-2	7	8	1	8	10

Table D3 – Seabreeze Bridge LC4 Measured and Predicted Transverse Strains – B P-R

Sensor Location	LC4 - Section A (μstrain)			LC4 - Section C (μstrain)		
	Measured	Pucher	Homberg	Measured	Pucher	Homberg
Wing	-6	0	0	-6	0	0
Left Top Slab	-19	-14	-23	-17	-15	-23
Mid Top Slab	53	82	129	33	84	134
Top Web	-7	-24	-37	-16	-28	-45
Bottom Web	-3	-8	-13	0	-4	-7
Left Bot. Slab	-3	-5	-9	2	3	4

11.1.2 Smart Road Bridge

Table D4 – Smart Road Bridge LC1 Measured and Predicted Transverse Strains – B P-R

Sensor Location	LC1 - Section A (με)			LC1 - Section C (με)		
	Measured	Pucher	Homberg	Measured	Pucher	Homberg
Wing	9	15	18	7	15	18
Left Haunch	1	-8	-10	-3	-9	-11
Middle Top Slab	1	-2	-3	-1	-3	-4
Right Haunch	0	6	7	0	6	7
Top Right Web	-1	4	4	0	5	6
Mid Right Web	-1	2	2	0	3	4
Right Bottom Slab	1	-6	-7	1	-7	-8
Left Bottom Slab	-4	3	4	-2	3	3
Mid Left Web	2	4	5	0	5	6
Top Left Web	2	6	7	-	-	-

Table D5 – Smart Road Bridge LC2 Measured and Predicted Transverse Strains – B P-R

Sensor Location	LC2 - Section A (με)			LC2 - Section C (με)		
	Measured	Pucher	Homberg	Measured	Pucher	Homberg
Wing	1	0	0	-1	0	0
Left Haunch	-1	6	7	-1	6	7
Middle Top Slab	1	-2	-3	0	-3	-4
Right Haunch	1	-8	-10	1	-9	-11
Top Right Web	2	6	7	1	6	8
Mid Right Web	0	4	5	-1	5	6
Right Bottom Slab	-3	3	4	-2	3	4
Left Bottom Slab	1	-6	-7	1	-6	-8
Mid Left Web	-1	2	2	0	3	4
Top Left Web	-1	-7	-9	-	-	-

Table D6 – Smart Road Bridge LC3 Measured and Predicted Transverse Strains – B P-R

Sensor Location	LC3 - Section A (με)			LC3 - Section C (με)		
	Measured	Pucher	Homberg	Measured	Pucher	Homberg
Wing	11	15	18	8	15	18
Left Haunch	1	-2	-3	-3	-3	-3
Middle Top Slab	2	-5	-6	-1	-7	-8
Right Haunch	1	-2	-3	1	-3	-3
Top Right Web	2	9	11	1	11	13
Mid Right Web	-1	6	7	1	8	10
Right Bottom Slab	-3	-3	-4	-1	-4	-4
Left Bottom Slab	-3	-3	-4	-1	-4	-4
Mid Left Web	1	6	7	0	8	10
Top Left Web	2	9	11	-	-	-

Table D7 – Smart Road Bridge LC4 Measured and Predicted Transverse Strains – B P-R

Sensor Location	LC4 - Section A (με)			LC4 - Section C (με)		
	Measured	Pucher	Homberg	Measured	Pucher	Homberg
Wing	11	15	18	7	15	18
Left Haunch	3	-7	-10	-6	-7	-8
Middle Top Slab	17	23	37	14	24	37
Right Haunch	-4	1	4	-4	1	1
Top Right Web	-4	-3	-7	-2	-3	-5
Mid Right Web	-4	-2	-5	-1	-3	-4
Right Bottom Slab	-2	-2	-4	2	-3	-3
Left Bottom Slab	-5	4	8	-2	4	6
Mid Left Web	-3	-1	-2	-1	-1	-3
Top Left Web	-1	-2	-5	-	-	-

Table D8 – Smart Road Bridge LC5 Measured and Predicted Transverse Strains – B P-R

Sensor Location	LC5 - Section A (με)			LC5 - Section C (με)		
	Measured	Pucher	Homberg	Measured	Pucher	Homberg
Wing	3	0	0	1	0	0
Left Haunch	-5	-5	-9	-7	-5	-8
Middle Top Slab	21	54	63	20	56	65
Right Haunch	-3	-5	-8	-3	-4	-7
Top Right Web	-8	-10	-13	-4	-12	-16
Mid Right Web	-7	-6	-8	-3	-9	-11
Right Bottom Slab	-2	4	6	2	4	7
Left Bottom Slab	-2	3	3	1	3	4
Mid Left Web	-6	-6	-9	-2	-9	-12
Top Left Web	-4	-10	-14	-	-	-

11.1.3 Varina-Enon Bridge

Table D9 – Varina-Enon Bridge LC4 Measured and Predicted Transverse Strains – B P-R

Sensor Location	LC4 - Section D (με)			LC4 - Section C (με)		
	Measured	Pucher	Homberg	Measured	Pucher	Homberg
Top Slab	-6	-4	-4	-2	-4	-4
R Top Slab	-3	-31	-36	-	-31	-36
R Haunch	-3	-23	-26	-4	-23	-26
R Wing	-19	-30	-34	-	-30	-34
R Top Web	9	18	21	14	18	21
R Bot Web	-5	22	25	-3	22	25
R Bot Slab	-9	16	18	-5	16	18

Table D10 – Varina-Enon Bridge LC5 Measured and Predicted Transverse Strains – B P-R

Sensor Location	LC5 - Section D (με)			LC5 - Section C (με)		
	Measured	Pucher	Homberg	Measured	Pucher	Homberg
Top Slab	-12	-4	-4	-3	-4	-4
R Top Slab	-7	-32	-37	-	-32	-37
R Haunch	-7	-24	-27	-6	-24	-27
R Wing	-26	-31	-35	-	-31	-35
R Top Web	13	19	21	23	19	21
R Bot Web	-6	23	26	-7	23	26
R Bot Slab	-15	16	19	-9	16	19

Table D11 – Varina-Enon Bridge LC6 Measured and Predicted Transverse Strains – B P-R

Sensor Location	LC6 - Section D (με)			LC6 - Section C (με)		
	Measured	Pucher	Homberg	Measured	Pucher	Homberg
Top Slab	23	18	26	5	18	26
R Top Slab	10	25	44	-	25	44
R Haunch	-9	-20	-23	-7	-20	-23
R Wing	-25	-30	-34	-	-30	-34
R Top Web	2	0	-6	-10	0	-6
R Bot. Web	-14	3	-3	-6	3	-3
R Bot. Slab	-12	3	-1	-5	3	-1

11.2 Bottom Pin-Pin (B P-P) Frame Model Results

11.2.1 Seabreeze Bridge

Table D12 – Seabreeze Bridge LC1 Measured and Predicted Transverse Strains – B P-P

Sensor Location	LC1 - Section A (με)			LC1 - Section B (με)		
	Measured	Pucher	Homberg	Measured	Pucher	Homberg
Wing	-42	-46	-51	-19	-46	-51
Left Top Slab	-1	-27	-30	-5	-24	-27
Mid Top Slab	1	-3	-3	-1	-6	-6
Top Web	4	30	33	8	38	42
Bottom Web	-4	16	18	-2	17	19
Left Bot. Slab	-7	27	31	-2	6	7

Table D13 – Seabreeze Bridge LC3 Measured and Predicted Transverse Strains – B P-P

Sensor Location	LC3 - Section A (με)			LC3 - Section B (με)		
	Measured	Pucher	Homberg	Measured	Pucher	Homberg
Wing	-4	0	0	-3	0	0
Left Haunch	-19	-22	-30	-14	-21	-29
Middle Top Slab	38	55	85	27	58	89
Top Right Web	-5	-21	-30	-11	-24	-34
Mid Right Web	-2	-4	-6	1	3	4
Right Bottom Slab	-2	6	6	1	7	9

Table D14 – Seabreeze Bridge LC4 Measured and Predicted Transverse Strains – B P-P

Sensor Location	LC4 - Section A (με)			LC4 - Section B (με)		
	Measured	Pucher	Homberg	Measured	Pucher	Homberg
Wing	-6	0	0	-6	0	0
Left Haunch	-19	-14	-23	-17	-15	-23
Middle Top Slab	53	81	129	33	84	134
Top Right Web	-7	-24	-37	-16	-28	-45
Mid Right Web	-3	-8	-13	0	-4	-7
Right Bottom Slab	-3	-7	-11	2	2	3

11.2.2 Smart Road Bridge

Table D15 – Smart Road Bridge LC1 Measured and Predicted Transverse Strains – B P-P

Sensor Location	LC1 - Section A (με)			LC1 - Section B (με)		
	Measured	Pucher	Homberg	Measured	Pucher	Homberg
Wing	9	15	18	7	15	18
Left Haunch	1	-8	-10	-3	-9	-11
Middle Top Slab	1	-2	-3	-1	-3	-4
Right Haunch	0	6	7	0	6	7
Top Right Web	-1	4	4	0	5	6
Mid Right Web	-1	2	2	0	3	4
Right Bottom Slab	1	-6	-7	1	-6	-8
Left Bottom Slab	-4	3	4	-2	3	4
Mid Left Web	2	4	5	0	5	6
Top Left Web	2	6	7	-	-	-

Table D16 – Smart Road Bridge LC2 Measured and Predicted Transverse Strains – B P-P

Sensor Location	LC2 - Section A (με)			LC2 - Section B (με)		
	Measured	Pucher	Homberg	Measured	Pucher	Homberg
Wing	1	0	0	-1	0	0
Left Haunch	-1	6	7	-1	6	7
Middle Top Slab	1	-2	-3	0	-3	-4
Right Haunch	1	-8	-10	1	-9	-11
Top Right Web	2	6	7	1	6	8
Mid Right Web	0	4	5	-1	5	6
Right Bottom Slab	-3	3	4	-2	3	4
Left Bottom Slab	1	-6	-7	1	-6	-7
Mid Left Web	-1	2	2	0	3	4
Top Left Web	-1	-7	-9	-	-	-

Table D17 – Smart Road Bridge LC3 Measured and Predicted Transverse Strains – B P-P

Sensor Location	LC3 - Section A (με)			LC3 - Section B (με)		
	Measured	Pucher	Homberg	Measured	Pucher	Homberg
Wing	11	15	18	8	15	18
Left Haunch	1	-2	-3	-3	-3	-3
Middle Top Slab	2	-5	-6	-1	-7	-8
Right Haunch	1	-2	-3	1	-3	-3
Top Right Web	2	9	11	1	11	13
Mid Right Web	-1	6	7	1	8	10
Right Bottom Slab	-3	-2	-3	-1	-3	-4
Left Bottom Slab	-3	-2	-3	-1	-3	-4
Mid Left Web	1	6	7	0	8	10
Top Left Web	2	-2	-2	-	-	-

Table D18 – Smart Road Bridge LC4 Measured and Predicted Transverse Strains – B P-P

Sensor Location	LC4 - Section A (με)			LC4 - Section B (με)		
	Measured	Pucher	Homberg	Measured	Pucher	Homberg
Wing	11	15	18	7	15	18
Left Haunch	3	-7	-10	-6	-7	-8
Middle Top Slab	17	23	37	14	24	37
Right Haunch	-4	1	4	-4	1	1
Top Right Web	-4	-3	-7	-2	-3	-5
Mid Right Web	-4	-2	-5	-1	-3	-4
Right Bottom Slab	-2	-3	-4	2	-3	-3
Left Bottom Slab	-5	4	7	-2	4	5
Mid Left Web	-3	-1	-2	-1	-1	-3
Top Left Web	-1	-2	-1	-	-	-

Table D19 – Smart Road Bridge LC5 Measured and Predicted Transverse Strains – B P-P

Sensor Location	LC5 - Section A (με)			LC5 - Section B (με)		
	Measured	Pucher	Homberg	Measured	Pucher	Homberg
Wing	3	0	0	1	0	0
Left Haunch	-5	-5	-9	-7	-5	-8
Middle Top Slab	21	54	63	20	56	65
Right Haunch	-3	-5	-8	-3	-5	-7
Top Right Web	-8	-10	-13	-4	-12	-16
Mid Right Web	-7	-6	-8	-3	-9	-11
Right Bottom Slab	-2	3	5	2	4	6
Left Bottom Slab	-2	2	2	1	3	3
Mid Left Web	-6	-6	-9	-2	-9	-12
Top Left Web	-4	-8	-11	-	-	-

11.2.3 Varina-Enon Bridge

Table D20 – Varina-Enon Bridge LC4 Measured and Predicted Transverse Strains – B P-P

Sensor Location	LC4 - Section D (με)			LC4 - Section C (με)		
	Measured	Pucher	Homberg	Measured	Pucher	Homberg
Top Slab	-6	-4	-4	-2	-4	-4
R Top Slab	-3	-31	-36	-	-31	-36
R Haunch	-3	-23	-26	-4	-23	-26
R Wing	-19	-30	-34	-	-30	-34
R Top Web	9	18	21	14	18	21
R Bot Web	-5	22	25	-3	22	25
R Bot Slab	-9	16	19	-5	16	19

Table D21 – Varina-Enon Bridge LC5 Measured and Predicted Transverse Strains – B P-P

Sensor Location	LC5 - Section D (με)			LC5 - Section C (με)		
	Measured	Pucher	Homberg	Measured	Pucher	Homberg
Top Slab	-12	-4	-4	-3	-4	-4
R Top Slab	-7	-32	-37	-	-32	-37
R Haunch	-7	-24	-27	-6	-24	-27
R Wing	-26	-31	-35	-	-31	-35
R Top Web	13	19	21	23	19	21
R Bot Web	-6	23	26	-7	23	26
R Bot Slab	-15	17	19	-9	17	19

Table D22 – Varina-Enon Bridge LC6 Measured and Predicted Transverse Strains – B P-P

Sensor Location	LC6 - Section D (με)			LC6 - Section C (με)		
	Measured	Pucher	Homberg	Measured	Pucher	Homberg
Top Slab	23	18	26	5	18	26
R Top Slab	10	25	44	-	25	44
R Haunch	-9	-20	-23	-7	-20	-23
R Wing	-25	-30	-34	-	-30	-34
R Top Web	2	0	-6	-10	0	-6
R Bot Web	-14	3	-3	-6	3	-3
R Bot Slab	-12	3	-1	-5	3	-1

11.3 Top Pin-Roller (T P-R) Frame Model Results

11.3.1 Seabreeze Bridge

Table D23 – Seabreeze Bridge LC1 Measured and Predicted Transverse Strains – T P-R

Sensor Location	LC1 - Section A (με)			LC1 - Section B (με)		
	Measured	Pucher	Homberg	Measured	Pucher	Homberg
Wing	-42	-46	-51	-19	-46	-51
Left Top Slab	-1	-23	-26	-5	-21	-23
Mid Top Slab	1	-3	-3	-1	-6	-6
Top Web	4	33	37	8	41	45
Bottom Web	-4	15	17	-2	10	12
Left Bot. Slab	-7	18	20	-2	0	0

Table D24 – Seabreeze Bridge LC3 Measured and Predicted Transverse Strains – T P-R

Sensor Location	LC3 - Section A (με)			LC3 - Section B (με)		
	Measured	Pucher	Homberg	Measured	Pucher	Homberg
Wing	-4	0	0	-3	0	0
Left Haunch	-19	-22	-30	-14	-21	-28
Middle Top Slab	38	55	85	27	58	89
Top Right Web	-5	-21	-30	-11	-24	-34
Mid Right Web	-2	-4	-6	1	3	3
Right Bottom Slab	-2	6	8	1	7	10

Table D25 – Seabreeze Bridge LC4 Measured and Predicted Transverse Strains – T P-R

Sensor Location	LC4 - Section A (με)			LC4 - Section B (με)		
	Measured	Pucher	Homberg	Measured	Pucher	Homberg
Wing	-6	0	0	-6	0	0
Left Haunch	-19	-16	-25	-17	-16	-25
Middle Top Slab	53	82	129	33	84	134
Top Right Web	-7	-25	-39	-16	-29	-46
Mid Right Web	-3	-8	-13	0	-2	-4
Right Bottom Slab	-3	-3	-4	2	4	7

11.3.2 Smart Road Bridge

Table D26 – Smart Road Bridge LC1 Measured and Predicted Transverse Strains – T P-R

Sensor Location	LC1 - Section A (με)			LC1 - Section B (με)		
	Measured	Pucher	Homberg	Measured	Pucher	Homberg
Wing	9	15	18	7	15	18
Left Haunch	1	-8	-9	-3	-8	-10
Middle Top Slab	1	-2	-3	-1	-3	-4
Right Haunch	0	6	7	0	5	6
Top Right Web	-1	3	4	0	4	5
Mid Right Web	-1	1	2	0	3	3
Right Bottom Slab	1	-5	-6	1	-5	-6
Left Bottom Slab	-4	2	2	-2	1	2
Mid Left Web	2	4	5	0	6	7
Top Left Web	2	5	6	-	-	-

Table D27 – Smart Road Bridge LC2 Measured and Predicted Transverse Strains – T P-R

Sensor Location	LC2 - Section A (με)			LC2 - Section B (με)		
	Measured	Pucher	Homberg	Measured	Pucher	Homberg
Wing	1	0	0	-1	0	0
Left Haunch	-1	6	7	-1	5	6
Middle Top Slab	1	-2	-3	0	-3	-4
Right Haunch	1	-8	-9	1	-8	-10
Top Right Web	2	6	8	1	7	8
Mid Right Web	0	4	5	-1	6	7
Right Bottom Slab	-3	2	2	-2	2	2
Left Bottom Slab	1	-5	-6	1	-5	-6
Mid Left Web	-1	1	2	0	3	3
Top Left Web	-1	-7	-8	-	-	-

Table D28 – Smart Road Bridge LC3 Measured and Predicted Transverse Strains – T P-R

Sensor Location	LC3 - Section A (με)			LC3 - Section B (με)		
	Measured	Pucher	Homberg	Measured	Pucher	Homberg
Wing	11	15	18	8	15	18
Left Haunch	1	-2	-3	-3	-3	-3
Middle Top Slab	2	-5	-6	-1	-7	-8
Right Haunch	1	-2	-3	1	-3	-3
Top Right Web	2	9	11	1	11	13
Mid Right Web	-1	6	7	1	8	10
Right Bottom Slab	-3	-3	-4	-1	-4	-4
Left Bottom Slab	-3	-3	-4	-1	-4	-4
Mid Left Web	1	6	7	0	8	10
Top Left Web	2	-2	-2	-	-	-

Table D29 – Smart Road Bridge LC4 Measured and Predicted Transverse Strains – T P-R

Sensor Location	LC4 - Section A (με)			LC4 - Section B (με)		
	Measured	Pucher	Homberg	Measured	Pucher	Homberg
Wing	11	15	18	7	15	18
Left Haunch	3	-7	-10	-6	-7	-7
Middle Top Slab	17	23	37	14	24	37
Right Haunch	-4	0	3	-4	1	0
Top Right Web	-4	-4	-8	-2	-4	-6
Mid Right Web	-4	-3	-6	-1	-3	-5
Right Bottom Slab	-2	-2	-3	2	-2	-2
Left Bottom Slab	-5	3	7	-2	3	4
Mid Left Web	-3	0	-2	-1	-1	-2
Top Left Web	-1	-3	-1	-	-	-

Table D30 – Smart Road Bridge LC5 Measured and Predicted Transverse Strains – T P-R

Sensor Location	LC5 - Section A (με)			LC5 - Section B (με)		
	Measured	Pucher	Homberg	Measured	Pucher	Homberg
Wing	3	0	0	1	0	0
Left Haunch	-5	-5	-9	-7	-5	-8
Middle Top Slab	21	54	63	20	56	65
Right Haunch	-3	-5	-8	-3	-4	-7
Top Right Web	-8	-10	-13	-4	-12	-15
Mid Right Web	-7	-6	-8	-3	-9	-11
Right Bottom Slab	-2	4	6	2	4	6
Left Bottom Slab	-2	3	3	1	4	4
Mid Left Web	-6	-7	-9	-2	-9	-12
Top Left Web	-4	-8	-11	-	-	-

11.3.3 Varina-Enon Bridge

Table D31 – Varina-Enon Bridge LC4 Measured and Predicted Transverse Strains – T P-R

Sensor Location	LC4 - Section D (με)			LC4 - Section C (με)		
	Measured	Pucher	Homberg	Measured	Pucher	Homberg
Top Slab	-6	-4	-4	-2	-4	-4
R Top Slab	-3	-22	-26	-	-22	-26
R Haunch	-3	-16	-19	-4	-16	-19
R Wing	-19	-30	-34	-	-30	-34
R Top Web	9	25	29	14	25	29
R Bot Web	-5	12	14	-3	12	14
R Bot Slab	-9	4	4	-5	4	4

Table D32 – Varina-Enon Bridge LC5 Measured and Predicted Transverse Strains – T P-R

Sensor Location	LC5 - Section D (με)			LC5 - Section C (με)		
	Measured	Pucher	Homberg	Measured	Pucher	Homberg
Top Slab	-12	-4	-4	-3	-4	-4
R Top Slab	-7	-23	-26	-	-23	-26
R Haunch	-7	-17	-19	-6	-17	-19
R Wing	-26	-31	-35	-	-31	-35
R Top Web	13	26	29	23	26	29
R Bot Web	-6	13	15	-7	13	15
R Bot Slab	-15	4	5	-9	4	5

Table D33 – Varina-Enon Bridge LC6 Measured and Predicted Transverse Strains – T P-R

Sensor Location	LC6 - Section D (με)			LC6 - Section C (με)		
	Measured	Pucher	Homberg	Measured	Pucher	Homberg
Top Slab	23	18	26	5	18	26
R Top Slab	10	26	43	-	26	43
R Haunch	-9	-19	-24	-7	-19	-24
R Wing	-25	-30	-34	-	-30	-34
R Top Web	2	1	-7	-10	1	-7
R Bot Web	-14	2	-2	-6	2	-2
R Bot Slab	-12	1	1	-5	1	1

11.4 Top Pin-Pin (T P-P) Frame Model Results

11.4.1 Seabreeze Bridge

Table D34 – Seabreeze Bridge LC1 Measured and Predicted Transverse Strains – T P-P

Sensor Location	LC1 - Section A (με)			LC1 - Section B (με)		
	Measured	Pucher	Homberg	Measured	Pucher	Homberg
Wing	-42	-46	-51	-19	-46	-51
Left Top Slab	-1	-22	-25	-5	-21	-23
Mid Top Slab	1	5	6	-1	-6	-6
Top Web	4	20	23	8	41	45
Bottom Web	-4	12	14	-2	10	12
Left Bot. Slab	-7	20	23	-2	0	0

Table D35 – Seabreeze Bridge LC3 Measured and Predicted Transverse Strains – T P-P

Sensor Location	LC3 - Section A (με)			LC3 - Section B (με)		
	Measured	Pucher	Homberg	Measured	Pucher	Homberg
Wing	-4	0	0	-3	0	0
Left Haunch	-19	-23	-32	-14	-21	-28
Middle Top Slab	38	47	74	27	58	89
Top Right Web	-5	-8	-12	-11	-24	-34
Mid Right Web	-2	-1	-2	1	3	3
Right Bottom Slab	-2	4	4	1	7	10

Table D36 – Seabreeze Bridge LC4 Measured and Predicted Transverse Strains – T P-P

Sensor Location	LC4 - Section A (με)			LC4 - Section B (με)		
	Measured	Pucher	Homberg	Measured	Pucher	Homberg
Wing	-6	0	0	-6	0	0
Left Haunch	-19	-17	-26	-17	-16	-25
Middle Top Slab	53	74	118	33	84	134
Top Right Web	-7	-13	-20	-16	-29	-46
Mid Right Web	-3	-5	-8	0	-2	-4
Right Bottom Slab	-3	-5	-9	2	4	7

11.4.2 Smart Road Bridge

Table D37 – Smart Road Bridge LC1 Measured and Predicted Transverse Strains – T P-P

Sensor Location	LC1 - Section A (με)			LC1 - Section B (με)		
	Measured	Pucher	Homberg	Measured	Pucher	Homberg
Wing	9	15	18	7	15	18
Left Haunch	1	-7	-8	-3	-7	-9
Middle Top Slab	1	2	3	-1	2	3
Right Haunch	0	6	8	0	7	8
Top Right Web	-1	0	0	0	0	0
Mid Right Web	-1	-1	-1	0	0	0
Right Bottom Slab	1	-4	-5	1	-4	-5
Left Bottom Slab	-4	3	4	-2	3	3
Mid Left Web	2	2	3	0	2	3
Top Left Web	2	5	6	-	-	-

Table D38 – Smart Road Bridge LC2 Measured and Predicted Transverse Strains – T P-P

Sensor Location	LC2 - Section A (με)			LC2 - Section B (με)		
	Measured	Pucher	Homberg	Measured	Pucher	Homberg
Wing	1	0	0	-1	0	0
Left Haunch	-1	6	8	-1	7	8
Middle Top Slab	1	2	3	0	2	3
Right Haunch	1	-7	-8	1	-7	-9
Top Right Web	2	3	4	1	3	3
Mid Right Web	0	2	3	-1	2	3
Right Bottom Slab	-3	3	4	-2	3	4
Left Bottom Slab	1	-4	-5	1	-4	-4
Mid Left Web	-1	-1	-1	0	0	0
Top Left Web	-1	-7	-8	-	-	-

Table D39 – Smart Road Bridge LC3 Measured and Predicted Transverse Strains – T P-P

Sensor Location	LC3 - Section A (με)			LC3 - Section B (με)		
	Measured	Pucher	Homberg	Measured	Pucher	Homberg
Wing	11	15	18	8	15	18
Left Haunch	1	-1	-1	-3	-1	-1
Middle Top Slab	2	5	5	-1	5	6
Right Haunch	1	-1	-1	1	-1	-1
Top Right Web	2	3	3	1	3	3
Mid Right Web	-1	2	2	1	2	3
Right Bottom Slab	-3	-1	-1	-1	-1	-1
Left Bottom Slab	-3	-1	-1	-1	-1	-1
Mid Left Web	1	2	2	0	2	3
Top Left Web	2	-1	-2	-	-	-

Table D40 – Smart Road Bridge LC4 Measured and Predicted Transverse Strains – T P-P

Sensor Location	LC4 - Section A (με)			LC4 - Section B (με)		
	Measured	Pucher	Homberg	Measured	Pucher	Homberg
Wing	11	15	18	7	15	18
Left Haunch	3	-8	-11	-6	-8	-8
Middle Top Slab	17	21	31	14	21	32
Right Haunch	-4	0	2	-4	0	-1
Top Right Web	-4	-2	-4	-2	-2	-2
Mid Right Web	-4	-2	-3	-1	-2	-2
Right Bottom Slab	-2	-2	-4	2	-2	-3
Left Bottom Slab	-5	3	5	-2	3	3
Mid Left Web	-3	1	1	-1	1	0
Top Left Web	-1	-3	-2	-	-	-

Table D41 – Smart Road Bridge LC5 Measured and Predicted Transverse Strains – T P-P

Sensor Location	LC5 - Section A (με)			LC5 - Section B (με)		
	Measured	Pucher	Homberg	Measured	Pucher	Homberg
Wing	3	0	0	1	0	0
Left Haunch	-5	-7	-12	-7	-7	-12
Middle Top Slab	21	43	49	20	43	49
Right Haunch	-3	-7	-11	-3	-7	-11
Top Right Web	-8	-3	-4	-4	-3	-4
Mid Right Web	-7	-2	-2	-3	-2	-3
Right Bottom Slab	-2	1	2	2	1	2
Left Bottom Slab	-2	0	0	1	1	0
Mid Left Web	-6	-2	-3	-2	-2	-3
Top Left Web	-4	-8	-12	-	-	-

11.4.3 Varina-Enon Bridge

Table D42 – Varina-Enon Bridge LC4 Measured and Predicted Transverse Strains – T P-P

Sensor Location	LC4 - Section D (με)			LC4 - Section C (με)		
	Measured	Pucher	Homberg	Measured	Pucher	Homberg
Top Slab	-6	2	3	-2	2	3
R Top Slab	-3	-16	-19	-	-16	-19
R Haunch	-3	-14	-16	-4	-14	-16
R Wing	-19	-30	-34	-	-30	-34
R Top Web	9	15	18	14	15	18
R Bot Web	-5	11	13	-3	11	13
R Bot Slab	-9	6	7	-5	6	7

Table D43 – Varina-Enon Bridge LC5 Measured and Predicted Transverse Strains – T P-P

Sensor Location	LC5 - Section D (με)			LC5 - Section C (με)		
	Measured	Pucher	Homberg	Measured	Pucher	Homberg
Top Slab	-12	2	3	-3	2	3
R Top Slab	-7	-17	-19	-	-17	-19
R Haunch	-7	-14	-16	-6	-14	-16
R Wing	-26	-31	-35	-	-31	-35
R Top Web	13	16	18	23	16	18
R Bot Web	-6	12	13	-7	12	13
R Bot Slab	-15	7	8	-9	7	8

Table D44 – Varina-Enon Bridge LC6 Measured and Predicted Transverse Strains – T P-P

Sensor Location	LC6 - Section D (με)			LC6 - Section C (με)		
	Measured	Pucher	Homberg	Measured	Pucher	Homberg
Top Slab	23	18	23	5	18	23
R Top Slab	10	26	41	-	26	41
R Haunch	-9	-19	-24	-7	-19	-24
R Wing	-25	-30	-34	-	-30	-34
R Top Web	2	1	-4	-10	1	-4
R Bot Web	-14	2	-1	-6	2	-1
R Bot Slab	-12	1	0	-5	1	0

11.5 Pin supports at top and bottom of each web (4P) frame model results

11.5.1 Seabreeze Bridge

Table D45 – Seabreeze Bridge LC1 Measured and Predicted Transverse Strains – 4P

Sensor Location	LC1 - Section A (με)			LC1 - Section B (με)		
	Measured	Pucher	Homberg	Measured	Pucher	Homberg
Wing	-42	-46	-51	-19	-46	-51
Left Top Slab	-1	-9	-10	-5	-11	-13
Mid Top Slab	1	5	6	-1	6	6
Top Web	4	30	34	8	28	32
Bottom Web	-4	7	7	-2	-4	-4
Left Bot. Slab	-7	-6	-6	-2	-7	-8

Table D46 – Seabreeze Bridge LC3 Measured and Predicted Transverse Strains – 4P

Sensor Location	LC3 - Section A (με)			LC3 - Section B (με)		
	Measured	Pucher	Homberg	Measured	Pucher	Homberg
Wing	-4	0	0	-3	0	0
Left Haunch	-19	-22	-31	-14	-22	-31
Middle Top Slab	38	47	75	27	46	74
Top Right Web	-5	-8	-12	-11	-6	-10
Mid Right Web	-2	-2	-3	1	0	0
Right Bottom Slab	-2	0	1	1	1	2

Table D47 – Seabreeze Bridge LC4 Measured and Predicted Transverse Strains – 4P

Sensor Location	LC4 - Section A (με)			LC4 - Section B (με)		
	Measured	Pucher	Homberg	Measured	Pucher	Homberg
Wing	-6	0	0	-6	0	0
Left Haunch	-19	-21	-33	-17	-20	-31
Middle Top Slab	53	74	118	33	74	117
Top Right Web	-7	-16	-25	-16	-14	-23
Mid Right Web	-3	-4	-6	0	1	2
Right Bottom Slab	-3	2	4	2	3	5

11.5.2 Smart Road Bridge

Table D48 – Smart Road Bridge LC1 Measured and Predicted Transverse Strains – 4P

Sensor Location	LC1 - Section A (με)			LC1 - Section B (με)		
	Measured	Pucher	Homberg	Measured	Pucher	Homberg
Wing	9	15	18	7	15	18
Left Haunch	1	-4	-5	-3	-5	-6
Middle Top Slab	1	2	3	-1	2	3
Right Haunch	0	4	4	0	4	5
Top Right Web	-1	-1	-2	0	-1	-2
Mid Right Web	-1	-1	-1	0	-1	-1
Right Bottom Slab	1	1	1	1	1	2
Left Bottom Slab	-4	-2	-2	-2	-2	-2
Mid Left Web	2	3	3	0	3	4
Top Left Web	2	3	3	-	-	-

Table D49 – Smart Road Bridge LC2 Measured and Predicted Transverse Strains – 4P

Sensor Location	LC2 - Section A (με)			LC2 - Section B (με)		
	Measured	Pucher	Homberg	Measured	Pucher	Homberg
Wing	1	0	0	-1	0	0
Left Haunch	-1	4	4	-1	4	5
Middle Top Slab	1	2	3	0	2	3
Right Haunch	1	-4	-5	1	-5	-6
Top Right Web	2	4	5	1	4	5
Mid Right Web	0	3	3	-1	3	4
Right Bottom Slab	-3	-2	-2	-2	-2	-3
Left Bottom Slab	1	1	1	1	1	2
Mid Left Web	-1	-1	-1	0	-1	-1
Top Left Web	-1	-4	-5	-	-	-

Table D50 – Smart Road Bridge LC3 Measured and Predicted Transverse Strains – 4P

Sensor Location	LC3 - Section A (με)			LC3 - Section B (με)		
	Measured	Pucher	Homberg	Measured	Pucher	Homberg
Wing	11	15	18	8	15	18
Left Haunch	1	-1	-1	-3	-1	-1
Middle Top Slab	2	5	5	-1	5	6
Right Haunch	1	-1	-1	1	-1	-1
Top Right Web	2	3	3	1	3	3
Mid Right Web	-1	2	2	1	2	3
Right Bottom Slab	-3	-1	-1	-1	-1	-1
Left Bottom Slab	-3	-1	-1	-1	-1	-1
Mid Left Web	1	2	2	0	2	3
Top Left Web	2	-1	-2	-	-	-

Table D51 – Smart Road Bridge LC4 Measured and Predicted Transverse Strains – 4P

Sensor Location	LC4 - Section A (με)			LC4 - Section B (με)		
	Measured	Pucher	Homberg	Measured	Pucher	Homberg
Wing	11	15	18	7	15	18
Left Haunch	3	-6	-7	-6	-6	-6
Middle Top Slab	17	21	31	14	21	32
Right Haunch	-4	-2	-1	-4	-2	-3
Top Right Web	-4	-3	-6	-2	-3	-4
Mid Right Web	-4	-2	-3	-1	-2	-3
Right Bottom Slab	-2	1	2	2	1	2
Left Bottom Slab	-5	-1	-2	-2	-1	-1
Mid Left Web	-3	1	1	-1	1	1
Top Left Web	-1	-5	-5	-	-	-

Table D52 – Smart Road Bridge LC5 Measured and Predicted Transverse Strains – 4P

Sensor Location	LC5 - Section A (με)			LC5 - Section B (με)		
	Measured	Pucher	Homberg	Measured	Pucher	Homberg
Wing	3	0	0	1	0	0
Left Haunch	-5	-8	-12	-7	-7	-12
Middle Top Slab	21	43	49	20	43	49
Right Haunch	-3	-7	-10	-3	-7	-10
Top Right Web	-8	-3	-3	-4	-3	-3
Mid Right Web	-7	-2	-2	-3	-2	-2
Right Bottom Slab	-2	0	0	2	1	0
Left Bottom Slab	-2	1	1	1	1	1
Mid Left Web	-6	-2	-3	-2	-2	-4
Top Left Web	-4	-8	-11	-	-	-

11.5.3 Varina-Enon Bridge

Table D53 – Varina-Enon Bridge LC4 Measured and Predicted Transverse Strains – 4P

Sensor Location	LC4 - Section D (με)			LC4 - Section C (με)		
	Measured	Pucher	Homberg	Measured	Pucher	Homberg
Top Slab	-6	2	3	-2	2	3
R Top Slab	-3	-7	-8	-	-7	-8
R Haunch	-3	-7	-8	-4	-7	-8
R Wing	-19	-30	-34	-	-30	-34
R Top Web	9	22	26	14	22	26
R Bot Web	-5	1	1	-3	1	1
R Bot Slab	-9	-6	-6	-5	-6	-6

Table D54 – Varina-Enon Bridge LC5 Measured and Predicted Transverse Strains – 4P

Sensor Location	LC5 - Section D (με)			LC5 - Section C (με)		
	Measured	Pucher	Homberg	Measured	Pucher	Homberg
Top Slab	-12	2	3	-3	2	3
R Top Slab	-7	-7	-8	-	-7	-8
R Haunch	-7	-7	-8	-6	-7	-8
R Wing	-26	-31	-35	-	-31	-35
R Top Web	13	23	26	23	23	26
R Bot Web	-6	1	1	-7	1	1
R Bot Slab	-15	-6	-7	-9	-6	-7

Table D55 – Varina-Enon Bridge LC6 Measured and Predicted Transverse Strains – 4P

Sensor Location	LC6 - Section D (με)			LC6 - Section C (με)		
	Measured	Pucher	Homberg	Measured	Pucher	Homberg
Top Slab	23	18	23	5	18	23
R Top Slab	10	28	40	-	28	40
R Haunch	-9	-18	-25	-7	-18	-25
R Wing	-25	-30	-34	-	-30	-34
R Top Web	2	2	-4	-10	2	-4
R Bot Web	-14	0	0	-6	0	0
R Bot Slab	-12	-1	1	-5	-1	1

11.6 B P-R frame model with KSPAN results, Section A only

11.6.1 Seabreeze Bridge

Table D56 – Seabreeze Bridge LC1 Measured and Predicted Transverse Strains – B P-R and K_{SPAN}

Sensor Location	LC1 - Section A (με)		
	Measured	Pucher	Homberg
Wing	-42	-45	-50
Left Top Slab	-1	-26	-29
Mid Top Slab	1	-3	-3
Top Web	4	29	33
Bottom Web	-4	16	17
Left Bot. Slab	-7	25	27

Table D57 – Seabreeze Bridge LC3 Measured and Predicted Transverse Strains – B P-R and K_{SPAN}

Sensor Location	LC3 - Section A (με)		
	Measured	Pucher	Homberg
Wing	-4	0	0
Left Haunch	-19	-22	-30
Middle Top Slab	38	55	85
Top Right Web	-5	-21	-30
Mid Right Web	-2	-4	-6
Right Bottom Slab	-2	7	8

Table D58 – Seabreeze Bridge LC4 Measured and Predicted Transverse Strains – B P-R and K_{SPAN}

Sensor Location	LC4 - Section A (με)		
	Measured	Pucher	Homberg
Wing	-6	0	-1
Left Haunch	-19	-15	-23
Middle Top Slab	53	81	129
Top Right Web	-7	-24	-37
Mid Right Web	-3	-8	-13
Right Bottom Slab	-3	-5	-8

11.6.2 Smart Road Bridge

Table D59 – Smart Road Bridge LC1 Measured and Predicted Transverse Strains – B P-R and K_{SPAN}

Sensor Location	LC1 - Section A (με)		
	Measured	Pucher	Homberg
Wing	9	15	18
Left Haunch	1	-8	-10
Middle Top Slab	1	-2	-3
Right Haunch	0	6	7
Top Right Web	-1	4	4
Mid Right Web	-1	2	2
Right Bottom Slab	1	-6	-7
Left Bottom Slab	-4	3	4
Mid Left Web	2	4	5
Top Left Web	2	6	7

Table D60 – Smart Road Bridge LC2 Measured and Predicted Transverse Strains – B P-R and K_{SPAN}

Sensor Location	LC2 - Section A (με)		
	Measured	Pucher	Homberg
Wing	1	0	0
Left Haunch	-1	6	7
Middle Top Slab	1	-2	-3
Right Haunch	1	-8	-10
Top Right Web	2	6	7
Mid Right Web	0	4	5
Right Bottom Slab	-3	3	4
Left Bottom Slab	1	-6	-7
Mid Left Web	-1	2	2
Top Left Web	-1	-7	-9

Table D61 – Smart Road Bridge LC3 Measured and Predicted Transverse Strains – B P-R and K_{SPAN}

Sensor Location	LC3 - Section A (με)		
	Measured	Pucher	Homberg
Wing	11	15	18
Left Haunch	1	-2	-3
Middle Top Slab	2	-5	-6
Right Haunch	1	-2	-3
Top Right Web	2	9	11
Mid Right Web	-1	6	7
Right Bottom Slab	-3	-3	-4
Left Bottom Slab	-3	-3	-4
Mid Left Web	1	6	7
Top Left Web	2	-2	-2

Table D62 – Smart Road Bridge LC4 Measured and Predicted Transverse Strains – B P-R and K_{SPAN}

Sensor Location	LC4 - Section A (με)		
	Measured	Pucher	Homberg
Wing	11	15	18
Left Haunch	3	-7	-10
Middle Top Slab	17	23	37
Right Haunch	-4	1	4
Top Right Web	-4	-3	-7
Mid Right Web	-4	-2	-5
Right Bottom Slab	-2	-2	-4
Left Bottom Slab	-5	4	8
Mid Left Web	-3	-1	-2
Top Left Web	-1	-2	-1

Table D63 – Smart Road Bridge LC5 Measured and Predicted Transverse Strains – B P-R and K_{SPAN}

Sensor Location	LC5 - Section A (με)		
	Measured	Pucher	Homberg
Wing	3	0	0
Left Haunch	-5	-5	-9
Middle Top Slab	21	54	63
Right Haunch	-3	-5	-8
Top Right Web	-8	-10	-13
Mid Right Web	-7	-6	-8
Right Bottom Slab	-2	4	6
Left Bottom Slab	-2	3	3
Mid Left Web	-6	-6	-9
Top Left Web	-4	-8	-11

11.6.3 Varina-Enon Bridge

Table D64 – Varina-Enon Bridge LC4 Measured and Predicted Transverse Strains – B P-R and K_{SPAN}

Sensor Location	LC4 - Section D (με)		
	Measured	Pucher	Homberg
Top Slab	-6	-3	-4
R Top Slab	-3	-22	-26
R Haunch	-3	-16	-19
R Wing	-19	-25	-29
R Top Web	9	19	22
R Bot Web	-5	15	17
R Bot Slab	-9	8	10

Table D65 – Varina-Enon Bridge LC5 Measured and Predicted Transverse Strains – B P-R and K_{SPAN}

Sensor Location	LC5 - Section D (με)		
	Measured	Pucher	Homberg
Top Slab	-12	-4	-4
R Top Slab	-7	-23	-26
R Haunch	-7	-17	-19
R Wing	-26	-26	-29
R Top Web	13	20	22
R Bot Web	-6	15	17
R Bot Slab	-15	9	10

Table D66 – Varina-Enon Bridge LC6 Measured and Predicted Transverse Strains – B P-R and K_{SPAN}

Sensor Location	LC6 - Section D (με)		
	Measured	Pucher	Homberg
Top Slab	23	18	26
R Top Slab	10	26	43
R Haunch	-9	-19	-24
R Wing	-25	-29	-35
R Top Web	2	0	-6
R Bot Web	-14	2	-2
R Bot Slab	-12	2	0

11.7 B P-R frame model with KIS results

11.7.1 Seabreeze Bridge

Table D67 – Seabreeze Bridge LC1 Measured and Predicted Transverse Strains – B P-R and K_{IS}

Sensor Location	LC1 - Section A (με)		
	Measured	Pucher	Homberg
Wing	-42	-37	-41
Left Top Slab	-1	-18	-20
Mid Top Slab	1	-2	-3
Top Web	4	27	30
Bottom Web	-4	12	13
Left Bot. Slab	-7	14	15

Table D68 – Seabreeze Bridge LC3 Measured and Predicted Transverse Strains – B P-R and K_{IS}

Sensor Location	LC3 - Section A (με)		
	Measured	Pucher	Homberg
Wing	-4	-2	-3
Left Top Slab	-19	-21	-30
Mid Top Slab	38	55	85
Top Web	-5	-19	-27
Bottom Web	-2	-4	-6
Left Bot. Slab	-2	5	6

Table D69 – Seabreeze Bridge LC4 Measured and Predicted Transverse Strains – B P-R and K_{IS}

Sensor Location	LC4 - Section A (με)		
	Measured	Pucher	Homberg
Wing	-6	-4	-7
Left Top Slab	-19	-17	-27
Mid Top Slab	53	81	129
Top Web	-7	-22	-34
Bottom Web	-3	-7	-11
Left Bot. Slab	-3	-2	-3

11.7.2 Smart Road Bridge

Table D70 – Smart Road Bridge LC1 Measured and Predicted Transverse Strains – B P-R and K_{IS}

Sensor Location	LC1 - Section A (με)		
	Measured	Pucher	Homberg
Wing	9	11	14
Left Haunch	1	-6	-7
Middle Top Slab	1	-2	-2
Right Haunch	0	4	5
Top Right Web	-1	3	4
Mid Right Web	-1	1	2
Right Bottom Slab	1	-4	-5
Left Bottom Slab	-4	2	2
Mid Left Web	2	3	4
Top Left Web	2	4	5

Table D71 – Smart Road Bridge LC2 Measured and Predicted Transverse Strains – B P-R and K_{IS}

Sensor Location	LC2 - Section A (με)		
	Measured	Pucher	Homberg
Wing	1	1	1
Left Haunch	-1	4	5
Middle Top Slab	1	-2	-2
Right Haunch	1	-6	-7
Top Right Web	2	5	6
Mid Right Web	0	3	4
Right Bottom Slab	-3	2	2
Left Bottom Slab	1	-4	-5
Mid Left Web	-1	1	2
Top Left Web	-1	-5	-6

Table D72 – Smart Road Bridge LC3 Measured and Predicted Transverse Strains – B P-R and K_{IS}

Sensor Location	LC3 - Section A (με)		
	Measured	Pucher	Homberg
Wing	11	12	14
Left Haunch	1	-2	-2
Middle Top Slab	2	-4	-5
Right Haunch	1	-2	-2
Top Right Web	2	8	9
Mid Right Web	-1	5	6
Right Bottom Slab	-3	-3	-3
Left Bottom Slab	-3	-3	-3
Mid Left Web	1	5	6
Top Left Web	2	-1	-2

Table D73 – Smart Road Bridge LC4 Measured and Predicted Transverse Strains – B P-R and K_{IS}

Sensor Location	LC4 - Section A (με)		
	Measured	Pucher	Homberg
Wing	11	14	17
Left Haunch	3	-6	-8
Middle Top Slab	17	23	36
Right Haunch	-4	-1	1
Top Right Web	-4	-3	-6
Mid Right Web	-4	-2	-5
Right Bottom Slab	-2	-2	-2
Left Bottom Slab	-5	3	6
Mid Left Web	-3	0	-2
Top Left Web	-1	-4	-3

Table D74 – Smart Road Bridge LC5 Measured and Predicted Transverse Strains – B P-R and K_{IS}

Sensor Location	LC5 - Section A (με)		
	Measured	Pucher	Homberg
Wing	3	4	5
Left Haunch	-5	-6	-10
Middle Top Slab	21	53	61
Right Haunch	-3	-5	-8
Top Right Web	-8	-8	-11
Mid Right Web	-7	-5	-7
Right Bottom Slab	-2	3	5
Left Bottom Slab	-2	2	3
Mid Left Web	-6	-5	-7
Top Left Web	-4	-8	-11

11.7.3 Varina-Enon Bridge

Table D75 – Varina-Enon Bridge LC4 Measured and Predicted Transverse Strains – B P-R and K_{IS}

Sensor Location	LC4 - Section D (με)		
	Measured	Pucher	Homberg
Top Slab	-6	-3	-4
R Top Slab	-3	-16	-18
R Haunch	-3	-11	-13
R Wing	-19	-21	-24
R Top Web	9	19	22
R Bot Web	-5	10	11
R Bot Slab	-9	3	4

Table D76 – Varina-Enon Bridge LC5 Measured and Predicted Transverse Strains – B P-R and K_{IS}

Sensor Location	LC5 - Section D (με)		
	Measured	Pucher	Homberg
Top Slab	-12	-3	-4
R Top Slab	-7	-16	-19
R Haunch	-7	-12	-13
R Wing	-26	-22	-24
R Top Web	13	19	22
R Bot Web	-6	10	11
R Bot Slab	-15	3	4

Table D77 – Varina-Enon Bridge LC6 Measured and Predicted Transverse Strains – B P-R and K_{IS}

Sensor Location	LC6 - Section D (με)		
	Measured	Pucher	Homberg
Top Slab	23	18	25
R Top Slab	10	27	42
R Haunch	-9	-18	-24
R Wing	-25	-29	-36
R Top Web	2	1	-6
R Bot Web	-14	1	-2
R Bot Slab	-12	1	1

11.8 B P-R frame model with KBEF results

11.8.1 Seabreeze Bridge

Table D78 – Seabreeze Bridge LC1 Measured and Predicted Transverse Strains – B P-R and K_{BEF}

Sensor Location	LC1 - Section A (με)		
	Measured	Pucher	Homberg
Wing	-42	-34	-38
Left Top Slab	-1	-16	-17
Mid Top Slab	1	-2	-3
Top Web	4	26	29
Bottom Web	-4	11	12
Left Bot. Slab	-7	11	12

Table D79 – Seabreeze Bridge LC3 Measured and Predicted Transverse Strains – B P-R and K_{BEF}

Sensor Location	LC3 - Section A (με)		
	Measured	Pucher	Homberg
Wing	-4	-2	-4
Left Haunch	-19	-21	-29
Middle Top Slab	38	54	85
Top Right Web	-5	-19	-26
Mid Right Web	-2	-4	-6
Right Bottom Slab	-2	5	5

Table D80 – Seabreeze Bridge LC4 Measured and Predicted Transverse Strains – B P-R and K_{BEF}

Sensor Location	LC4 - Section A (με)		
	Measured	Pucher	Homberg
Wing	-6	-6	-9
Left Haunch	-19	-18	-28
Middle Top Slab	53	81	129
Top Right Web	-7	-21	-33
Mid Right Web	-3	-7	-10
Right Bottom Slab	-3	-1	-2

11.8.2 Smart Road Bridge

Table D81 – Smart Road Bridge LC1 Measured and Predicted Transverse Strains – B P-R and K_{BEF}

Sensor Location	LC1 - Section A (με)		
	Measured	Pucher	Homberg
Wing	9	11	13
Left Haunch	1	-6	-7
Middle Top Slab	1	-2	-2
Right Haunch	0	4	5
Top Right Web	-1	3	3
Mid Right Web	-1	1	2
Right Bottom Slab	1	-4	-5
Left Bottom Slab	-4	2	2
Mid Left Web	2	3	4
Top Left Web	2	4	4

Table D82 – Smart Road Bridge LC2 Measured and Predicted Transverse Strains – B P-R and K_{BEF}

Sensor Location	LC2 - Section A (με)		
	Measured	Pucher	Homberg
Wing	1	1	1
Left Haunch	-1	4	5
Middle Top Slab	1	-2	-2
Right Haunch	1	-6	-7
Top Right Web	2	5	6
Mid Right Web	0	3	4
Right Bottom Slab	-3	2	2
Left Bottom Slab	1	-4	-5
Mid Left Web	-1	1	2
Top Left Web	-1	-5	-6

Table D83 – Smart Road Bridge LC3 Measured and Predicted Transverse Strains – B P-R and K_{BEF}

Sensor Location	LC3 - Section A (με)		
	Measured	Pucher	Homberg
Wing	11	11	13
Left Haunch	1	-2	-2
Middle Top Slab	2	-4	-5
Right Haunch	1	-2	-2
Top Right Web	2	7	9
Mid Right Web	-1	5	6
Right Bottom Slab	-3	-2	-3
Left Bottom Slab	-3	-2	-3
Mid Left Web	1	5	6
Top Left Web	2	-1	-2

Table D84 – Smart Road Bridge LC4 Measured and Predicted Transverse Strains – B P-R and K_{BEF}

Sensor Location	LC4 - Section A (με)		
	Measured	Pucher	Homberg
Wing	11	14	17
Left Haunch	3	-6	-8
Middle Top Slab	17	23	36
Right Haunch	-4	-1	1
Top Right Web	-4	-3	-6
Mid Right Web	-4	-2	-4
Right Bottom Slab	-2	-1	-2
Left Bottom Slab	-5	3	5
Mid Left Web	-3	0	-2
Top Left Web	-1	-4	-4

Table D85 – Smart Road Bridge LC5 Measured and Predicted Transverse Strains – B P-R and K_{BEF}

Sensor Location	LC5 - Section A (με)		
	Measured	Pucher	Homberg
Wing	3	4	6
Left Haunch	-5	-6	-10
Middle Top Slab	21	52	61
Right Haunch	-3	-5	-8
Top Right Web	-8	-8	-10
Mid Right Web	-7	-5	-6
Right Bottom Slab	-2	3	4
Left Bottom Slab	-2	2	3
Mid Left Web	-6	-5	-7
Top Left Web	-4	-8	-11

11.8.3 Varina-Enon Bridge

Table D86 – Varina-Enon Bridge LC4 Measured and Predicted Transverse Strains – B P-R and K_{BEF}

Sensor Location	LC4 - Section D (με)		
	Measured	Pucher	Homberg
Top Slab	-6	-3	-4
R Top Slab	-3	-15	-17
R Haunch	-3	-11	-12
R Wing	-19	-20	-23
R Top Web	9	19	21
R Bot Web	-5	9	10
R Bot Slab	-9	2	3

Table D87 – Varina-Enon Bridge LC5 Measured and Predicted Transverse Strains – B P-R and K_{BEF}

Sensor Location	LC5 - Section D (με)		
	Measured	Pucher	Homberg
Top Slab	-12	-3	-4
R Top Slab	-7	-15	-17
R Haunch	-7	-11	-13
R Wing	-26	-21	-23
R Top Web	13	19	22
R Bot Web	-6	9	10
R Bot Slab	-15	2	3

Table D88 – Varina-Enon Bridge LC6 Measured and Predicted Transverse Strains – B P-R and K_{BEF}

Sensor Location	LC6 - Section D (με)		
	Measured	Pucher	Homberg
Top Slab	23	18	25
R Top Slab	10	27	42
R Haunch	-9	-18	-24
R Wing	-25	-29	-36
R Top Web	2	1	-6
R Bot Web	-14	1	-1
R Bot Slab	-12	1	1

11.9 4P frame model with KSPAN results

11.9.1 Seabreeze Bridge

Table D89 – Seabreeze Bridge LC1 Measured and Predicted Transverse Strains – B P-R and K_{SPAN}

Sensor Location	LC1 - Section A (με)		
	Measured	Pucher	Homberg
Wing	-42	-45	-51
Left Top Slab	-1	-9	-10
Mid Top Slab	1	5	6
Top Web	4	30	33
Bottom Web	-4	7	7
Left Bot. Slab	-7	-6	-6

Table D90 – Seabreeze Bridge LC3 Measured and Predicted Transverse Strains – B P-R and K_{SPAN}

Sensor Location	LC3 - Section A (με)		
	Measured	Pucher	Homberg
Wing	-4	0	0
Left Haunch	-19	-22	-31
Middle Top Slab	38	47	75
Top Right Web	-5	-8	-12
Mid Right Web	-2	-2	-3
Right Bottom Slab	-2	0	1

Table D91 – Seabreeze Bridge LC4 Measured and Predicted Transverse Strains – B P-R and K_{SPAN}

Sensor Location	LC4 - Section A (με)		
	Measured	Pucher	Homberg
Wing	-6	0	0
Left Haunch	-19	-21	-33
Middle Top Slab	53	74	118
Top Right Web	-7	-16	-25
Mid Right Web	-3	-4	-6
Right Bottom Slab	-3	2	4

11.9.2 Smart Road Bridge

Table D92 – Smart Road Bridge LC1 Measured and Predicted Transverse Strains – B P-R and K_{SPAN}

Sensor Location	LC1 - Section A (με)		
	Measured	Pucher	Homberg
Wing	9	15	18
Left Haunch	1	-4	-5
Middle Top Slab	1	2	3
Right Haunch	0	4	4
Top Right Web	-1	-1	-2
Mid Right Web	-1	-1	-1
Right Bottom Slab	1	1	1
Left Bottom Slab	-4	-2	-2
Mid Left Web	2	3	3
Top Left Web	2	3	3

Table D93 – Smart Road Bridge LC2 Measured and Predicted Transverse Strains – B P-R and K_{SPAN}

Sensor Location	LC2 - Section A (με)		
	Measured	Pucher	Homberg
Wing	1	0	0
Left Haunch	-1	4	4
Middle Top Slab	1	2	3
Right Haunch	1	-4	-5
Top Right Web	2	4	5
Mid Right Web	0	3	3
Right Bottom Slab	-3	-2	-2
Left Bottom Slab	1	1	1
Mid Left Web	-1	-1	-1
Top Left Web	-1	-4	-5

Table D94 – Smart Road Bridge LC3 Measured and Predicted Transverse Strains – B P-R and K_{SPAN}

Sensor Location	LC3 - Section A (με)		
	Measured	Pucher	Homberg
Wing	11	15	18
Left Haunch	1	-1	-1
Middle Top Slab	2	5	5
Right Haunch	1	-1	-1
Top Right Web	2	3	3
Mid Right Web	-1	2	2
Right Bottom Slab	-3	-1	-1
Left Bottom Slab	-3	-1	-1
Mid Left Web	1	2	2
Top Left Web	2	-1	-2

Table D95 – Smart Road Bridge LC4 Measured and Predicted Transverse Strains – B P-R and K_{SPAN}

Sensor Location	LC4 - Section A (με)		
	Measured	Pucher	Homberg
Wing	11	15	18
Left Haunch	3	-6	-7
Middle Top Slab	17	21	31
Right Haunch	-4	-2	-1
Top Right Web	-4	-3	-6
Mid Right Web	-4	-2	-3
Right Bottom Slab	-2	1	2
Left Bottom Slab	-5	-1	-2
Mid Left Web	-3	1	1
Top Left Web	-1	-5	-5

Table D96 – Smart Road Bridge LC5 Measured and Predicted Transverse Strains – B P-R and K_{SPAN}

Sensor Location	LC5 - Section A (με)		
	Measured	Pucher	Homberg
Wing	3	0	0
Left Haunch	-5	-8	-12
Middle Top Slab	21	43	49
Right Haunch	-3	-7	-10
Top Right Web	-8	-3	-3
Mid Right Web	-7	-2	-2
Right Bottom Slab	-2	0	0
Left Bottom Slab	-2	1	1
Mid Left Web	-6	-2	-3
Top Left Web	-4	-8	-11

11.9.3 Varina-Enon Bridge

Table D97 – Varina-Enon Bridge LC4 Measured and Predicted Transverse Strains – B P-R and K_{SPAN}

Sensor Location	LC4 - Section D (με)		
	Measured	Pucher	Homberg
Top Slab	-6	2	3
R Top Slab	-3	-7	-8
R Haunch	-3	-7	-8
R Wing	-19	-29	-33
R Top Web	9	21	25
R Bot Web	-5	1	1
R Bot Slab	-9	-5	-6

Table D98 – Varina-Enon Bridge LC5 Measured and Predicted Transverse Strains – B P-R and K_{SPAN}

Sensor Location	LC5 - Section D (με)		
	Measured	Pucher	Homberg
Top Slab	-12	2	3
R Top Slab	-7	-7	-8
R Haunch	-7	-7	-8
R Wing	-26	-30	-34
R Top Web	13	22	25
R Bot Web	-6	1	1
R Bot Slab	-15	-5	-6

Table D99 – Varina-Enon Bridge LC6 Measured and Predicted Transverse Strains – B P-R and K_{SPAN}

Sensor Location	LC6 - Section D (με)		
	Measured	Pucher	Homberg
Top Slab	23	18	23
R Top Slab	10	28	40
R Haunch	-9	-18	-25
R Wing	-25	-30	-35
R Top Web	2	2	-4
R Bot Web	-14	0	0
R Bot Slab	-12	-1	1

11.10 4P frame model with KIS results

11.10.1Seabreeze Bridge

Table D100 – Seabreeze Bridge LC1 Measured and Predicted Transverse Strains – 4P and K_{IS}

Sensor Location	LC1 - Section A (με)		
	Measured	Pucher	Homberg
Wing	-42	-42	-47
Left Top Slab	-1	-8	-9
Mid Top Slab	1	5	5
Top Web	4	28	31
Bottom Web	-4	6	7
Left Bot. Slab	-7	-5	-6

Table D101 – Seabreeze Bridge LC3 Measured and Predicted Transverse Strains – 4P and K_{IS}

Sensor Location	LC3 - Section A (με)		
	Measured	Pucher	Homberg
Wing	-4	-1	-1
Left Haunch	-19	-22	-30
Middle Top Slab	38	47	75
Top Right Web	-5	-8	-12
Mid Right Web	-2	-2	-3
Right Bottom Slab	-2	0	1

Table D102 – Seabreeze Bridge LC4 Measured and Predicted Transverse Strains – 4P and K_{IS}

Sensor Location	LC4 - Section A (με)		
	Measured	Pucher	Homberg
Wing	-6	-2	-3
Left Haunch	-19	-21	-33
Middle Top Slab	53	74	118
Top Right Web	-7	-15	-23
Mid Right Web	-3	-4	-6
Right Bottom Slab	-3	2	3

11.10.2Smart Road Bridge

Table D103 – Smart Road Bridge LC1 Measured and Predicted Transverse Strains – 4P and K_{IS}

Sensor Location	LC1 - Section A (με)		
	Measured	Pucher	Homberg
Wing	9	13	16
Left Haunch	1	-4	-4
Middle Top Slab	1	2	3
Right Haunch	0	3	4
Top Right Web	-1	-1	-1
Mid Right Web	-1	-1	-1
Right Bottom Slab	1	1	1
Left Bottom Slab	-4	-2	-2
Mid Left Web	2	2	3
Top Left Web	2	2	3

Table D104 – Smart Road Bridge LC2 Measured and Predicted Transverse Strains – 4P and K_{IS}

Sensor Location	LC2 - Section A (με)		
	Measured	Pucher	Homberg
Wing	1	1	1
Left Haunch	-1	3	4
Middle Top Slab	1	2	3
Right Haunch	1	-4	-4
Top Right Web	2	4	5
Mid Right Web	0	2	3
Right Bottom Slab	-3	-2	-2
Left Bottom Slab	1	1	1
Mid Left Web	-1	-1	-1
Top Left Web	-1	-4	-4

Table D105 – Smart Road Bridge LC3 Measured and Predicted Transverse Strains – 4P and K_{IS}

Sensor Location	LC3 - Section A (με)		
	Measured	Pucher	Homberg
Wing	11	14	16
Left Haunch	1	0	-1
Middle Top Slab	2	4	5
Right Haunch	1	0	-1
Top Right Web	2	3	3
Mid Right Web	-1	2	2
Right Bottom Slab	-3	-1	-1
Left Bottom Slab	-3	-1	-1
Mid Left Web	1	2	2
Top Left Web	2	-1	-2

Table D106 – Smart Road Bridge LC4 Measured and Predicted Transverse Strains – 4P and K_{IS}

Sensor Location	LC4 - Section A (με)		
	Measured	Pucher	Homberg
Wing	11	14	17
Left Haunch	3	-5	-6
Middle Top Slab	17	21	31
Right Haunch	-4	-3	-2
Top Right Web	-4	-2	-5
Mid Right Web	-4	-1	-3
Right Bottom Slab	-2	1	2
Left Bottom Slab	-5	-1	-1
Mid Left Web	-3	1	1
Top Left Web	-1	-5	-6

Table D107 – Smart Road Bridge LC5 Measured and Predicted Transverse Strains – 4P and K_{IS}

Sensor Location	LC5 - Section A (με)		
	Measured	Pucher	Homberg
Wing	3	1	2
Left Haunch	-5	-8	-13
Middle Top Slab	21	44	49
Right Haunch	-3	-7	-10
Top Right Web	-8	-3	-3
Mid Right Web	-7	-2	-2
Right Bottom Slab	-2	0	0
Left Bottom Slab	-2	1	1
Mid Left Web	-6	-2	-3
Top Left Web	-4	-8	-11

11.10.3Varina-Enon Bridge

Table D108 – Varina-Enon Bridge LC4 Measured and Predicted Transverse Strains – 4P and K_{IS}

Sensor Location	LC4 - Section D (με)		
	Measured	Pucher	Homberg
Top Slab	-6	2	2
R Top Slab	-3	-6	-7
R Haunch	-3	-6	-7
R Wing	-19	-27	-30
R Top Web	9	20	23
R Bot Web	-5	1	1
R Bot Slab	-9	-5	-6

Table D109 – Varina-Enon Bridge LC5 Measured and Predicted Transverse Strains – 4P and K_{IS}

Sensor Location	LC5 - Section D (με)		
	Measured	Pucher	Homberg
Top Slab	-12	2	3
R Top Slab	-7	-6	-7
R Haunch	-7	-6	-7
R Wing	-26	-28	-31
R Top Web	13	21	23
R Bot Web	-6	1	1
R Bot Slab	-15	-5	-6

Table D110 – Varina-Enon Bridge LC6 Measured and Predicted Transverse Strains – 4P and K_{IS}

Sensor Location	LC6 - Section D (με)		
	Measured	Pucher	Homberg
Top Slab	23	18	24
R Top Slab	10	28	40
R Haunch	-9	-18	-25
R Wing	-25	-30	-35
R Top Web	2	2	-4
R Bot Web	-14	0	0
R Bot Slab	-12	-1	1

11.11 4P frame model with KBEF results

11.11.1Seabreeze Bridge

Table D111 – Seabreeze Bridge LC1 Measured and Predicted Transverse Strains – 4P and K_{BEF}

Sensor Location	LC1 - Section A (με)		
	Measured	Pucher	Homberg
Wing	-42	-41	-46
Left Top Slab	-1	-8	-9
Mid Top Slab	1	5	5
Top Web	4	27	30
Bottom Web	-4	6	7
Left Bot. Slab	-7	-5	-5

Table D112 – Seabreeze Bridge LC3 Measured and Predicted Transverse Strains – 4P and K_{BEF}

Sensor Location	LC3 - Section A (με)		
	Measured	Pucher	Homberg
Wing	-4	-1	-2
Left Haunch	-19	-22	-30
Middle Top Slab	38	48	75
Top Right Web	-5	-8	-11
Mid Right Web	-2	-2	-3
Right Bottom Slab	-2	0	1

Table D113 – Seabreeze Bridge LC4 Measured and Predicted Transverse Strains – 4P and K_{BEF}

Sensor Location	LC4 - Section A (με)		
	Measured	Pucher	Homberg
Wing	-6	-3	-4
Left Haunch	-19	-21	-33
Middle Top Slab	53	75	118
Top Right Web	-7	-14	-23
Mid Right Web	-3	-3	-5
Right Bottom Slab	-3	2	3

11.11.2Smart Road Bridge

Table D114 – Smart Road Bridge LC1 Measured and Predicted Transverse Strains – 4P and K_{BEF}

Sensor Location	LC1 - Section A (με)		
	Measured	Pucher	Homberg
Wing	9	11	13
Left Haunch	1	-6	-7
Middle Top Slab	1	-2	-2
Right Haunch	0	4	5
Top Right Web	-1	3	3
Mid Right Web	-1	1	2
Right Bottom Slab	1	-4	-5
Left Bottom Slab	-4	2	2
Mid Left Web	2	3	4
Top Left Web	2	4	4

Table D115 – Smart Road Bridge LC2 Measured and Predicted Transverse Strains – 4P and K_{BEF}

Sensor Location	LC2 - Section A (με)		
	Measured	Pucher	Homberg
Wing	1	1	1
Left Haunch	-1	4	5
Middle Top Slab	1	-2	-2
Right Haunch	1	-6	-7
Top Right Web	2	5	6
Mid Right Web	0	3	4
Right Bottom Slab	-3	2	2
Left Bottom Slab	1	-4	-5
Mid Left Web	-1	1	2
Top Left Web	-1	-5	-6

Table D116 – Smart Road Bridge LC3 Measured and Predicted Transverse Strains – 4P and K_{BEF}

Sensor Location	LC3 - Section A (με)		
	Measured	Pucher	Homberg
Wing	11	11	13
Left Haunch	1	-2	-2
Middle Top Slab	2	-4	-5
Right Haunch	1	-2	-2
Top Right Web	2	7	9
Mid Right Web	-1	5	6
Right Bottom Slab	-3	-2	-3
Left Bottom Slab	-3	-2	-3
Mid Left Web	1	5	6
Top Left Web	2	-1	-2

Table D117 – Smart Road Bridge LC4 Measured and Predicted Transverse Strains – 4P and K_{BEF}

Sensor Location	LC4 - Section A (με)		
	Measured	Pucher	Homberg
Wing	11	14	17
Left Haunch	3	-6	-8
Middle Top Slab	17	23	36
Right Haunch	-4	-1	1
Top Right Web	-4	-3	-6
Mid Right Web	-4	-2	-4
Right Bottom Slab	-2	-1	-2
Left Bottom Slab	-5	3	5
Mid Left Web	-3	0	-2
Top Left Web	-1	-4	-4

Table D118 – Smart Road Bridge LC5 Measured and Predicted Transverse Strains – 4P and K_{BEF}

Sensor Location	LC5 - Section A (με)		
	Measured	Pucher	Homberg
Wing	3	4	6
Left Haunch	-5	-6	-10
Middle Top Slab	21	52	61
Right Haunch	-3	-5	-8
Top Right Web	-8	-8	-10
Mid Right Web	-7	-5	-6
Right Bottom Slab	-2	3	4
Left Bottom Slab	-2	2	3
Mid Left Web	-6	-5	-7
Top Left Web	-4	-8	-11

11.11.3Varina-Enon Bridge

Table D119 – Varina-Enon Bridge LC4 Measured and Predicted Transverse Strains – 4P and K_{BEF}

Sensor Location	LC4 - Section D (με)		
	Measured	Pucher	Homberg
Top Slab	-6	2	2
R Top Slab	-3	-6	-7
R Haunch	-3	-6	-7
R Wing	-19	-26	-30
R Top Web	9	20	22
R Bot Web	-5	1	1
R Bot Slab	-9	-5	-6

Table D120 – Varina-Enon Bridge LC5 Measured and Predicted Transverse Strains – 4P and K_{BEF}

Sensor Location	LC5 - Section D (με)		
	Measured	Pucher	Homberg
Top Slab	-12	2	2
R Top Slab	-7	-6	-7
R Haunch	-7	-6	-7
R Wing	-26	-27	-31
R Top Web	13	20	23
R Bot Web	-6	1	1
R Bot Slab	-15	-5	-6

Table D121 – Varina-Enon Bridge LC6 Measured and Predicted Transverse Strains – 4P and K_{BEF}

Sensor Location	LC6 - Section D (με)		
	Measured	Pucher	Homberg
Top Slab	23	18	24
R Top Slab	10	28	40
R Haunch	-9	-18	-25
R Wing	-25	-30	-35
R Top Web	2	2	-4
R Bot Web	-14	0	0
R Bot Slab	-12	-1	1

11.12 Uniform Surface Loading Shell Model with Barrier Rails

11.12.1Seabreeze Bridge

Table D122 – Seabreeze Bridge LC1 Measured and Predicted Transverse Strains – Uniform Surface Loading Shell Model with Barriers

Sensor Location	LC1 - Section A (με)			LC1 - Section B (με)		
	Measured	Thin Shells	Thick Shells	Measured	Thin Shells	Thick Shells
Wing	-42	-34	-35	-19	-33	-32
Left Top Slab	-1	-3	-2	-5	-11	-12
Mid Top Slab	1	1	0	-1	0	0
Top Web	4	17	21	8	23	22
Bottom Web	-4	-3	-4	-2	-5	-4
Left Bot. Slab	-7	-11	-14	-2	-7	-7

Table D123 – Seabreeze Bridge LC3 Measured and Predicted Transverse Strains – Uniform Surface Loading Shell Model with Barriers

Sensor Location	LC3 - Section A (με)			LC3 - Section B (με)		
	Measured	Thin Shells	Thick Shells	Measured	Thin Shells	Thick Shells
Wing	-4	-2	-3	-3	-5	-6
Left Haunch	-19	-25	-25	-14	-27	-26
Middle Top Slab	38	36	36	27	32	24
Top Right Web	-5	-11	-17	-11	-16	-17
Mid Right Web	-2	-1	-3	1	2	2
Right Bottom Slab	-2	9	8	1	4	4

Table D124 – Seabreeze Bridge LC4 Measured and Predicted Transverse Strains – Uniform Surface Loading Shell Model with Barriers

Sensor Location	LC4 - Section A (με)			LC4 - Section B (με)		
	Measured	Thin Shells	Thick Shells	Measured	Thin Shells	Thick Shells
Wing	-6	-4	-4	-6	-8	-9
Left Haunch	-19	-16	-17	-17	-23	-23
Middle Top Slab	53	49	49	33	45	45
Top Right Web	-7	-15	-20	-16	-23	-22
Mid Right Web	-3	-3	-6	0	1	1
Right Bottom Slab	-3	-2	0	2	4	4

11.12.2Smart Road Bridge

Table D125 – Smart Road Bridge LC1 Measured and Predicted Transverse Strains – Uniform Surface Loading Shell Model with Barriers

Sensor Location	LC1 - Section A (με)			LC1 - Section B (με)		
	Measured	Thin Shells	Thick Shells	Measured	Thin Shells	Thick Shells
Wing	9	10	10	7	11	10
Left Haunch	1	2	1	-3	0	0
Middle Top Slab	1	1	1	-1	-1	-1
Right Haunch	0	-1	-1	0	-1	-1
Top Right Web	-1	-1	-1	0	-1	-1
Mid Right Web	-1	0	0	0	0	0
Right Bottom Slab	1	4	4	1	1	1
Left Bottom Slab	-4	-5	-5	-2	4	4
Mid Left Web	2	2	2	0	-3	-3
Top Left Web	2	3	3	-	-	-

Table D126 – Smart Road Bridge LC2 Measured and Predicted Transverse Strains – Uniform Surface Loading Shell Model with Barriers

Sensor Location	LC2 - Section A (με)			LC2 - Section B (με)		
	Measured	Thin Shells	Thick Shells	Measured	Thin Shells	Thick Shells
Wing	1	0	0	-1	0	0
Left Haunch	-1	-2	-2	-1	0	0
Middle Top Slab	1	0	0	0	-1	-1
Right Haunch	1	2	2	1	-1	-1
Top Right Web	2	2	2	1	-1	-1
Mid Right Web	0	1	1	-1	4	4
Right Bottom Slab	-3	-3	-3	-2	2	2
Left Bottom Slab	1	4	4	1	-3	-3
Mid Left Web	-1	0	0	0	4	4
Top Left Web	-1	-1	-1	-	-	-

Table D127 – Smart Road Bridge LC3 Measured and Predicted Transverse Strains – Uniform Surface Loading Shell Model with Barriers

Sensor Location	LC3 - Section A (με)			LC3 - Section B (με)		
	Measured	Thin Shells	Thick Shells	Measured	Thin Shells	Thick Shells
Wing	11	10	9	8	11	10
Left Haunch	1	0	0	-3	-1	-1
Middle Top Slab	2	1	1	-1	-1	-1
Right Haunch	1	0	0	1	-1	-2
Top Right Web	2	1	1	1	-1	-1
Mid Right Web	-1	1	1	1	4	4
Right Bottom Slab	-3	1	1	-1	2	2
Left Bottom Slab	-3	-1	-1	-1	1	1
Mid Left Web	1	2	2	0	1	1
Top Left Web	2	2	2	-	-	-

Table D128 – Smart Road Bridge LC4 Measured and Predicted Transverse Strains – Uniform Surface Loading Shell Model with Barriers

Sensor Location	LC4 - Section A (με)			LC4 - Section B (με)		
	Measured	Thin Shells	Thick Shells	Measured	Thin Shells	Thick Shells
Wing	11	12	11	7	12	12
Left Haunch	3	8	1	-6	-6	-7
Middle Top Slab	17	11	11	14	9	9
Right Haunch	-4	-11	-11	-4	-11	-11
Top Right Web	-4	-8	-8	-2	-7	-7
Mid Right Web	-4	-4	-5	-1	-7	-7
Right Bottom Slab	-2	7	7	2	-2	-2
Left Bottom Slab	-5	-4	-4	-2	7	7
Mid Left Web	-3	-3	-3	-1	-1	-1
Top Left Web	-1	-4	-4	-	-	-

Table D129 – Smart Road Bridge LC5 Measured and Predicted Transverse Strains – Uniform Surface Loading Shell Model with Barriers

Sensor Location	LC5 - Section A (με)			LC5 - Section B (με)		
	Measured	Thin Shells	Thick Shells	Measured	Thin Shells	Thick Shells
Wing	3	1	0	1	1	0
Left Haunch	-5	-10	-8	-7	-13	-14
Middle Top Slab	21	28	29	20	33	33
Right Haunch	-3	-3	-9	-3	-3	-9
Top Right Web	-8	-6	-10	-4	-9	-9
Mid Right Web	-7	-4	-6	-3	-9	-9
Right Bottom Slab	-2	1	5	2	-4	-4
Left Bottom Slab	-2	4	0	1	6	6
Mid Left Web	-6	-4	-7	-2	3	3
Top Left Web	-4	-5	-8	-	-	-

11.12.3Varina-Enon Bridge

Table D130 – Varina-Enon Bridge LC4 Measured and Predicted Transverse Strains – Uniform Surface Loading Shell Model with Barriers

Sensor Location	LC4 - Section D (με)			LC4 - Section C (με)		
	Measured	Thin Shells	Thick Shells	Measured	Thin Shells	Thick Shells
Top Slab	-5.5	0	0	-2	0	0
R Top Slab	-3	-1	-1	-	-	-
R Haunch	-3	-2	-2	-4	-4	-3
R Wing	-19	-23	-22	-	-	-
R Top Web	8.75	11	11	14	8	8
R Bot Web	-4.5	-4	-4	-3	-1	-1
R Bot Slab	-8.75	-10	-10	-5	-6	-6

Table D131 – Varina-Enon Bridge LC5 Measured and Predicted Transverse Strains – Uniform Surface Loading Shell Model with Barriers

Sensor Location	LC5 - Section D (με)			LC5 - Section C (με)		
	Measured	Thin Shells	Thick Shells	Measured	Thin Shells	Thick Shells
Top Slab	-12	-1	-1	-3	0	0
R Top Slab	-6.5	-5	-3	-	-	-
R Haunch	-6.5	-2	-2	-6	-4	-4
R Wing	-26	-27	-26	-	-	-
R Top Web	13	14	15	23	10	10
R Bot Web	-6	-7	-7	-7	-2	-2
R Bot Slab	-14.5	-15	-14	-9	-9	-9

Table D132 – Varina-Enon Bridge LC6 Measured and Predicted Transverse Strains – Uniform Surface Loading Shell Model with Barriers

Sensor Location	LC6 - Section D (με)			LC6 - Section C (με)		
	Measured	Thin Shells	Thick Shells	Measured	Thin Shells	Thick Shells
Top Slab	22.5	20	20	5	11	11
R Top Slab	10	8	7	-	-	-
R Haunch	-9	-6	-6	-7	-6	-6
R Wing	-25	-31	-30	-	-	-
R Top Web	2	-15	-15	-10	-16	-16
R Bot Web	-14	-14	-13	-6	-5	-5
R Bot Slab	-12	-10	-9	-5	-1	-1

11.13 Uniform Surface Loading Shell Model without Barrier Rails

11.13.1Seabreeze Bridge

Table D133 – Seabreeze Bridge LC1 Measured and Predicted Transverse Strains – Uniform Surface Loading Shell Model without Barriers

Sensor Location	LC1 - Section A (με)			LC1 - Section B (με)		
	Measured	Thin Shells	Thick Shells	Measured	Thin Shells	Thick Shells
Wing	-42	-49	-49	-19	-47	-45
Left Top Slab	-1	-5	-5	-5	-14	-15
Mid Top Slab	1	-1	-1	-1	-1	-1
Top Web	4	26	26	8	27	27
Bottom Web	-4	-5	-5	-2	-6	-6
Left Bot. Slab	-7	-15	-15	-2	-9	-9

Table D134 – Seabreeze Bridge LC3 Measured and Predicted Transverse Strains – Uniform Surface Loading Shell Model without Barriers

Sensor Location	LC3 - Section A (με)			LC3 - Section B (με)		
	Measured	Thin Shells	Thick Shells	Measured	Thin Shells	Thick Shells
Wing	-4	-4	-4	-3	-4	-5
Left Haunch	-19	-25	-25	-14	-27	-26
Middle Top Slab	38	27	27	27	24	24
Top Right Web	-5	-17	-17	-11	-18	-18
Mid Right Web	-2	-3	-3	1	2	2
Right Bottom Slab	-2	8	8	1	5	4

Table D135 – Seabreeze Bridge LC4 Measured and Predicted Transverse Strains – Uniform Surface Loading Shell Model without Barriers

Sensor Location	LC4 - Section A (με)			LC4 - Section B (με)		
	Measured	Thin Shells	Thick Shells	Measured	Thin Shells	Thick Shells
Wing	-6	-5	-5	-6	-6	-7
Left Haunch	-19	-17	-17	-17	-23	-23
Middle Top Slab	53	49	49	33	45	45
Top Right Web	-7	-19	-19	-16	-24	-23
Mid Right Web	-3	-5	-5	0	1	1
Right Bottom Slab	-3	-1	0	2	5	4

11.13.2Smart Road Bridge

Table D136 – Smart Road Bridge LC1 Measured and Predicted Transverse Strains – Uniform Surface Loading Shell Model without Barriers

Sensor Location	LC1 - Section A (με)			LC1 - Section B (με)		
	Measured	Thin Shells	Thick Shells	Measured	Thin Shells	Thick Shells
Wing	9	16	15	7	16	15
Left Haunch	1	1	0	-3	-1	-1
Middle Top Slab	1	-1	-1	-1	-1	-1
Right Haunch	0	-2	-2	0	0	-1
Top Right Web	-1	0	0	0	0	0
Mid Right Web	-1	0	0	0	1	1
Right Bottom Slab	1	3	3	1	4	4
Left Bottom Slab	-4	-6	-6	-2	-4	-4
Mid Left Web	2	3	3	0	2	2
Top Left Web	2	4	4	-	-	-

Table D137 – Smart Road Bridge LC2 Measured and Predicted Transverse Strains – Uniform Surface Loading Shell Model without Barriers

Sensor Location	LC2 - Section A (με)			LC2 - Section B (με)		
	Measured	Thin Shells	Thick Shells	Measured	Thin Shells	Thick Shells
Wing	1	0	0	-1	0	0
Left Haunch	-1	-2	-2	-1	0	0
Middle Top Slab	1	-1	-1	0	-1	-1
Right Haunch	1	0	0	1	-1	-2
Top Right Web	2	4	4	1	5	5
Mid Right Web	0	2	2	-1	2	2
Right Bottom Slab	-3	-5	-5	-2	-4	-4
Left Bottom Slab	1	4	4	1	4	4
Mid Left Web	-1	0	0	0	1	1
Top Left Web	-1	0	0	-	-	-

Table D138 – Smart Road Bridge LC3 Measured and Predicted Transverse Strains – Uniform Surface Loading Shell Model without Barriers

Sensor Location	LC3 - Section A (με)			LC3 - Section B (με)		
	Measured	Thin Shells	Thick Shells	Measured	Thin Shells	Thick Shells
Wing	11	16	15	8	16	15
Left Haunch	1	-1	-1	-3	-1	-1
Middle Top Slab	2	-2	-2	-1	-2	-2
Right Haunch	1	-1	-1	1	-2	-2
Top Right Web	2	4	4	1	5	5
Mid Right Web	-1	3	3	1	3	3
Right Bottom Slab	-3	-1	-1	-1	0	0
Left Bottom Slab	-3	-1	-1	-1	0	0
Mid Left Web	1	3	3	0	3	3
Top Left Web	2	4	4	-	-	-

Table D139 – Smart Road Bridge LC4 Measured and Predicted Transverse Strains – Uniform Surface Loading Shell Model without Barriers

Sensor Location	LC4 - Section A (με)			LC4 - Section B (με)		
	Measured	Thin Shells	Thick Shells	Measured	Thin Shells	Thick Shells
Wing	11	16	16	7	16	16
Left Haunch	3	7	6	-6	-8	-8
Middle Top Slab	17	9	9	14	11	11
Right Haunch	-4	-12	-11	-4	-7	-7
Top Right Web	-4	-6	-6	-2	-7	-7
Mid Right Web	-4	-4	-4	-1	-2	-2
Right Bottom Slab	-2	6	6	2	8	7
Left Bottom Slab	-5	-4	-4	-2	-1	-1
Mid Left Web	-3	-2	-2	-1	-2	-2
Top Left Web	-1	-2	-2	-	-	-

Table D140 – Smart Road Bridge LC5 Measured and Predicted Transverse Strains – Uniform Surface Loading Shell Model without Barriers

Sensor Location	LC5 - Section A (με)			LC5 - Section B (με)		
	Measured	Thin Shells	Thick Shells	Measured	Thin Shells	Thick Shells
Wing	3	0	0	1	0	0
Left Haunch	-5	-2	-2	-7	-13	-14
Middle Top Slab	21	27	27	20	31	31
Right Haunch	-3	-10	-10	-3	-9	-9
Top Right Web	-8	-8	-8	-4	-9	-9
Mid Right Web	-7	-5	-5	-3	-4	-4
Right Bottom Slab	-2	4	4	2	6	6
Left Bottom Slab	-2	1	1	1	3	3
Mid Left Web	-6	-6	-6	-2	-4	-4
Top Left Web	-4	-8	-8	-	-	-

11.13.3Varina-Enon Bridge

Table D141 – Varina-Enon Bridge LC4 Measured and Predicted Transverse Strains – Uniform Surface Loading Shell Model without Barriers

Sensor Location	LC4 - Section D (με)			LC4 - Section C (με)		
	Measured	Thin Shells	Thick Shells	Measured	Thin Shells	Thick Shells
Top Slab	-5.5	-1	-1	-2	0	0
R Top Slab	-3	-3	-3	-	-	-
R Haunch	-3	-3	-3	-4	-5	-5
R Wing	-19	-28	-27	-	-	-
R Top Web	8.75	13	13	14	10	10
R Bot Web	-4.5	-4	-4	-3	-1	-1
R Bot Slab	-8.75	-11	-10	-5	-7	-7

Table D142 – Varina-Enon Bridge LC5 Measured and Predicted Transverse Strains – Uniform Surface Loading Shell Model without Barriers

Sensor Location	LC5 - Section D (με)			LC5 - Section C (με)		
	Measured	Thin Shells	Thick Shells	Measured	Thin Shells	Thick Shells
Top Slab	-12	-2	-2	-3	-1	-1
R Top Slab	-6.5	-5	-3	-	-	-
R Haunch	-6.5	-2	-2	-6	-5	-5
R Wing	-26	-31	-30	-	-	-
R Top Web	13	16	16	23	12	13
R Bot Web	-6	-7	-7	-7	-2	-2
R Bot Slab	-14.5	-15	-15	-9	-10	-10

Table D143 – Varina-Enon Bridge LC6 Measured and Predicted Transverse Strains – Uniform Surface Loading Shell Model without Barriers

Sensor Location	LC6 - Section D (με)			LC6 - Section C (με)		
	Measured	Thin Shells	Thick Shells	Measured	Thin Shells	Thick Shells
Top Slab	22.5	19	20	5	11	11
R Top Slab	10	8	6	-	-	-
R Haunch	-9	-6	-7	-7	-7	-7
R Wing	-25	-34	-34	-	-	-
R Top Web	2	-14	-14	-10	-14	-14
R Bot Web	-14	-13	-13	-6	-5	-5
R Bot Slab	-12	-10	-10	-5	-2	-2

11.14 Influence Surface Shell Model with Thin Shells and Barrier Rails

11.14.1Seabreeze Bridge

Table D144 – Seabreeze Bridge LC1 Measured and Predicted Transverse Strains – Influence Surface Loading Shell Model with Barriers

Sensor Location	LC1 - Section A (με)		LC1 - Section B (με)	
	Measured	Thin Shells w/ Barriers	Measured	Thin Shells w/ Barriers
Wing	-42	-43	-19	-34
Left Top Slab	-1	-3	-5	-12
Mid Top Slab	1	0	-1	-1
Top Web	4	28	8	-29
Bottom Web	-4	-9	-2	-3
Left Bot. Slab	-7	-13	-2	7

Table D145 – Seabreeze Bridge LC3 Measured and Predicted Transverse Strains – Influence Surface Loading Shell Model with Barriers

Sensor Location	LC3 - Section A (με)		LC3 - Section B (με)	
	Measured	Thin Shells w/ Barriers	Measured	Thin Shells w/ Barriers
Wing	-4	-3	-3	-5
Left Haunch	-19	-33	-14	-35
Middle Top Slab	38	39	27	42
Top Right Web	-5	-22	-11	-15
Mid Right Web	-2	-5	1	1
Right Bottom Slab	-2	10	1	4

Table D146 – Seabreeze Bridge LC4 Measured and Predicted Transverse Strains – Influence Surface Loading Shell Model with Barriers

Sensor Location	LC4 - Section A (με)		LC4 - Section B (με)	
	Measured	Thin Shells w/ Barriers	Measured	Thin Shells w/ Barriers
Wing	-6	-5	-6	-8
Left Haunch	-19	-15	-17	-29
Middle Top Slab	53	54	33	53
Top Right Web	-7	-26	-16	-20
Mid Right Web	-3	-8	0	3
Right Bottom Slab	-3	0	2	3

11.14.2Smart Road Bridge

Table D147 – Smart Road Bridge LC1 Measured and Predicted Transverse Strains – Influence Surface Loading Shell Model with Barriers

Sensor Location	LC1 - Section A (με)		LC1 - Section B (με)	
	Measured	Thin Shells w/ Barriers	Measured	Thin Shells w/ Barriers
Wing	9	11	7	12
Left Haunch	1	1	-3	-1
Middle Top Slab	1	0	-1	-1
Right Haunch	0	-2	0	0
Top Right Web	-1	-2	0	0
Mid Right Web	-1	0	0	1
Right Bottom Slab	1	7	1	4
Left Bottom Slab	-4	-8	-2	-4
Mid Left Web	2	2	0	3
Top Left Web	2	4	-	-

Table D148 – Smart Road Bridge LC2 Measured and Predicted Transverse Strains – Influence Surface Loading Shell Model with Barriers

Sensor Location	LC2 - Section A (με)		LC2 - Section B (με)	
	Measured	Thin Shells w/ Barriers	Measured	Thin Shells w/ Barriers
Wing	1	-1	-1	0
Left Haunch	-1	-2	-1	-1
Middle Top Slab	1	0	0	-1
Right Haunch	1	2	1	-1
Top Right Web	2	3	1	4
Mid Right Web	0	2	-1	2
Right Bottom Slab	-3	-6	-2	-4
Left Bottom Slab	1	6	1	4
Mid Left Web	-1	0	0	1
Top Left Web	-1	-1	-	-

Table D149 – Smart Road Bridge LC3 Measured and Predicted Transverse Strains – Influence Surface Loading Shell Model with Barriers

Sensor Location	LC3 - Section A (με)		LC3 - Section B (με)	
	Measured	Thin Shells w/ Barriers	Measured	Thin Shells w/ Barriers
Wing	11	11	8	12
Left Haunch	1	-1	-3	-2
Middle Top Slab	2	1	-1	-2
Right Haunch	1	0	1	-1
Top Right Web	2	1	1	4
Mid Right Web	-1	1	1	3
Right Bottom Slab	-3	2	-1	0
Left Bottom Slab	-3	-2	-1	0
Mid Left Web	1	2	0	3
Top Left Web	2	3	-	-

Table D150 – Smart Road Bridge LC4 Measured and Predicted Transverse Strains – Influence Surface Loading Shell Model with Barriers

Sensor Location	LC4 - Section A (με)		LC4 - Section B (με)	
	Measured	Thin Shells w/ Barriers	Measured	Thin Shells w/ Barriers
Wing	11	11	7	14
Left Haunch	3	5	-6	-1
Middle Top Slab	17	13	14	13
Right Haunch	-4	-12	-4	-12
Top Right Web	-4	-9	-2	-6
Mid Right Web	-4	-5	-1	-2
Right Bottom Slab	-2	12	2	7
Left Bottom Slab	-5	-7	-2	-1
Mid Left Web	-3	-3	-1	-2
Top Left Web	-1	-3	-	-

Table D151 – Smart Road Bridge LC5 Measured and Predicted Transverse Strains – Influence Surface Loading Shell Model with Barriers

Sensor Location	LC5 - Section A (με)		LC5 - Section B (με)	
	Measured	Thin Shells w/ Barriers	Measured	Thin Shells w/ Barriers
Wing	3	-1	1	0
Left Haunch	-5	-8	-7	-11
Middle Top Slab	21	38	20	30
Right Haunch	-3	-6	-3	-10
Top Right Web	-8	-12	-4	-9
Mid Right Web	-7	-7	-3	-4
Right Bottom Slab	-2	8	2	6
Left Bottom Slab	-2	0	1	3
Mid Left Web	-6	-7	-2	-6
Top Left Web	-4	-10	-	-

11.14.3Varina-Enon Bridge

Table D152 – Varina-Enon Bridge LC4 Measured and Predicted Transverse Strains – Influence Surface Loading Shell Model with Barriers

Sensor Location	LC4 - Section D (με)		LC4 - Section C (με)	
	Measured	Thin Shells w/ Barriers	Measured	Thin Shells w/ Barriers
Top Slab	-5.5	0	-2	0
R Top Slab	-3	-3	-	-
R Haunch	-3	-3	-4	-4
R Wing	-19	-28	-	-
R Top Web	8.75	13	14	10
R Bot Web	-4.5	-4	-3	-1
R Bot Slab	-8.75	-11	-5	-7

Table D153 – Varina-Enon Bridge LC5 Measured and Predicted Transverse Strains – Influence Surface Loading Shell Model with Barriers

Sensor Location	LC5 - Section D (με)		LC5 - Section C (με)	
	Measured	Thin Shells w/ Barriers	Measured	Thin Shells w/ Barriers
Top Slab	-12	-1	-3	0
R Top Slab	-6.5	-5	-	-
R Haunch	-6.5	-2	-6	-5
R Wing	-26	-28	-	-
R Top Web	13	18	23	15
R Bot Web	-6	-8	-7	-2
R Bot Slab	-14.5	-18	-9	-10

Table D154 – Varina-Enon Bridge LC6 Measured and Predicted Transverse Strains – Influence Surface Loading Shell Model with Barriers

Sensor Location	LC6 - Section D (με)		LC6 - Section C (με)	
	Measured	Thin Shells w/ Barriers	Measured	Thin Shells w/ Barriers
Top Slab	22.5	25	5	11
R Top Slab	10	7	-	-
R Haunch	-9	-10	-7	-6
R Wing	-25	-33	-	-
R Top Web	2	-16	-10	-9
R Bot Web	-14	-16	-6	-6
R Bot Slab	-12	-12	-5	-3

12 Appendix E: Data Processing

As with most data acquisition programs, the output data is presented as time series data. Using the tracking mechanism outlined in Section 3.1.2.4, the time series data was converted to truck position assuming a constant truck speed between longitudinal locations of interest this conversion is demonstrated in Figure E1. In all truck position domain plots all data points between the locations of interest are presented without curve fit or significant changes to the sensor readings, with the exception of zeroing the data to a point of known zero response (e.g. when the truck is off the bridge).

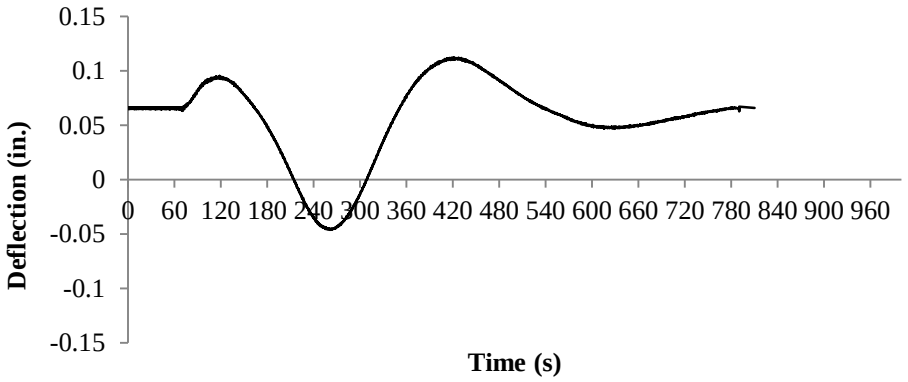

(a)

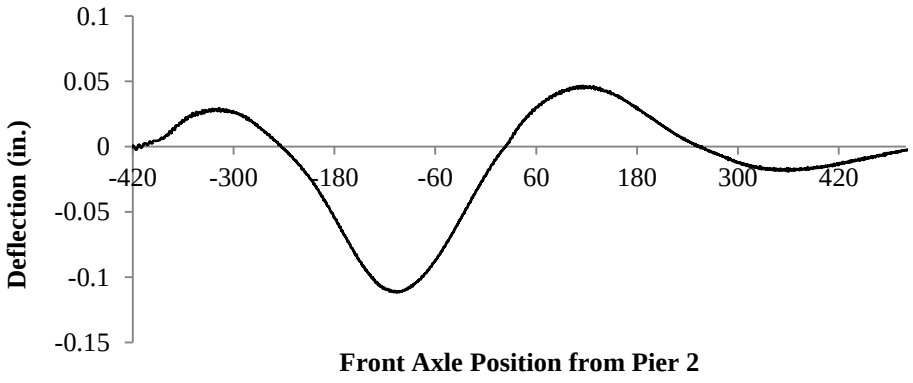

(b)

Figure E1 – Example Comparison of Time Domain Data (a) and Zeroed Front Axle Position Domain Data (b)

Furthermore, the data was zeroed in all cases when the truck was off the bridge. For the Seabreeze and Varina-Enon Bridges, the zero point was when the truck finished its pass was no longer on the structure, but for the Smart Road Bridge, the zero location was prior to the trucks

coming on the bridge. The data presented in the measured response versus truck position plots, as well as tabulated maximum and minimum values was minimally processed. No other manual post-processing was perfomed on the data obtained from the data acquisition systems.

The CR9000X (Seabreeze Bridge only) uses the CRBasic operating system. The only data processing applied to the raw data was the built in CR9000X integration time. This function repeats measurements at a specified rate and averages the results over the specified integration time. This practice reduces the noise output by the square root of the measurements made (CSI 2012). The integration time was set at 40 µs, which is the default when using the RTDAQ Program Generator function for the CR9000X. The CR9000X measures the sensors every 10 µs so each data point is an average of four data data points over 40 µs.

For the STS data acquisition system (Smart Road and Varina-Enon Bridge tests) all data processing was internal. For additional information regarding the internal STS data filtering or conditioning contact Bridge Diagnostics Inc.